Mathematical Problems in Engineering

Mathematical Problems of Multi-Coupling Effect in Geological Engineering

Lead Guest Editor: Gan Feng
Guest Editors: Feng Xiong and Junlong Shang

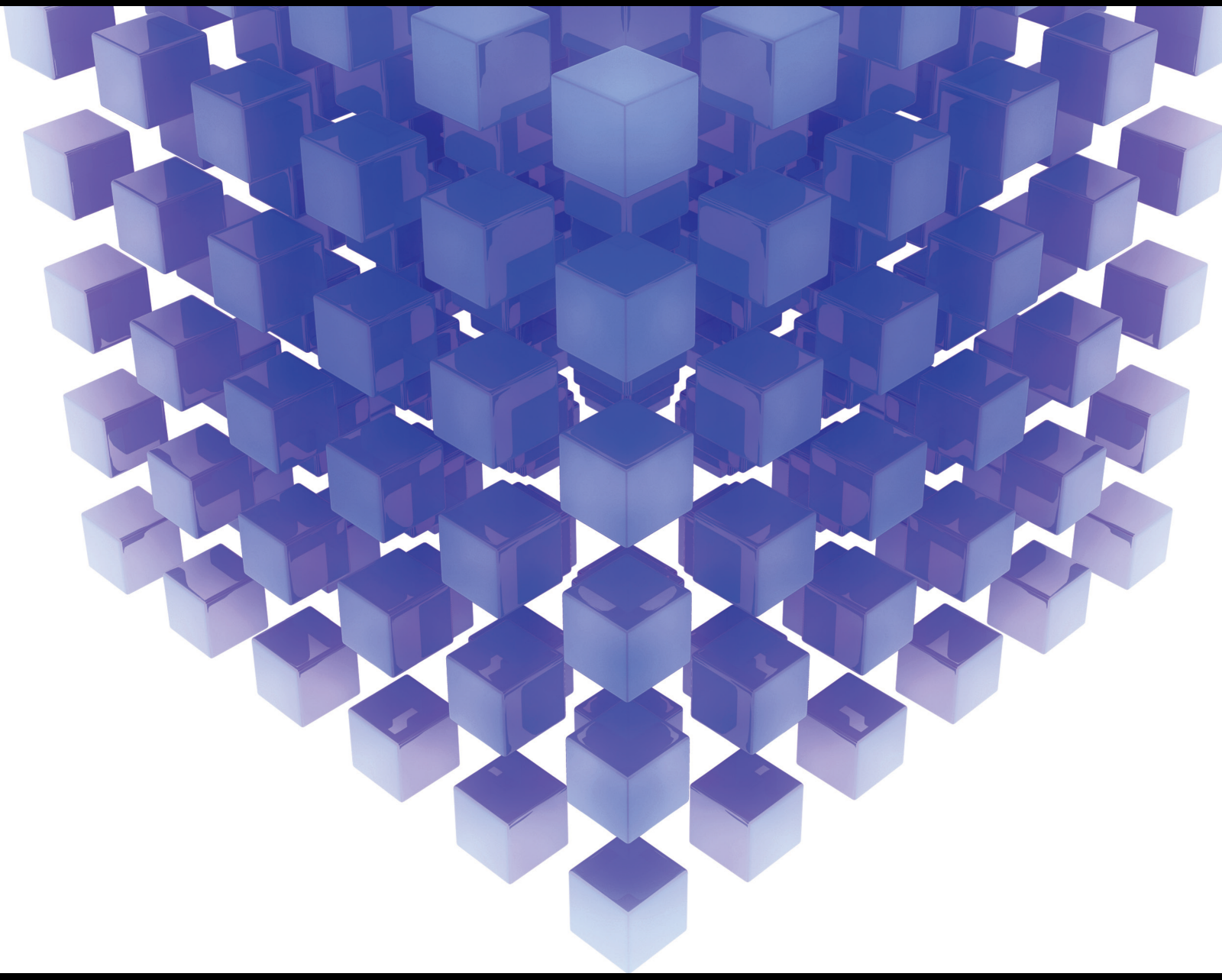

Mathematical Problems of Multi-Coupling Effect in Geological Engineering

Mathematical Problems in Engineering

Mathematical Problems of Multi-Coupling Effect in Geological Engineering

Lead Guest Editor: Gan Feng
Guest Editors: Feng Xiong and Junlong Shang

Contents

Spatial Pattern of Underground Space Development in Major Cities in China: Evaluation and Analysis
Xiaochun Hong and Xiang Ji
Research Article (21 pages), Article ID 2125776, Volume 2021 (2021)

Study on the Formation Mechanism of Rock Burst Caused by Seam Floor Slip under an Ultrathick Conglomerate
Zhiyong Ma, Wenkai Feng, Zhen Wang, Fujin Lin, and Dayong Li
Research Article (9 pages), Article ID 9285832, Volume 2021 (2021)

Strain Incremental Adjustment Method of Cable Force of Composite Saddle Anchor Span of Single-Tower Single-Span Ground-Anchored Suspension Bridge
Long Yu, Wei Xu, Da-bing Zhang, Xu-ming Ma, and Yong-hong Wu
Research Article (13 pages), Article ID 2956496, Volume 2021 (2021)

A Dynamic Method to Predict the Earthquake-Triggered Sliding Displacement of Slopes
Wenkai Feng, Zhichun Lu, Xiaoyu Yi, and Shan Dong
Research Article (11 pages), Article ID 4872987, Volume 2021 (2021)

Experimental and Numerical Analysis of Soil Cracking Characteristics under Evaporation
Di Feng, Jiakun Gong, Xiaodong Ni, and Jie Ren
Research Article (10 pages), Article ID 3790345, Volume 2021 (2021)

Application of Slope Radar (S-SAR) in Emergency Monitoring of the "11.03" Baige Landslide
Xu Wei and Feng Wenkai
Research Article (12 pages), Article ID 2060311, Volume 2021 (2021)

Development and Application of the 3D Model Test System for Water and Mud Inrush of Water-Rich Fault Fracture Zone in Deep Tunnels
Yanhui Guo, Zhijun Kong, Jin He, and Ming Yan
Research Article (16 pages), Article ID 8549094, Volume 2021 (2021)

Investigation on Rock Strata Fracture Regulation and Rock Burst Prevention in Junde Coal Mine
Fengnian Wang, Gan Li, and Chi Liu
Research Article (11 pages), Article ID 2583707, Volume 2021 (2021)

Difference of Microfeatures among Diagenetic Facies in Tight Sandstone Reservoirs of the Triassic Yanchang Formation in the Midwestern Region, Ordos Basin
Jian Shi, Xiaolong Wan, Qichao Xie, Shuxun Zhou, Yan Zhou, Dazhong Ren, and Rongjun Zhang
Research Article (11 pages), Article ID 5611786, Volume 2021 (2021)

Analysis of Microscopic Main Controlling Factors for Occurrence of Movable Fluid in Tight Sandstone Gas Reservoirs Based on Improved Grey Correlation Theory
Xuefei Lu, Fengjuan Dong, Xiaolong Wei, PengTao Wang, Na Liu, and Dazhong Ren
Research Article (8 pages), Article ID 3158504, Volume 2021 (2021)

Innovative Control Technique for the Floor Heave in Goaf-Side Entry Retaining Based on Pressure Relief by Roof Cutting

Guangyuan Yu, Jiong Wang, Jinzhu Hu, Daoyong Zhu, Han Sun, Xingen Ma, Wei Ming, and Wenfei Li

Research Article (17 pages), Article ID 7163598, Volume 2021 (2021)

Hindawi
Mathematical Problems in Engineering
Volume 2021, Article ID 2125776, 21 pages
https://doi.org/10.1155/2021/2125776

Research Article

Spatial Pattern of Underground Space Development in Major Cities in China: Evaluation and Analysis

Xiaochun Hong [1] **and Xiang Ji** [1,2]

[1] *School of Mechanics and Civil Engineering, China University of Mining and Technology, Xuzhou, Jiangsu 221116, China*
[2] *Jiangsu Collaborative Innovation Center for Building Energy Saving and Construction Technology, Jiangsu Vocational Institute of Architectural Technology, Xuzhou, Jiangsu 221116, China*

Correspondence should be addressed to Xiang Ji; jixiang0615@yeah.net

Received 23 October 2021; Revised 15 November 2021; Accepted 17 November 2021; Published 24 December 2021

Academic Editor: Feng Xiong

Underground space development has gradually become an organic part of China's urban development and construction. Comprehensively developing underground space scientifically and rationally to give full play to its comprehensive benefits is the main problem faced by China's underground space development at this stage. This research starts with the measurement of the level of urban underground space (UUS) development. This paper constructs a UUS development level measurement indicator system, which is composed of Construction of UUS (D1), urban economic development indicators (D2), and urban population development indicators (D3), which has 12 secondary indicators, and then we use entropy-TOPSIS method to quantitatively evaluate the development level of underground public space in 39 prefecture-level cities and above in my country and analyze its spatial differentiation. The results show that the urban agglomeration has the characteristics of "high-high" cluster distribution with the development level of underground space. However, the overall level of underground space development in China's major cities is not high and there are apparent differences in the level of UUS development. In terms of spatial distribution, the sustainable development level of cities in the eastern coastal regions of China is relatively high, with towns in the central and northeastern areas ranking second and western towns and northeastern cities ranking the lowest. At the same time, we found that there is a mismatch between the underground space development index and the economic population development index in the evaluation index. Finally, some suggestions are put forward to realize the balanced development of UUS development in our country.

1. Introduction

Since the reform and opening up, with the rapid development of China's economy, the amount of underground space development in China's cities has increased year by year [1]. Since 1997, UUS development regulations have increased year by year (Figure 1). On October 28, 2019, the Global Underground Space Development and Utilization Shanghai Summit released the "Shanghai Declaration" on the global underground space development and utilization. One of the essential topics is: using underground space to save land resources and improve land-use efficiency. Underground space development is to meet current and future human needs for the rapid growth of cities. However, conflicts, resource waste, and environmental effects caused by the fragmented story are becoming increasingly prominent. Therefore, promoting the coordinated development of underground spaces in different regions is essential to promote sustainable urban development [2].

From the perspective of the overall development pattern of UUS in China, the lack of top-level design and overall planning at the national strategic level has led to the widespread waste of underground space resources in different degrees, and the shallow resources in more developed cities have been almost exhausted; the development of underground space industry is uneven; the underground space industry chain still needs to be integrated; the market potential has not been fully tapped; and the investment in the core competitiveness of underground space majors such as scientific and technological innovation, information

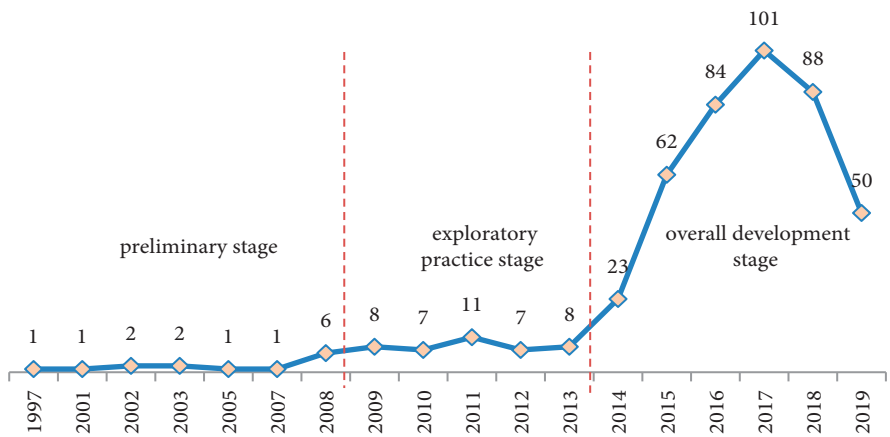

Figure 1: Number of laws and regulations promulgated related to UUS development.

technology services, cutting-edge technology, and intelligence cultivation is insufficient, and these obvious weaknesses need to be improved [3]. Among them, the unbalanced development of UUS is particularly prominent so that it has been affected in the construction of underground space governance system, planning and construction, and information management construction and has been regretted by people from all walks of life committed to the cause of underground space [4]. Under the background of changing urban problems and great differences in the three-dimensional process of urban space, the development of UUS in China is facing the urgent needs of adjustment, optimization, transformation, and upgrading. China has made great progress in the development of UUS, but there are also many conflicts and unresolved problems.

In this context, analyzing the influencing factors of UUS development level in China, revealing the distribution of constituent elements of underground space development level in major cities in China, and exploring the spatial pattern of UUS development level in China can effectively provide decision support and services for the government, enterprises, and the public. The evaluation and analysis of the UUS development level is an essential subject of comprehensive statistics. Related research on the relationship between the development level of urban underground space and economic development and the relationship between the development level of urban underground space and urban population development has been relatively mature [5]. Still, urban underground space is a supplement to urban ground space and its expansion. The current situation is affected by various factors such as the development of ground land, the population distribution of the city in which it is located, population vitality, and the economic development of the city in which it is located. Therefore, it is essential to construct a measurement index system of urban underground space development levels composed of multiple factors, to explore the distribution of urban underground space development levels and various relationships between indicators and the development level of urban underground space [6]. Based on the socio-economic statistical data, this study quantitatively evaluates the development level of UUS in China. By constructing the UUS development level measurement index system including underground space development, urban development, and urban population distribution and comprehensively using the enterprise TOPSIS method, this paper measures the UUS development level and analyzes the spatial pattern, which provides the index model and method support for the evaluation of urban development level in China and provides a reference for the monitoring of urbanization process. The rest of this paper is organized as follows. The second section analyzes the factors affecting UUS development and the measurement method of the development level of UUS through literature review. The third section introduces the research area and data. The fourth section presents the research methods, including constructing the UUS development level index system, the evaluation method, and the index system's weighting method. Next, Section 5 will elaborate on the results and discussion. Finally, in Section 6, this paper gives conclusions, suggests suggestions, and looks forward to the future research process.

2. Literature Review

The research on the measurement of UUS development has a long history, including UUS construction planning, spatial planning, ecological planning, and so on. For example, the density ratio model of UUS is used to measure the density of UUS [7], the low-carbon effect of UUS [8], the sustainability evaluation of UUS [9], the geological environment analysis of UUS [10], the assessment of underground space resources [11], the vitality measurement of UUS [12], the capacity measurement of underground space [13], the accessibility measurement of UUS [14], and so on; we can see that the measurement and design of UUS include all aspects of the whole life cycle from planning to planning, from design to construction, and from management to operation and maintenance. Furthermore, since underground space does not exist independently and is often built under urban roads or urban plots, its development is related to geological characteristics [15], the land price [16], location of development projects [17], urban economic development level [11], advantage degree of UUS construction [18], connection degree with urban planning [19, 20], and the development

potential of UUS [21]. In recent decades, the rapid development of China's economy and the immediate improvement of urbanization have effectively promoted urban population agglomeration. The process of urbanization in developed countries has entered the middle and late stages as early as last century [22]. Therefore, most of the relevant theories and case studies outside China in this study focus on the last century. Relevant theories and case studies on China have been concentrated in recent years. Our research matched this situation with the differences in development stages in different regions.

The function and layout of UUS are critical factors for developing and utilizing UUS. Boivin (1991) described the Montreal underground pedestrian street network, which connected 44 buildings and 9 subway stations [23]. Polzin (1999) analyzed the relationship between subway and land use by challenging some traditional concepts [24]. Admiraal proposed a bottom-up underground space planning idea, involving several studies on three-dimensional land planning conducted by cob in the Netherlands and obtained a practical method called "underground space development potential map." This concept has been used in the southern Netherlands to avoid the waste of resources caused by top-down underground space Planning [25]. Bélanger discussed the development model of the underground network and its future as an essential urban infrastructure and paid attention to the origin and transformation of the Toronto underground pedestrian network to illustrate its multidimensional nature. In addition, Li et al. (2016) studied the demand and driving factors of underground space in three subway station areas [17]. Peng et al. (2018) studied the land use and underground space utilization around two subway stations in Shanghai and Osaka, Japan. By summarizing the analysis of underground space function and layout distribution of the two cases, they outlined the station centre layout and commercial street centre layout modes represented by the two cases. The station centre layout emphasizes the smooth transfer of people between different transportation modes. The central layout of the commercial street not only emphasizes traffic transfer but also emphasizes the intensive commercial development and a higher plot ratio of the space under the urban road. It is pointed out that with the urban development, the development model of urban underground public space will change from the central layout of the commercial street to the central design of the station [26]. Through the above search on the influencing factors affecting the development of UUS and the development and utilization of UUS, we can see that the product of UUS includes urban underground transportation facilities [27], underground municipal facilities [28, 29], underground comprehensive disaster prevention facilities [30], underground public service facilities [31], demand and scale prediction, spatial layout, planning control, facility construction, and so on [32]. Its core is to underground some urban functions to meet users' diversified needs for urban operations [33]. These factors have different effects in promoting the development of urban underground space. The level of economic growth is a decisive factor restricting the development and utilization of urban underground space. Domestic and foreign practical experience shows that when the per capita GDP is 200 to 300 US dollars, the product of urban underground space can gradually satisfy urban economic development that requires rapid development of urban underground space when the per capita GDP is 500 to 2,000 US dollars. When the per capita GDP exceeds 2,000 US dollars, the function and scale of urban underground space development are flourishing. The early development of urban underground love space was affected by the international situation, national protection, and civilian needs. The influence of city scale on urban underground space is reflected in the underground space development index corresponding to the population scale. The large scale of underground space in cities with large population-scale will derive more diverse functions of underground space. Due to the limitations of urban geological conditions, geographic environment, and underground space development technology, urban underground space development has also undergone corresponding changes. In addition, human psychological factors and the shaping of the urban underground space environment affect the vitality of the underground space, thereby affecting urban underground space development.

Urban underground space development is comprehensively affected by the development project itself, urban economic growth, and urban population development. In recent years, China has carried out a large number of UUS development projects. Therefore, it has also established a guidance and control index system with Chinese characteristics formulated by different government agencies [34–37]. At the same time, many scholars began to pay attention to the spatial distribution characteristics of UUS construction. Qualitative and quantitative methods have been used in many studies. The qualitative analysis mainly focuses on the process [38], path [39], and causes [40] of UUS development. Quantitative research specifically includes a comprehensive evaluation of UUS development level [40], driving force analysis of UUS development [41], and trend analysis [3, 42]. The concentration of UUS construction in economically developed areas is the primary trend of UUS construction, which will promote the construction and development of urban agglomeration systems [43]. Although many existing studies have explained the structure of UUS, there are few studies on the integration of underground space, urban development, and population.

Standardization, weighting, and aggregation in measurement methods are usually the basic UUS construction evaluation [44, 45]. The selected weight method is the crucial step of evaluation, and the weight results directly affect the conclusion of the study. Weighting methods can be divided into two categories. The subjective method determines the weight coefficient of each index through a comprehensive consultation score, mainly including the analytic hierarchy process (AHP) [46] and the Delphi method [47]. The subjective weight calculation method is greatly affected by the questionnaire object. Targeted conclusions can be drawn when studying a single city. However, once targeting a more comprehensive range of research objects, this method may exaggerate or reduce the impact of some indicators, and it is

easy to lead to inaccurate reflection of the relationship between indicators. Objective methods determine the weight of each index according to the internal relationship and the change degree between different indexes, mainly including principal component analysis (PCA) [48], entropy method [49], grey associative analysis [50], and factor analysis [51]. Therefore, the selection of enterprise TOPSIS method as the method of this study can meet the needs of this study on the measurement of UUS construction level in different regions and different economic development levels in China.

3. Study Areas and Data

3.1. Study Areas. By the end of 2019, China's total prefecture level and above cities have reached 337, including four municipalities directly under the central government and 222 prefecture-level cities. The development of UUS has a strong correlation with urban economic development [20] and urban population development [52]. At present, the cities that develop UUS on a large scale in China are mainly concentrated in the municipalities directly under the central government, significant regional cities, and other subway construction cities. China's urban construction subway sets a threshold for economic development and urban population. Combined with the previous literature review, we know that the development level of urban underground space is affected by the city scale, urban economic development level, urban geological environment, underground space development technology, and underground space environmental design. In addition, the level of social and economic development promotes the development of urban underground space to different degrees [53]. Therefore, we comprehensively consider the current product of urban underground space in China and find that these factors have a high degree of consistency in the threshold requirements for urban underground space development and urban rail transit construction [54]. Therefore, 39 cities with subway construction in China are selected as the research area of this study (Figure 2).

Up to now, the latest data obtained by various indicators are the data in 2020. But as we know, COVID-19 has had a more significant impact on the city construction in the world by the end of 2019; especially in early 2020, during the period of preventing and controlling COVID-19, China's city construction activities almost stagnated. With the Chinese government's rapid and effective epidemic prevention and control policy, China's urban construction and economic development are gradually on track. However, there is still a big gap compared with the situation in 2019. In particular, the economic development data of Wuhan and Guangzhou affected by the epidemic in 2020 cannot reflect the actual objective status of urban economic development. Therefore, among the different databases of COVID-19, we chose 2019 data as the primary data of this study.

3.2. Data Resource. The data used in this study are from China's official statistical yearbook and research report. Among them, D_{11}~D_{15} data are from the blue book 2020 on UUS construction in China and China Urban Construction Statistical Yearbook 2020; $D_{21} \sim D_{23}$, D_{31}, and D_{32} data are from China Urban Statistics Yearbook 2020; and D_{24} and D_{33} data are from China urban vitality Research Report 2019.

4. Study Methods

4.1. Construction of the Index System. Urban underground space development belongs to the category of urban construction. Urban construction is closely related to urban economic development level, population-scale, and population density. Therefore, UUS development involves urban development, society, economy, and other aspects and is an auxiliary means for planners to select schemes. Therefore, the index system is composed of the UUS construction index (D_1), urban economic development index (D_2), and urban population index (D_3) (Figure 3). Following the principles of independence, practicability, and operability, the index layer is constructed. We determine the measurement index system of the UUS development level, including 3 criteria layer indexes and 12 index layer indexes [55].

The comprehensiveness and simplification of indicators should be fully considered in extracting indicators. Neither important indicators nor too many indicators should be omitted, resulting in cross-indicators and increasing the difficulty of evaluation. The index system should be clearly positioned and structured to avoid redundancy. The meaning of the index is clear and convenient for quantitative evaluation [56]. According to the existing research results and the purpose of this study, the measurement index system of the UUS development level is summarized in Table 1.

4.2. Calculating Index Weight Using Entropy Weight Method. Index weighting is the basis of evaluation. The index system consists of qualitative and quantitative indicators. Therefore, it is necessary to deal with the indicators dimensionless first and then carry out comprehensive weighting. The entropy weight method calculates the weight based on the dimensionless results, which are more objective. The primary process is as follows:

(1) Index dimensional standardization

The indicator units and dimensions in the indicator system are different and cannot be compared directly. Therefore, the indicators need to be dimensionless. When we deal with positive indicators, the standardized calculation method is as follows:

$$x'_{ij} = \frac{x_{ij} - x_j^{\min}}{x_j^{\max} - x_j^{\min}}. \tag{1}$$

When we deal with negative indicators, the standardized calculation method is as follows:

$$x'_{ij} = \frac{x_j^{\max} - x_{ij}}{x_j^{\max} - x_j^{\min}}. \tag{2}$$

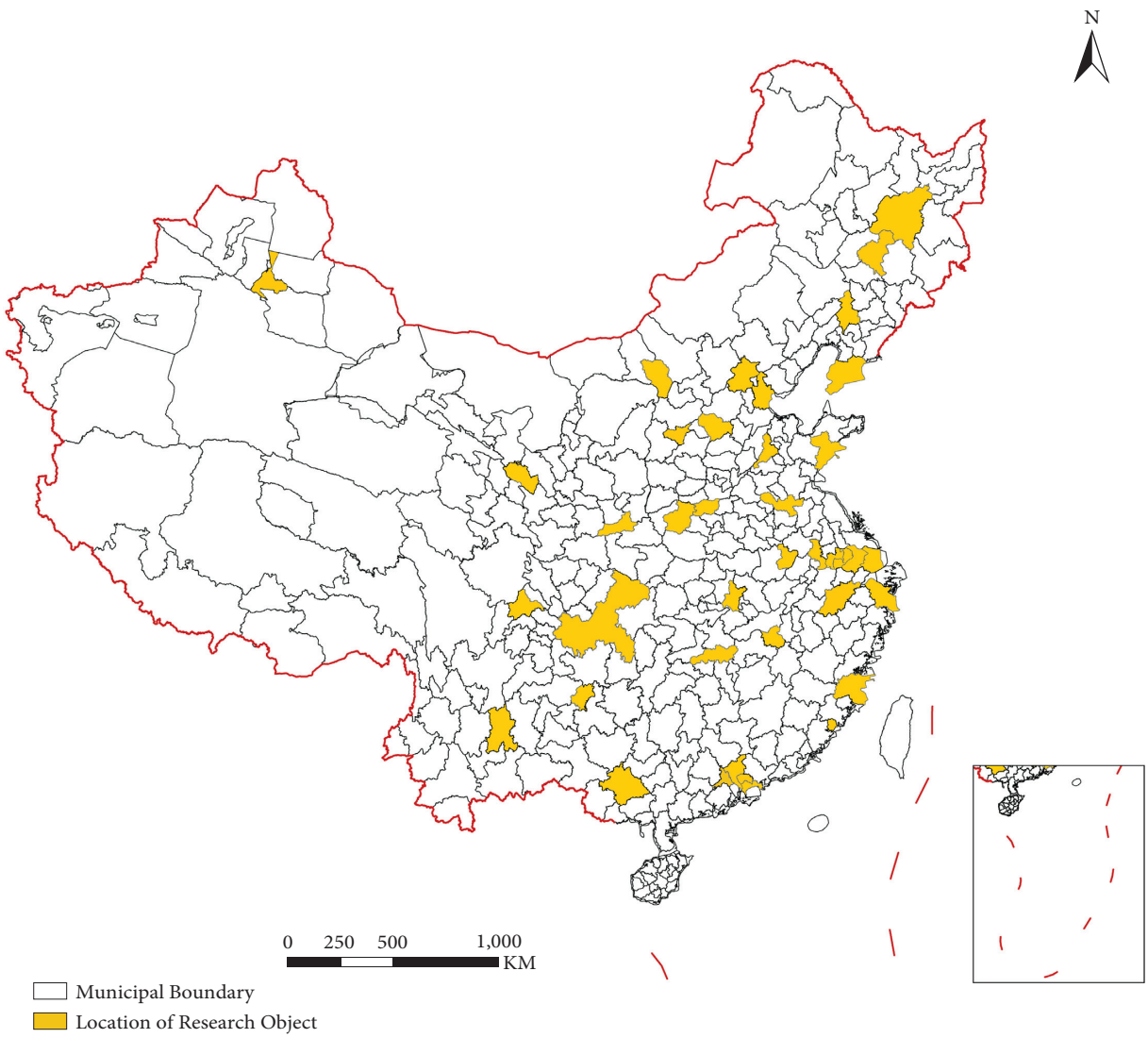

Figure 2: Space distribution of major Chinese cities based on the level measure of underground space development.

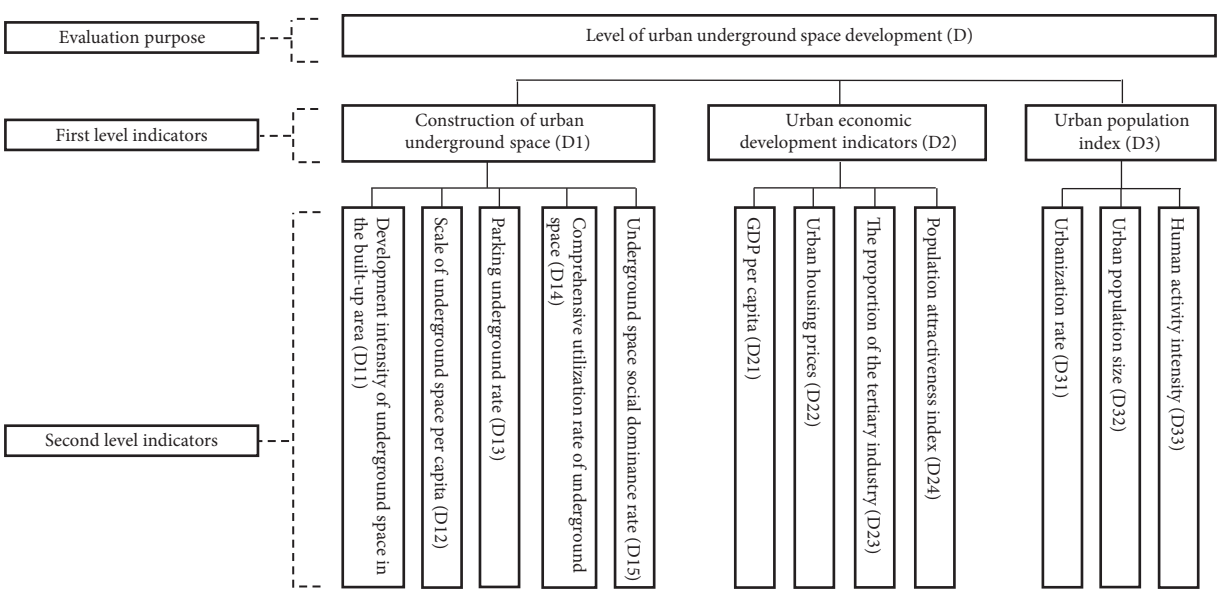

Figure 3: Index system for UUS development level.

Table 1: Summary table of the index system of UUS development level.

Target layer	Code layer	Index layer	Indicator meaning	References
Level of UUS development (D)	Construction of UUS (D_1)	Development intensity of underground space in the built-up area (D_{11})	The ratio of the construction area of underground space development in built-up areas to the area of built-up areas is an important indicator to measure the orderly and connotative development of underground space resource utilization. The higher the development intensity, the higher the economic benefits of land use.	[1, 2, 5, 7]
		Scale of underground space per capita (D_{12})	Per capita ownership of UUS construction area is an important indicator to measure the level of UUS construction.	[4, 7, 8, 11, 20, 21]
		Parking underground rate (D_{13})	The ratio of urban underground parking spaces to the city's actual total parking spaces is an important indicator to measure the functional structure of UUSs and the rational allocation of infrastructure.	[30, 35, 37, 39]
		Comprehensive utilization rate of underground space (D_{14})	The proportion of urban underground public service space to the total scale of underground space measures the degree of comprehensive utilization of UUS market-oriented development.	[10, 12, 18–20]
		Underground space social dominance rate (D_{15})	The ratio of urban ordinary underground space to the total underground space is an index that measures the degree of social and policy-led development of UUS development.	[8, 10, 12, 16, 17, 19]
	Urban economic development indicators (D_2)	GDP per capita (D_{21})	GDP per capita is an effective tool for people to understand and grasp the macroeconomic performance of a country or region and is often used as an indicator of economic development in development economics.	[42–45]
		Urban housing prices (D_{22})	Urban housing price is a measure of the value of urban land.	[15, 16, 18, 19]
		The proportion of the tertiary industry (D_{23})	The proportion of the tertiary industry is an indicator to measure the amount of building development of the city's tertiary industry.	[39, 41]
		Population attractiveness index (D_{24})	Using the city's resident population attractiveness index, the ratio of the new inflow resident population to the new inflow resident population in all cities across the country is expressed, and the urban development trend is objectively presented.	[39–41]
	Urban population index (D_3)	Urbanization rate (D_{31})	It is a measure of urbanization.	[14–16]
		Urban population size (D_{32})	Within the urban area, the total population is counted according to the permanent resident population.	[9–11, 37, 38]
		Human activity intensity (D_{33})	Urban night light value intensity can be used as an effective form of representation of human activity.	[39, 41]

(2) Normalization of index results

We further translate the standardized values according to a specific range to unify the index results into a comparable area, to eliminate the negative value or poor comparability of modelling results after dimensionless processing of some indexes. The standardized numerical translation calculation method is as follows:

$$x_{ij}'' = H + x_{ij}', \tag{3}$$

where H is the translation amplitude of the standardized value, taken as 1.

(3) Dimensionless index value

The index value is dimensionless. Generally, the data is dimensionless by using the numerical specific gravity distribution. The calculation method is as follows:

$$y_{ij} = \frac{x''_{ij}}{\sum_{i=1}^{n} x''_{ij}}. \tag{4}$$

(4) Calculation of entropy

$$e_j = -\frac{1}{\ln n} \sum_{i=1}^{n} y_{ij} \ln y_{ij}. \tag{5}$$

(5) Calculation of difference coefficient

$$g_j = 1 - e_j, \tag{6}$$

where $j = 1, 2, \ldots p$.

(6) Calculation of index weight

$$\omega_j = \frac{g_j}{\sum_{j=1}^{P} g_j}, \tag{7}$$

where $j = 1, 2, \ldots p$.

4.3. TOPSIS Model. TOPSIS is a typical measurement method, which can make full use of the information of the original data, and its results can accurately reflect the gap between the evaluation schemes. The basic process of the model is: first unify the original data matrix with the index type (generally forward processing, i.e., the larger the value of the index, the better the representative object itself. The indicators constructed in this study are positive indicators), obtain the forward matrix, standardize the forward matrix to eliminate the influence of each index dimension, find the best scheme and the worst scheme in the limited system, then calculate the distance between each evaluation object and the best approach and the worst scenario, and obtain the relative proximity between each evaluation object and the best system, which can be used as the basis for evaluating the advantages and disadvantages. This method has no strict restrictions on the distribution of data and the content of samples, and the data calculation is relatively simple. The specific steps are as follows.

4.3.1. Matrix Standardization. Assuming that there are n objects to be evaluated and M evaluation indexes (which have been forward converted through the first step), the forward matrix is as follows:

$$X_{ij} = \begin{bmatrix} x_{11} & x_{12} & \ldots & x_{1m} \\ x_{21} & x_{21} & \ldots & x_{2m} \\ \ldots & \ldots & \ldots & \ldots \\ x_{n1} & x_{n2} & \ldots & x_{nm} \end{bmatrix}. \tag{8}$$

The processed data is subjected to vector normalization, and the following formula transforms the vector normalization:

$$b_{ij} = \frac{a_{ij}}{\sqrt{\sum_{i=1}^{x_{ij}} a_{ij}^2}, \quad i = 1, \ldots, m,\ j = 1, \ldots, n}. \tag{9}$$

The most significant feature of this method is that after normalization, the square sum of the same attribute value of each scheme is 1. Therefore, it is often used to calculate the Euclidean distance between each scheme and a virtual scheme (such as ideal solution point or negative ideal solution point) and weight it to obtain the weighted normalization matrix.

Assuming that there are n evaluation objects, the standardized matrix of m evaluation indexes is Z, as follows:

$$Z = \begin{bmatrix} z_{11} & z_{12} & \ldots & z_{1m} \\ z_{21} & z_{21} & \ldots & z_{2m} \\ \ldots & \ldots & \ldots & \ldots \\ z_{n1} & z_{n2} & \ldots & z_{nm} \end{bmatrix}. \tag{10}$$

4.3.2. Determining Positive Ideal Solution C^* and Negative Ideal Solution. Suppose the j-th attribute value of positive ideal solution C^* is c_j^*, and assume that the j-th attribute value of negative ideal solution C^0 is c_j^0.

$$\begin{aligned} &\text{positive ideal solution } c_j^* = \max_i c_{ij}\ j = 1, 2, \ldots n, \\ &\text{negative ideal solution } c_j^0 = \min_i c_{ij}\ j = 1, 2, \ldots n. \end{aligned} \tag{11}$$

4.3.3. Calculating the Euclidean Distance between Each Scheme and the Ideal Point and the Negative Ideal Point. According to Euclidean distance, the distance d_i^* and d_i^0 between scheme i and the ideal and negative points are calculated as follows:

$$d_i^* = \left[\sum_{j=1}^{n} \left(c_{ij} - \max_i \{c_{ij}\}\right)^2\right]^{1/2}, \tag{12}$$

$$d_i^0 = \left[\sum_{j=1}^{n} \left(c_{ij} - \min_i \{c_{ij}\}\right)^2\right]^{1/2}. \tag{13}$$

4.3.4. Calculating the Comprehensive Measure Index. We use equations (11) and (12) to calculate the distance d_i^* from each scheme to the positive ideal solution and the distance d_i^0 from the negative ideal solution. We then calculate the comprehensive evaluation index C_i for each city i. The calculation method is as follows:

$$C_i = \frac{d_i^0}{d_i^0 + d_i^*}. \tag{14}$$

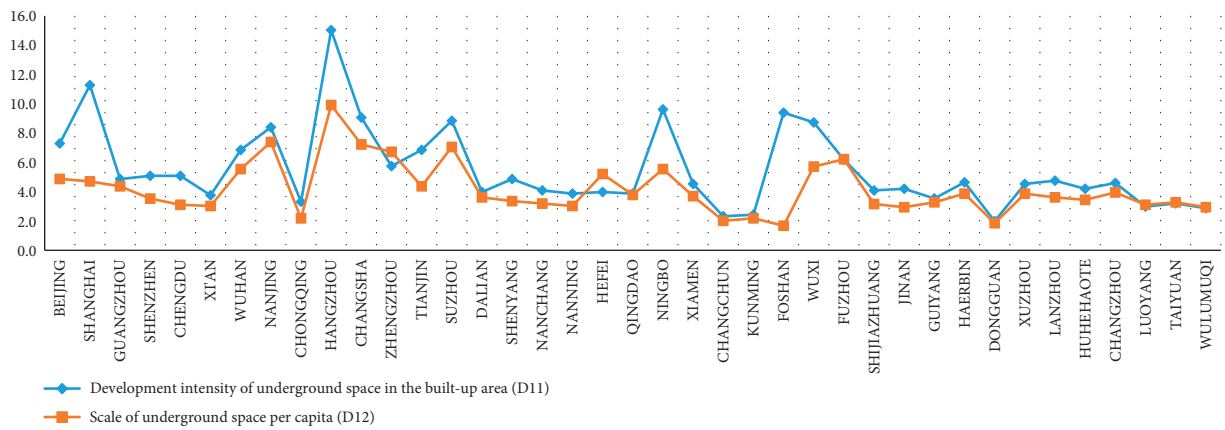

Figure 4: The distribution of the data for the indicators D_{11} and D_{12}.

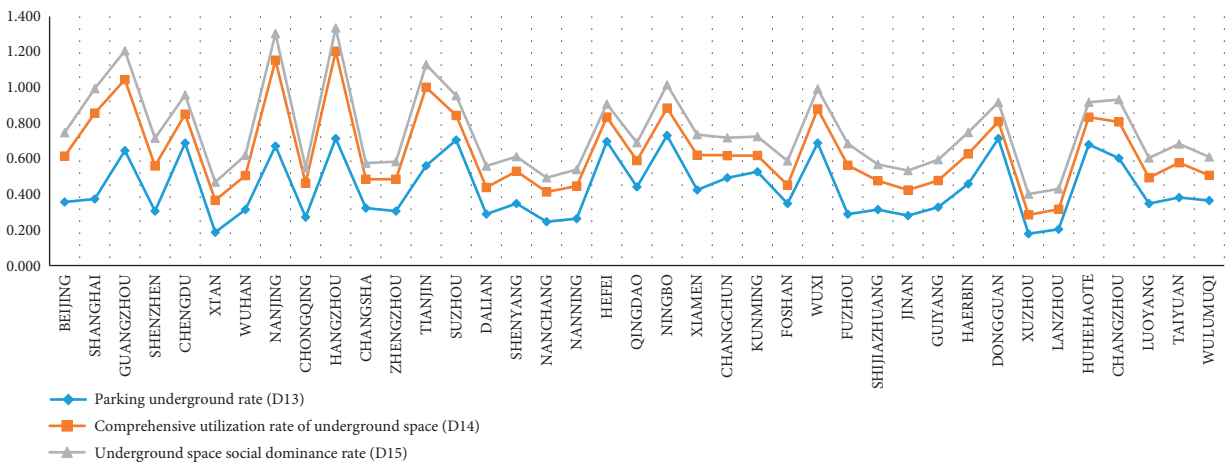

Figure 5: The distribution of the data for the indicators D_{13}, D_{14}, and D_{15}.

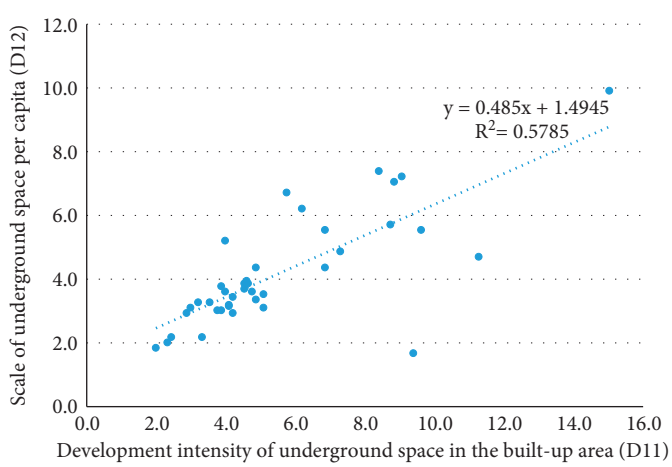

Figure 6: Correlation analysis of D_{11} and D_{12}.

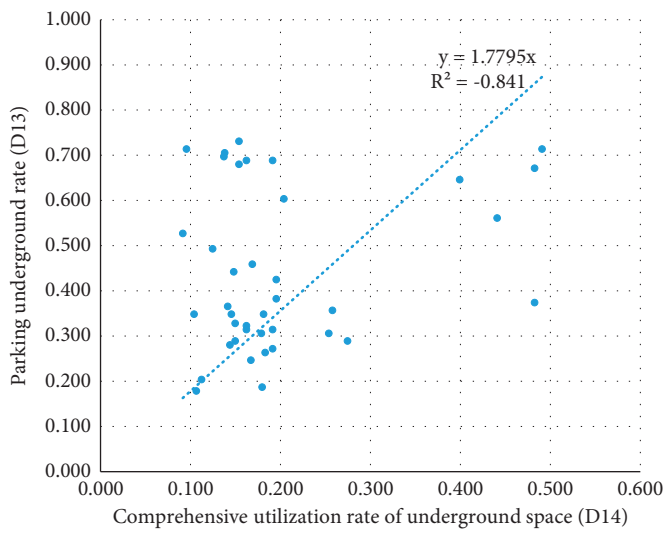

Figure 7: Correlation analysis of D_{14} and D_{13}.

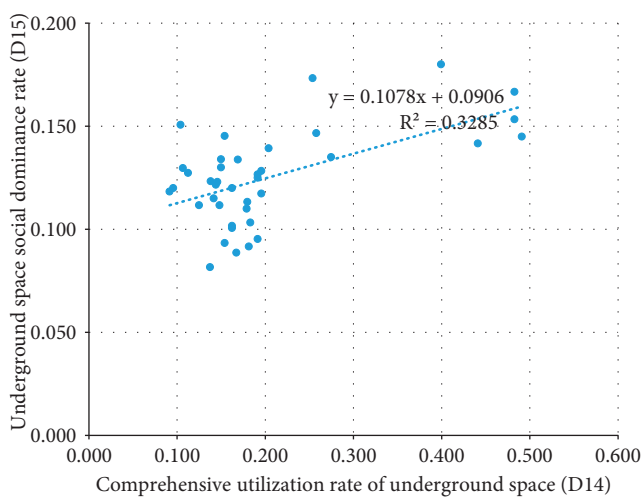

Figure 8: Correlation analysis of D_{14} and D_{15}.

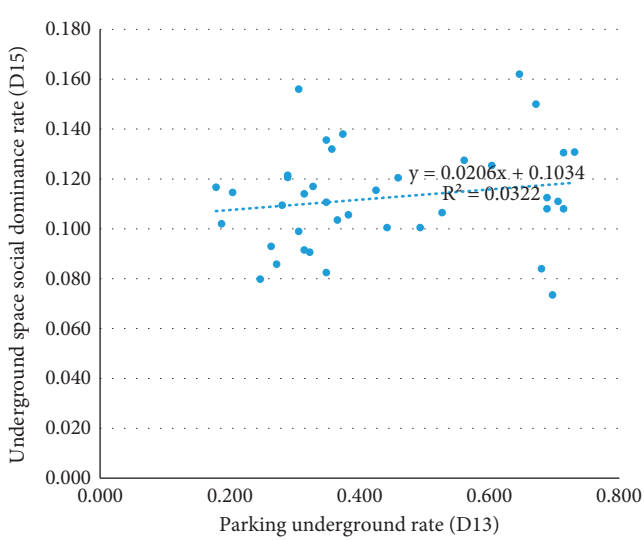

Figure 9: Correlation analysis of D_{13} and D_{15}.

5. Results and Discussion

5.1. Analysis of Results

5.1.1. Statistical Results of Indicators. Our evaluation of the development intensity of underground space in the built-up area (D11) shows that the top ten cities are Hangzhou, Shanghai, Ningbo, Foshan, Changsha, Suzhou, Wuxi, Nanjing, Beijing, and Wuhan (Figure 4)). Our evaluation of the per-capita size of underground space (D12) shows that the top ten cities are Hangzhou, Nanjing, Changsha, Suzhou, Zhengzhou, Fuzhou, Wuxi, Ningbo, Wuhan, and Beijing (Figure 4). The evaluation result of the parking underground rate (D13) shows that the top ten cities are Ningbo, Dongguan, Hangzhou, Suzhou, Hefei, Chengdu, Hohhot, Changzhou, Wuxi, Nanjing, and Guangzhou (Figure 4). Our evaluation of comprehensive utilization rate of underground space (D14) shows that the top ten cities are Hangzhou, Shanghai, Nanjing, Tianjin, Guangzhou, Fuzhou, Beijing, Changzhou, Taiyuan, and Wuhan (Figure 5). Thus, it can be seen that although the ranking of cities corresponding to various indicators of UUS construction is slightly different, it is relatively concentrated in Shanghai, Hangzhou, Nanjing, Shenzhen, Guangzhou, Suzhou, and other economically developed cities.

However, the measurement of UUS development level is composed of UUS construction, economic development, and population development. For example, as Beijing is the capital of China, its underground space development is greatly affected by the administration. Although UUS development is significant and the degree of UUS construction is low, as the economic centre of northern China, Beijing's population, and economic development level are among the best in China. Hence, its UUS development level is not low. According to the obtained UUS construction data, we found that the development intensity of underground space in the built-up area (D11) and scale of underground space per capital (D12) has a robust correlation (Figure 6). There is also a strong positive correlation between the parking underground rate (D13), comprehensive utilization

Table 2: Summary of measurement results of UUS development level.

	D	D_1	D_2	D_3
Beijing	0.63103	0.4525	0.85364	0.69048
Shanghai	0.66136	0.59111	0.74375	0.75697
Guangzhou	0.65725	0.62183	0.7028	0.56872
Shenzhen	0.62155	0.45241	0.7427	0.73008
Chengdu	0.50886	0.43607	0.43974	0.58511
Xi'an	0.40182	0.19748	0.34907	0.56097
Wuhan	0.43865	0.36847	0.46542	0.43258
Nanjing	0.63474	0.75647	0.503	0.52357
Chongqing	0.29661	0.15285	0.28027	0.4904
Hangzhou	0.68897	0.83627	0.54571	0.61085
Changsha	0.44395	0.37548	0.37513	0.53255
Zhengzhou	0.41036	0.33867	0.39271	0.47256
Tianjin	0.47549	0.56889	0.34839	0.43857
Suzhou	0.54409	0.54431	0.494	0.53159
Dalian	0.29167	0.2969	0.22065	0.26324
Shenyang	0.31455	0.21731	0.25803	0.36588
Nanchang	0.26733	0.14448	0.20228	0.36742
Nanning	0.37518	0.18539	0.28978	0.49776
Hefei	0.42277	0.39819	0.33864	0.41257
Qingdao	0.35766	0.29766	0.35471	0.33448
Ningbo	0.49194	0.58199	0.35155	0.39477
Xiamen	0.48212	0.35245	0.45416	0.52579
Changchun	0.24641	0.28512	0.15903	0.16565
Kunming	0.40438	0.31411	0.32006	0.45475
Foshan	0.46103	0.38683	0.31904	0.57703
Wuxi	0.48672	0.53672	0.40963	0.38675
Fuzhou	0.37854	0.42044	0.31571	0.35329
Shijiazhuang	0.25176	0.19928	0.2339	0.27941
Jinan	0.32663	0.24047	0.32733	0.34443
Guiyang	0.37401	0.394	0.24138	0.45393
Harbin	0.32989	0.3784	0.34589	0.10158
Dongguan	0.48021	0.39589	0.35968	0.59385
Xuzhou	0.26595	0.25839	0.14612	0.31533
Lanzhou	0.36286	0.25227	0.27358	0.43259
Huhehaote	0.38499	0.38486	0.29974	0.31561
Changzhou	0.41430	0.46412	0.34372	0.29199
Luoyang	0.22920	0.26472	0.11211	0.21258
Taiyuan	0.38161	0.28277	0.27436	0.4355
Wulumuqi	0.35289	0.2429	0.36047	0.32129

Table 3: Corresponding standards for the closeness of UUS development level.

Rank	Range of D	Level of development	Number of cities	Percentage of cities
Level 1	> 0.8	Excellent	0	0
Level 2	0.6~0.8	Good	6	15.39
Level 3	0.3~0.6	General	15	38.46
Level 4	0~0.3	Poor	18	46.15

rate of underground space (D14), underground space social governance rate (D15), and other indicators Figures 7–9) There is a strong correlation. In addition, there is also a strong correlation between UUS construction indicators and urban population data and urban economic development data, indicating that urban population data and urban economic development play a positive role in promoting the development of UUS.

5.1.2. Analysis of Final Measurement Results. The underground space development level of 39 major cities in China calculated by the index system constructed in this study is shown in Table 2. According to the research results of existing scholars, the closeness degree is divided into four grade standards to characterize the development degree corresponding to the development level of UUS in the study area, as shown in Table 3.

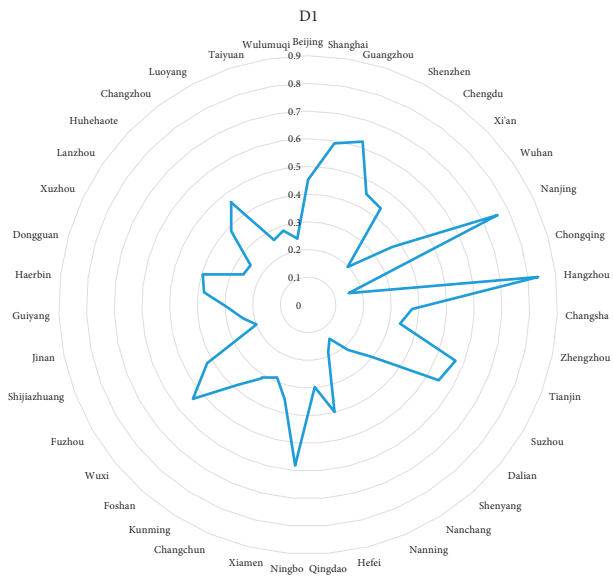

Figure 10: Radar chart of evaluation results of $D1$.

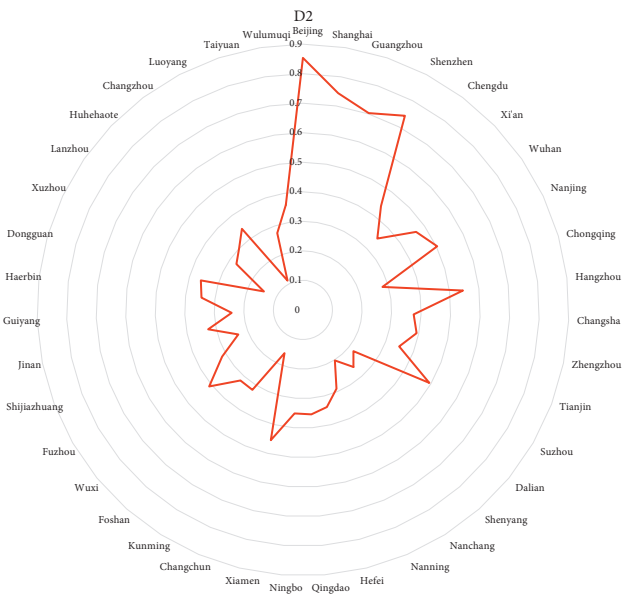

Figure 11: Radar chart of evaluation results of $D2$.

Figure 12: Radar chart of evaluation results of $D3$.

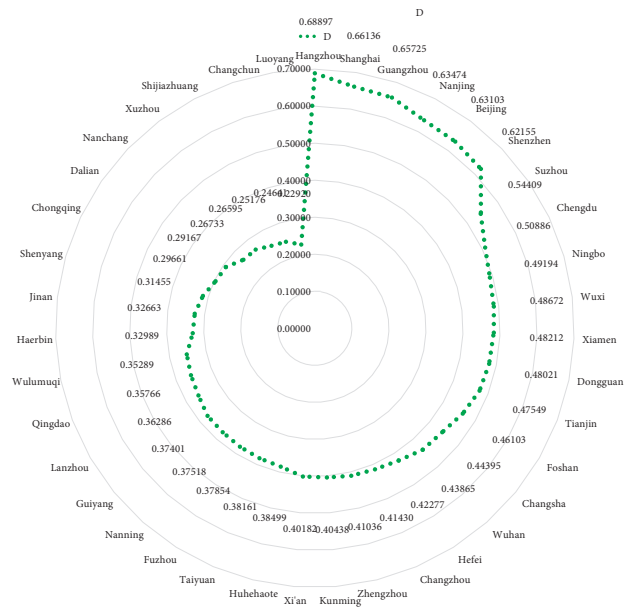

Figure 13: Radar chart of evaluation results of D.

Among the first-level indicators, the underground space development of Nanjing and Hangzhou far exceeds that of other cities (Figure 10); the urban economic development of Beijing and Shanghai far exceeds that of other cities (Figure 11); and the population development indicators of Shanghai, Shenzhen, and Hangzhou are relatively high (Figure 12). Thus, we can see that the distribution of the three indicators is relatively reasonable, and the index results do not fully tend to any city. Furthermore, this also proves the rationality of constructing the evaluation index system in this study. Under the influence of the first-class indicators that comprehensively reflect the development level of UUS, we can see that Hangzhou has the highest development level of underground space in major cities in China, with a D value of 0.68897, which has not reached the "excellent" level.

Shanghai, Guangzhou, Nanjing, Beijing, and Shenzhen (Figure 13), accounting for 15.39% of the total sample (Table 3). Nearly half of the evaluation results of UUS development levels are between 0 and 0.3. The main cities selected in this study are cities with much underground space development in recent years. We can see that the underground space development level is low overall and has an excellent local effect.

Figure 14 shows the distribution of the results of the UUS development level. The results show that the top ten cities are Hangzhou, Shanghai, Guangzhou, Nanjing, Beijing,

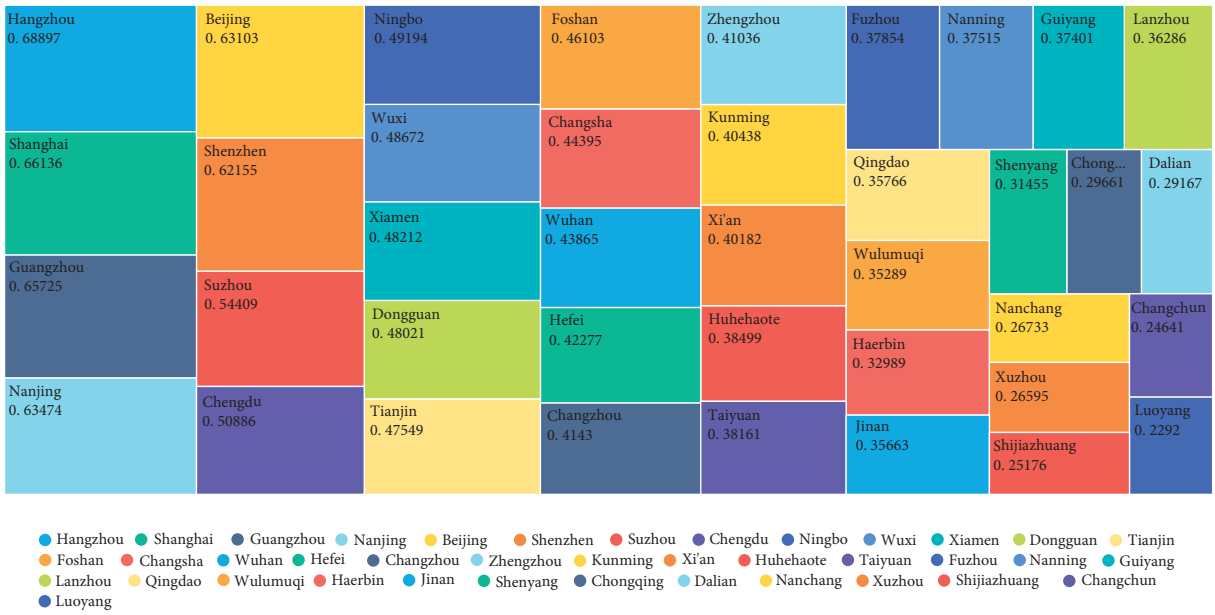

Figure 14: Results distribution of D.

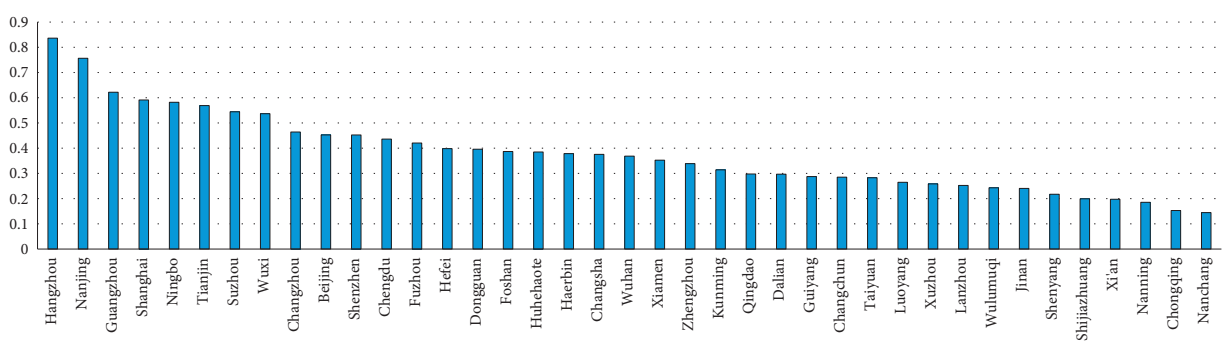

Figure 15: Distribution of calculation results of underground space development index.

Shenzhen, Suzhou, Chengdu, Ningbo, and Wuxi. Except that Chengdu is a central city and Beijing is a northern city, other cities are located in the southeast coastal provinces. In addition, due to the implementation of transit-oriented development (TOD) to guide urban development in recent years, many subway lines have been built, promoting the improvement of the development level of UUS.

5.2. Spatial Distribution of Underground Space Development Level

5.2.1. Spatial Distribution Analysis of Subindicators

Distribution Law of Underground Space Development Index Results. The development index of UUS is highly consistent with the spatial distribution of China's three major urban agglomerations. According to Tables 2 and 3, Hangzhou is in the first level; Nanjing and Guangzhou are in the second level' and the top ten are Shanghai, Ningbo, Tianjin, Suzhou, Wuxi, Changzhou, and Beijing (Figure 15), mainly distributed in the urban agglomerations of Yangtze River Delta and Beijing-Tianjin-Hebei metropolitan region. The urban agglomerations of Pearl River Delta are lower than other urban agglomerations. The low underground space development intensity causes the problem and per capita underground space area index (Figure 16).

Distribution Law of Urban Economic Development Index Results. Beijing, Shanghai, Shenzhen, and Guangzhou (Figure 17) rank at the forefront of urban economic development indicators. These cities are China's economic central cities. However, compared with the development indicators of UUS, only the economic development indicators of Guangzhou match the development indicators of underground space. The urban agglomerations of Yangtze River Delta economic development index is better than that of Pearl River Delta and Beijing-Tianjin-Hebei region; a new urban economic development centre with Chengdu-Chongqing region as the core has been formed in the central part (Figure 18).

By comparing and analyzing the distribution law of UUS development indicators and urban economic development

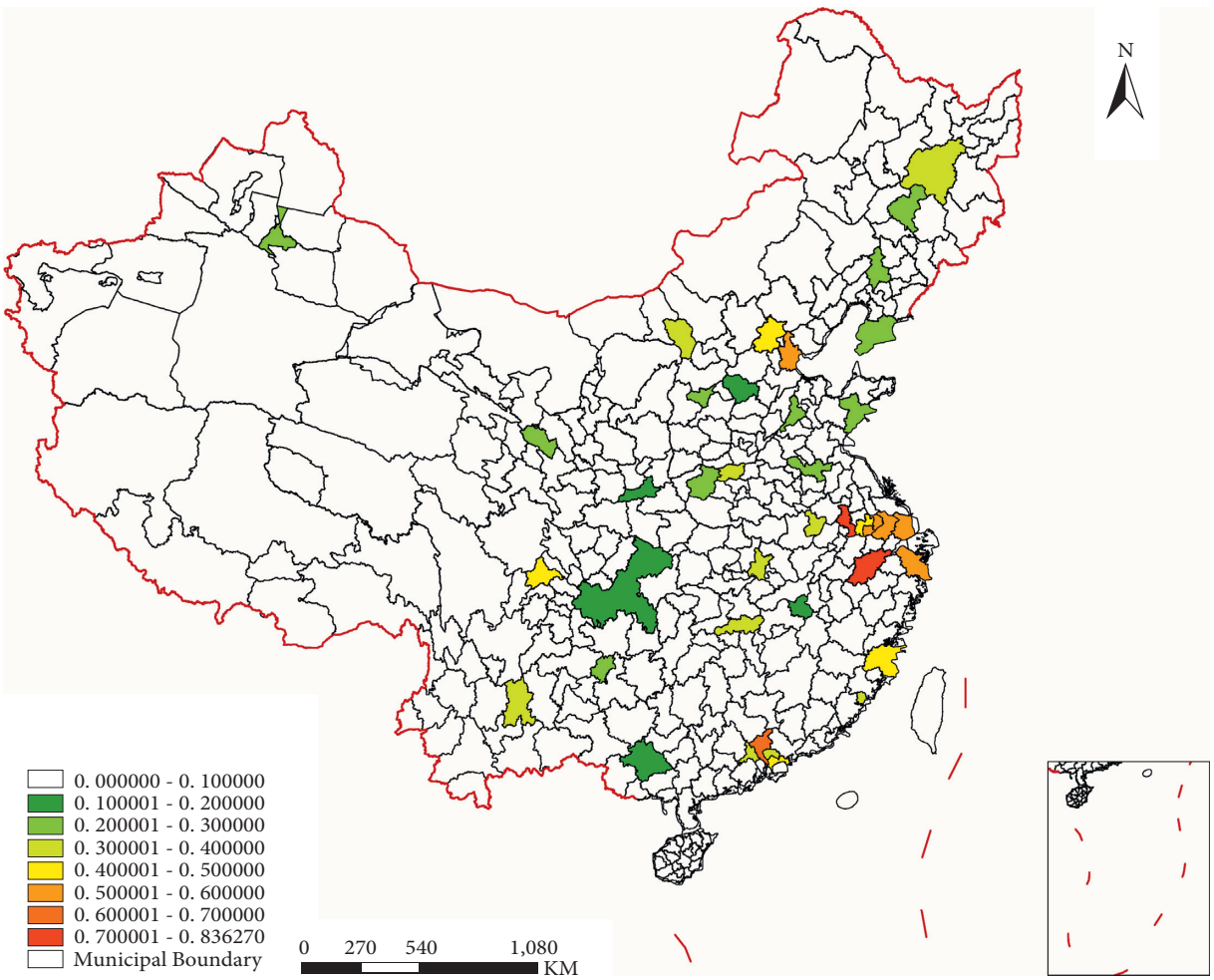

Figure 16: Spatial distribution of underground space development index calculation results.

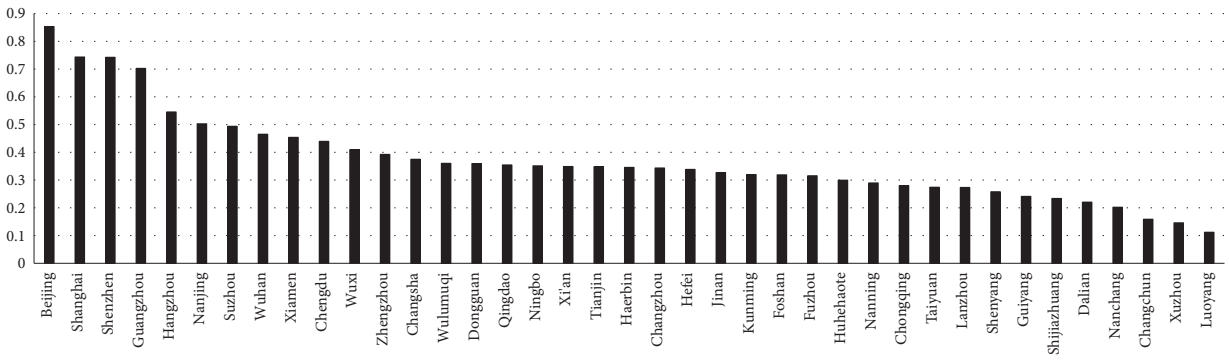

Figure 17: Distribution of calculation results of urban economic development indicators.

indicators, we can see that the measurement results of underground space development in Hangzhou, Nanjing, Wuxi, and Changzhou are higher than economic development, which does not match the relationship between UUS and urban economic population (Figure 19). This is mainly because these regions' early urbanization and economic development are much higher than those of other regions, making these cities realize earlier that we can solve the contradiction with economic and population expansion through the development of underground space. Guangzhou, Shenzhen, and other cities in the Pearl River Delta are located in hilly areas, with a good level of landscape economic development and low urban land utilization rate. Therefore, the demand for underground space development will be below. However, in recent years, there has been no new land development in Shenzhen. In the future, underground space development for urban expansion will promote the further development of UUS.

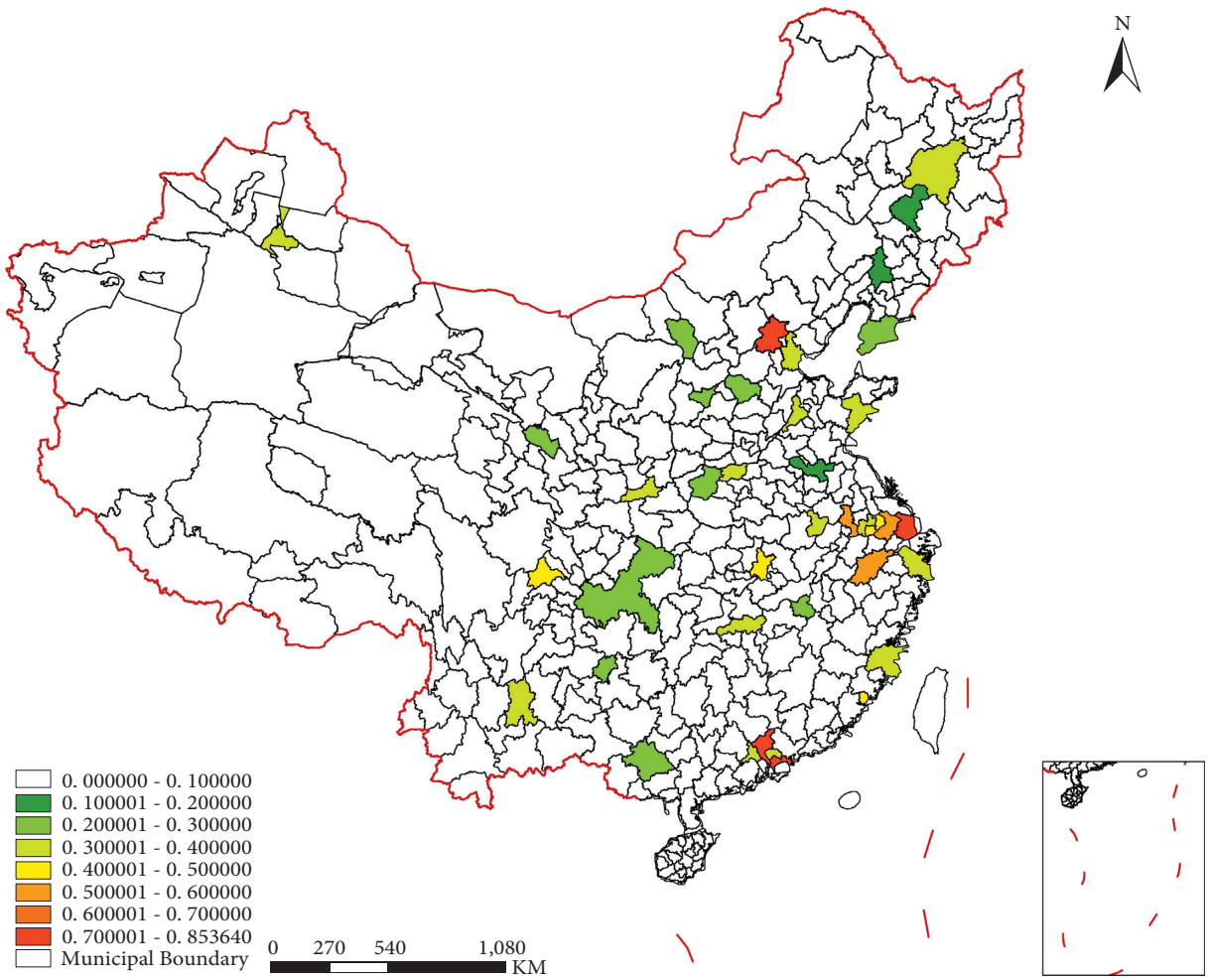

Figure 18: Spatial distribution of calculation results of urban economic development indicators.

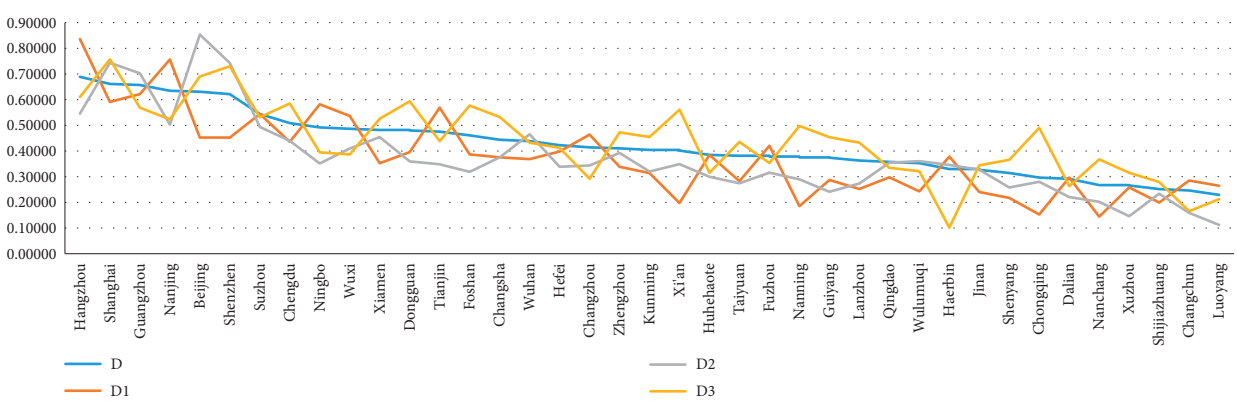

Figure 19: Comparative analysis diagram of the measurement results of each index.

Distribution Law of Urban Population Development Index Results. "Hu Huanyong line" is the comparison line for dividing China's population density proposed by Chinese geographer Hu in 1935. According to "Hu Huanyong line," the southeast half accounts for 43.8% of the national land area and 94.1% of the total population. "Hu Huanyong line" has also become the dividing line of urbanization level to some extent. The urbanization level of most of the southeast provinces, autonomous regions, and cities along this line is higher than the national average level. Most of the northwest provinces and regions are lower than the national average level. In this study, underground space development is based on dense population and a high level of economic development. Therefore, the main cities are concentrated in the south of the "Hu Huanyong line"

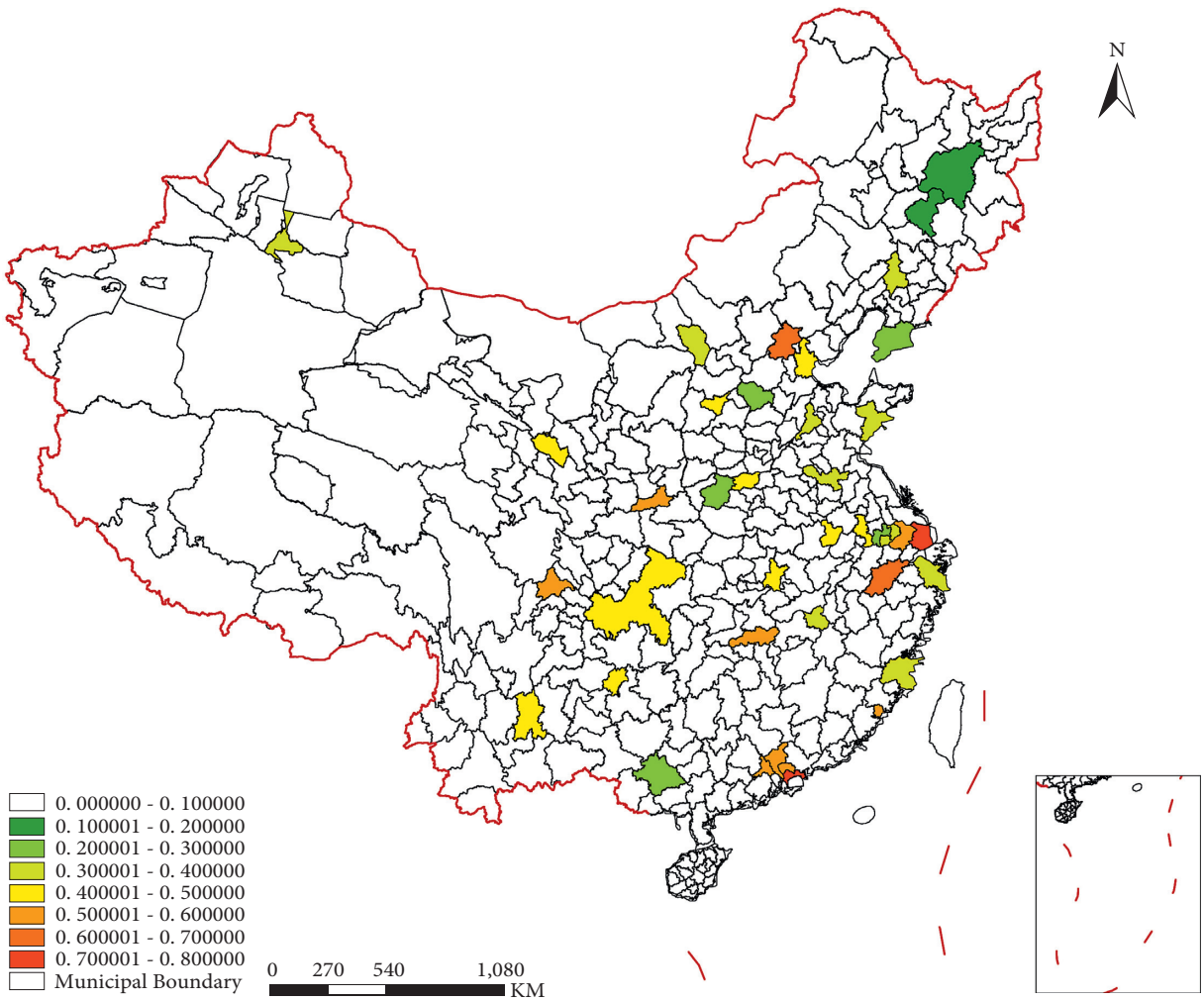

Figure 20: Spatial distribution of urban population development level indicators.

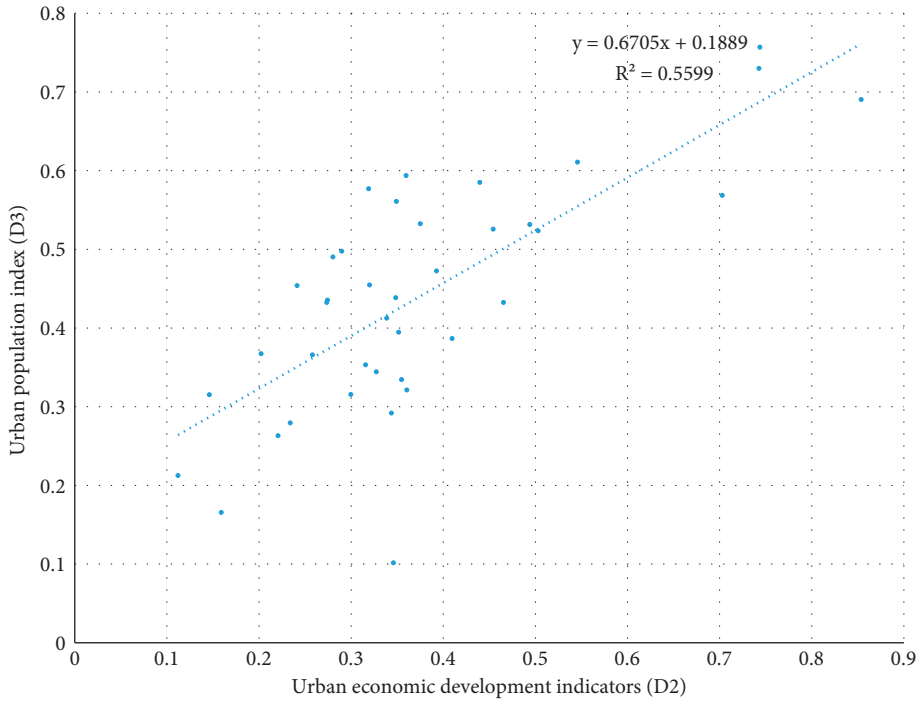

Figure 21: Correlation of the index D_2 and the index D_3.

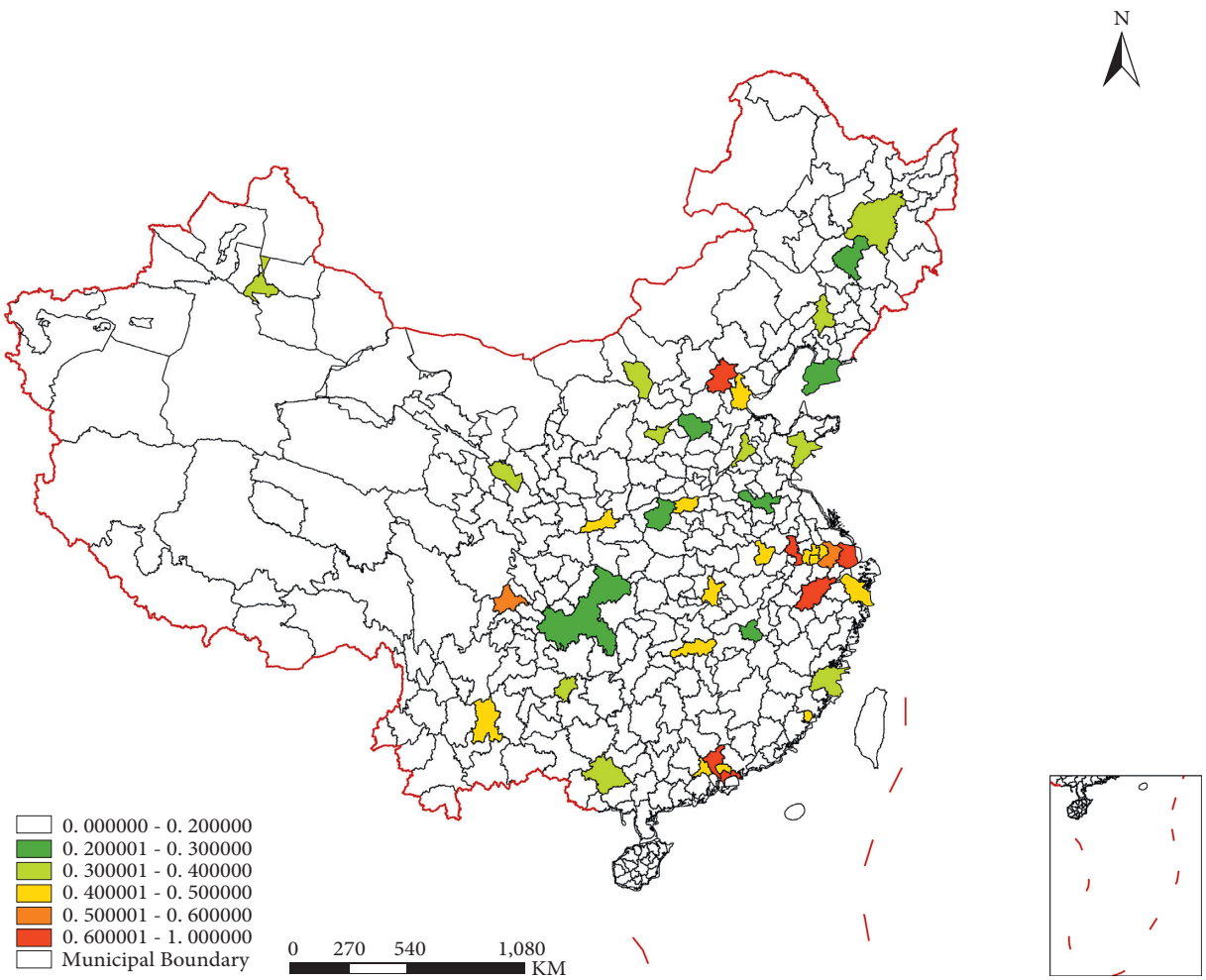

Figure 22: Distribution map of underground space development level in major cities in China.

(Figure 20). In addition to the higher urbanization level and human activity intensity in cities such as Dongguan and Foshan in the Pearl River Delta, resulting in higher urban population development level than UUS development and urban economic development, the population distribution results of each city are highly correlated with the level of urban economic development (Figure 21).

5.2.2. Spatial Distribution Law of Development Level. Figure 22 shows the spatial distribution law of the UUS development level in China. We can see that the urban agglomerations of Yangtze River Delta, the urban agglomerations of Pearl River Delta, Beijing-Tianjin-Hebei metropolitan region, and Chengdu-Chongqing urban agglomeration are the regions with high UUS development levels in China. The main reason is that the urban agglomerations of Yangtze River Delta and the urban agglomerations of Pearl River Delta bring together China's primary social resources, scientific and technological innovation forces, and capital market, which is conducive to promoting the development and utilization of UUS. Its underground space is ample in scale and full of functions, and also its policy support documents and management system are relatively perfect. In the urban agglomerations of Yangtze River Delta in 2019, the growth rates of the new building area of underground space in Zhejiang Province and Jiangsu Province were 12% and 9%, respectively, and the growth rate of the new building area of underground space in Guangdong Province was 20%, both far exceeding the national average growth rate of 2.05%. The development level of central cities such as Changsha and Wuhan is also high. The development of underground space mainly focuses on constructing urban underground facilities systems such as subway and urban pipe galleries, which matches the current urban development pattern in China.

However, some cities such as Xi'an, Chongqing, and Nanchang have high economic development levels and population density, but the development level of underground space is deficient, which undoubtedly affects the city's sustainable development. Because the statistical calibre of this study is municipal jurisdiction, Chongqing, as a municipality directly under the central government, has a large area of a noncentral urban area, which has a significant impact on its underground space development indicator. Chongqing is an administrative region with a provincial

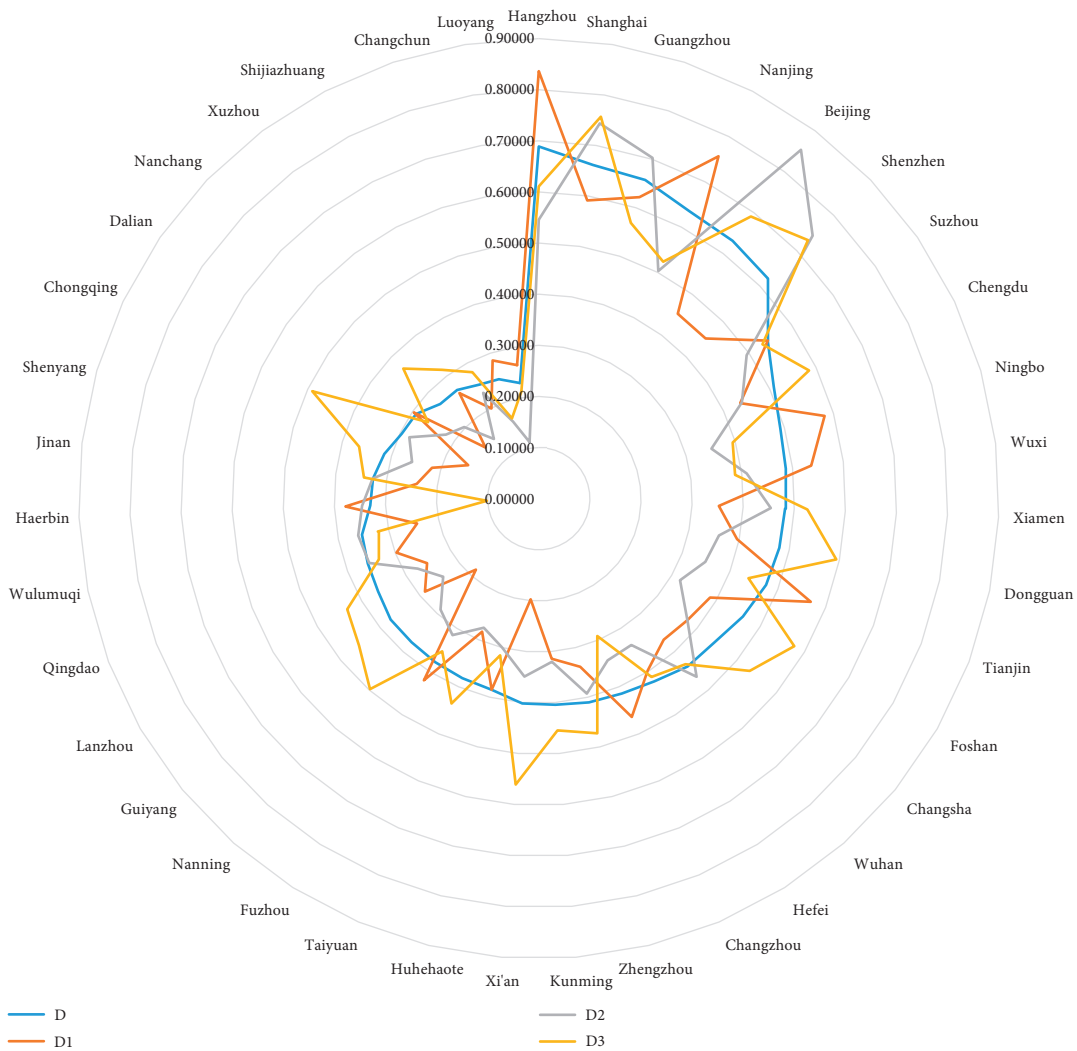

Figure 23: Comprehensive analysis of primary index measurement results.

structure, so we should combine the analysis of the results with the characteristics of the central city. What needs particular explanation is that although Chongqing is a municipal administrative region, the structure of Chongqing is a provincial structure. In other words, in addition to the main urban area of Chongqing, the urbanization process of other counties and districts is in line with the central metropolitan area. Compared with the urban area, it appears to be very slow, which undoubtedly affects the relevant indicator results of Chongqing. Suppose we put aside sites other than the central metropolitan area. In that case, the relevant indicators of Chongqing's urban economic development, population development, and underground space development are fundamental. The top one is because Chongqing is located in a mountainous area, and urban construction needs to consider the topography fully. The central metropolitan area of cluster development bears a large amount of urban population. Combined with the construction of rail transit, it connects multiple functional clusters throughout Chongqing. As far as the central metropolitan area is concerned, the development level of underground space in Chongqing is very advanced [57]. Although the population development index of Harbin and Changchun is low, their underground space develops well, mainly because Harbin and Changchun are located in the middle temperate zone [58]. The climate is characterized by warm summer and cold winter, which lasts for about five months. In cold winter, their underground space activity comfort is higher than the ground, similar to the development and utilization of Montreal underground city in Canada [59].

6. Conclusions and Suggestions

6.1. Conclusions. This study constructs the UUS development index system from 12 indexes in 3 aspects: underground space development, urban economic development, and urban population development [60]. The entropy weight TOPSIS method is used to measure the underground space development level of 39 major cities in China. Based on the analysis of the results, the conclusions are as follows:

(1) The law of UUS development along urban agglomeration

As we all know, China's urban spatial pattern is mainly composed of the urban agglomerations of Yangtze River Delta, the urban agglomerations of Pearl River Delta, Beijing-Tianjin-Hebei metropolitan region, and Chengdu-Chongqing urban agglomeration. The urban agglomeration structure plays a significant role in driving regional economic development and promoting urban comprehensive benefits. As a space carrier, architecture and underground space are undoubtedly its material guarantee [61]. The 39 major cities in this study have a spatial clustering phenomenon in the comprehensive index, and the spatial clustering phenomenon of the three secondary indicators is undeniable. According to the comprehensive index, the urban agglomerations of the Yangtze River Delta, the urban agglomerations of Pearl River Delta, and the Beijing-Tianjin-Hebei metropolitan region are the areas with a high level of UUS development. As Chengdu-Chongqing urban agglomeration is located in the west, only two central cities are selected for this study case; other regional economic and population indicators are poor, so they cannot support UUS development. Therefore, the development level of UUS is the urban agglomerations of Yangtze River Delta > the urban agglomerations of Pearl River Delta > Beijing-Tianjin-Hebei metropolitan region > Chengdu-Chongqing urban agglomeration, indicating that the development of urban population and economy in the urban agglomeration area has a significant impact on promoting the development of UUS; urban cluster development can promote the development level of UUS.

(2) Unbalanced regional development of UUS

The cities measured in this study are mainly cities with urban economic development and population development at the head of China. The development of UUS has a high correlation with urban rail transit [62]. Therefore, based on screening economic and population development, 39 cities with urban rail transit are selected. These cities are mainly distributed in the south of the famous "Hu Huanyong line," and this matches the current development law of our country. There is a spatial clustering phenomenon in the comprehensive measure (d). The "high-high" clustering areas are the urban agglomerations of Yangtze River Delta, the urban agglomerations of Pearl River Delta, and the Beijing-Tianjin -Hebei metropolitan region. The overall level of other regions is not high except in Chengdu. The UUS development, economic development, and population development of the urban agglomeration in which the "high-high" cluster area is located are very balanced, indicating that the development of urban cluster is conducive to comprehensively improving various indicators of each city and promoting the development of UUS in the city. The population development level of other cities is high, such as in Zhengzhou, and the economic development level is high, such as in Chongqing. The development level of underground space is high. For example, the comprehensive index of the UUS development level in Harbin is not high. These cities have great underground space development potential. In the future, the rapid development of UUS may be realized with urban development.

(3) Unbalanced development of indicators

As an essential part of urban space, UUS serves urban residents. Therefore, its underground space development often matches urban economic development and population development. Once it does not match, there may be urban traffic congestion, low spatial efficiency, poor environmental quality, and other problems. According to the results of the three primary indicators of underground space development, urban economic development, and urban population development measured in this study, most UUS development indicators in China match well with economic development and urban population development. There are relatively few urban problems in these cities. However, there is an imbalance in the development of indicators, including the advanced development of a class of underground space indicators higher than the indicators of economic development and population development and planning the city's future development. The representative cities are Hangzhou, Nanjing, Ningbo, Tianjin, Zhengzhou, and Harbin (Figure 23). For example, Hangzhou took the construction of urban public space as the focus of urban development during the 12th Five-Year Plan period, which focused on urban construction in terms of large-scale transportation hub layout, underground corridor construction, and in-depth development, making full use of underground space to improve urban functions, alleviate traffic congestion, improve the regional environment, create more comfortable underground space and public activity facilities, and meet people's growing "quality demand" for underground space. As a result, the indicators of underground space, regional economic development, and population development develop together, mainly including Guangzhou, Beijing, Shenzhen, Xiamen, Xi'an, Nanning, Chongqing, and Nanchang. With the transformation of China's urban development from incremental expansion to stock optimization, these cities' underground space development indicators will increase rapidly in the future.

6.2. Proposal. Because of the development law of underground space in major cities in China, which shows the law of development around urban agglomeration, the development of UUS has the problems of unbalanced regional development and uncoordinated development among indicators. Therefore, in order to promote the healthy and

balanced development of UUS in China, based on the relevant analysis of this study, we put forward the following suggestions:

(1) We should promote the sustainable development of underground space, economy, and population. The result of underground space should not rely too much on the guidance of urban policies. The involvement of social capital in promoting the development and utilization of urban underground public space is conducive to promoting the efficiency of the three-dimensional growth of the metropolitan area. The result of underground space should aim at meeting the use of urban residents. The collaborative development of underground space, economy, and population is the way to promote the rational development of UUS. This study shows that cities with a high development level of UUS generally have a high index coordination degree, confirming the necessity of balanced development.

(2) The government should take effective measures to narrow the development gap between eastern and western China and ensure the balanced development of UUS in China. Of course, this balanced development is based on the coordinated development of underground space, economy, and population. This study found significant differences in the development level of underground space between the western region and other regions in social, economic, and environmental indicators and the overall situation. At the same time, the differences between cities in the western region are also very huge. At this stage, China's "western development strategy," "finance of northeast old industrial base," "rise of central China," and other preferential policies in underdeveloped areas can provide more national support for the economic development of these regions. The population of most cases corresponding to this study is growing continuously. Therefore, under the background of sustained economic and population growth, the development difference of regional underground space development level will gradually narrow.

(3) We should support the exploration of effective evaluation methods and feedback mechanisms for UUS development vitality. On the one hand, the evaluation method can qualitatively or quantitatively reflect the UUS development level. On the other hand, the feedback mechanism can help the government find the problems hindering the development level of UUS to scientifically formulate corresponding improvement strategies and improve the efficiency of the vertical utilization of urban space.

6.3. Future Research Prospects. In fact, in addition to the three types of factors mentioned in this study, the influencing factors of UUS development level are more complex in China, such as political factors, urban rail transit construction, urban landform constraints, and urban development strategy. Under the influence of politics, the development level of underground space socialization in Beijing, China's political centre is low. Under the influence of landform, the diversity of underground space development in Chongqing is good. With the promotion of TOD development strategy, the development level of underground space in Chengdu has maintained a high level in recent years. At present, more than ten cities in China have opened or built rail transit. With the promotion of urban rail transit, the development of UUS is also developing rapidly. Therefore, in the follow-up research, we will add urban rail transit as the influencing factor affecting the development level of UUS and explore the relevant laws of the integrated development of UUS and rail transit.

Data Availability

The data used to support the study can be obtained from the corresponding author upon request.

Conflicts of Interest

The authors declare that there are no conflicts of interest regarding the publication of this article.

Acknowledgments

The authors appreciate the financial support of this work provided by the Postgraduate Research and Practice Innovation Program of Jiangsu Province, under grant nos. KYCX21-2271 and 2018YFC0704903; the National Natural Science Foundation of China, under grant no. 51778611; and the National Key R&D Program Projects of China.

References

[1] H. H. Zhu, F. Peng, X. Li, and C. Liu, "Development strategy on UUS planning in China," *Strategic Study of Chinese Academy of Engineering*, vol. 19, no. 6, pp. 12–17, 2018.

[2] F. L. Peng, Y. K. Qiao, S. Sabri, B. Atazadeh, and A. Rajabifard, "A collaborative approach for UUS development toward sustainable development goals: critical dimensions and future directions," *Frontiers of Structural and Civil Engineering*, vol. 15, no. 4, pp. 20–45, 2021.

[3] Q. H. Qian, "Present state, problems and development trends of UUS in China," *Tunnelling and Underground Space Technology*, vol. 55, no. 5, pp. 280–289, 2016.

[4] Q. H. Qian, "Scientific use of the UUS to construction the harmonious livable and beautiful city," *Hazard Control in Tunnelling and Underground Engineering*, vol. 1, no. 1, pp. 1–7, 2019.

[5] Y. Liu, F. Dai, and P. Pei, "A wing-crack extension model for tensile response of saturated rocks under coupled static-dynamic loading," *International Journal of Rock Mechanics and Mining Sciences*, vol. 146, Article ID 104893, 2021.

[6] Z. Tao, Y. Shu, X. Yang, Y. Peng, Q. Chen, and H. Zhang, "Physical model test study on shear strength characteristics of slope sliding surface in Nanfen open-pit mine," *International Journal of Mining Science and Technology*, vol. 30, no. 3, pp. 421–429, 2020.

[7] H. Yuan, Y. He, J. Zhou, Y. Li, and Z. Shen, "Research on compactness ratio model of UUS and compact development mechanism of rail transit station affected area," *Sustainable Cities and Society*, vol. 55, no. 10, pp. 1–30, 2020.

[8] Y.-K. Qiao, F.-L. Peng, S. Sabri, and A. Rajabifard, "Low carbon effects of urban underground space," *Sustainable cities and society*, vol. 45, no. 12, pp. 451–459, 2019.

[9] R. Zargarian, D. Hunt, P. Braithwaite, N. Bobylev, and C. Rogers, "A new sustainability framework for UUS," *Proceedings of the Institution of Civil Engineers-Engineering Sustainability*, vol. 171, no. 5, pp. 1–16, 2016.

[10] H. Yu, Y. Bao, and Y. H. Wang, "Analysis of geo-environmental hazards in UUS development in Shanghai," *Natural Hazards*, vol. 75, no. 3, pp. 2067–2079, 2015.

[11] M.-s. Zhang, H. Q. Wang, H.-q. Wang et al., "Evaluation of urban underground space resources using a negative list method: taking Xi'an City as an example in China," *China Geology*, vol. 3, no. 1, pp. 124–136, 2020.

[12] Y. Xu and X. Chen, "Quantitative analysis of spatial vitality and spatial characteristics of urban underground space (UUS) in metro area," *Tunnelling and Underground Space Technology*, vol. 111, no. 10, Article ID 103875, 2021.

[13] L. He, Y. Song, S. Dai, and K. Durbak, "Quantitative research on the capacity of urban underground space - the case of Shanghai, China," *Tunnelling and Underground Space Technology*, vol. 32, no. 6, pp. 168–179, 2012.

[14] F. V. D. Hoeven and A. Van Nes, "Improving the design of UUS in metro stations using the space syntax methodology," *Tunnelling and Underground Space Technology*, vol. 40, no. 9, pp. 64–74, 2013.

[15] D. V. L. Hunt, I. Jefferson, and C. D. F. Rogers, "Assessing the sustainability of underground space usage - a toolkit for testing possible urban futures," *Journal of Mountain Science*, vol. 8, no. 2, pp. 211–222, 2011.

[16] Y.-K. Qiao, F.-L. Peng, and Y. Wang, "Monetary valuation of urban underground space: a critical issue for the decision-making of urban underground space development," *Land Use Policy*, vol. 69, no. 8, pp. 12–24, 2017.

[17] P. Bélanger, "Underground landscape: the urbanism and infrastructure of Toronto's downtown pedestrian network," *Tunnelling and Underground Space Technology*, vol. 22, no. 3, pp. 272–292, 2007.

[18] R. Kimmo, J. Ritola, and K. Rauhala, "Underground space in land-use planning," *Tunnelling and Underground Space Technology*, vol. 13, no. 1, pp. 39–49, 1998.

[19] D. V. L. Hunt, L. O. Makana, I. Jefferson, and C. D. F. Rogers, "Liveable cities and urban underground space," *Tunnelling and Underground Space Technology*, vol. 55, no. 5, pp. 8–20, 2016.

[20] H. Admiraal and A. Cornaro, "Why underground space should be included in urban planning policy - and how this will enhance an urban underground future," *Tunnelling and Underground Space Technology*, vol. 55, no. 5, pp. 214–220, 2016.

[21] X. Wang, F. Zhen, X. Huang, M. Zhang, and Z. Liu, "Factors influencing the development potential of urban underground space: structural equation model approach," *Tunnelling and Underground Space Technology*, vol. 38, no. 6, pp. 235–243, 2013.

[22] Y. Liu and F. Dai, "A review of experimental and theoretical research on the deformation and failure behavior of rocks under cyclic loads," *Journal of Rock Mechanics and Geotechnical Engineering*, vol. 13, no. (5), pp. 1203–1230, 2021.

[23] D. J. Boivin, "Montreal's underground network: a study of the downtown pedestrian system," *Tunnelling and Underground Space Technology*, vol. 6, no. 1, pp. 83–91, 1991.

[24] S. E. Polzin, "Transportation/land-use relationship: public transit's impact on land use," *Journal of Urban Planning and Development*, vol. 125, no. 4, pp. 135–151, 1999.

[25] J. B. Admiraal, "A bottom-up approach to the planning of underground space," *Tunnelling and Underground Space Technology*, vol. 21, no. 3, pp. 464-465, 2006.

[26] J. Peng and F.-L. Peng, "Layout Patterns of Underground Space Comprehensive Utilization Around Metro Station for Urban Commercial Area," in *Proceedings of the GeoShanghai 2018 International Conference:Tunnelling and Underground Construction*, pp. 587–596, Springer, Manhattan, NY, USA, January,2018.

[27] G.-L. Jia, R.-G. Ma, and Z.-H. Hu, "Review of urban transportation network design problems based on CiteSpace," *Mathematical Problems in Engineering*, vol. 2019, Article ID 5735702, 22 pages, 2019.

[28] Y.-H. Dong, F.-L. Peng, Y.-K. Qiao, J.-B. Zhang, and X.-L. Wu, "Measuring the monetary value of environmental externalities derived from urban underground facilities: towards a better understanding of sustainable underground spaces," *Energy and Buildings*, vol. 250, no. 1, Article ID 111313, 2021.

[29] Y. P. Hu, K. X. Zhang, J. Yang, and Y. H. Wu, "Application of hierarchical facility location-routing problem with optimization of an underground logistic system: a case study in China," *Mathematical Problems in Engineering*, vol. 2018, Article ID 7235048, 10 pages, 2018.

[30] S.-C. Liu, F.-L. Peng, Y.-K. Qiao, and J.-B. Zhang, "Evaluating disaster prevention benefits of underground space from the perspective of urban resilience," *International Journal of Disaster Risk Reduction*, vol. 58, no. 5, Article ID 102206, 2021.

[31] Y. K. Qiao, F. L. Peng, X. L. Wu, and S. F. Ding, "Underground space planning in urban built-up areas: a case study of Qingdao, China," in *Proceedings of the 16th World Conference of the Associated Research Centers for the Urban Underground Space (ACUUS)*, 16th ACUUS Conference Organizing Committee, Hong Kong, China, November 2018.

[32] G. Golany, *Urban Underground Space Design in China: Vernacular and Modern Practice*, University of Delaware Press, Newark, Delaware, 1989.

[33] N. Bobylev, "Transitions to a high density urban underground space," *Procedia Engineering*, vol. 165, no. 10, pp. 184–192, 2016.

[34] L. He, S. Z. Dai, and Y. Shu, "Discussion on some problems of UUS planning," *Chinese Journal of Underground Space and Engineering*, vol. 31, no. 5, pp. 825–829, 2011, in Chinese.

[35] J. X. Zheng, C. Wang, and Y. Sun, "Research on key control elements of UUS planning —— takes Tianjin Xiaobailou area as an example," *Chinese Journal of Underground Space and Engineering*, vol. 32, no. 5, pp. 889–895, 2012, in Chinese.

[36] H. Yuan, S. Z. Dai, and X. R. Liu, "Study on underground space in chongqing," *Chinese Journal of Underground Space and Engineering*, vol. 34, no. 1, pp. 1–5, 2014, in Chinese.

[37] G. Y. Cai, Q. Y. He, and J. H. Yao, "Preparation system and content of underground space planning from the spatial and temporal perspective," *Chinese Journal of Underground Space and Engineering*, vol. 37, no. 5, pp. 1145–1149, 2017, in Chinese.

[38] Z.-L. Chen, J.-Y. Chen, H. Liu, and Z.-F. Zhang, "Present status and development trends of underground space in

Chinese cities: evaluation and analysis," *Tunnelling and Underground Space Technology*, vol. 71, no. 8, pp. 253–270, 2018.

[39] G. Swensen, "Tensions between urban heritage policy and compact city planning - a Practice review," *Planning Practice and Research*, vol. 35, no. 5, pp. 555–574, 2020.

[40] Z. Chen, L. Su, and C. Zhang, "Research on the synergy degree of aboveground and underground space along urban rail transit from the perspective of urban sustainable development," *Sustainability*, vol. 8, no. 9, p. 934, 2016.

[41] M. Vidó, T. Hámor, and L. Czirok, "Underground space, the legal governance of a critical resource in circular economy," *Resources Policy*, vol. 73, no. 10, Article ID 102171, 2021.

[42] X. Wang, X. J. Huang, and J. Tang, "Fuzzy synthesis evaluation on the development potential of UUS resource," *Journal of Beijing University of Technology*, vol. 36, no. 2, pp. 213–218, 2010, in Chinese.

[43] H. Xie, Y. Zhang, Y. Chen, Q. Peng, Z. Liao, and J. Zhu, "A case study of development and utilization of urban underground space in Shenzhen and the Guangdong-Hong Kong-Macao Greater Bay Area," *Tunnelling and Underground Space Technology*, vol. 107, no. 1, Article ID 103651, 2021.

[44] R. K. Singh, H. R. Murty, S. K. Gupta, and A. K. Dikshit, "An overview of sustainability assessment methodologies," *Ecological Indicators*, vol. 9, no. 2, pp. 189–212, 2009.

[45] O. Vitor and P. Pinho, "Evaluation in urban planning: advances and prospects," *Journal of Planning Literature*, vol. 24, no. 4, pp. 343–361, 2010.

[46] X. Hong, X. Ji, and Z. Wu, "Architectural colour planning strategy and planning implementation evaluation of historical and cultural cities based on different urban zones in Xuzhou (China)," *Color Research & Application*, vol. 46, no. 6, Article ID 22736, 2021.

[47] P. Sajida, M. Kamruzzaman, and T. Yigitcanlar, "Developing policy scenarios for sustainable urban growth management: a Delphi approach," *Sustainability*, vol. 9, no. 10, pp. 343–361, 2017.

[48] J. S. Deng, K. Wang, Y. H. Deng, and G. J. Qi, "PCA-based land-use change detection and analysis using multitemporal and multisensor satellite data," *International Journal of Remote Sensing*, vol. 29, no. 16, pp. 4823–4838, 2008.

[49] Y. Wang, J. Li, G. Zhang, Y. Li, and M. H. Asare, "Fuzzy evaluation of comprehensive benefit in urban renewal based on the perspective of core stakeholders," *Habitat International*, vol. 66, no. 6, pp. 163–170, 2017.

[50] Y. Liu, R. Li R, and X. Song, "Grey associative analysis of regional urbanization and eco-environment coupling in China," *Acta Geographica Sinica*, vol. 60, no. 2, pp. 237–247, 2005.

[51] D. Ouyang, X. Zhu, X. Liu, R. He, and Q. Wan, "Spatial differentiation and driving factor Analysis of urban construction land change in county-level city of guangxi, China," *Land*, vol. 10, no. 7, p. 691, 2021.

[52] B. Wout, "Urban underground space: solving the problems of today's cities," *Tunnelling and Underground Space Technology*, vol. 55, no. 5, pp. 245–248, 2016.

[53] M. Z. Gao, J. Xie, J. Guo, Y. Q. Lu, Z. Q. He, and C. Li, "Fractal evolution and connectivity characteristics of mining-induced crack networks in coal masses at different depths," *Geomechanics and Geophysics for Geo-Energy and Geo-Resources*, vol. 7, no. 1, 2021.

[54] M. Z. Gao, J. Xie, Y. N. Gao et al., "Mechanical behavior of coal under different mining rates: a case study from laboratory experiments to field testing," *International Journal of Mining Science and Technology*, vol. 31, no. 2021, pp. 825–841, 2021.

[55] R. L. Schalock, M. A. Verdugo, and J. van Loon, "Understanding organization transformation in evaluation and program planning," *Evaluation and Program Planning*, vol. 67, no. 4, pp. 53–60, 2018.

[56] G. Kimia, M. Hamzenejad, and A. Meshkini, "An analysis of the spatial distribution pattern of social-cultural services and their equitable physical organization using the TOPSIS technique: the case-study of Tehran, Iran," *Sustainable Cities and Society*, vol. 51, no. 11, Article ID 101708, 2019.

[57] X. Li, K. Peng, J. Peng, and H. Xu, "Effect of cyclic wetting-drying treatment on strength and failure behavior of two quartz-rich sandstones under direct shear," *Rock Mechanics and Rock Engineering*, vol. 54, no. 11, pp. 5953–5960, 2021.

[58] X. Li, K. Peng, J. Peng, and D. Hou, "Experimental investigation of cyclic wetting-drying effect on mechanical behavior of a medium-grained sandstone," *Engineering Geology*, vol. 293, Article ID 106335, 2021.

[59] C. Zhu, M. C. He, Z. G. Tao, Q. X. Meng, and X. H. Zhang, "Recognition and prevention of rockfall vulnerable area in open-pit mines based on slope stability analysis," *Geomechanics and Engineering*, vol. 26, no. 5, pp. 441–452, 2021.

[60] C. Zhu, K. Zhang, H. Cai et al., "Combined application of optical fibers and CRLD bolts to monitor deformation of a pit-in-pit foundation," *Advances in Civil Engineering*, vol. 2019, no. 1, 16 pages, Article ID 2572034, 2019.

[61] Z. B. Wang, "Land spatial development based on carrying capacity, land development potential, and efficiency of urban agglomerations in China," *Sustainability*, vol. 10, no. 2, p. 4701, 2018.

[62] L. Wu, H. Xia, X. Cao, C. Zhang, and C. Dai, "Research on quantitative demand of underground space development for urban rail transit station areas: a case study of metro line 1 in Xuzhou, China," *Urban Rail Transit*, vol. 4, no. 4, pp. 257–273, 2018.

Hindawi
Mathematical Problems in Engineering
Volume 2021, Article ID 9285832, 9 pages
https://doi.org/10.1155/2021/9285832

Research Article

Study on the Formation Mechanism of Rock Burst Caused by Seam Floor Slip under an Ultrathick Conglomerate

Zhiyong Ma,[1,2,3] **Wenkai Feng**,[1] **Zhen Wang**,[2,3] **Fujin Lin**,[2,3] **and Dayong Li**[2,3]

[1]*State Key Laboratory of Geohazard Prevention and Geoenvironment Protection, Chengdu University of Technology, Chengdu 610059, China*
[2]*State Key Laboratory of the Gas Disaster Detecting, Preventing and Emergency Controlling, Chongqing 400037, China*
[3]*CCTEG Chongqing Research Institute, Chongqing 400037, China*

Correspondence should be addressed to Zhiyong Ma; mazhiyong@stu.cdut.edu.cn and Wenkai Feng; fengwenkai@cdut.cn

Received 15 October 2021; Revised 9 November 2021; Accepted 11 November 2021; Published 17 December 2021

Academic Editor: Gan Feng

A rock burst accident occurred on coalface 13230 of the Gengcun Coal Mine in Henan Province. Through a field investigation, theoretical analysis, and microseismic monitoring, we studied how the rock burst, which was caused by overall seam floor slip and instability, occurring under an ultrathick conglomerate. Because the overlying ultrathick conglomerate in the mined-out zone close to coalface 13230 had been inadequately mined, the leading section of the coalface was under a high level of stress. Combined with the tectonic stresses from the F_{16} faultage and the soft floor structure, these factors caused the floor of this coalface to trigger the overall slip-type rock burst. In this paper, an estimation model of the ultimate bearing capacity of a seam floor under an ultrathick conglomerate and the advancing abutment pressure on the coalface is presented. This model is used to show that the ultimate bearing capacity of the seam floor on coalface 13230 is 26.3 MPa, and the abutment pressure is far more than the floor bearing capacity. We also present pressure relief and reinforced supporting measures, which can effectively prevent floor slip-type rock bursts from occurring. The results of this study provide a reference for the prevention and control of floor slip-type rock bursts in coal mining under an ultrathick conglomerate.

1. Introduction

A rock burst is the sudden release of elastic energy accumulated by a coal and rock mass. Such events have become a common type of dynamic disaster that seriously threatens mine production safety [1–8]. The average thickness of the coal seam in the Yima Coal Field in Henan is 10 m. The roof of this seam is made of an ultrathick conglomerate. The top coal mining approach used in this area leaves clear traces of rock bursts. Unlike common dynamic rock burst disasters, rock bursts in the Yima Coal Field occur on the seam floor. As the burial depth and mining intensity increase, more and more macroenergy events have occurred on the stope of the Yima Coal Field in recent years. These events have decreased the area of the two roadways on the coalface and resulted in casualties and damages to facilities, posing a major threat to production safety.

Rock bursts may be caused by many factors. Based on statistics of rock burst accidents, Zhang et al. [2] and Guo et al. [9] found that these factors can include coal seam overburden, geological conditions, burst tendency, and excavation activities. Jiang [10] et al. studied the evolution characteristics of the rock burst risk at different mining widths in deep mines. Based on the coupling hypothesis of static and dynamic stresses, Wu et al. [11] studied the formation mechanism of rock bursts. Wang et al. [12] and Zhang et al. [13] studied the mechanism of rock bursts triggered by isolated coal pillars and presented an energy distribution model under a static load for coal pillars. Chen [14] et al. studied the effect of temperature on rock burst hazards. Based on many accident cases, Xu et al. [15] studied the energy sources and main control factors of rock bursts. The formation mechanism of rock bursts is complicated.

Mature rock burst theories include the strength theory, the energy theory, the burst tendency theory, the three-criterion theory, and the instability theory. In recent years, scholars have made great achievements in researching the formation mechanism of rock bursts. Dai et al. [16], Hu et al. [17], and DOU et al. [18] studied the effect of faults on rock bursts. They believed that roof migration can activate faults and trigger rock bursts. Jiang [19, 20] studied the creep characteristics of deep coal masses under high stresses. Xu et al. [21] discussed the formation mechanism of rock bursts on the coalface based on microseismic monitoring results and obtained precursory information. Pan [22] et al. studied the formation mechanism of rock bursts when there are two soft coal seams. Yu et al. [23] studied the formation mechanism of rock bursts when there is an ultrathick conglomerate.

As previously mentioned, many studies have been conducted on the triggering factors and formation mechanism of rock bursts. However, few studies have considered the formation mechanism of rock bursts on the seam floor under an ultrathick roof conglomerate. Hence, further study is required. This paper is based on the rock burst accident that occurred on the fully mechanized coalface 13230 in the east-3 mining zone of coal seam 2-3 in the Gengcun Coal Mine, which includes the Yima Coal Field. Through a microseismic monitoring, a theoretical analysis, and a field investigation, this paper analyses the formation mechanism of floor rock bursts when an ultrathick conglomerate is mined, identifies the formation mechanism of rock bursts in the Yima Coal Field, and proposes specific control measures for the prevention and control of rock bursts in similar conditions.

2. Engineering Background

2.1. Overview of the Accident. At 10 : 42 : 20 on December 22, 2015, a rock burst occurred in the conveyor gateway on coalface 13230 in the Gengcun Coal Mine. According to the microseismic monitoring results, the seismic source was 830.7 m in front of the coalface and 3.0 m under the seam floor, which was 7.9 m away from the upper side of the conveyor gateway. The magnitude of the rock burst was 2.1, and the energy produced was 6.3×10^5 J. When the rock burst occurred, the roadway within 160 m from the end of the conveyor gateway to the coalface was immediately damaged: the floor bulged, both sides contracted, the hydraulic lifting device was seriously deformed, bent, and broken, and the equipment was overturned. The accident caused two deaths. The conditions at the accident site were as follows.

The cross section of the roadway was reduced to 3/4 of the original size, and the conveyor gateway, which was 80 m away from the most severely damaged coalface, was nearly closed. Among the 35 hydraulic lifting devices used for forepoling, 30 were damaged. The large stand columns were broken in seven of the lifting devices, bent in 11, and toppled over in 12; equipment trains were displaced or turned over; the belt was displaced or stopped running. The impact of the accident on the roadway of the conveyor gateway is shown in Figure 1:

2.2. Engineering Background of the Coalface Where the Accident Occurred. Coalface 13230 is in the east wing of the downhill roadway in the east-3 mining zone (2-3) of the Gengcun Coal Mine. In the north, the fully mechanized coalface 13210 has been mined. The west and south sides have unmined coal mass 2-3. The mine-out area of coalfaces 21121 and 21141 of the Qianqiu Mine lies to the east of the open-off cut, and the F_{16} faultage, with a drop height of 50–500 m, is 600–700 m underneath the cut. The coal seam 2–3 on this coalface has a thickness of 10.4 m, and the average mining depth is 633 m. The seam includes greyish-white sandy mudstone with a thickness of 280 m and a conglomerate bed with a thickness of 380 m over the roof of the coalface. With incomplete roof caving, the mine has a surface subsidence coefficient of 0.30–0.70. Below the conveyor gateway floor of the coalface, there is a 1.5-m-thick coal seam, and the seam floor contains low-strength carbonaceous mudstone with a thickness of 1–3 m. The roof and coal seam of the coalface have a high rock burst risk, while the floor features a low risk. Until the accident occurred, the coalface had advanced 32.8 m on average. For the relative position of the coalface, see Figure 2.

2.3. Formation Conditions of Rock Burst

2.3.1. Geostress Characteristics. Rock bursts are closely related to the geostress in a coal mass [24]. To ensure a thorough understanding of the geomechanical environment of the deep surrounding rocks in the Gengcun Coal Mine, we conducted geostress tests on the conveyor gateway of coalface 13230, the downhill roadway in the east-3 mining zone of the Gengcun Coal Mine, and the track gateway of coalface 21141 in the nearby Qianqiu Coal Mine (test point 1 was 250 m away from the conveyor gateway of coalface 13230; test point 2 was 380 m away from the conveyor gateway of coalface 13230; test point 3 was on the downhill roadway of coalface 13230; test point 4 was 55 m away from the track gateway of coalface 21141 in the Qianqiu Coal Mine). The layout of in-situ stress measuring points is marked in Figure 2(a). The test results are shown in Table 1.

According to the geostress test results, the stress of the primary rock is slightly higher than the medium level, and the four test points are all far away from the mined-out zone, which can reflect the stress of the primary rock. The three (75%) test points are dominated by vertical stress, and one (25%) test point has tectonic stress. Therefore, coalface 13230 and the area near the coal pillar between the mines are subject to both vertical stress and horizontal tectonic stress, creating stress conditions for the occurrence of rock bursts.

2.3.2. Ultrathick Conglomerate. The results show that the bending property of the roof is proportional to the fifth power of the roof overhang length. The more elastic energy is stored, the more likely the occurrence of a rock burst is [25]. After a large area of coalfaces 21101, 21221, and 21141 in the Qianqiu Coal Mine, which are located to the east of coalface 13230, was mined out, the mine has a surface subsidence coefficient of 0.30–0.70, with incomplete roof caving. A large

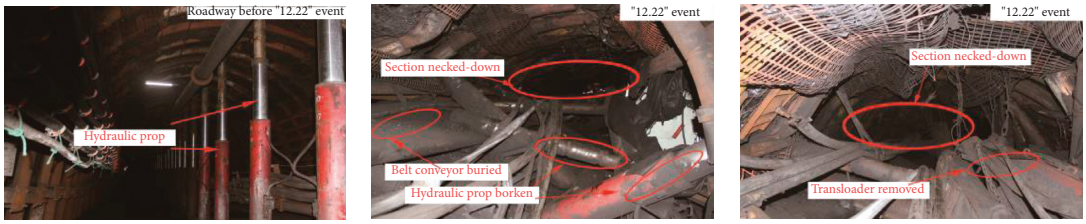

(a) (b) (c)

Figure 1: Photos of roadway's damage after the "12.22"event in the 13230 working face. (a) Transport gateway before "12.22″event. (b) Transport gateway when "12.22″event.

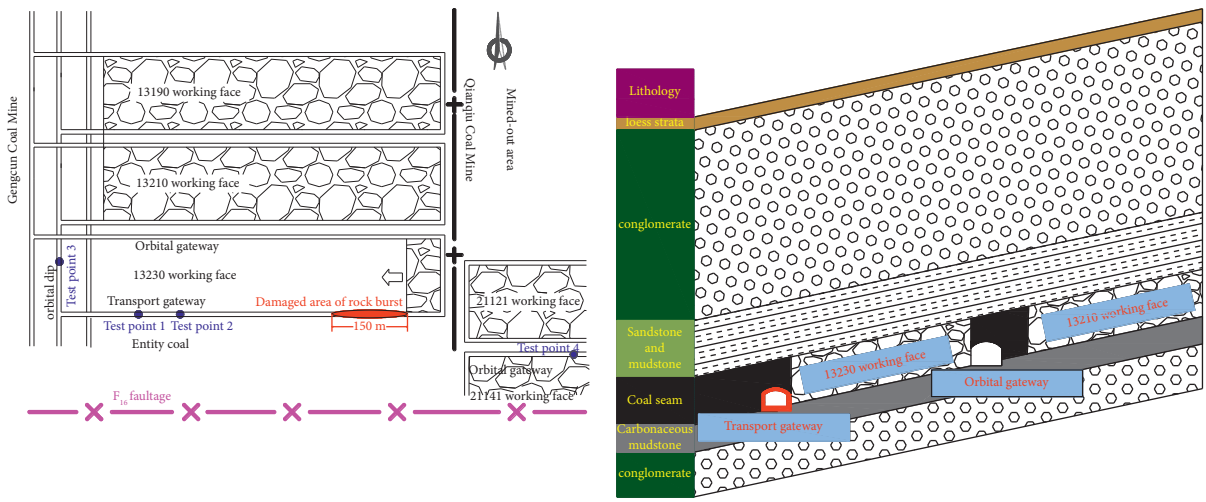

(a) (b)

Figure 2: Relative position of coalface 13230. (a) Planar view. (b) Profile.

Table 1: Geostress test results in the deep part of the Gengcun Coal Mine.

Test point	H (m)	σ_v (mpa)	σ_H (mpa)	σ_h (mpa)	k
1	621	15.53	12.58	7.09	0.81
2	622	15.55	13.93	7.29	0.89
3	599	14.98	14.84	7.69	0.99
4	633	15.83	17.51	9.05	1.11

H: buried depth of the test point, σ_v: vertical stress, σ_H: maximum horizontal stress, σ_h: minimum horizontal stress, and k: side pressure ratio.

area of the overlying ultrathick conglomerate is suspended, and the ultrathick conglomerate acts as a whole on the overlying strata below so that the stress is transferred to coalface 13230. As a result, the stress is concentrated in the advancing abutment of the coal seam, and coalface 13230 is under a relatively high vertical stress at the beginning of mining. High stress levels can easily produce very large pressures on coalfaces and even trigger rock bursts [26, 27].

2.3.3. F_{16} Thrust Faultage. The F_{16} faultage, with a drop height of 50–500 m, is located 600–700 m below coalface 13230. Based on the core exposed by geological drilling in the Gengcun Coal Mine, the extrusion force of the F_{16} faultage near the coalface causes the stratum cut by a normal fault to have a large-scale northward thrust-slip movement along the top face of the mudstone stratum. At the same time, the fault interface between blocks shows the characteristics of torsional faults due to the differential movement of fault blocks. The thrust caused by a large extrusion force of the fault and the instability of the overlying ultrathick conglomerate roof under the influence of dynamic pressure will also make the F_{16} faultage active [22]. The coal mass on coalface 13230 is under a high level of stress. Based on experience in adjacent mines, the position closer to the F_{16} faultage is more susceptible to rock bursts.

2.3.4. "Strong-Weak" Coal and Rock Structure. The area damaged by rock bursts of coalface 13230 leaves a coal floor with a thickness of 1.5–5 m and low-strength carbonaceous

mudstone with a thickness of 1–3 m on the floor. The part below the damaged area is directly connected with the basal conglomerate with a thickness of several metres to more than 10 m. Conglomerate and sandstone are hard, while coal seams and mudstone are soft. Clamped by the hard roof and floor, on the one hand, the coal seam suddenly ruptures at the side direction or gradually expands towards the mining space under high pressure. On the other hand, the resistance and deformation at the junction between the coal and the rock block the development of the previously mentioned process. In this case, there is a very high shear stress and a very high normal stress at the junction between the coal seam and the surrounding rock, which will trigger rock bursts once the stress exceeds a certain limit.

3. Mechanism of Floor Slip-Type Rock Burst

3.1. Estimation of Maximum Floor Bearing Capacity. After the underground roadway is excavated, the stress from the surrounding rock is redistributed, and a high abutment pressure zone appears in the leading section of the roadway. The soft floor has a low strength. Then, the roadway floor will have a slip field under the influence of abutment pressure [28, 29]. The plastic slip failure of the roadway floor is assumed to comply with the Mohr-Coulomb criterion. According to Prandtl's analysis of the ultimate bearing capacity in soil mechanics [24], an estimation model for the ultimate bearing capacity of floor slip is established, as shown in Figure 3. Assume that H is the burial depth of the roadway, m, c is the cohesive force, Mpa, and φ is the internal friction angle,°.

Depending on the stress field and movement trend, the floor slip field can be divided into an active zone COD, a transition zone BOC, and a passive zone AOB. The COD slip line field in the COD compresses in the vertical direction and expands in the horizontal direction under concentrated high stress levels. The entire large-area soft floor is squeezed to slip to the transition zone BOC in flow conditions. BOC is clamped by COD and AOB and transfers stress to AOB according to the motion trajectory under the compression and expansion of COD. As a result, the entire floor of AOB slips to the mining space, causing a rock burst on the seam floor.

According to the slip line field theory, there are two slip lines, that is, α cluster and β cluster. In COD and AOB, both α cluster and β cluster are straight, and the stress field is uniform. In BOC, α cluster is straight, while β cluster is logarithmic spiral, and BOC is a simple slip line field [30, 31].

In AOB, according to the related theory and analysis of Cauchy boundary values [32], the stress state of AOB S_{AOB} is as follows:

$$\begin{cases} S_{AOB} = \dfrac{c \cot \varphi}{1 - \sin \varphi}, \\ \theta = \pi. \end{cases} \tag{1}$$

θ is the angle between the first principal stress of AOB and the x-axis. It can be seen from formula (1) that the stress value at point B is $S_B = c\cot\varphi/1 - \sin\varphi$.

In BOC, according to the nature of the slip line field, the stress value of point B S_B and that of point C S_C on the same β cluster in BOC have the following relationship:

$$LnS_B + 2\theta_B \cot 2\ \mu = LnS_C + 2\theta_C \cot 2\mu, \tag{2}$$

where θ_B is the angle between the first principal stress at point B and the x-axis, $\theta_B = p$; θ_C is the angle between the first principal stress at point C and the x-axis; μ is the angle between α cluster and β cluster. We can obtain the stress value at point C S_C by substituting S_B at point B into formula (2):

$$S_C = \frac{c \cot \varphi \cdot e^{2(\pi - \theta_c)\cot 2\mu}}{1 - \sin \phi}. \tag{3}$$

In COD, the surface DO is the first principal stress plane, and the boundary conditions of the floor surface DO are as follows: the vertical stress is q_0, and the tangential stress is 0. Based on the theoretical analysis of mixed boundary values [33], the stress state of point C in COD can be obtained:

$$\begin{cases} S_C = \dfrac{q_0 + c \cot \varphi \cdot e^{\pi \tan \varphi}}{1 + \sin \phi}, \\ \theta = \dfrac{\pi}{2}. \end{cases} \tag{4}$$

According to the nature of the slip line field, we can obtain the stress value at point D S_D:

$$S_D = \frac{c \cot \varphi}{1 - \sin \phi} e^{\pi \tan \varphi}. \tag{5}$$

Based on formulas (4) and (5), the ultimate bearing capacity q_0 of the floor can be obtained as follows:

$$q_0 = c \cot \varphi \frac{1 + \sin \phi}{1 - \sin \phi} e^{\pi \tan \varphi} - c \cot \varphi. \tag{6}$$

According to the physical and mechanical properties of the coal seam 2-3, we can obtain the maximum bearing capacity of floor slip in the coal seam 2-3 using formula (6), that is, 26.3 MPa.

3.2. Estimation of Failure Depth of the Roadway Floor. According to the studies on how the mine pressure and rock stratum affect the failure scope of the mining floor, an estimation model for the failure scope of floor slip is established, as shown in Figure 4.

The slip line field theory and Rankine's earth pressure theory are used to analyse the maximum floor failure depth [34]: COD bears the active earth pressure P_a at active limit equilibrium; and DOA bears the passive earth pressure P_p at passive limit equilibrium.

$$P_a = \gamma\left(h_{\max} + h + h_g\right) - 2c\sqrt{K_a}, \tag{7}$$

$$P_p = \gamma h_{\max} K_p + 2c\sqrt{K_p}, \tag{8}$$

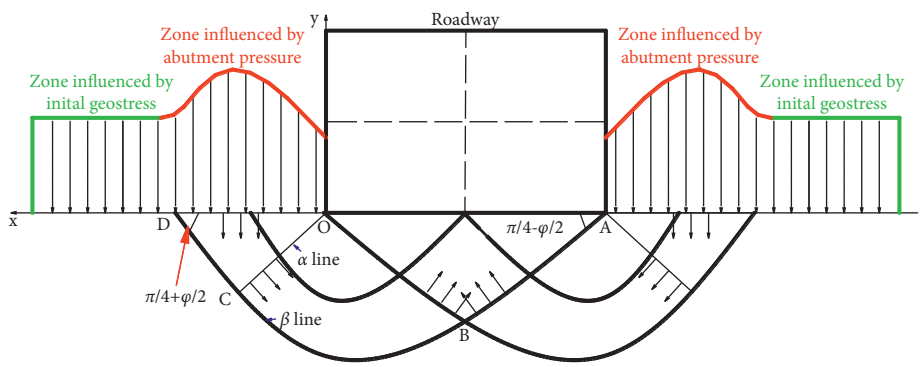

Figure 3: Estimation model for ultimate bearing capacity of floor slip.

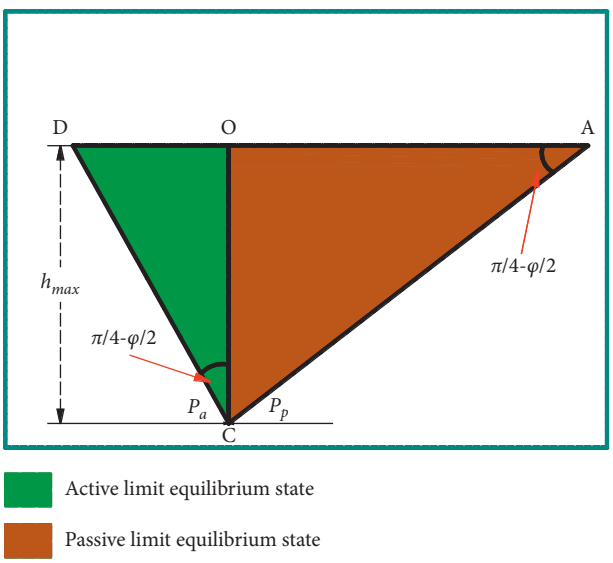

Figure 4: Estimation model for floor failure depth.

where the active earth pressure coefficient $K_a = \tan^2(45^\circ - \varphi)$ and the passive earth pressure coefficient $K_p = \tan^2(45^\circ + \varphi)$. Because point C is at limit equilibrium and the active earth pressure is equal to the passive earth pressure, the maximum failure depth of the roadway floor can be obtained as follows:

$$h_{\max} = \frac{(h_g + h)\tan^2(45^\circ - \phi/2) - 2c/\gamma}{\left[\tan^2(45^\circ + \phi/2) - \tan^2(45^\circ - \phi/2)\right]}. \quad (9)$$

$h_{\max}$ is the maximum failure depth of the roadway floor, m; γ is the average unit weight of the coal and rock over the floor, KN/m^3; h is the roadway height, m; and h_g is the height of the roadway pressure arch, m.

The height of the roadway on the coalface where the accident occurred is 4.2 m, and the internal friction angle of the coal and rock on the seam floor is 25°. The unit weight of the coal and rock over the floor is 2610 KN/m^3. From formula (9), we can estimate that the maximum failure depth of the floor on the coalface where the accident occurred is 5.39 m. The total thickness of the soft floor and bottom coal in the burst-stricken area is 7.93 m on average, which is close to the theoretically estimated maximum floor failure depth.

3.3. Estimation of Advancing Abutment Pressure. The mined-out zones of coalfaces 21121 and 21141 in the Qianqiu Coal Mine, with surface subsidence coefficients ranging from 0.30 to 0.70, are located to the east of coalface 13230. With incomplete caving, the roof is half overhang. The fracture height of the rock stratum is approximately half of the width of the mined-out zone. According to the analysis of the stress transmission mechanism of the half-suspended roof structure, the weight Q transferred to the coal mass on the adjacent coalface is 1/4 of the weight of the fault zone and 1/2 of the weight of the zone without fault on the overlying strata in the mined-out zone of the half-suspended roof. The angle o between the line connecting the separation end on one side of the mined-out zone and the horizontal direction is called the movement angle of the rock strata [20]. The estimation model for stress increment transferred from the high conglomerate stratum to the coal mass on one side of the coalface is shown in Figure 5.

The vertical stress σ_Q applied on the floor is composed of the abutment pressure σ_q generated by the dead weight of the overlying strata and the abutment pressure increment $\Delta\sigma$:

$$\sigma_Q = \sigma_q + \Delta\sigma = \sigma_q + \sum_{i=1}^{n} \sigma_i. \quad (10)$$

Floor burst is likely to occur when the vertical principal stress applied on the floor exceeds the load carried by the floor. In formula (10), σ_q is the abutment pressure generated by the dead weight of the coal seam, and $\Delta\sigma$ is the pressure transmitted from the suspended and exposed part of the ith key stratum to the coal mass on one side, $i = 1 \sim n$.

According to the conditions of coalface 13230 and its adjacent mined-out zone, we can estimate the stress using formula (10). Affected by the mined-out zones of coalfaces 21121 and 21141 in the Qianqiu Coal Mine, the strike abutment pressure of coalface 13230 produces an influence within 197 m, the peak stress is 98 m away from the coalface, and the maximum abutment pressure is 47.2 MPa. The maximum abutment pressure exceeds the bearing capacity of the seam floor, and the peak stress area appears close to the location where the most severe burst occurred (80 m away from the coalface).

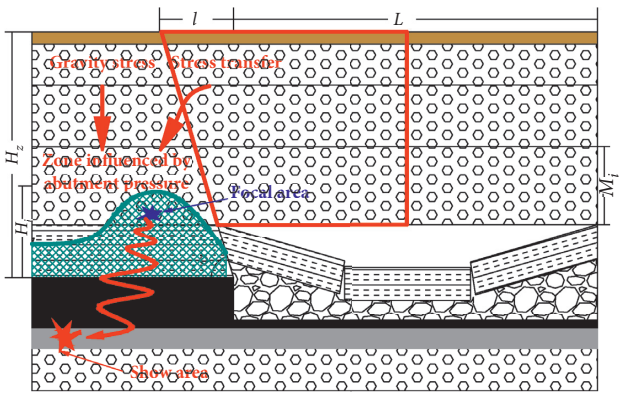

Figure 5: Estimation model for strike abutment pressure.

3.4. Formation Mechanism of Floor Slip Burst. After the coal seam is excavated, the coal mass in front of the coalface generates a high vertical stress under the influence of stress transfer because of the incomplete caving of the ultrathick conglomerate, and the coal seam expands under a high stress and results in plastic deformation [35–37]. Affected by the coupling of ultrathick conglomerate activity, excavation disturbance, and fault activation, burst will occur on the coalface when the load bearing limit of the coal mass is exceeded. In the meantime, the floor of the coalface undergoes plastic expansion under a high stress and creates a slip field at the bottom corner of the roadway. The burst failure and instability of the coal mass on the coalface enable the floor of the coalface to move along the slip line. When the bearing capacity of coal and rock mass is exceeded, a large-scale slip burst will be triggered instantly. Therefore, the floor slip burst occurs concurrently with the coal seam instability-caused burst. From the overturning direction of the equipment trains and pillars on the coalface where the accident occurred and the burst of coal mass in the roadway of the conveyor gateway, we can know that the expansion impact force comes from the two bottom corners of the roadway where the slip line field is roughly located.

4. Control of Rock Bursts

4.1. Control Method of Rock Bursts. According to the formation mechanism of rock bursts caused by overall floor slip and instability, we know that this type of rock burst is mainly related to the stress concentration and ultimate bearing capacity of the floor. Therefore, for the rock burst caused by floor slip and instability, we can stop the transfer of the floor stress to avoid the production of a slip line field, increase the floor bearing capacity, and reduce the concentration of coal stress on the coalface so that the high-stress zone will migrate to the deep coal mass.

(1) *Floor Pressure Relief.* Floor pressure relief holes can be drilled at the two bottom corners of the roadway, which are vertical to the side of the roadway, with a downward inclination angle of $45^\circ \pm 5^\circ$. The drill hole has a diameter of ≥120 mm and a hole pitch of 1 m, until the final hole reaches the hard rock stratum of the floor. Except for the floor pressure relief holes at the bottom corners of the roadway, 3-4 floor pressure relief holes can be drilled along the cross section of the roadway to prevent stress transmission along the roadway floor. The floor pressure relief holes can be drilled for charging and blasting. If the small depth of the floor pressure relief holes is not favourable for sealing and blasting, water can be injected into the floor pressure relief holes for softening.

(2) *Coal Pressure Relief.* Dense large-diameter pressure relief holes can be drilled on the coal mass at the side of the roadway to reduce the coal strength and expansion stress so that the abutment pressure can migrate to the deep part, creating conditions for the slow release of elastic energy. According to the estimated range of the advancing abutment pressure, coal pressure relief should be performed within 197 m in front of the coalface so that it can be extracted under low stress.

(3) *Reinforced Supports.* Within the key dangerous burst area and the influence range of the advancing abutment pressure on the coalface, in addition to the original anchor rod, anchor cable, anchor net, and 36U-shaped shed, a gate-type antiburst support and a hydraulic lifting device can be used to reinforce the supports to further improve the compression resistance, burst resistance, protection capability, and floor bearing capacity of the roadway. The basic and reinforced supports of the roadway on-site are shown in Figure 6.

4.2. Control Effect of Rock Bursts. Microseismic monitoring technology is based on seismology and acoustic emission. The rock burst prevention and control effect can be indirectly assessed by arranging sensors to monitor and collect microseismic signals when a microseismic energy event occurs. An ESG (Engineering Seismology Group, Kingston, Canada) microseismic monitoring system was installed on coalface 13230, with one ESG microseismic sensor deployed every 200 m in the track gateway and conveyor gateway, which covers the entire mining area of coalface 13230. The microseismic monitoring arrangement is shown in Figure 7.

The microseismic energy evolution characteristics can be obtained by analysing the microseismic energy prior to the rock burst on coalface 13230. As shown in Figure 8, before the rock burst accident occurred, only a few low-energy microseismic events occurred, and there were no obvious signs prior to these events. After the rock burst occurred, the mine was shut down. Without excavation disturbance on the coalface, the overlying ultrathick conglomerate was relatively stable. There are a few microseismic events that are all less than the "fourth power," resulting in low energy. After production was resumed at the coalface, by taking measures including floor breaking, dense drilling of the coal mass for pressure relief, and gate-type supporting, microseismic energy events of the "fifth power" accounted for 5%, those of the "fourth power" accounted for 60%, and those of the "third power" accounted for 30%. At the end of mining on the coalface, despite the dynamic phenomenon, no

Figure 6: Basic and reinforced supports of the roadway.

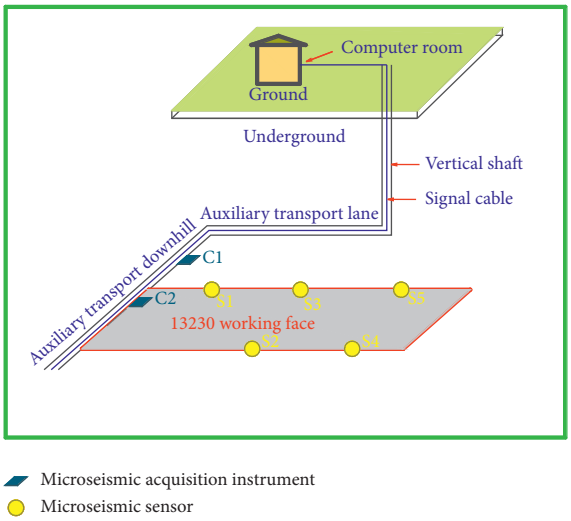

Figure 7: ESG microseismic monitoring arrangement.

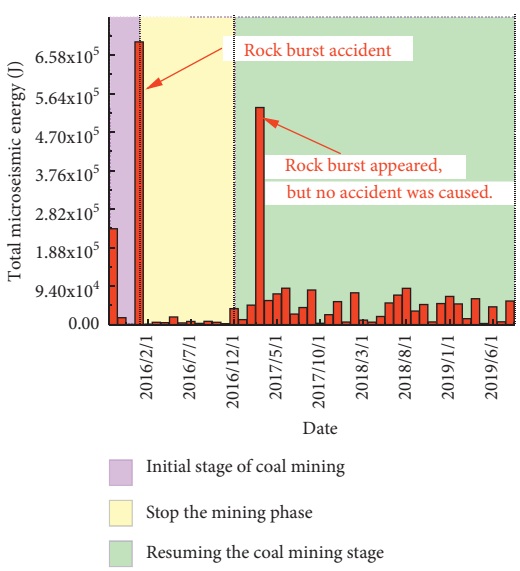

Figure 8: Microseismic energy evolution before and after production resumption.

destructive rock burst accident occurred under the reinforced protection of the gate-type support. The mining on this face was smoothly completed in June 2020.

5. Conclusion

(1) The formation mechanism of the rock burst on coalface 13230 in the Gengcun Coal Mine is obtained. Due to the insufficient collapse of the giant thick conglomerate overlying the working face, the leading abutment pressure of the working face is greater than the bearing capacity of the floor, and then the rock burst occurs.

(2) An estimation model for the ultimate bearing capacity and failure depth of floor slip is established. The ultimate bearing capacity of the floor is 26.3 MPa. When the ultimate bearing capacity is exceeded, the roadway floor of the coalface may undergo overall slip burst. The maximum floor failure depth is 5.39 m, which exceeds the total thickness of part of the roadway bottom coal and direct floor.

(3) An estimation model for advancing abutment pressure in the case of insufficient roof caving is established. The advancing abutment pressure produces an influence within 197 m ahead of the coalface. The peak value zone is within 98 m in front of the coalface. The peak stress is 47.2 MPa. These estimated results basically coincide with the failure scope and strength of the rock burst.

Data Availability

The data used to support the findings of this study are available from the corresponding author upon request.

Conflicts of Interest

The authors declare that they have no conflicts of interest.

Acknowledgments

This study was supported by the National Natural Science Foundation of China (grant nos. 41977252 and U2005205); the State Key Laboratory of Geohazard Prevention and Geoenvironment Protection Independent Research Project (grant no. SKLGP2020Z001); and the State Key Laboratory of Geohazard Prevention and Geoenvironment Protection

Open Fund (grant nos. SKLGP2019K010 and SKLGP2020K015).

References

[1] M. T. Gao, Z. Q. Song, and H. Q. Duan, "Mechanical properties and control rockburst mechanism of coal and rock mass with bursting liability in deep mining," *Shock and Vibration*, vol. 2020, Article ID 8833863, 15 pages, 2020.

[2] Q. Zhang, E. Wang, X. Feng, C. Wang, L. Qiu, and H. Wang, "Assessment of rockburst risk in deep mining: an improved comprehensive index method," *Natural Resources Research*, vol. 30, no. 2, pp. 1817–1834, 2021.

[3] C. Zhu, K. Zhang, H. Cai et al., "Combined application of optical fibers and CRLD bolts to monitor deformation of a pit-in-pit foundation," *Advances in Civil Engineering*, vol. 2019, no. 1, 16 pages, Article ID 2572034, 2019.

[4] C. Zhu, M. C. He, Z. G. Tao, Q. X. Meng, and X. H. Zhang, "Recognition and prevention of rockfall vulnerable area in open-pit mines based on slope stability analysis," *Geomechanics and Engineering*, vol. 26, no. 5, pp. 441–452, 2021.

[5] X. Li, K. Peng, J. Peng, and D. Hou, "Experimental investigation of cyclic wetting-drying effect on mechanical behavior of a medium-grained sandstone," *Engineering Geology*, vol. 293, p. 106335, 2021.

[6] X. Li, K. Peng, J. Peng, and H. Xu, "Effect of cyclic wetting-drying treatment on strength and failure behavior of two quartz-rich sandstones under direct shear," *Rock Mechanics and Rock Engineering*, vol. 54, no. 11, pp. 5953–5960, 2021.

[7] M. Z. Gao, J. Xie, Y. N. Gao et al., "Mechanical behavior of coal under different mining rates: a case study from laboratory experiments to field testing," *International Journal of Mining Science and Technology*, vol. 31, pp. 825–841, 2021.

[8] M. Gao, J. Xie, J. Guo, Y. Lu, Z. He, and C. Li, "Fractal evolution and connectivity characteristics of mining-induced crack networks in coal masses at different depths," *Geomechanics and Geophysics for Geo-Energy and Geo-Resources*, vol. 7, no. 1, p. 9, 2021.

[9] L. Guo, C. J. Zhou, and Z. Ru, "Underground engineering rock burst review of Research," *Applied Mechanics and Materials*, vol. 2156, pp. 1161–1166, 2013.

[10] B. Jiang, H. Ji, L. Fu, S. Gu, T. Zou, and J. Lu, "Research on evaluation index and application of rockburst risk in deep strip mining," *Shock and Vibration*, vol. 2020, no. 1, 10 pages, Article ID 8824323, 2020.

[11] W. Cai, X. Bai, G. Si, W. Cao, S. Gong, and L. Dou, "A monitoring investigation into rock burst mechanism based on the coupled theory of static and dynamic stresses," *Rock Mechanics and Rock Engineering*, vol. 53, no. 12, pp. 5451–5471, 2020.

[12] B. Wang, S. Zhu, F. Jiang, J. Liu, X. Shang, and X. Zhang, "Investigating the width of isolated coal pillars in deep hard-strata mines for prevention of mine seismicity and rockburst," *Energies*, vol. 13, no. 17, p. 4293, 2020.

[13] D. Li, J. Zhang, Y. Sun, and G. Li, "Evaluation of rockburst hazard in deep coalmines with large protective island coal pillars," *Natural Resources Research*, vol. 30, no. 2, pp. 1835–1847, 2021.

[14] G. Chen, T. Li, G. Zhang, H. Yin, and H. Zhang, "Temperature effect of rock burst for hard rock in deep-buried tunnel," *Natural Hazards*, vol. 72, no. 2, pp. 915–926, 2014.

[15] L. M. Xu, K. X. Lu, Y. S. Pan, and Z. J. Qin, "Study on rock burst characteristics of coal mine roadway in China," *Energy Sources, Part A: Recovery, Utilization, and Environmental Effects*, vol. 2019, Article ID 1655114, 2019.

[16] L. P. Dai, Y. S. Pan, and Z. H. Li, "Quantitative mechanism of roadway rockbursts in deep extra-thick coal seams: theory and case histories," *Tunnelling and Underground Space Technology*, vol. 111, Article ID 103861, 2021.

[17] S. C. Hu, Y. L. Tan, and J. G. Ning, "Multiparameter monitoring and prevention of fault-slip rock burst," *Shock and Vibration*, vol. 2017, Article ID 7580109, 8 pages, 2017.

[18] G. A. Zhu, L. M. Dou, and Y. Liu, "Dynamic behavior of fault slip induced by stress waves," *Shock and Vibration*, vol. 2016, Article ID 4386836, 13 pages, 2016.

[19] M. Zhang and F. Jiang, "Rock burst criteria and control based on an abutment-stress-transfer model in deep coal roadways," *Energy Science & Engineering*, vol. 8, no. 8, pp. 2966–2975, 2020.

[20] S. T. Zhu, D. C. Ge, and F. X. Jiang, "Rock burst mechanism under coupling action of working face square and regional tectonic stress," *Shock and Vibration*, vol. 2021, Article ID 5538179, 11 pages, 2021.

[21] C. Xu, Q. Fu, X. Cui, K. Wang, Y. Zhao, and Y. Cai, "Apparent-depth effects of the dynamic failure of thick hard rock strata on the underlying coal mass during underground mining," *Rock Mechanics and Rock Engineering*, vol. 52, no. 5, pp. 1565–1576, 2019.

[22] J. F. Pan, S. H. Liu, and S. W. Wang, "A new theoretical view of rockburst and its engineering application," *Advances in Civil Engineering*, vol. 2018, Article ID 4683457, 12 pages, 2018.

[23] Z. X. Yu, J. L. Wen, and H. T. Ma, "Research on the evolution law of spatial structure of overlying strata and evaluation of rock burst risks in deep well strip mining," *Geotechnical & Geological Engineering*, vol. 2021, pp. 1–13, 2021.

[24] W. J. Guo, Y. Y. Li, and D. W. Yin, "Mechanisms of rock burst in hard and thick upper strata and rock-burst controlling technology," *Arabian Journal of Geosciences*, vol. 9, no. 10, Article ID 2596, 2016.

[25] J. Wen, H. Li, F. Jiang, Z. Yu, H. Ma, and X. Yang, "Rock burst risk evaluation based on equivalent surrounding rock strength," *International Journal of Mining Science and Technology*, vol. 29, no. 4, pp. 571–576, 2019.

[26] W.-Y. Guo, T.-B. Zhao, Y.-L. Tan, F.-H. Yu, S.-C. Hu, and F.-Q. Yang, "Progressive mitigation method of rock bursts under complicated geological conditions," *International Journal of Rock Mechanics and Mining Sciences*, vol. 96, pp. 11–22, 2017.

[27] M. C. He, J. Y. Li, and F. Q. Ren, "Rock burst criterion based on clay mineral content," *Arabian Journal of Geosciences*, vol. 13, no. 4, pp. 1–8, 2020.

[28] Y. Zhao, N. Liu, X. Zheng, and N. Zhang, "Mechanical model for controlling floor heave in deep roadways with U-shaped steel closed support," *International Journal of Mining Science and Technology*, vol. 25, no. 5, pp. 713–720, 2015.

[29] Y. Yang, S. Wei, and S. Zhao, "Research on the destructional pattern of surrounding rock of roadway induced by dynamic disturbance," *Geotechnical & Geological Engineering*, vol. 37, no. 5, pp. 4447–4459, 2019.

[30] Z. J. Li, S. B. Li, and X. L. Zhao, "Floor heave controlling technology of deep soft rock roadway," *Applied Mechanics and Materials*, vol. 170–173, pp. 68–71, 2012.

[31] Y. Qiu, Y. H. Lu, C. A. You, and Q. Y. Liu, "Parameter design of anti-slide pile control method in floor heave," *Applied Mechanics and Materials*, vol. 170–173, pp. 541–544, 2012.

[32] P. Dang, J. Y. Du, and T. Qian, "Boundary value problems for periodic analytic functions," *Boundary Value Problems*, vol. 2015, no. 1, pp. 1–28, 2015.

[33] D. A. Giuseppina, "Multiplicity results for nonlinear mixed boundary value problem," *Boundary Value Problems*, vol. 2012, no. 1, pp. 1–12, 2012.

[34] M. Iskander, Z. Chen, M. Omidvar, and I. Guzman, "Rankine pseudo-static earth pressure for c-ϕ soils," *Mechanics Research Communications*, vol. 51, pp. 51–55, 2013.

[35] X. F. Shi, X. K. Zhang, and F. X. Jiang, "Study on practice of rockburst accident prevention in multi-seam mining controlled by large fault and hard roof," *Geotechnical & Geological Engineering*, vol. 38, pp. 1–11, 2020.

[36] F. Xiong, Q. Jiang, and C. Xu, "Fast equivalent micro-scale pipe network representation of rock fractures obtained by computed tomography for fluid flow simulations," *Rock Mechanics and Rock Engineering*, vol. 54, no. 2, pp. 937–953, 2021.

[37] F. Xiong, C. Zhu, and Q. Jiang, "A novel procedure for coupled simulation of thermal and fluid flow models for rough-walled rock fractures," *Energies*, vol. 14, p. 951, 2021.

Hindawi
Mathematical Problems in Engineering
Volume 2021, Article ID 2956496, 13 pages
https://doi.org/10.1155/2021/2956496

Research Article

Strain Incremental Adjustment Method of Cable Force of Composite Saddle Anchor Span of Single-Tower Single-Span Ground-Anchored Suspension Bridge

Long Yu,[1] **Wei Xu**,[1] **Da-bing Zhang**,[2] **Xu-ming Ma**,[2] **and Yong-hong Wu**[1]

[1]*Faculty of Architectural Engineering, Kunming University of Science and Technology, Kunming, Yunnan 650500, China*
[2]*China Railway Bridge Science Research Institute Co., Ltd., Wuhan, Hubei 430000, China*

Correspondence should be addressed to Long Yu; 514633006@qq.com and Yong-hong Wu; 496567227@qq.com

Received 11 October 2021; Revised 9 November 2021; Accepted 10 November 2021; Published 30 November 2021

Academic Editor: Gan Feng

To improve the efficiency of cable force adjustment of composite saddle anchor span of single-tower single-span ground-anchored suspension bridge, a strain incremental adjustment method is proposed. The analytical calculation model is established according to the relative spatial position of the cable strand and the saddle groove of the composite saddle, and the target cable force of the cable strands is calculated by the target position of the composite saddle in the cable-stayed bridge and construction phases. Considering the coupling relationship between the cable strand and the composite saddle, the calculation formula of the change in main span main cable force and anchor span cable force after the adjustment of a single cable strand is derived. Based on the condition of equilibrium of forces along the slip surface of the composite saddle, the slip amount of composite saddle after a round of cable strand adjustment is obtained, then the adjustment amount of actual construction of the cable strands is also obtained through the strain incremental adjustment method. With the help of a numerical simulation platform, the calculation program of the cable force adjustment of composite saddle anchor span is established by an iterative solution method. In this paper, taking the Jinsha River Bridge at Hutiao Gorge as a research object, the adjustment of cable force of composite saddle anchor span is analyzed and calculated. The research results indicate that the calculated cable force is obtained by the strain incremental adjustment method, and it is similar to the measured cable force. The cable strand adjustment and optimization method avoids excessive repeated stretching and relaxation of a single cable strand in the process of multiple rounds of cable strand adjustment and reduces the amount of construction adjustment. This method can effectively reduce the times of cable strand adjustment and improve the efficiency of adjusting the anchor span cable force.

1. Introduction

The single-tower single-span ground-anchored suspension bridge has only one tower, and the other end of the main cable is anchored on the tunnel anchor bolt after passing the composite saddle structure. This type of bridge is fully adapted to the steep terrain of the mountain, reducing a bridge tower and a side span. Compared with the common saddle of the multitower suspension bridge, the composite saddle on the single-tower suspension bridge has the functions of both tower saddle and splay saddle. The change of the saddle position will lead to the change of the main cable shape of the main span and the anchor span cable force. The anchor span of the composite saddle is controlled by the cable strand tension [1–3], and the accuracy of cable force adjustment will affect the reliability of the overall structure of the suspension bridge [4–9]. The composite saddle is directly connected with the main cable of the main span. Compared with the force at both ends of the splay saddle, the force at both ends of the composite saddle is greater, and the requirements of the adjustment accuracy of the cable forces are higher. Therefore, it is still difficult to adjust the anchor span cable force of the composite saddle quickly and accurately.

In the process of cable strand construction adjustment, the difference between the measured cable force and the

target cable force is usually used to determine the adjustment amount [10]. This method does not take into account the coupling relationship between the cable strand and the cable saddle. After the adjustment of a single cable strand, the change of the cable force will change the position of the cable saddle. When the position of the endpoint of the cable strand changes, the cable force of the adjusted cable strand cannot reach the target cable force through a round of adjustment, and the efficiency and the accuracy of cable strand adjustment are greatly reduced. At present, there is little research on composite saddle structure, which is basically in the phase of the model test [11]. For the research of the adjustment method of the anchor span cable force, most of them take the splay saddle structure as the research object. Through the analysis of the spatial geometric relationship of cable strands [12–14], the cable force of the splay saddle at the target position is obtained. Considering the influence of temperature on cable strand tension, the cable strand tension adjustment method under the influence of temperature change is obtained [15]. For the measured cable force, boundary constraints, stiffness, and material characteristics of cable strand are mainly considered [10, 16–20]. The accurately measured frequency is obtained by the energy method and the frequency method, to improve the measurement accuracy of cable force.

To quickly and accurately control the composite saddle anchor span, this paper establishes the calculation method of strain incremental adjustment of composite saddle anchor span of single-tower single-span ground-anchored suspension bridge and develops the numerical simulation program with the help of programming software [21–23]. According to the relative spatial position of the cable strand and the composite saddle, the target cable force of the composite saddle at the target position is obtained. The coupling relationship between the cable strand and the composite saddle in the cable strand adjustment phase is analyzed, and the actual adjustment amount of the cable strand is obtained by the strain increment method, so that the purpose of accurate cable strand adjustment can be realized through a round of adjustment theoretically. The method is applied to the process of the cable strand adjustment calculation, and the practicability of the method is verified by comparing the field measured data.

2. Structure of Composite Saddle and Characteristics of Anchor Span Cable Strand

2.1. Structural Characteristics of the Composite Saddle. The composite saddle is a unique structure of a single-tower single-span ground-anchored suspension bridge. It is located on the buttress platform between the main span and the anchor span and plays the role of supporting, deflecting, and dispersing the main cable. Its structure is shown in Figure 1. The composite saddle changes the span of the main span and the anchor span through the activity of the bottom roller shaft, to balance the force at both ends of the saddle. Compared with the deflection angle of the main cable and the cable strand of the traditional rock shaft splay saddle, the deflection angle of the main cable and the anchor span cable strand at both ends of the composite saddle is larger, and the radial force of the main cable and the cable strand is larger.

2.2. Distribution Characteristics of Anchor Span Cable Strand. The cable strand is a spatial curve in the saddle groove of the composite saddle. Through the top and side view of the cable saddle, the deflection of the cable strand can be divided into horizontal bending and vertical bending. The horizontal bending curve is an arc segment with a small angle on a circle, and the vertical bending curve is an arc segment with a multisegment radius gradually decreasing. As shown in Figure 2, the cable strand passes through the starting point of vertical bending (*Point a*), the fixed point (*Point b*), the starting point of horizontal bending (*Point c*), the endpoint of horizontal bending (*Point d*), and the endpoint of vertical bending *(Point e*) in turn in the saddle groove. The cable strand starts vertical bending deflection first and then horizontal bending deflection. The cable strand ends the horizontal bending deflection first, then the vertical bending deflection, and finally be pulled to the position of the corresponding anchor point on the anchor surface. The composite saddle slides in the longitudinal direction along the horizontal plane of the buttress, which changes the tangent point of the cable strand at the anchor span side in the saddle groove, resulting in the changes of the coordinates of *Point e*, the unstressed length of the suspended segment of the cable strand and the cable force of the cable strand.

3. Calculation Principle of Anchor Span Cable Strand Adjustment

Basic assumptions, ① the cable strand is an ideal flexible cable with small deformation, which satisfies Hooke's law, and the section deformation can be ignored. ② The deformation of the composite saddle is very small and can be ignored in the process of cable force adjustment. ③ The cable strand does not slide relatively in the saddle groove. ④ In the process of cable force adjustment, the stiffness of the main tower is large enough, and the offset is small, and the change of the main span caused by it can be ignored.

3.1. Basic Principle of Anchor Span Cable Strand Adjustment. The anchor span is controlled by the cable strand tension. When the cable force of each cable strand can reach the target cable force, the composite saddle can slide to the target position through the cable force adjustment. Before the cable force adjustment, the measured cable force is obtained by field measurement, and the theoretical target cable force is calculated by the analytical method. The difference of cable force is calculated by the measured cable force and the target cable force, and then the actual adjustment of the cable strand can be obtained by iterative solution.

According to the relative spatial position of cable strands in the cable-stayed bridge state, the horizontal bending and the vertical bending angles of cable strands are calculated, then the unstressed length from *Point b* to the anchor point of cable strands in the anchor span is calculated. The

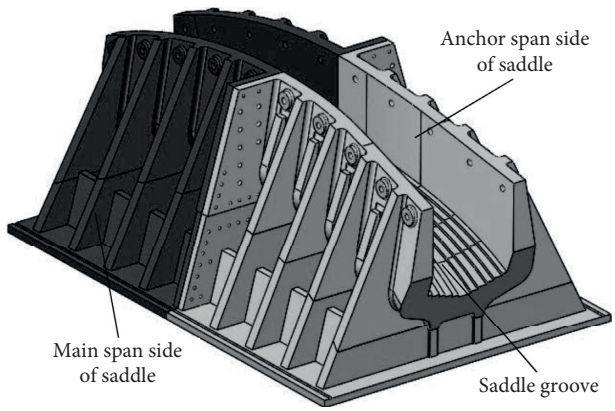

Figure 1: Structural drawing of the composite saddle.

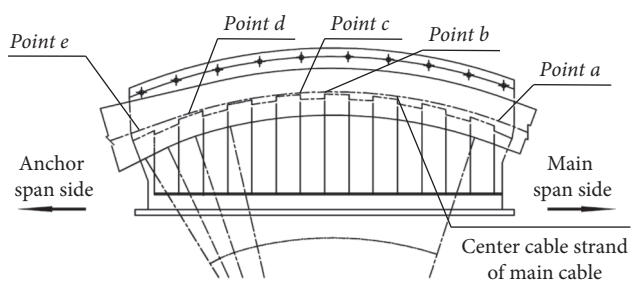

Figure 2: Side view of the composite saddle.

unstressed length represents the original length of the cable strand when there is no force on the cable strand. There is a certain offset between the position of the composite saddle in the construction phase and that in the cable-stayed bridge phase. According to the unstressed length of the cable strand and the target offset of the composite saddle, the target cable force can be calculated. By comparing the target cable force with the measured cable force, the initial value of the cable strand adjustment can be calculated by using the pitch method [10]. Through the difference of cable force and the longitudinal tensile stiffness of cable strand, the rotation direction and the number of turns of the bolt are calculated by the pitch method.

Because the composite saddle will slip during cable strand adjustment, the actual strain after cable strand adjustment deviates from the calculated value, and the remaining cable strands will produce strain increment due to the slide of the composite saddle. The strain incremental adjustment method can obtain the adjustment amount of actual construction by superimposing the adjustment amount of change of multiple rounds of cable strand adjustment. According to the initial value of cable strand adjustment, a round of adjustment of all cable strands can be calculated. Considering the coupling relationship between the cable strand and the composite saddle, the strain increment of all cable strands after adjustment of each cable strand can be calculated, and then the change of actual adjustment amount is obtained. Through multiple rounds of cycle iterative calculation, the cable forces of all cable strands approach the target cable force. Through superimposing the cable force adjustment amount caused by multiple rounds of strain increment of each cable strand, the adjustment amount of actual construction of cable strand can be obtained.

3.2. Calculation of Horizontal and Vertical Bending Angles. According to the spatial trend of the cable strand in the saddle groove and the cable strand of the suspended segment, the analytical calculation model of cable force of cable strand is established. In the process of calculating the target cable force, the problem of calculating the deflection angle of the cable strand will be encountered. According to the spatial distribution of the cable strand in the saddle groove, the spatial curve of the cable strand is divided into horizontal bending and vertical bending. Under the horizontal bending coordinate system, the horizontal bending angle of the cable strand can be calculated. The approximate calculation method of horizontal bending angle θ is shown in Figure 3.

In the figure, A, B, and C are *Point c*, *Point d*, and the anchor point, and R_0 is the horizontal bending radius. φ and x_1 are the auxiliary angle and the auxiliary line. The longitudinal direction of the bridge is the X-axis, the transverse direction of the bridge is the Y-axis, and the vertical direction is the Z-axis. Δx_0 and Δy_0 are the difference of the coordinates between *Point c* and the anchor point. It can be seen from Figure 3, φ can be written as

$$\phi = \arctan \frac{\Delta y_0}{\Delta x_0}. \tag{1}$$

Compared with the anchor span, the offset caused by the angle of the cable strand is very small, and φ is approximately equal to θ. x_1 can be written as

$$x_1 = R_0 \tan \frac{\phi}{2}. \tag{2}$$

The corrected horizontal bending angle θ is

$$\theta = \arctan \frac{\Delta y_0}{\Delta x_0 - x_1}. \tag{3}$$

Similarly, according to the coordinates of *Point a* and the anchor point under the vertical bending plane, the radii of different circular arc segments are brought in to calculate the vertical bending angle by the above method. The circular arc segment where *Point e* is located is judged by the calculated vertical bending angle, and the radius of the circular arc segment is the same as that used in calculating the vertical bending angle, then the calculated vertical bending angle is accurate. According to the intersection coordinates between the circular arc segments, the coordinates of *Point e* are calculated through the vertical bending angle and the radius of the circular arc segment. θ_{Hi} and θ_{Vi} represent horizontal and vertical bending angles of the ith cable strand.

3.3. Calculation of a Round of Cable Strand Adjustment. Under the action of uniformly distributed load along the cable length, the shape of the suspension segment is catenary [24–34]. The cable segment from *Point e* to the anchor point

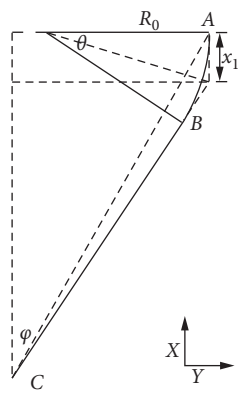

Figure 3: Calculation of horizontal bending angle of anchor span cable strand.

is catenary, while the main cable shape of the main span in the cable-stayed bridge state is segmented catenary with concentrated force, and the analytical solution of the catenary is

$$l = \frac{HS_0}{EA} + \frac{H}{w}\left\{\ln\left[V + \sqrt{H^2 + V^2}\right] - \ln\left[V - W + \sqrt{H^2 + (V - W)^2}\right]\right\},$$
$$h = \frac{WS_0 - 2VS_0}{2EA} - \frac{1}{w}\left[\sqrt{H^2 + V^2} - \sqrt{H^2 + (V - W)^2}\right], \tag{4}$$

where $W = wS_0$, w is the self-weight intensity, and l and h are the span and the elevation difference of both endpoints. S_0 is the unstressed length, and H and V are the horizontal and vertical force at the cable end. E and A are the elastic modulus and the section area of the suspension segment.

Considering the influence of temperature on the unstressed length and the self-weight intensity of the cable segment, the catenary formula at a certain temperature can be derived by replacing S_{0t} and w_0:

$$S_{0t} = (1 + \lambda\Delta t)S_0,$$
$$w_0 = \frac{w}{1 + \lambda\Delta t}, \tag{5}$$

where S_{0t} and w_0 are the unstressed lengths and the self-weight intensity of the suspension segment at a certain temperature. λ is the coefficient of temperature expansion, and Δt is the temperature difference.

Segmented catenary with concentrated force is as shown in Figure 4. The horizontal force H_i and the vertical force V_i at the left end of the ith segment are

$$H_i = H,$$
$$V_i = V_{i-1} - wS_{0,i-1} - P_{i-1} = V - \sum_{j=1}^{i-1} wS_{0j} - \sum_{j=1}^{i-1} P_j, \tag{6}$$

where P_i is the concentrated force of the ith sling on the main cable. S_{0i} is the unstressed length of the ith suspension cable, and $S_{0,i-1}$ is the unstressed length of the $(i-1)$th suspension cable. Through bringing in the above formula, the analytical solution of the segmented catenary is

$$l = \frac{H}{EA}\sum_{i=1}^{n} S_{0i} + \frac{H}{w}\sum_{i=1}^{n}\left\{\ln\left[V_i + \sqrt{H^2 + V_i^2}\right] - \ln\left[V_i - wS_{0i} + \sqrt{H^2 + (V - wS_{0i})^2}\right]\right\},$$
$$h = \frac{1}{2EA}\sum_{i=1}^{n}\left(wS_{0i}^2 - 2VS_{0i}\right) - \frac{1}{w}\sum_{i=1}^{n}\left[\sqrt{H^2 + V_i^2} - \sqrt{H^2 + \left(V_i^2 - wS_{0i}\right)^2}\right]. \tag{7}$$

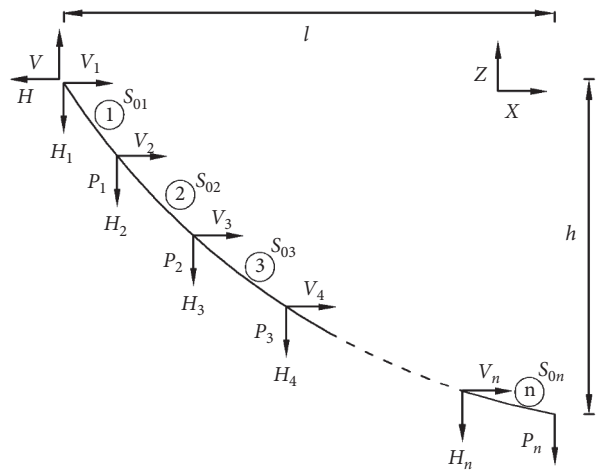

Figure 4: Segmented catenary with concentrated force.

For the above formula, the complete differential of H and V is

$$\begin{bmatrix} \mathrm{d}l \\ \mathrm{d}h \end{bmatrix} = \begin{bmatrix} \dfrac{\partial l}{\partial H} & \dfrac{\partial l}{\partial V} \\ \dfrac{\partial h}{\partial H} & \dfrac{\partial h}{\partial V} \end{bmatrix} \begin{bmatrix} \mathrm{d}H \\ \mathrm{d}V \end{bmatrix} = R \begin{bmatrix} \mathrm{d}H \\ \mathrm{d}V \end{bmatrix}, \tag{8}$$

where R is the flexibility matrix, $\mathrm{d}l$ and $\mathrm{d}h$ are the differential form of span l and elevation difference h. The stiffness matrix is $K = R^{-1}$.

According to the checking calculation, the change of sling force caused by the slide of the composite saddle has little impact on the horizontal component of main cable tension in the whole process of cable strand adjustment construction, then the sling cable force can be regarded as a fixed value. When the slip amount of composite saddle is ΔS, the amount ΔH and ΔV of change of cable force of the main span is

$$\begin{bmatrix} \Delta H \\ \Delta V \end{bmatrix} = K \begin{bmatrix} \Delta S \\ 0 \end{bmatrix}. \tag{9}$$

After the ith cable strand adjustment, the slip amount of the composite saddle is ΔS_i. The component of change of the main cable tension of the main span along the horizontal direction is ΔH_i.

As the span from *Point e* to the anchor point is short, and the cable force is large, the suspended segment of the cable strand can be calculated as a straight line, and its spatial position is as shown in Figure 5. O is the anchor point, and D is *Point e*. The plane XOZ is the vertical bending plane, and the plane XOY is the horizontal bending plane. The angle α between the OD and its projection on the plane XOY and the angle β between the projection and the X-axis can be calculated. Then, the target cable force and the unstressed length S_{0i} under the target slip amount can be calculated, and the adjustment amount Δl_i of cable strand by pitch method can be calculated. The coordinate difference Δx, Δy, and Δz between *Point e* and the anchor point at the current position can be obtained.

When adjusting the ith cable strand of anchor span, the sum ΔF_i of the amount of change of the cable force along the sliding surface is

$$\Delta F_i = EA\frac{\Delta l_i}{S_{0i}}\cos\alpha_i\cos\beta_i - EA\sum_{j=1}^{n}\left(\frac{\Delta\varepsilon_j}{S_{0j}}\cos\alpha_j\cos\beta_j\right), \tag{10}$$

$$\Delta\varepsilon_j = \sqrt{\Delta x_j^2 + \Delta y_j^2 + \Delta z_j^2} - \sqrt{\left(\Delta x_j - \Delta S_i\right)^2 + \Delta y_j^2 + \Delta z_j^2}, \tag{11}$$

where $\Delta\varepsilon_j/S_{0j}$ is the strain increment, and the angle α_i between the OD of the ith cable strand and its projection on the plane XOY and the angle β_i between the projection and the X-axis can be calculated. During the adjustment of the ith strand, the process can be understood in two parts: the change of the cable force of the ith strand and the change of the cable force of all strands. In equation (10), the first half on the right of the equal sign represents the cable force change of the ith cable strand after it is adjusted according to the initial adjustment, and the second half represents the sum of the cable force changes of all cable strands after the ith cable strand is adjusted. $\Delta\varepsilon_j$ is the deformation after adjusting the jth cable strand in equation (11).

$\Delta F_i = \Delta H_i$ is obtained by the equilibrium relationship, and the slip amount ΔS_i can be calculated by iterative solution. The updated coordinates are $\Delta x_j' = \Delta x_j - \Delta S_i$, $\Delta y_j' = \Delta y_j$ and $\Delta z_j' = \Delta z_j$, and $(i+1)$th adjustment amount is

$$\Delta l_{i+1}' = \Delta l_{i+1} - \sqrt{\Delta x_{i+1}^2 + \Delta y_{i+1}^2 + \Delta z_{i+1}^2} + \sqrt{\Delta x_{i+1}'^2 + \Delta y_{i+1}'^2 + \Delta z_{i+1}'^2}. \tag{12}$$

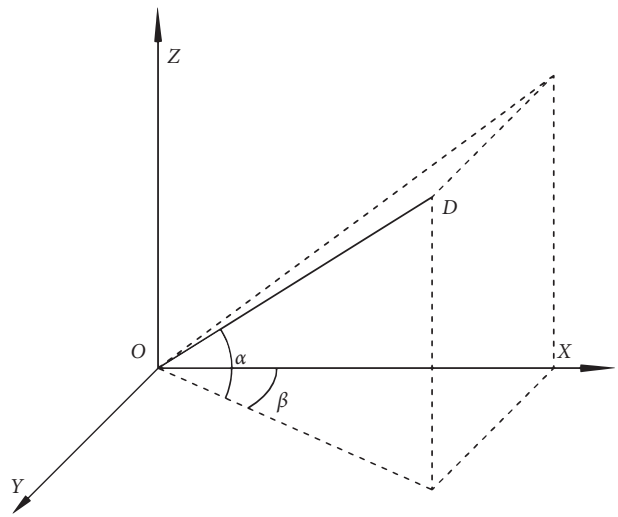

Figure 5: Spatial position of the cable strand.

The updated main span is $l_{i+1} = l_i + \Delta S_i$, and l_i is the main span after adjusting the ith strand. All cable strands are cycled. After a round of cable strand adjustment, the sum of the slip amount is

$$\Delta S = \sum_{i=1}^{n} \Delta S_i. \tag{13}$$

When the composite saddle slides to the current position, the force of each cable strand can be calculated. The force is

$$T_i' = T_i + EA\frac{\Delta l_i - \sqrt{\Delta x_i^2 + \Delta y_i^2 + \Delta z_i^2} + \sqrt{(\Delta x_i - \Delta S)^2 + \Delta y_i^2 + \Delta z_i^2}}{S_{0i}}, \tag{14}$$

where T_i is the measured cable force and T_i' is calculated by the strain increment of the cable strand. The initial cable force is updated to T_i' by the above formula. The current composite saddle position is regarded as the initial position, $\Delta x_i' = \Delta x_i - \Delta S$, $\Delta y_i' = \Delta y_i$, and $\Delta z_i' = \Delta z_i$, and the main span is $l' = l + \Delta S$. The initial adjustment amount of each strand caused by strain increment is updated to

$$\Delta l_i' = \sqrt{\Delta x_i^2 + \Delta y_i^2 + \Delta z_i^2} - \sqrt{(\Delta x_i - \Delta S)^2 + \Delta y_i^2 + \Delta z_i^2}. \tag{15}$$

The difference ΔT_i between the current cable force and the target cable force is calculated circularly through the above formula. When ΔT_i meets the accuracy requirements, the initial adjustment amount of each cable strand in the overall cycle phase is superimposed to obtain the actual adjustment amount of each anchor span cable strand. When all cable strands are adjusted for m rounds, the difference between the calculated cable forces and the target cable forces of all cable strands can meet the accuracy requirements, and the adjustment amount of the actual construction of the ith cable strand is

$$\Delta L_i = \sum_{j=1}^{m} \Delta l_{ij}', \tag{16}$$

where $\Delta l_{ij}'$ is the adjustment amount of the ith cable strand of the jth round of cable strand adjustment.

4. Adjustment Method of Anchor Span Cable Strand and Its Program Implementation

4.1. Calculation Process of Target Cable Force. According to the position of the composite saddle and the spatial position of the cable strand in the saddle groove under the cable-stayed bridge phase, the analytical calculation model of the cable strand is established with 18°C as the reference temperature, and the unstressed length of all cable strands from *Point b* to the anchor point is calculated. The process is as shown in Figure 6(a), which can be applied to calculate the cable force at any construction phase. According to the slip amount of composite saddle, the coordinates of *Point a*, the span, and the elevation difference from *Point e* to the anchor *point c*an be calculated, and the anchor span cable force at the current position of the composite saddle is calculated by using the catenary formula. This anchor span cable force is the theoretical target cable force, and it is the cable force at the anchor surface end of the cable strand. When the composite saddle slides to the target position, this method can also be used to calculate the cable force of each cable strand. For example, the pre-bias position of the composite saddle is known when there is no external load on the main cable, and the target cable force at the anchor end can be calculated according to the pre-bias position. The process is as shown in Figure 6(b), where the tangent angle represents the angle between the tangent at *point e* and the X-axis.

In the process of calculating the length of the spatial curve of the cable strand in the saddle groove, the stressed length is approximately calculated by dividing the interpolation points. The stressed length represents the actual length of the cable

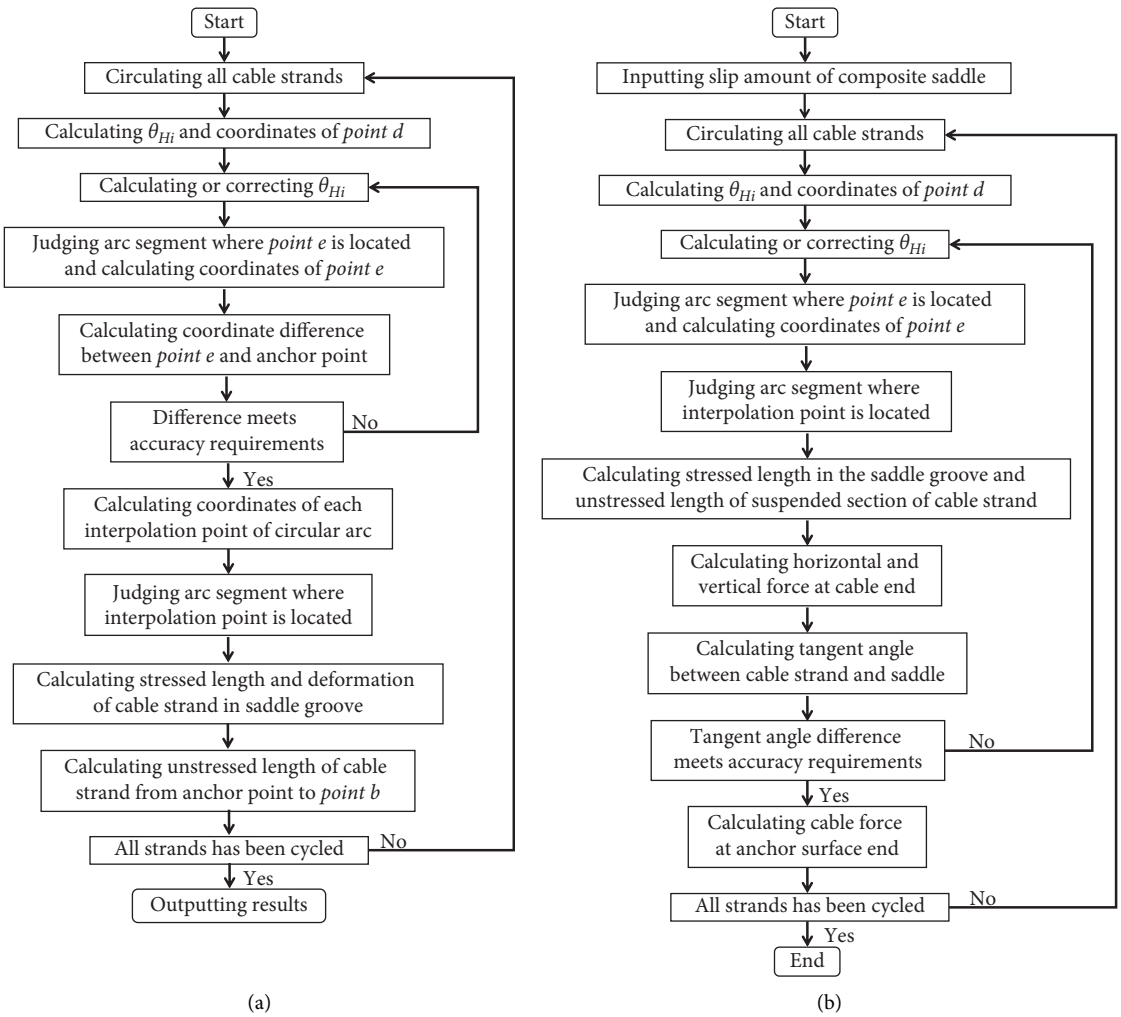

Figure 6: Calculation process of target cable force. (a) Calculation process of cable-stayed bridge phase and (b) calculation process of construction phase.

strand under the action of force. According to the field observation and calculation, during the sliding process of the composite saddle, most of *Point d* of the cable strands are in the first circular arc saddle groove of the composite saddle, and *Point e* is in the other circular arc saddle grooves. To ensure that the actual length calculation of the cable strands in the saddle groove has higher accuracy, the cable segment from *Point d* to *Point e* needs to be divided into more interpolation points. Through the checking calculation, when it is divided into 400 segments, the calculation of cable strand space curve length has high accuracy, which can meet the actual calculation needs of the project.

4.2. Calculation Process of a Round of Cable Strand Adjustment. The target cable force, the initial adjustment amount, and the cable force of each sling are known. Through the calculation process of a round of adjustment of all cable strands, the slip amount of composite saddle, the strain increment of all cable strands, and the current cable force can be calculated, and the calculation process is as shown in Figure 7. If the difference between the current cable force and the target cable force does not meet the accuracy requirements, it is necessary to update the tangent point coordinates between the composite saddle and the main cable of the main span, the span of the main span, and the initial adjustment amount of all cable strands for the iterative calculation of the second round of cable strand adjustment.

4.3. Overall Calculation Process of Strain Incremental Adjustment Method. After a round of cable strand adjustment calculation, the difference between the current cable force and the target cable force of most cable strands often cannot be within the required accuracy range, and multiple rounds of cable strand adjustment calculation are required. A strain incremental adjustment method is proposed to obtain the adjustment amount of the actual construction. The overall calculation process is as follows:

(1) After a round of cable strand adjustment calculation, the updated cable strand adjustment amount $\Delta l_i'$, the span of main span l', and the coordinates of *Point e* are obtained.

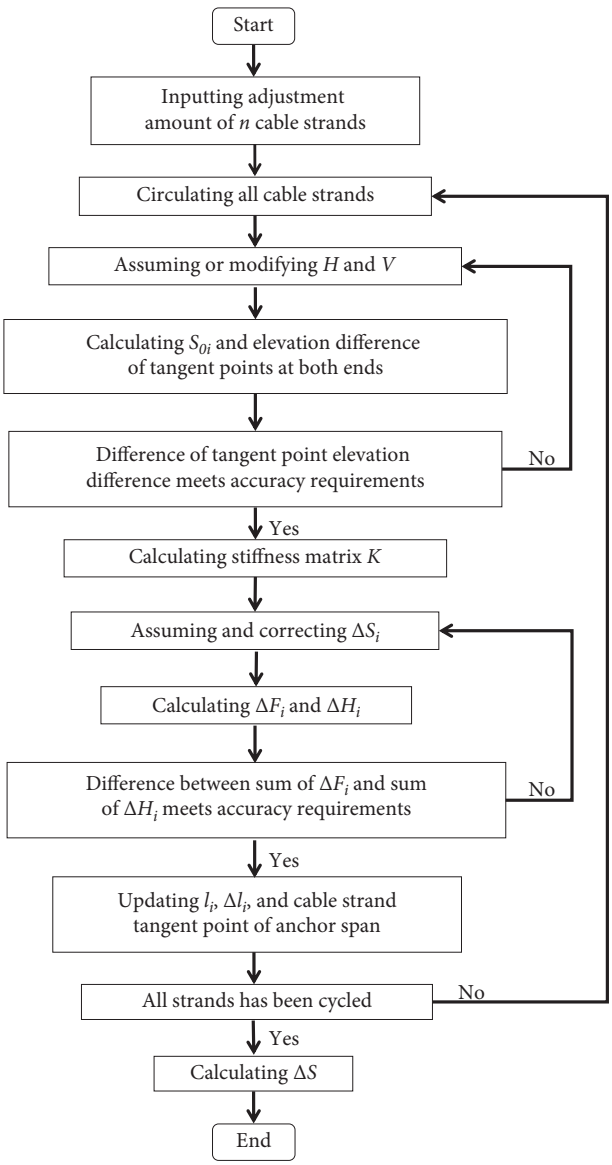

Figure 7: Calculation process of a round of adjustment of all cable strands.

(2) The slip amount of composite saddle after adjusting all cable strands in a round is superimposed. The actual cable force of all cable strands at the current position and the difference ΔT_i between the actual cable force and the target cable force are calculated, and the error accuracy ε of all strands is determined.

(3) All cable strands errors meet the accuracy requirements, i.e., $\max|\Delta T_i| \leq \varepsilon$. If not, the cable strand adjustment is calculated again by returning to step 1, and the sum of the slip amount of the composite saddle after a round of adjustment calculation is updated.

(4) After m rounds of cable strand adjustment calculation, all cable strands errors meet the accuracy requirements. The amount of change of cable strand adjustment amount caused by strain increment in each phase is superimposed, i.e., equation (16), to obtain the adjustment amount of all cable strands in actual construction.

5. Example Analysis

5.1. Project Description. The Jinsha River Bridge at Hutiao Gorge of Xiangli expressway is the single-tower single-span ground-anchored suspension bridge with a main span of 766 m. Due to the influence of topographic and geological conditions [35–40], the anchor form of Lijiang bank is designed as a gravity anchor, and the anchor form of Shangri La bank is designed as a tunnel anchor. The main cable is composed of 97 cable strands, and each cable strand is composed of 127 galvanized steel wires with a diameter of 5.4 mm, with a tensile strength of 1770 MPa and an elastic modulus of 2.0×10^5 MPa. The composite saddle is located between the main span and the anchor span of Shangri La bank, and the anchor span is 30 m, overall layout is as shown in Figure 8.

5.2. Calculation and Program Verification of Target Cable Force. After the erection of the main cable, the composite saddle in the current position has occurred a slide of 82 mm towards the anchor span, compared with the composite saddle of the cable-stayed bridge position. Before adjusting the cable force, it is necessary to measure the initial cable force of each cable strand at the anchor surface end of the cable strand. The measured initial cable force is shown in Figure 9.

Compared with the composite saddle of the cable-stayed bridge position, the composite saddle in the pre-bias position has occurred slide of 89 mm towards the anchor span. The anchor span cable force is adjusted in multiple rounds so that the cable force of all cable strands approaches the theoretical value, and the composite saddle slides 7 mm towards the anchor span. The theoretical value is calculated by the finite element model. The actual construction adjustment amount of multiple rounds of each cable strand is superimposed. The superposition value is as shown in Figure 10, in which the positive value represents stretching and the negative value represents relaxation.

According to the field measured data and the overall structure calculation, the horizontal and vertical forces of the main cable at the main span side of the composite saddle are 159183.8 kN and 58517.3 kN in the cable-stayed bridge phase. When there is no external load on the main cable, the pre-bias position of the composite saddle is taken as the target position, and the target cable force can be calculated. According to the program of the calculation process at the cable-stayed bridge phase, the parameters such as the tension of the main cable, the arrangement position of the cable strand in the saddle groove, the coordinates of the anchor surface, and the measured temperature of 18.2°C are input, and the unstressed length from *Point b* to the anchor point of cable strand at the current temperature can be output. The calculated unstressed length at the cable-stayed bridge phase is input. According to the program of the calculation process of the construction phase, the target cable force of the cable strand at the current temperature can be output, when the

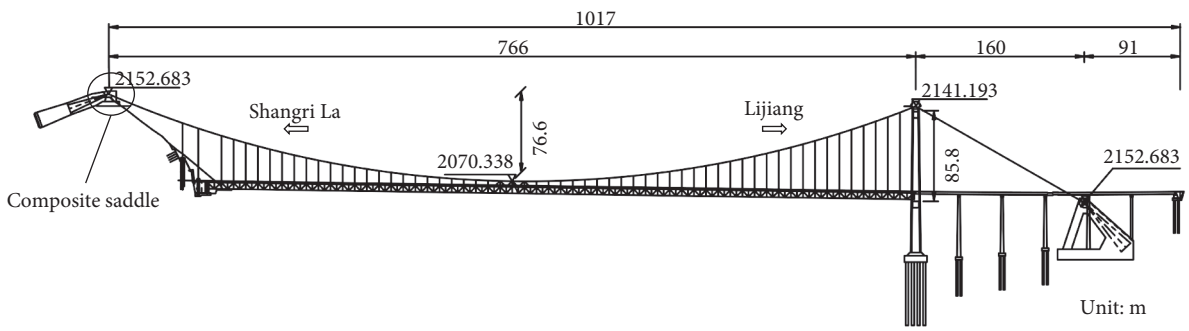

Figure 8: Overall layout of Jinsha River Bridge at Hutiao Gorge.

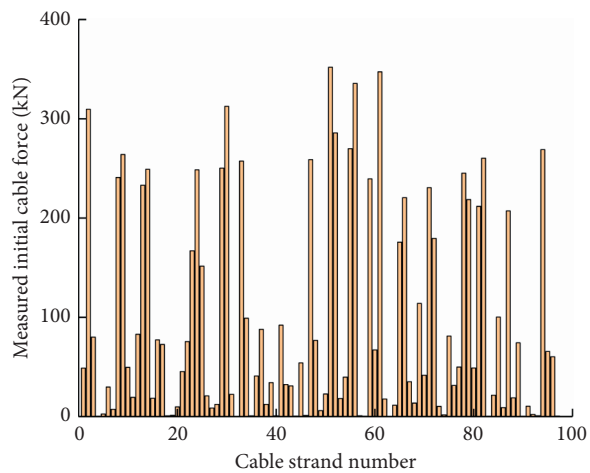

Figure 9: Measured cable force before cable strand adjustment.

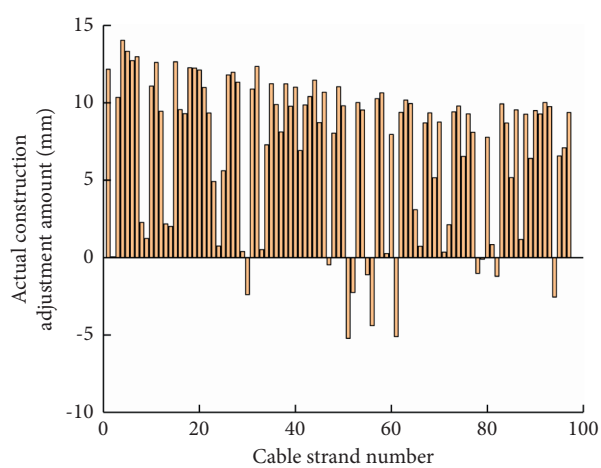

Figure 10: Actual construction adjustment of cable strand.

composite saddle is at the target position. The anchor point of the central cable strand is the coordinate origin of the anchor surface. As shown in Figure 11, the lowest layer of anchor surface cable strand is the first layer, and the uppermost layer is the 21st layer. When there is no external load on the main cable, the target cable force of the cable strand is regular, and the cable force increases gradually from the top to the bottom of the anchor surface.

By comparing the target cable force with the measured cable force after the last round of cable strand adjustment, the difference is shown in Figure 12.

It can be seen from Figure 12 that the difference after the last round of cable strand adjustment is within 2 kN, which proves that the target cable force calculated by the calculation program of the cable-stayed bridge and construction phase has high accuracy.

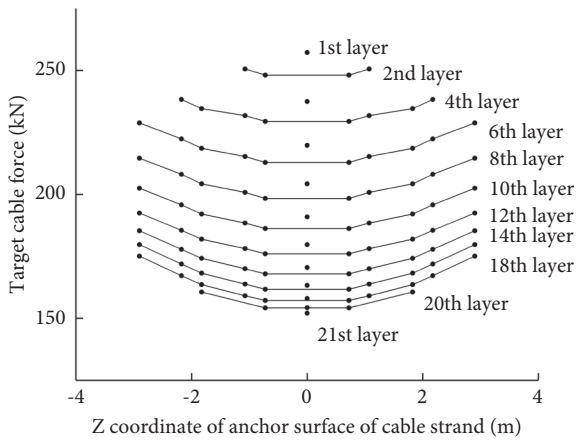

Figure 11: Target cable force.

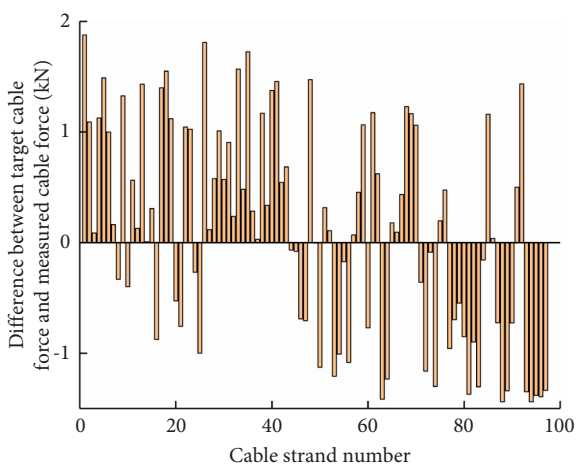

Figure 12: Difference between measured cable force and target cable force.

5.3. Calculation and Optimization of Cable Strand Adjustment. The superposition value of multiple rounds of actual construction adjustment amount is taken as the initial adjustment amount of cable strands, and then the cable force value after a round of cable strand adjustment is calculated. To verify the practicability of the calculation program of a round of adjustment of all cable strands, the calculated cable force calculated by a round of cable strand adjustment is compared with the measured cable force after the last round of cable strand adjustment. The difference between the measured cable force and the calculated cable force is shown in Figure 13.

It can be seen from Figure 13 that the difference of all cable strands is within 2.5 kN, and the sum of the slip amount of the composite saddle is 7.11 mm, which verifies the practicability of the calculation program of a round of adjustment of all cable strands.

Due to the excessive adjustment of a single cable strand in the cable strand adjustment process, there will be relative slippage between cable strands. To avoid relative slippage, it is necessary to adjust all cable strands in multiple rounds. The measured cable force before the first round of cable

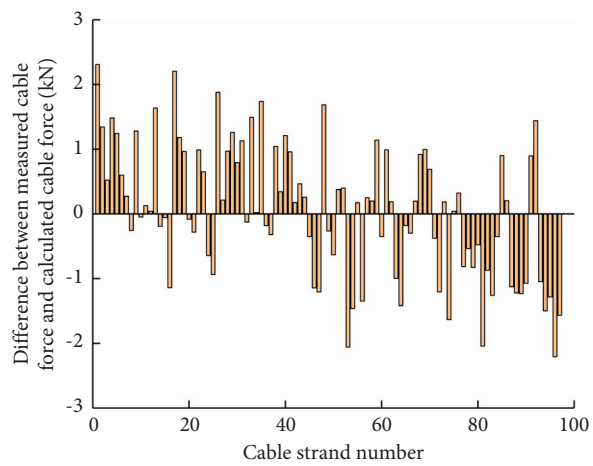

Figure 13: Difference between measured cable force and calculated cable force.

strand adjustment is taken as the initial value. To optimize the multiple rounds adjustment of all cable strands, the pre-bias position of the composite saddle is taken as the target position, and the cable force in Figure 10 is taken as the target cable force.

When the amount of change of cable force during cable strand adjustment is 50 kN, there is no relative slippage between cable strands, and there is a large safety coefficient. According to the calculation results in the previous section, the difference between the target cable force and the initial cable force is between −175.95 kN and 250.21 kN. The cable force adjustment difference of each round is 50 kN, and the cable strand construction adjustment is carried out continuously in 5 rounds. For cable strands with the cable force difference of more than 200 kN, 200 kN is taken as the target cable force of the first round, and the initial adjustment amount of the cable strand is calculated. For cable strands with the cable force difference of less than 200 kN, the adjustment amount is 0, and the calculation error accuracy ε is 0.1 kN. According to the strain incremental adjustment method, the adjustment amount of all cable strands, the cable force value of all cable strands, and the slip amount of the composite saddle in the first round are calculated, and the calculated cable force value of all cable strands after adjustment is taken as the initial value. Through repeating the above steps, 150 kN is taken as the target cable force of the second round with the cable force difference of more than 150 kN, and the adjustment amount of the cable strand with the cable force difference of less than 150 kN is set to 0, etc. According to the strain incremental adjustment method, the adjustment amount of the cable strand and the slip amount of the composite saddle are calculated in 5 rounds, which is shown in Figures 14 and 15.

As seen in the figure above, 13, 48, 69, 85, and 97 cable strands are adjusted, respectively, in 5 rounds of cable strand adjustment. Compared with the conventional method of adjusting all cable strands in each round, the optimization method avoids excessive repeated stretching and relaxation of a single cable strand in the process of multiple rounds of cable strand adjustment, reducing the amount of

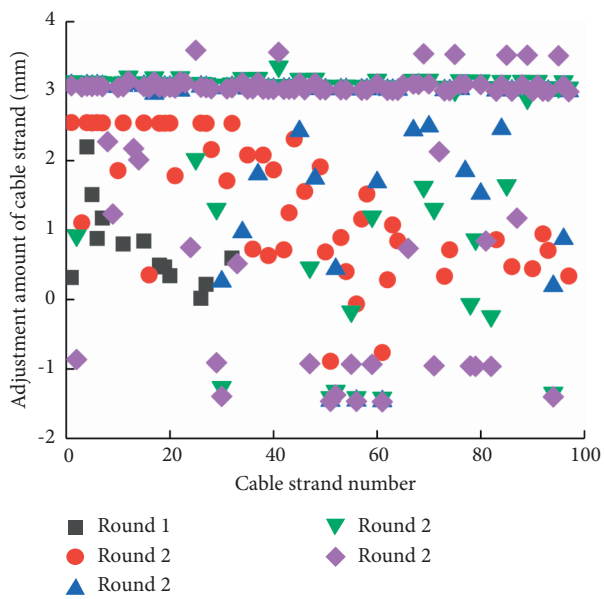

Figure 14: Adjustment amount of cable strand of 5 rounds.

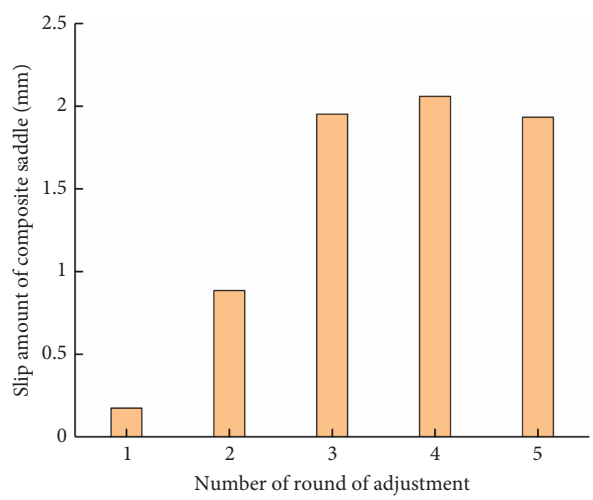

Figure 15: Slip amount of composite saddle.

construction adjustment, and it also avoids the relative slippage between cable strands in the process of cable strand adjustment. The superposition value of the slip amount of the composite saddle after the 5 rounds of cable strand adjustment is 7.0038 mm, which shows that the composite saddle can return to the target pre-bias position through cable force adjustment.

6. Conclusion

For the cable force adjustment of composite saddle anchor span of single-tower single-span ground-anchored suspension bridge, a strain incremental adjustment method is proposed. The calculation of theoretical target cable force and the cable force adjustment is studied by the analytical calculation method. The Jinsha River Bridge at Hutiao Gorge is taken as the research object, and the following conclusions are shown:

(1) A strain incremental adjustment method of cable force of composite saddle anchor span of single-tower single-span ground-anchored suspension bridge is proposed. Under the premise of ignoring the influencing factors such as the construction environment, this method can adjust the cable force of anchor span cable strand to the target cable force in a round theoretically and can achieve the purpose of precise adjustment. Compared with the conventional method, it improves the cable strand adjustment efficiency.

(2) The target cable force value of cable strand, the calculated cable force value of cable strand, and the slip amount of composite saddle are calculated by this method. By comparing the calculated values with the measured values, the practicability of this method is verified.

(3) To avoid the relative slippage between cable strands in the process of cable strand adjustment, the adjustment amount of multiple rounds of cable strands is optimized. Compared with the conventional method of adjusting all cable strands in each round, this optimization method avoids excessive repeated stretching and relaxation of a single cable strand in the process of multiple rounds of cable strand adjustment and reduces the amount of construction adjustment.

(4) Before the suspension bridge is opened to traffic, it is necessary to test the cable force of the composite saddle anchor span under the cable-stayed bridge state. If the difference between the target cable force and the measured cable force does not meet the requirements of cable strand adjustment accuracy, the target cable force and the actual adjustment amount can be calculated by inputting the sling force at each cable clamp under the current state.

Data Availability

The data used to support the findings of this study are included within the article.

Conflicts of Interest

The authors declare that there are no conflicts of interest regarding the publication of this study.

Acknowledgments

This study was sponsored by the National Natural Science Foundation of China (no. 51669009) and the Key Research and Development Projects of Science and Technology Department of Yunnan Province (no. 2018BC0008).

References

[1] J. W. Jung, D. J. Moon, J. W. Jung, S. K. Ro, and J. H. Park, *A Correlation Analysis Regarding the Temperature Effect for a*

Suspension Bridge, Springer International Publishing, New York, NY, USA, 2015.

[2] J. Nie, M. Tao, and J. Fan, "Research on cable anchorage systems for self-anchored suspension bridges with steel box girders," *Journal of Bridge Engineering*, vol. 16, no. 5, pp. 633–643, 2011.

[3] X. Wang, W. Yang, X. Zhang, and P. Zhu, "Experimental and numerical study on a novel cable anchorage system to improve the maintainability of suspension bridges," *Structure*, vol. 27, pp. 2126–2136, 2020.

[4] J. Lei, *Suspension Bridge Design*, Communications Press, Beijing, China, 2002.

[5] D. H. Choi, S. G. Gwon, and H. S. Na, "Simplified analysis for preliminary design of towers in suspension bridges," *Journal of Bridge Engineering*, vol. 19, no. 3, 2013.

[6] J. Li, A. Li, and M. Q. Feng, "Sensitivity and reliability analysis of a self-anchored suspension bridge," *Journal of Bridge Engineering*, vol. 18, no. 8, pp. 703–711, 2013.

[7] K. Mei, S. Sun, G. Jin, and Y. Sun, "Static and dynamic mechanical properties of long-span cable-stayed bridges using CFRP cables," *Advances in Civil Engineering*, vol. 2017, Article ID 6198296, 11 pages, 2017.

[8] H. Zhang, N. Sun, P. Wang, M. Liu, and Y. Li, "Optimization of cable force adjustment in cable-stayed bridge considering the number of stay cable strand adjustment," *Advances in Civil Engineering*, vol. 2020, Article ID 4527309, 20 pages, 2020.

[9] Z. Lu, C. Wei, M. Liu, and X. Deng, "Risk assessment method for cable system construction of long-span suspension bridge based on cloud model," *Advances in Civil Engineering*, vol. 2020, Article ID 4527309, 9 pages, 2020.

[10] D. Wang, Y. Li, and Y. Liu, "Analysis of refinement control of anchor cable tension for long-span suspension bridge," *China Journal of Highway and Transport*, vol. 27, no. 1, pp. 51–56, 2014.

[11] R. Shen, S. Xue, J. Ma, and B. Liu, "Experimental study of composite saddle of a single-tower single-span earth-anchored suspension bridge," *Bridge Construction*, vol. 49, no. 5, pp. 15–20, 2019.

[12] X. Luo, R. Xiao, and H. Xiang, "Analysis study of anchor span strand for suspension bridges," *Journal of Highway and Transportation Resecircular arch and Development*, vol. 21, no. 12, pp. 45–49, 2004.

[13] D. Qi, R. Shen, and M. Tang, "Study and application of anchorage-anchor span element for suspension bridge," *Journal of Highway and Transportation Resecircular arch and Development*, vol. 28, no. 2, pp. 82–92, 2011.

[14] S. Chen, C. Li, and H. Ke, "Strand tension calculation and monitoring of anchor span during construction of suspension bridges," *Journal of Transport Science and Engineering*, vol. 28, no. 4, pp. 32–36, 2012.

[15] H. Tan and R. Xiao, "Strand tension in anchor-span suspension bridge at different temperatures," *Journal of South China University of Technology: Natural Science Edition*, vol. 38, no. 9, pp. 118–122, 2010.

[16] M. M. Hassan, A. O. Nassef, and A. A. El Damatty, "Determination of optimum post-tensioning cable forces of cable-stayed bridges," *Engineering Structures*, vol. 44, pp. 248–259, 2012.

[17] H. K. Byeong and P. Taehyo, "Estimation of cable tension force using the frequency-based system identification method," *Journal of Sound and Vibration*, vol. 304, no. 3, pp. 660–676, 2007.

[18] X. Zhang, R. Shen, M. Tang, and H. Ye, "Accurate calculation and adjustment methods for cable forces of anchor-span strands of suspension bridges," *Journal of Southwest Jiaotong University*, vol. 47, no. 4, pp. 551–557, 2012.

[19] H. Tan, Z. Hou, Z. Qiu, J. Ji, and D. Chen, "The USGT method for suspender tensioning of self-anchored suspension bridges," *Advances in Civil Engineering*, vol. 2021, Article ID 6619924, 10 pages, 2021.

[20] Y. Sun, L. Zhang, and Z. Li, "Analysis of parameters influencing suspender target cable forces of self-anchored suspension bridge," *Bridge Construction*, vol. 45, no. 4, pp. 69–74, 2015.

[21] B. Atmaca, T. Dede, and M. Grzywinski, "Optimization of cables size and prestressing force for a single pylon cable-stayed bridge with Jaya algorithm," *Steel and Composite Structures*, vol. 34, no. 6, pp. 853–862, 2020.

[22] Z. Wang, N. Zhang, X. Du, S. Wang, and Q. Sun, "Multi-objective optimization of cable forces and counterweights for universal cable-stayed bridges," *Journal of Advanced Transportation*, vol. 2021, Article ID 6615746, 13 pages, 2021.

[23] B. Asgari, S. A. Osman, and A. Adnan, "A new multiconstraint method for determining the optimal cable stresses in cable-stayed bridges," *The Scientific World Journal*, vol. 2014, Article ID 503016, 9 pages, 2014.

[24] A. Andreu, L. Gil, and P. Roca, "A new deformable catenary element for the analysis of cable net structures," *Computers & Structures*, vol. 84, no. 29, pp. 1882–1890, 2006.

[25] W. Zhang, G. Tian, and Z. Liu, "Analytical study of uniform thermal effects on cable configuration of a suspension bridge during construction," *Journal of Bridge Engineering*, vol. 24, no. 11, 2016.

[26] M.-Y. Kim, M.-R. Jung, and M. M. Attard, "Unstrained length-based methods determining an optimized initial shape of 3-dimensional self-anchored suspension bridges," *Computers & Structures*, vol. 217, no. 5, pp. 18–35, 2019.

[27] Q. Gao, N. Hong, B. Guo, Y. Liu, and Q. Ma, "Calculation method for length of main cable at saddle in long-span suspension bridge," *Journal of Harbin Institute of Technology*, vol. 52, no. 9, pp. 57–62, 2020.

[28] J. He, C. Li, H. Ke et al., "A simplified calculation method of length adjustment of datum strand for the main cable with small sag," *Advances in Civil Engineering*, vol. 2019, Article ID 6075893, 8 pages, 2019.

[29] W.-m. Zhang, L.-y. Shi, L. Li, and Z. Liu, "Methods to correct unstrained hanger lengths and cable clamps' installation positions in suspension bridges," *Engineering Structures*, vol. 171, no. 5, pp. 202–213, 2018.

[30] X. Luo, R. Xiao, and H. Xiang, "Cable element based on exact analytical expressions," *Journal of Tongji University: Natural Science*, vol. 33, no. 4, pp. 445–450, 2005.

[31] P. Lu, J. Chen, J. Zhong, and P. Lu, "Optimization analysis model of self-anchored suspension bridge," *Mathematical Problems in Engineering*, vol. 2014, Article ID 403962, 8 pages, 2014.

[32] S. G. Gwon and D. H. Choi, "Continuum model for static and dynamic analysis of suspension bridges with a floating girder," *Journal of Bridge Engineering*, vol. 23, no. 10, 2018.

[33] C. Zhang, Q. Guo, and X. Zhang, "Determination of the strain-free configuration of multi-span cable," *Shock and Vibration*, vol. 2015, Article ID 890474, 6 pages, 2015.

[34] H. Wang, S. Qin, Z. Zhang, C. Huang, and W. Xu, "The basic differential equations of self-anchored cable-stayed suspension bridge," *Mathematical Problems in Engineering*, vol. 2010, Article ID 805195, 12 pages, 2010.

[35] X. Li, K. Peng, J. Peng, and D. Hou, "Experimental investigation of cyclic wetting-drying effect on mechanical behavior of a medium-grained sandstone," *Engineering Geology*, vol. 293, Article ID 106335, 2021.

[36] X. Li, K. Peng, J. Peng, and H. Xu, "Effect of cyclic wetting-drying treatment on strength and failure behavior of two quartz-rich sandstones under direct shear," *Rock Mechanics and Rock Engineering*, vol. 54, no. 11, pp. 5953–5960, 2021.

[37] Y. Wang, B. Zhang, B. Li, and C. Li, "A strain-based fatigue damage model for naturally fractured marble subjected to freeze-thaw and uniaxial cyclic loads," *International Journal of Damage Mechanics*, vol. 33, no. 9, pp. 1305–1323, 2021.

[38] M. Gao, J. Xie, Y. Gao et al., "Mechanical behavior of coal under different mining rates: a case study from laboratory experiments to field testing," *International Journal of Mining Science and Technology*, vol. 31, no. 5, pp. 825–841, 2021.

[39] M. Gao, J. Xie, J. Guo, Y. Lu, Z. He, and C. Li, "Fractal evolution and connectivity characteristics of mining-induced crack networks in coal masses at different depths," *Geomechanics and Geophysics for Geo-Energy and Geo-Resources*, vol. 7, no. 1, 2021.

[40] Z. Tao, C. Zhu, M. He, and M. Karakus, "A physical modeling-based study on the control mechanisms of negative Poisson's ratio anchor cable on the stratified toppling deformation of anti-inclined slopes," *International Journal of Rock Mechanics and Mining Sciences*, vol. 138, Article ID 10335, 2021.

Hindawi
Mathematical Problems in Engineering
Volume 2021, Article ID 4872987, 11 pages
https://doi.org/10.1155/2021/4872987

Research Article

A Dynamic Method to Predict the Earthquake-Triggered Sliding Displacement of Slopes

Wenkai Feng,[1] Zhichun Lu,[2,3] Xiaoyu Yi,[1] and Shan Dong[1,2]

[1]*State Key Laboratory of Geohazard Prevention and Geoenvironment Protection (Chengdu University of Technology), Chengdu 610059, China*
[2]*Three Gorges Research Center for Geohazards, China University of Geosciences, Wuhan 430074, China*
[3]*Faculty of Engineering, China University of Geosciences, Wuhan 430074, China*

Correspondence should be addressed to Shan Dong; dongshan1994@hotmail.com

Received 11 October 2021; Revised 29 October 2021; Accepted 30 October 2021; Published 15 November 2021

Academic Editor: Gan Feng

The earthquake-induced permanent displacement is an important index of the potential damage to a slope during an earthquake. The Newmark method assumes that a slope is a rigid-plastic body, and the seismic responses of sliding masses or seismic forces along the slide plane are ignored. The decoupled method considers no relative displacement across the sliding plane, so it overpredicts the seismic response of the sliding mass. Both dynamic and sliding analyses are performed in the coupled method, but when T_s/T_m is large, the results are unconservative. In this paper, a method is proposed to predict the earthquake-triggered sliding displacement of slopes. The proposed method is based on the Newmark rigid method, coupled method, and decoupled method considering both the forces at the sliding interface and the system dynamics under critical conditions. For the flexible system, the displacements are calculated with different stiffness values, and the results show that as the stiffness increases and tends to infinity, the critical acceleration and displacements of the proposed method are close to those of the Newmark method. The proposed method is also compared with the Newmark method with the period ratio T_s/T_m. At small values of T_s/T_m, the flexible system analysis results of the displacement are more conservative than those of the rigid block model; at larger values of T_s/T_m, the rigid block model is more conservative than the flexible system.

1. Introduction

An earthquake can trigger a number of geotechnical failures, including liquefaction, the collapse of loose deposits, landslides, rock falls, rock avalanches, and landslide dams. Among these events, landslides are highly damaging [1]. Earthquakes with magnitudes greater than 4.0 can trigger landslides on very susceptible slopes, and earthquakes with magnitudes greater than 6.0 can generate widespread landslides [2]. Permanent sliding displacement represents a common damage parameter used to evaluate the seismic stability of slopes. This displacement represents the cumulative downslope movement of a sliding mass due to earthquake shaking. The magnitude of sliding displacement has been correlated with the seismic performance of slopes [3]. Thus, the earthquake-induced sliding displacement of a system must be assessed in evaluations of earthquake-induced landslides [4].

The stability of slopes subjected to earthquakes can be evaluated in several ways. The simplest approach is the pseudostatic analysis method proposed by Terzaghi [5]. This strategy consists of generalizing the classical limit equilibrium method to the dynamic case; the equilibrium of the most important soil volume is assessed by assuming that seismic acceleration is represented by a static force. In pseudostatic analysis, the soil is assumed to be rigid; as a result, this formulation tends to yield conservative results [6, 7]. In fact, many slopes have experienced earthquake accelerations well above the yield thresholds but suffered little or no permanent displacement [8]. Conversely, because pseudostatic analysis is very inaccurate, slopes can be unstable at safety factors greater than 1 [5, 9, 10]. Another

limitation of the pseudostatic approach is the lack of information regarding permanent displacement. Given the above considerations, the Newmark method [11] was proposed as a simplified and reliable method of assessing seismic slope stability and calculating permanent displacement. The Newmark method analyses the dynamics of a rigid block sliding on a flat rough surface under earthquake shaking motion. The Newmark method uses two parameters associated with the yield acceleration and acceleration time history of the rigid foundation. The critical acceleration is defined as that acceleration at which the ground motion creates a destabilizing force sufficient to temporarily reduce the safety factor of the slope to less than 1, and sliding begins when the shear force at the contact surface exceeds the shear strength. Then, the relative velocity between the rigid block and foundation is integrated to calculate the relative sliding displacement.

Given its simplicity and reliability, the Newmark method has been widely used; however, the major limitation of this method is that the sliding mass is considered a rigid block. Makdisi and Seed [12] modified the Newmark procedure and performed a dynamic analysis of a rigid block. However, the modified Newmark procedure does not accurately model the force at the sliding interface because the sliding motion of the sliding mass is ignored. The decoupled method is generally overconservative or slightly unconservative. The nonlinear coupled stick-slip deformable sliding model was proposed by Rathje and Bray [13] for horizontal directional sliding. Compared to the rigid sliding block model, the nonlinear coupled stick-slip deformable sliding block model offers a more realistic representation of the dynamic response of an earth/waste structure by accounting for the deformability of the sliding mass and considering the simultaneous occurrence of a nonlinear dynamic response and periodic sliding episodes. Many researchers have also proposed displacement prediction methods. For example, Ambrasey and Menu [14] used 50 strong ground motion records from 11 worldwide earthquakes and proposed a sliding displacement predictive model based on Newmark rigid block analysis and found that the k_y/PGA ratio has a large influence on the sliding displacement of earthquake-triggered landslides. Qi [15] proposed an algorithm for the seismic permanent displacement of a rock slope considering the degradation law of the structural plane undulant angle. Zafarani and Soghrat [16] proposed an empirical prediction equation based on the peak ground acceleration (PGA) obtained in different parts of Iran. Jafarian et al. [17] proposed and developed an empirical model based on regression analyses. Dong et al. [18] proposed the calculation method of landslide displacement considering the deterioration effect of structural plane.

In this paper, a method is proposed to predict the earthquake-triggered sliding displacement of slopes. The proposed method for determining the earthquake-triggered sliding displacement of a slope is based on the coupled and Newmark methods. The procedures and dynamics of the stick and slip phases are studied to estimate the earthquake-triggered sliding displacement of landslides. The slope sliding mass is considered a lumped mass system, and the ground motion is considered horizontal. Dynamic analyses are performed based on the mechanical equilibrium equation under critical conditions to define the slope from stick to slip. The proposed method is compared with the Newmark rigid block method.

2. Previous Work

2.1. Newmark Method. To consider seismic conditions in slope stability analyses, Newmark [11] proposed the Newmark sliding rigid block method. The Newmark method [11] is a simplified formulation for seismic soil slope stability analysis that considers rigid block sliding on an inclined flat frictional surface.

2.1.1. Assumptions of the Newmark Method. The common assumptions and limitations of Newmark's method are as follows [11, 19]:

(1) The landslide is a rigid plastic body, and the mass does not deform internally, does not experience permanent displacement at accelerations below the critical (yield) level, and deforms plastically along a discrete basal shear surface when the critical acceleration is exceeded

(2) The static and dynamic shearing resistance of the soil are equal and constant

(3) No pore water pressure variations are considered

(4) The critical acceleration is not strain dependent and thus remains constant throughout the analysis

(5) The upslope resistance to sliding is assumed to be infinitely large, such that upslope displacement is prohibited

2.1.2. Critical Acceleration. This rigid block is subjected to the same seismic accelerations that occur during actual slope instability events. Therefore, when the static and dynamic forces exceed the shear strength of the sliding surface, F_s is reduced to 1.0, and the block is displaced. The critical acceleration can be defined as the minimum seismic acceleration required to overcome the shear resistance and initiate the displacement of the rigid block. Thus, critical acceleration is the most significant parameter and must be estimated first. In the Newmark method, the critical acceleration is exceeded when the inertial force acts in the downslope direction; therefore, resolving forces perpendicular to the inclined plane gives

$$\mathrm{FS}_d = \frac{\text{available resisting force}}{\text{pseudostatic driving force}} = \frac{\left[\cos\beta - k_y \sin\beta\right]\tan\varnothing}{\sin\beta + k_y \cos\beta}. \tag{1}$$

The yield acceleration is the minimum pseudostatic acceleration required to produce block instability.

$$k_y = \tan(\varnothing - \beta),$$
$$a_c = k_y g, \tag{2}$$

where a_c is the critical acceleration, k_y is the yield coefficient, g is the acceleration due to gravity, Φ is the friction angle between the block and the plane, β is the slope angle, and F_s is the safety factor.

2.1.3. Newmark Displacement. The Newmark displacement is the permanent sliding displacement experienced by the block when shaking with an acceleration that exceeds the critical value given by the above equation. Such a displacement can be obtained by the double time integration of the intervals of the excitation accelerogram which are above a_c (Figure 1). Notably, the segments that are below the bound (i.e., a_c) do not generate any displacement, given that they correspond to uphill acceleration.

2.2. Decoupled Method. Rathje and Bray [21] proposed a decoupled method that was modified from a generalized SDOF system with the mass and stiffness distributed along the height of the system. The mode shape in the decoupled method was introduced by considering the boundary condition for a horizontal deposit with a constant shear-wave velocity profile [9]. The governing equation of motion for the SDOF system is

$$\mathbf{M}\ddot{\mathbf{Y}}_1 + 2\lambda \mathbf{w}_1 \dot{\mathbf{Y}}_1 + w_1^2 \mathbf{Y}_1 = -\frac{\mathbf{L}_1}{\mathbf{M}_1} \cdot \ddot{u}_g(\mathbf{t}), \tag{3}$$

where Y_1 is the modal coordinate, $u_g(t)$ is the input ground motion, λ is the viscous material damping ratio, M_1 is the generalized mass distributed along the height of the system, L_1 is a mode shape term defining ground acceleration in the direction of the height of the system, and w_1 is a natural circular frequency associated with the fundamental period of the system.

Chopra and Zhang proposed the yield-equivalent base acceleration considering the acceleration profile of the system:

$$\mathbf{HEA}(t) = \frac{\mathbf{L}_1}{\mathbf{M}}\ddot{Y}_1 + \ddot{u}_g(t), \tag{4}$$

where M is the total mass of the soil deposit layer.

The equivalent acceleration time history is used as input acceleration in Newmark rigid block analysis to obtain the permanent displacement as follows:

$$\ddot{s} = -k_y g - \mathrm{HEA}(t) = -k_y g - \frac{\mathbf{L}_1}{\mathbf{M}}\ddot{\mathbf{Y}}_1 - \ddot{u}_g(t). \tag{5}$$

2.3. Coupled Analysis

2.3.1. Stick Phase. In coupled analysis [13], the dynamic response of the sliding mass and the permanent displacement are modelled together so that the effect of the plastic sliding displacement on ground motion is considered. The governing equation of the dynamic equilibrium of a multiple degree-of-freedom (MDOF) lumped mass system is given by

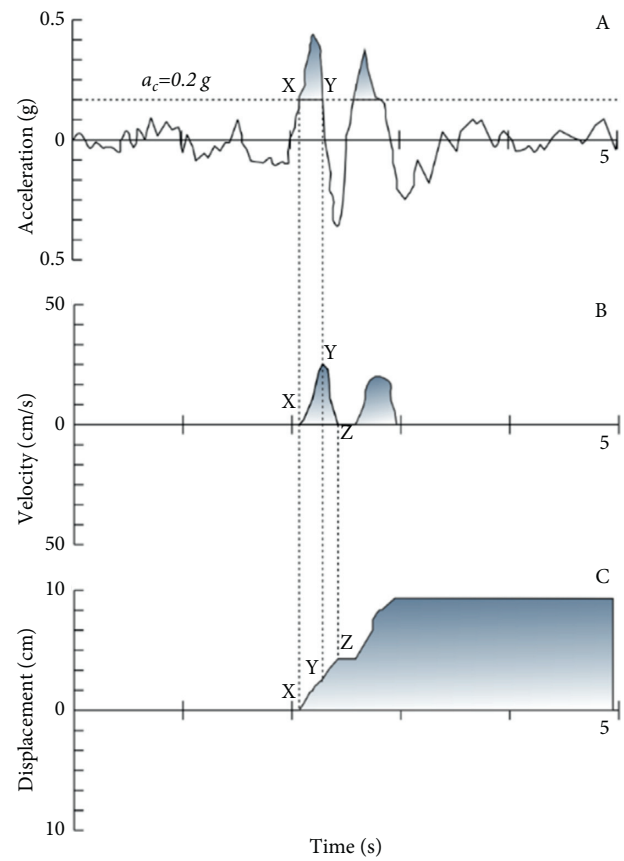

Figure 1: The Newmark integration algorithm (adapted from Kramer [20]). The strong-motion record having a hypothetical a_c of 0.2 g is superimposed. To the left of point X accelerations are less than a_c, and there is no displacement. To the right of point X those parts of the strong-motion record lying above a_c are integrated over time to derive a velocity profile of the block. Integration begins at point X and the velocity increases to point Y, the maximum velocity for this pulse. Past point Y the ground acceleration drops below a_c, but the block continues to move because of its inertia. Friction and ground motion in the opposite direction cause the block to decelerate until it stops at point Z. All pulses of the ground motion exceeding a_c are integrated to yield a cumulative displacement profile of the landslide block.

$$\mathbf{M}\ddot{u} + \mathbf{C}\dot{u} + \mathbf{K}u = -\mathbf{M} \cdot \mathbf{1} \cdot \ddot{u}_g, \tag{6}$$

where M, C, K, $\ddot{u}$, $\dot{u}$, u, and $\ddot{u}_g$ are the mass matrix, damping matrix, stiffness matrix, vector of the nodal relative accelerations, vector of the nodal relative velocities, vector of the nodal relative displacements, and the acceleration time history, respectively.

2.3.2. Slip Phase. When the force at the base of the sliding mass exceeds the frictional strength at the sliding mass/foundation interface for sliding in the positive direction, the following scalar equation can be obtained:

$$-\mathrm{M}_T\ddot{u}_g - 1^{\mathbf{T}}\mathbf{M}\cdot\ddot{\mathbf{u}} = uM_Tg, \tag{7}$$

where $\mathrm{M}_T\ddot{u}_g$ is the force due to the ground acceleration, $1^TM\cdot\ddot{u}$ is the force at the sliding interface from the non-uniform acceleration profile within the sliding mass, and uM_Tg is the frictional resistance at the sliding interface.

After sliding is initiated, the excitation at the base is the acceleration of the ground and the acceleration associated with the sliding displacement. The governing equation is

$$\mathbf{M}\ddot{u} + \mathbf{C}\dot{u} + \mathbf{Ku} = -\mathbf{M}\cdot 1\cdot\left(\ddot{s} + \ddot{u}_g\right), \tag{8}$$

where $\ddot{s}$ is the sliding acceleration at the base of the sliding mass. During sliding, the equilibrium at the shear interface is represented as follows:

$$-M_T\left(\ddot{s} + \ddot{u}_g\right) - 1^TM\cdot\ddot{u} = uM_Tg. \tag{9}$$

Combined with the above equation, the vector of the nodal acceleration during sliding is used to calculate the sliding acceleration at the base of the sliding mass with

$$\ddot{s} = -ug - \frac{1}{M_T}1^TM\cdot\ddot{u} - \ddot{u}_g. \tag{10}$$

3. The Proposed Method

In the proposed method, the direction of the ground motion is assumed to be contrary to the sliding direction. Because sliding in the uphill direction occurs only when the slope angle and friction angle are small (approaching level), this paper mainly considers sliding in the downslope direction.

3.1. Stick Condition. In this paper, a lumped mass system is considered, and the acceleration is considered horizontal (Figures 2 and 3). In the improved method, the processes consist of two phases, namely, stick and slip phases. Under stick conditions, the motion of each lumped mass in the parallel direction is described by the following ordinary differential equations:

$$\begin{aligned}
&m_1\ddot{u}_1 - (\dot{u}_2 - \mathrm{u}_1)c_2 + \dot{u}_1c_1 - (u_2 - \mathrm{u}_1)k_2 + u_1k_1 - m_1g\sin\theta = m_1\ddot{u}_g\cos\theta\\
&\qquad\cdots\\
&m_{n-1}\ddot{u}_{n-1} - (\dot{u}_n - \mathrm{u}_{n-1})c_n + (\dot{u}_{n-1} - \mathrm{u}_{n-2})c_{n-1} - (u_n - \mathrm{u}_{n-1})k_n + (u_{n-1} - \mathrm{u}_{n-2})k_{n-1} - m_{n-1}g\sin\theta = m_{n-1}\ddot{u}_g\cos\theta\\
&m_n\ddot{u}_n + (\dot{u}_n - \mathrm{u}_{n-1})c_n + (u_n - \mathrm{u}_{n-1})k_n - m_ng\sin\theta = m_n\ddot{u}_g\cos\theta.
\end{aligned} \tag{11}$$

Rearranging the equations yields the following relational expression:

$$\begin{aligned}
&m_1\ddot{u}_1 + (c_1 + c_2)\dot{u}_1 - c_2\dot{u}_2 + (k_1 + k_2)u_1 - k_2u_2 = m_1\ddot{u}_g\cos\theta + m_1g\sin\theta\\
&\qquad\cdots\\
&m_{N-1}\ddot{u}_{n-1} - c_{n-1}\dot{u}_{n-2} + (c_{n-1} + c_n)\dot{u}_{n-1} - c_n\dot{u}_n - k_{n-1}u_{n-2} + (k_{n-1} + k_n)u_{n-1} - k_nu_n = m_{n-1}\ddot{u}_g\cos\theta + m_{n-1}g\sin\theta\\
&m_n\ddot{u}_n - c_n\dot{u}_{n-1} + c_n\dot{u}_n - k_nu_n - k_nu_{n-1} = m_n\ddot{u}_g\cos\theta + m_ng\sin\theta.
\end{aligned} \tag{12}$$

These scalar equations can be combined to form a single $N\times N$ matrix equation:

$$\mathbf{M}\ddot{\mathbf{u}} + \mathbf{C}\dot{u} + \mathbf{Ku} = \mathbf{M}\cdot 1\left(\ddot{u}_g\cdot\cos\theta + g\sin\theta\right), \tag{13}$$

where M, C, and K are the mass matrix, damping matrix, and stiffness matrix, respectively. The damping matrix C is generated by a Rayleigh model as $\mathbf{C} = \alpha\mathbf{M} + \beta\mathbf{K}$. Additionally, $\ddot{u}_g$ is the acceleration time history at the slope base; θ is the slope angle; $\ddot{\mathbf{u}}$ is the vector of nodal relative accelerations; $\dot{\mathbf{u}}$ is the vector of nodal relative velocities; and $\mathbf{u}$ is the vector of nodal relative displacements.

3.2. Critical Condition. The critical condition is considered when the available resisting force is equal to the driving force. When the inertial force acts in the downslope direction, the resolving forces perpendicular to the inclined plane can be formulated as follows:

$$F_s = \frac{\text{available resisting force}}{\text{driving force}} = \frac{N\cdot\tan\varnothing}{1^{\mathbf{T}}\cdot\mathbf{M}\cdot\ddot{\mathbf{u}} + 1^{\mathbf{T}}\cdot\mathbf{M}\cdot 1\cdot\ddot{\mathbf{u}}_g\cos\theta + 1^{\mathbf{T}}\cdot\mathbf{M}\cdot 1\cdot g\sin\theta}. \tag{14}$$

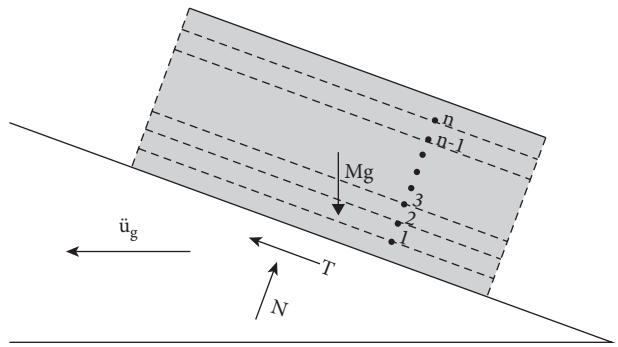

Figure 2: Schematic diagram of the system. The figure displays a block on an inclined plane with a slope characterized by an angle θ. T and N are the parallel (shear) and orthogonal (normal) reaction forces, respectively.

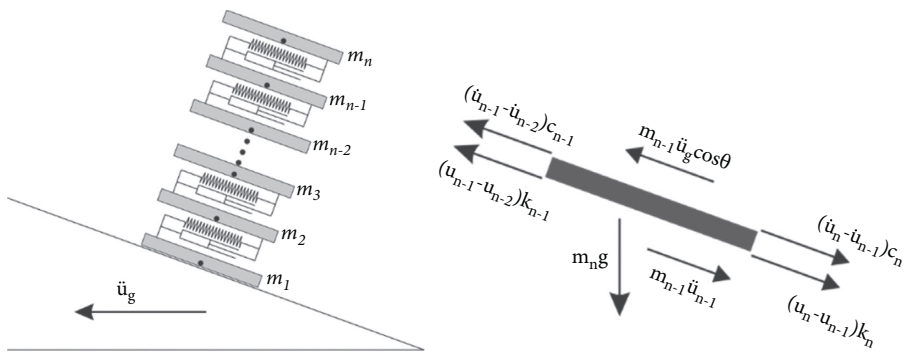

Figure 3: Mechanical analysis of the sliding mass during the sliding phase.

Distribution of forces perpendicular to the slope is

$$1^{\mathbf{T}} \cdot \mathbf{M} \cdot 1 \cdot \ddot{u}_g \sin\theta = \mathbf{g} \cdot 1^{\mathbf{T}} \cdot \mathbf{M} \cdot 1 \cdot \cos\theta - N. \quad (15)$$

The critical acceleration can be obtained when F_s equals 1.0:

$$a_c = g \tan(\varnothing - \theta) - \frac{1^T \cdot M \cdot \ddot{u}}{\mathbf{1}^{\mathbf{T}} \cdot \mathbf{M} \cdot \mathbf{1} \cdot \cos\theta \cdot (1 + \tan\varnothing \cdot \tan\theta)}, \quad (16)$$

where c is the cohesive force, N is the supporting force below the sliding surface, $\varnothing$ is the friction angle, and $\ddot{\mathbf{u}}$ is the vector of nodal relative accelerations in the stick phase.

3.3. Slip Condition. When the slope is excited by seismic forces, the mass begins to slide; this is the second (slip) phase. In this phase, the acceleration of the ground motion and the acceleration associated with the sliding displacement are considered. The matrix equation is as follows:

$$\mathbf{M}\ddot{u} + \mathbf{C}\dot{u} + \mathbf{K}\mathbf{u} = \mathbf{M} \cdot 1 \cdot \left(\ddot{u}_g \cdot \cos\theta - \ddot{s} + g \sin\theta\right), \quad (17)$$

where $\ddot{s}$ is the sliding acceleration at the base of the sliding mass ($\ddot{s}$ should be larger than $\ddot{u}$).

During sliding, the equilibrium at the shear interface is

$$\begin{aligned} &-1^{\mathbf{T}} \cdot \mathbf{M} \cdot 1 \cdot \ddot{u}_g \cos\theta + 1^{\mathbf{T}} \cdot \mathbf{M} \cdot 1 \cdot \ddot{s} + 1^{\mathbf{T}} \cdot \mathbf{M} \cdot \ddot{u} \\ &= -\left(1^T \cdot M \cdot 1 \cdot g \cos\theta - 1^{\mathbf{T}} \cdot \mathbf{M} \cdot 1 \cdot \ddot{u}_g \sin\theta\right) \cdot \tan\varnothing \\ &\quad + 1^{\mathbf{T}} \cdot \mathbf{M} \cdot 1 \cdot g \sin\theta. \end{aligned} \quad (18)$$

The formulations in (17) and (18) can be combined to obtain the following formula:

$$\mathbf{M}^* \ddot{\mathbf{u}} + \mathbf{C}\dot{u} + \mathbf{K}\mathbf{u} = \mathbf{M} \cdot 1 \cdot \left[g\left(\cos\theta - \ddot{u}_g \sin\theta\right) \cdot \tan\varnothing\right]. \quad (19)$$

In this equation, M^* is defined as follows:

$$\mathbf{M}^* = \mathbf{M} - \frac{1}{1^{\mathbf{T}}\mathbf{M}1} \cdot \mathbf{M}1 1^{\mathbf{T}}\mathbf{M}. \quad (20)$$

$\ddot{s}$ is defined as follows:

$$\ddot{s} = -\left(g \cos\theta - \ddot{u}_g \sin\theta\right)\tan\varnothing - \frac{1}{1 \cdot \mathbf{M} \cdot 1^{\mathbf{T}}} \cdot 1^T \cdot M \cdot \ddot{u} + \ddot{u}_g \cos\theta + g \sin\theta. \quad (21)$$

Under slip conditions, M^*, as defined in (20), is only used in the case with 1 or 2 DOFs. When the system has more than 2 DOFs, a new approach must be considered. These $N + 1$ equations can be arranged as follows:

$$\begin{gathered} -\mu N + \left(m_b + 1^{\mathbf{T}}\mathbf{M}1\right) g \sin\theta = -\left(m_b + 1^{\mathbf{T}}\mathbf{M}1\right)\left(\ddot{u}_g \cdot \cos\theta - \ddot{s}\right) + 1^{\mathbf{T}}\mathbf{M}\ddot{u}, \\ \mathrm{M}\ddot{d} + \mathbf{C}\dot{d} + \mathbf{K}\ \mathbf{d} = \mathbf{M}1\left(\ddot{u}_g \cdot \cos\theta - \ddot{s} + g \sin\theta\right). \end{gathered} \tag{22}$$

Some previous researchers have circumvented this problem by assigning a mass directly to the sliding surface [22, 23]. In the computer code (MATLAB) developed for this analysis, only half of the mass of the base element is assigned to the lumped mass for that element, and the other half is assigned to the sliding interface. This approach assures that $1^{\mathbf{T}} \cdot \mathbf{M} \cdot 1$ is not equal to the sum of the lumped mass, and therefore,$\mathbf{M}^*$ cannot be singular.

4. Discussion

4.1. Rigid Bock. Using the classical Newmark method considered under slip conditions, block sliding is obtained by integrating the part of the input acceleration that exceeds the critical level ($\ddot{u}_g - g \tan(\phi - \theta)$). Actually, the situation involves a relevant simplifying condition that is different from the proposed method in this paper. When the model is considered a rigid block, the details of the proposed method are as follows.

4.1.1. Stick Condition. The equation of motion of the block in parallel to the slope is

$$Mg \cdot \sin\theta - \tan\varnothing \cdot N = -M \cdot \ddot{u}_g \cdot \cos\theta. \tag{23}$$

The equation of motion of the block in the orthogonal directions is as follows:

$$Mg \cdot \cos\theta - N = M \cdot \ddot{u}_g \cdot \sin\theta. \tag{24}$$

4.1.2. Critical Condition. For the rigid block model, the critical acceleration is the same as the Newmark method. The yield acceleration is the minimum pseudostatic acceleration required to produce instability of the block. The critical acceleration is as follows:

$$\begin{aligned} k_y &= \tan(\varnothing - \theta), \\ a_c &= k_y g. \end{aligned} \tag{25}$$

4.1.3. Slip Condition. The equation of motion of the block in parallel to the slope is

$$Mg \cdot \sin\theta - \tan\varnothing \cdot N = -M \cdot \left(\ddot{u}_g \cdot \cos\theta - \ddot{s}\right). \tag{26}$$

The equation of motion of the block in the orthogonal directions is as follows:

$$Mg \cdot \cos\theta - N = M \cdot \ddot{u}_g \cdot \sin\theta. \tag{27}$$

$\ddot{s}$ should be

$$\begin{aligned} \ddot{s} &= g \cdot \sin\theta - \tan\varnothing \cdot g \cdot \cos\theta + \tan\varnothing \cdot \ddot{u}_g \cdot \sin\theta + \ddot{u}_g \\ &\quad \cdot \cos\theta. \end{aligned} \tag{28}$$

4.2. Sliding in the Uphill Direction. The sliding in the uphill direction occurs only when the slope angle and friction angle are small (approaching level). The equations are as follows.

4.2.1. Stick Condition. When in the stick condition, the scalar equations can be combined in a single $N \times N$ matrix equation as

$$\mathbf{M}\ddot{d} + \mathbf{C}\dot{d} + \mathbf{K}\ \mathbf{d} = -\mathbf{M}1\left(\ddot{u}_g \cos\theta - g \sin\theta\right). \tag{29}$$

4.2.2. Critical Condition. When the inertial force acts in the uphill direction, the resolving forces perpendicular to the inclined plane are given as follows:

$$F_s = \frac{\text{available resisting force}}{\text{driving force}} = \frac{N \cdot \tan\varnothing}{1^T \cdot M \cdot \ddot{u} + 1^T \cdot M \cdot 1 \cdot \ddot{u}_g \cos\theta + 1^T \cdot M \cdot 1 \cdot g \sin\theta}. \tag{30}$$

Distribution of forces perpendicular to the slope is

$$-1^T \cdot M \cdot 1 \cdot \ddot{u}_g \sin\theta = g \cdot 1^T \cdot M \cdot 1 \cdot \cos\theta - N. \quad (31)$$

The critical acceleration was obtained when F_s is equal to 1.0.

$$a_c = -g \tan(\varnothing - \theta) + \frac{1^T \cdot M \cdot \ddot{u}}{1^T \cdot M \cdot 1 \cdot \cos\theta \cdot (1 + \tan\varnothing \cdot \tan\theta)}. \quad (32)$$

4.2.3. Slip Condition. The matrix equation is as follows:

$$\mathbf{M}\ddot{\mathbf{u}} + \mathbf{C}\dot{u} + \mathbf{K}\mathbf{u} = -\mathbf{M} \cdot 1 \cdot \left(\ddot{u}_g \cdot \cos\theta + \ddot{s} - g \sin\theta\right), \quad (33)$$

where $\ddot{s}$ is the sliding acceleration at the base of the sliding mass ($\ddot{s}$ should be larger than $\ddot{u}$).

During sliding, the equilibrium at the shear interface is

$$\begin{aligned} &1^{\mathbf{T}} \cdot \mathbf{M} \cdot 1 \cdot \ddot{u}_g \cos\theta + 1^{\mathbf{T}} \cdot \mathbf{M} \cdot 1 \cdot \ddot{s} + 1^{\mathbf{T}} \cdot \mathbf{M} \cdot \ddot{u} \\ &= -\left(1^{\mathbf{T}} \cdot \mathbf{M} \cdot 1 \cdot g \cos\theta + 1^{\mathbf{T}} \cdot \mathbf{M} \cdot 1 \cdot \ddot{u}_g \sin\theta\right) \cdot \tan\varnothing \\ &\quad + 1^{\mathbf{T}} \cdot \mathbf{M} \cdot 1 \cdot g \sin\theta. \end{aligned} \quad (34)$$

Combining with the formulations of (33) and (34),

$$\mathbf{M}^*\ddot{\mathbf{u}} + \mathbf{C}\dot{u} + \mathbf{K}\mathbf{u} = \mathbf{M} \cdot 1 \cdot \left[\left(g \cos\theta + \ddot{u}_g \sin\theta\right) \cdot \tan\varnothing\right], \quad (35)$$

where M^* is defined as follows:

$$\mathbf{M}^* = \mathbf{M} - \frac{1}{1^{\mathbf{T}}\mathbf{M}1} \cdot \mathbf{M}1 1^{\mathbf{T}}\mathbf{M}. \quad (36)$$

$\ddot{s}$ is defined as

$$\ddot{s} = -\left(g \cos\theta + \ddot{u}_g \sin\theta\right)\tan\varnothing - \frac{1}{1 \cdot \mathbf{M} \cdot 1^{\mathbf{T}}} \cdot 1^{\mathbf{T}} \cdot \mathbf{M} \cdot \ddot{u} - \ddot{u}_g \cos\theta + g \sin\theta. \quad (37)$$

5. Example and Comparison

5.1. Example. To verify the validity and feasibility of this method, a simple case is chosen with an approximate sliding mass thickness of 8 m. When the slope in the stick phase is considered, it has 16 degrees of freedom. The parameters include a slope angle of 15°, a friction angle of 25°, and a unit weight of 20 kN/m^3. The Cholame-Shandon Array #5 record from the 1966 Parkfield earthquake ($M_w = 6.69$) was used in this simple case. In this example, the rigid block is calculated by the proposed method and the Newmark method. Figures 4 and 5 show that the sliding displacement of the proposed method is larger than that of the classical Newmark method. The Newmark displacement is 0.016 m, while the rigid block model in the proposed model is 0.177 m.

In addition, the flexible model is also calculated by computer code (MATLAB). In the flexible model, the critical acceleration obtained from the proposed method is not constant because the dynamics under critical conditions are considered. This approach should be more accurate than using the yield acceleration of the Newmark method. The procedure and the results of the proposed flexible method are shown in Figure 6. The displacements of the method proposed in this paper are 0.025 m, and the results are larger than the rigid block model.

5.2. Comparison

5.2.1. Comparison of the Proposed Flexible System Analysis with the Newmark Method. The coupled and decoupled methods are mainly aimed at the horizontal earth structure. The critical acceleration is the same as the Newmark critical acceleration. In this paper, the proposed method is compared with the Newmark method. The Newmark method assumes that the slope is a rigid-plastic body. Furthermore, the mass does not deform internally, does not experience a permanent displacement at accelerations below the critical or yield level, and deforms plastically along a discrete basal shear surface when the critical acceleration is exceeded. The results of the proposed method are calculated with different stiffness values, and the results of the proposed method are compared with the Newmark method; the results are shown in Figures 7 and 8.

In Figure 7, the critical accelerations are compared; in the Newmark rigid block method, the value of the critical acceleration is constant. Because the stiffness increases, the fluctuations in the vector of nodal relative accelerations decrease. As the stiffness increases, the critical acceleration obtained from the proposed method is close to the Newmark critical acceleration.

Figure 8 shows the displacement results. For small stiffness values, the displacements obtained with the proposed method and Newmark method display a large difference. As the stiffness increases, this difference in displacements decreases, and, at very large stiffnesses, the displacement values obtained with the proposed method are very close to those of the Newmark method.

5.3. Comparison of the Results with Different Period Ratios. The frequency content of these records was characterized by the mean period (T_m), defined as

$$\mathbf{T_m} = \frac{\sum_i \mathbf{C_i^2}\left(\mathbf{i}/\mathbf{f_i}\right)}{\sum_i \mathbf{C_i^2}}, \quad (38)$$

where C_i represents the Fourier amplitudes of the entire accelerogram and f_i represents the discrete Fourier transform frequencies between 0.25 and 20 Hz [24]. The

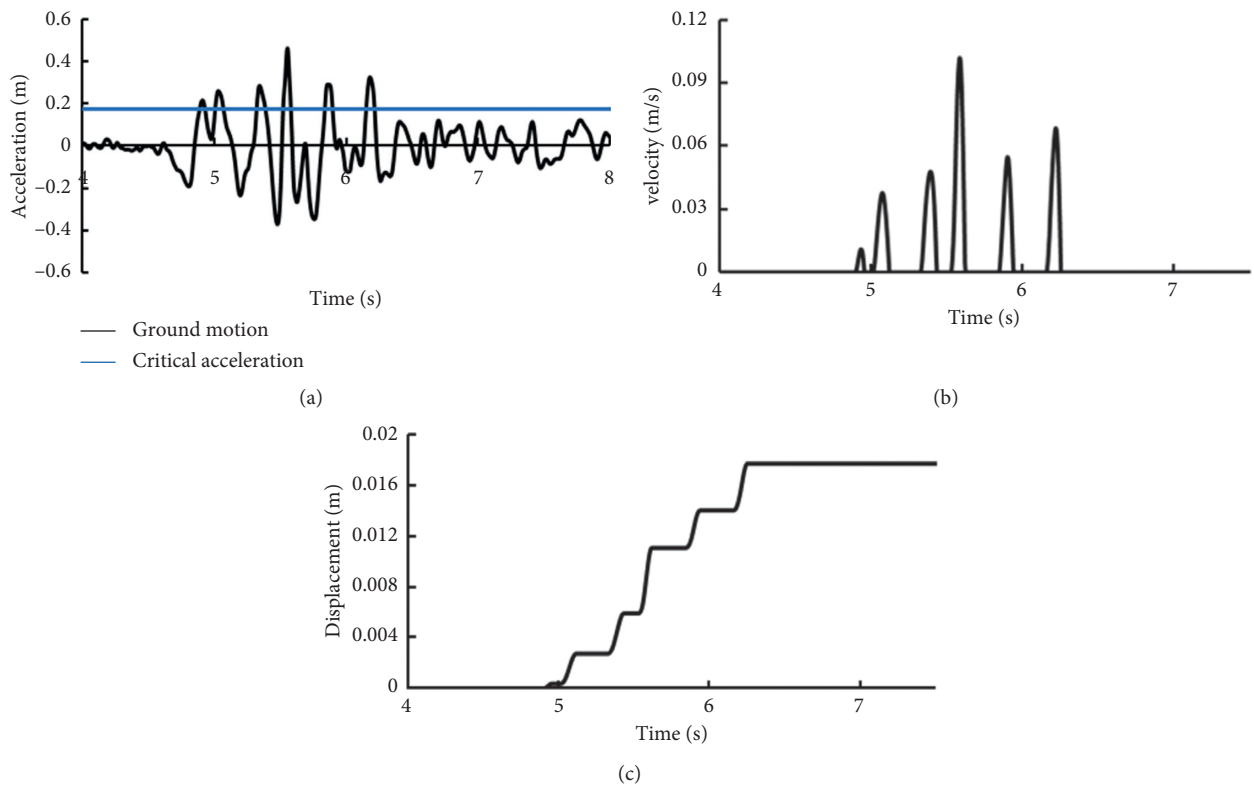

Figure 4: The results of the rigid block calculated by proposed method. (a) The ground motion; (b) the velocity of the sliding body; (c) the cumulative displacement.

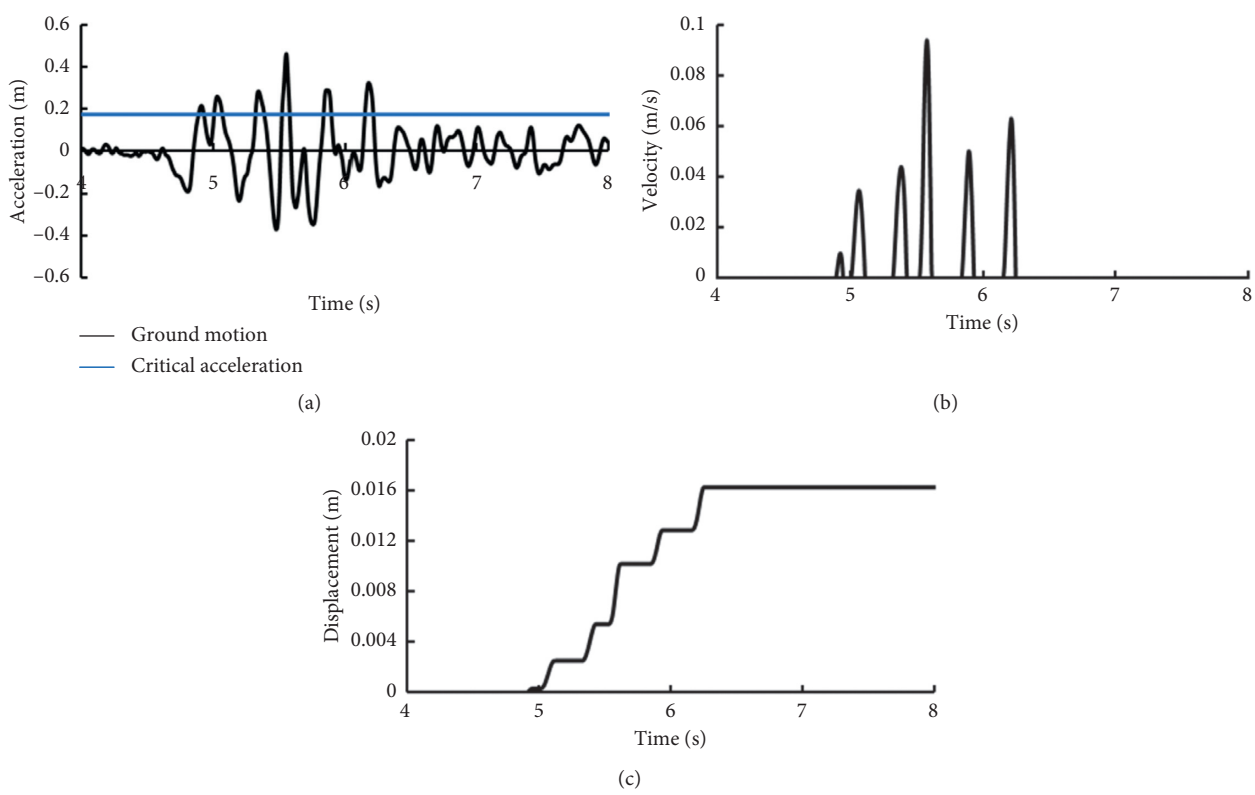

Figure 5: The results of the rigid block calculated by Newmark method. (a) The ground motion; (b) the velocity of the sliding body; (c) the cumulative displacement.

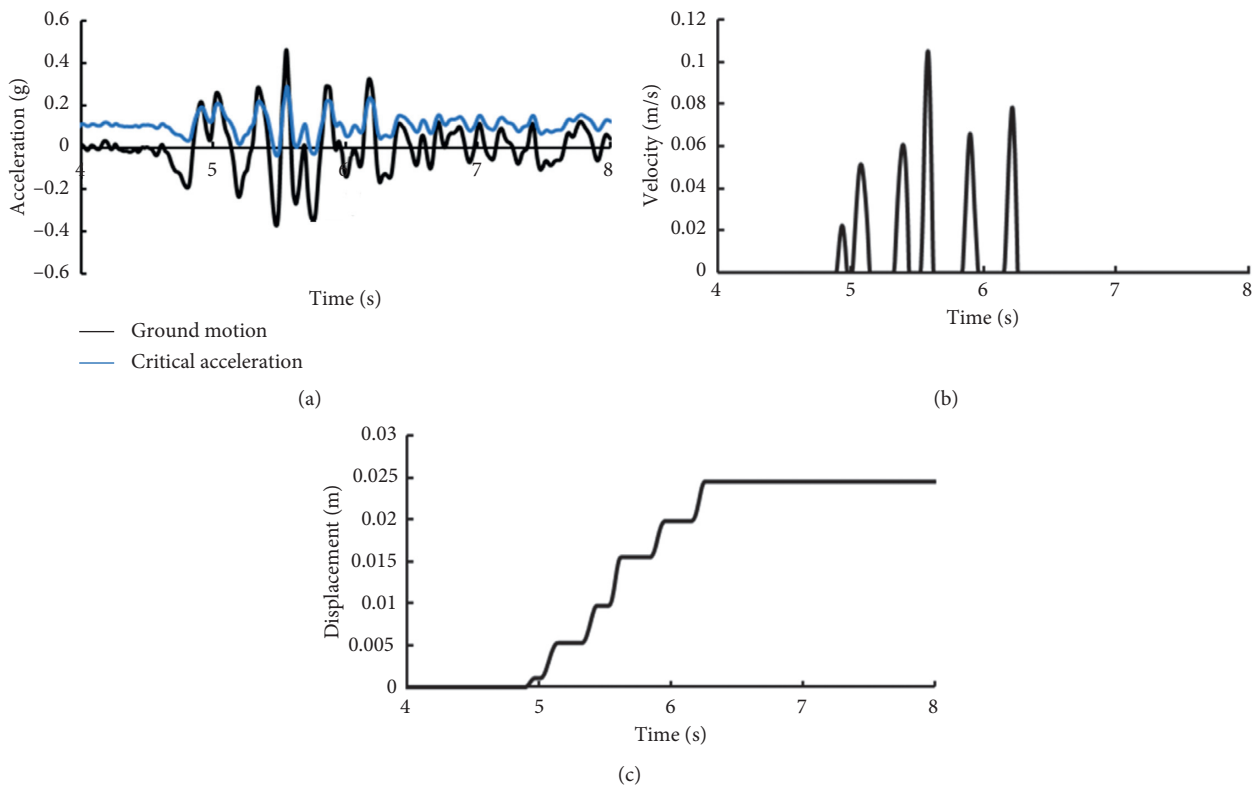

Figure 6: The results of the proposed method. (a) The ground motion; (b) the velocity of the sliding body; (c) the cumulative displacement.

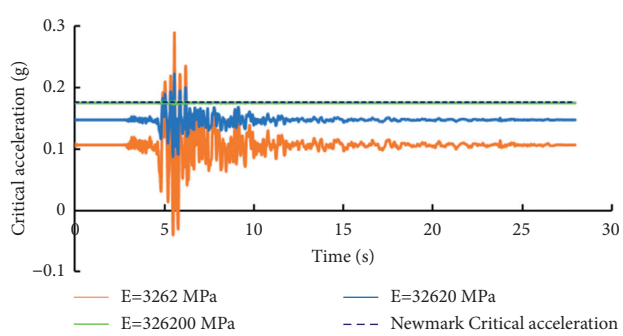

Figure 7: Comparisons of the critical acceleration.

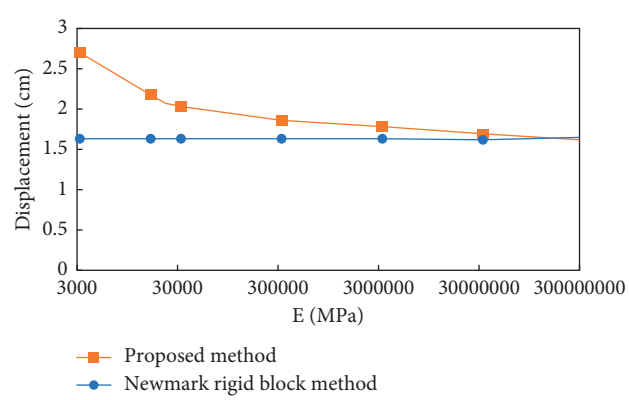

Figure 8: Comparisons of the sliding displacement variation with increasing stiffness.

fundamental period of the earth system is estimated as $T_s = 4H/V_s$. The period ratios of T_s/T_m will be used to present the results in this paper. The recorded ground motion of the Pacoima Dam Downstream record from the 1994 Northridge earthquake is used as the input motion (Figure 9), which is used in the Newmark rigid block method, the proposed rigid block model, and the flexible model. T_m of the record is equal to 0.47 s, and T_s is varied by changing the height of the systems. The shear-wave velocity of the soil is 2016 m/s, and the damping is considered as 15%. The parameters include a unit weight of 20 kN/m^3, a slope angle of 15°, and a friction angle of 17.4°.

Figure 10 presents the variation in the proposed and Newmark displacement with period ratio, T_s/T_m. The results show that, for the rigid block, the proposed method has a slightly larger one than the Newmark method

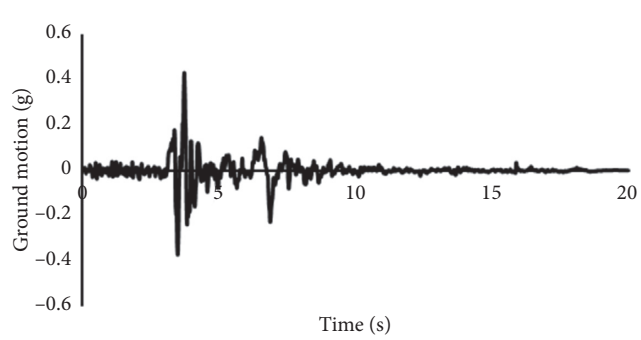

Figure 9: The ground motion of the Pacoima Dam Downstream record from the 1994 Northridge earthquake.

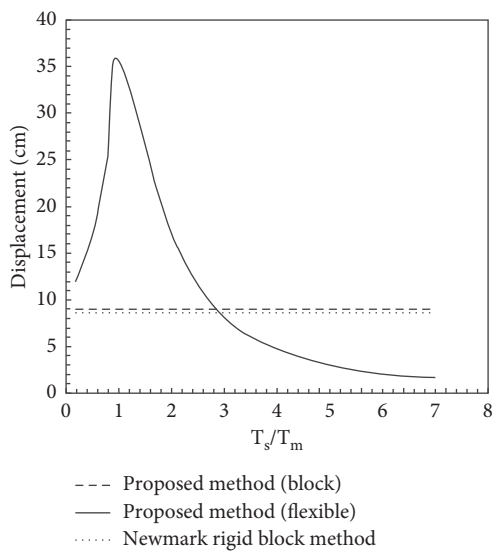

Figure 10: Variation in the sliding displacement with T_s/T_m for the Newmark method and the proposed method using the Pacoima Dam Downstream record.

because the proposed method considered the relative displacement. At small values of T_s/T_m, the flexible system analysis results of the displacement are larger than the results of the rigid block model. At larger values of T_s/T_m, the rigid block model is more conservative than the flexible system. In addition, the flexible system analysis never allows the full response to develop because as the response increases, sliding is initiated and is somewhat isolated from the base of the system.

6. Conclusion

The proposed method of the rigid block model has the same critical acceleration as the Newmark method. However, because the proposed method considers the relative displacement in the rigid block model, the proposed method is more conservative than the Newmark method. For the flexible system, the stiffness is increased in the proposed analysis, and when the stiffness tends to infinity, the results of the proposed method are close to those of the Newmark method. The proposed method is also compared with the Newmark method with the period ratio T_s/T_m. At small values of T_s/T_m, the flexible system analysis results of the displacement are larger than those of the rigid block model. At larger values of T_s/T_m, the rigid block model is more conservative than the flexible system.

Data Availability

The data used to support the findings of this study are available from the corresponding author upon request.

Conflicts of Interest

The authors declare that they have no conflicts of interest.

Acknowledgments

This work was supported in part by the National Natural Science Foundation of China (Grant nos. 41977252 and 41572291), the Sichuan Provincial Youth Science and Technology Innovation Team Special Projects of China (Grant no. 2017TD0018), the Team Project of Independent Research of SKLGP (Grant no. SKLGP2020Z001), and the State Key Laboratory of Geohazard Prevention and Geoenvironment Protection of the Chengdu University of Technology Open Fund (Grant nos. SKLGP2019K010 and SKLGP2020K015).

References

[1] D. K. Keefer, "Landslides caused by earthquakes," *The Geological Society of America Bulletin*, vol. 95, p. 406, 1984.

[2] R. W. Jibson, E. L. Harp, W. Schulz, and D. K. Keefer, "Large rock avalanches triggered by the m 7.9 denali fault, Alaska, earthquake of 3 november 2002," *Engineering Geology*, vol. 83, pp. 144–160, 2006.

[3] R. W. Jibson, E. L. Harp, and J. A. Michael, "A method for producing digital probabilistic seismic landslide hazard maps," *Engineering Geology*, vol. 58, no. 3-4, pp. 271–289, 2000.

[4] E. M. Rathje and G. Antonakos, "A unified model for predicting earthquake-induced sliding displacements of rigid and flexible slopes," *Engineering Geology*, vol. 122, pp. 51–60, 2011.

[5] K. Terzaghi, *Mechanisms of Landslides, Engineering Geology (Berdey) Volume*, Geological Society of America, Boulder, CO, USA, 1950.

[6] R. W. Day, *Geotechnical Earthquake Engineering*, McGraw-Hill, New York, NY, USA, 1996.

[7] R. Ohno, S. Niwa, H. Iwata, and S. Ozawa, *An Examination of the Stability of an Earthquake-Induced Landslide and Landslide Dam*, Springer, Berlin, Germany, 2013.

[8] R. C. Wilson and D. K. Keefer, "Dynamic analysis of a slope failure from the 6 august 1979 coyote lake, California, earthquake," *Bulletin of the Seismological Society of America*, vol. 73, pp. 863–877, 1983.

[9] H. B. Seed, K. L. Lee, and I. M. Idriss, "Analysis of sheffield dam failure," *Journal of the Soil Mechanics and Foundations Division*, vol. 95, 1969.

[10] H. B. Seed, K. L. Lee, I. M. Idriss, and F. I. Makdisi, "The slides in the san fernando dams during the earthquake of february 9, 1971," *Journal of Geotechnical and Geoenvironmental Engineering*, vol. 101, 1975.

[11] N. M. Newmark, "Effects of earthquakes on dams and embankments," *Geotechnique*, vol. 15, pp. 139–160, 1965.

[12] F. I. Makdisi and H. B. Seed, "Simplified procedure for estimating dam and embankment earthquake-induced deformations," *Journal of Geotechnical and Geoenvironmental Engineering*, vol. 104, 1978.

[13] E. M. Rathje and J. D. Bray, "Nonlinear coupled seismic sliding analysis of earth structures," *Journal of Geotechnical and Geoenvironmental Engineering*, vol. 126, pp. 1002–1014, 2000.

[14] N. N. Ambraseys and J. M. Menu, "Earthquake-induced ground displacements," *Earthquake Engineering and Structural Dynamics*, vol. 16, no. 7, pp. 985–1006, 1988.

[15] S. W. Qi, "Evaluation of the permanent displacement of rock mass slope considering deterioration of slide surface during

earthquake," *Chinese Journal of Geotechnical Engineering*, vol. 29, no. 3, pp. 452–457, 2007.

[16] H. Zafarani and M. Soghrat, "Simulation of ground motion in the zagros region of Iran using the specific barrier model and the stochastic method," *Bulletin of the Seismological Society of America*, vol. 102, pp. 2031–2045, 2012.

[17] Y. Jafarian, R. Vakili, A. S. Abdollahi, and M. H. Baziar, "Simplified soil liquefaction assessment based on cumulative kinetic energy density: attenuation law and probabilistic analysis," *International Journal of Geomechanics*, vol. 14, pp. 267–281, 2013.

[18] S. Dong, W. Feng, Y. Yin, R. Hu, H. Dai, and G. Zhang, "Calculating the permanent displacement of a rock slope based on the shear characteristics of a structural plane under cyclic loading," *Rock Mechanics and Rock Engineering*, vol. 53, pp. 4583–4598, 2020.

[19] R. W. Jibson, "Predicting earthquake-induced landslide displacements using newmark's sliding block analysis," *Transportation Research Record*, vol. 1411, pp. 9–17, 1993.

[20] L. Kramer, *Geotechnical Earthquake Engineering*, Prentice-Hall, Hoboken, NJ, USA, 1996.

[21] E. M. Rathje and J. D. Bray, "An examination of simplified earthquake-induced displacement procedures for earth structures," *Canadian Geotechnical Journal*, vol. 36, pp. 72–87, 1999.

[22] N. Mostaghel and J. Tanbakuchi, "Response of sliding structures to earthquake support motion," *Earthquake Engineering & Structural Dynamics*, vol. 11, pp. 729–748, 1983.

[23] J. D. Bray and T. Travasarou, "Simplified procedure for estimating earthquake-induced deviatoric slope displacements," *Journal of Geotechnical and Geoenvironmental Engineering*, vol. 133, no. 4, pp. 381–392, 2007.

[24] J. D. Bray and E. M. Rathje, "Earthquake-induced displacements of solid-waste landfills," *Journal of Geotechnical and Geoenvironmental Engineering*, vol. 124, no. 3, pp. 242–253, 1998.

Hindawi
Mathematical Problems in Engineering
Volume 2021, Article ID 3790345, 10 pages
https://doi.org/10.1155/2021/3790345

Research Article

Experimental and Numerical Analysis of Soil Cracking Characteristics under Evaporation

Di Feng,[1,2] **Jiakun Gong**,[3] **Xiaodong Ni**,[1,2] **and Jie Ren**[3]

[1]*Key Laboratory of Ministry of Education for Geomechanics and Embankment Engineering, Hohai University, Nanjing 210098, China*
[2]*College of Civil and Transportation Engineering, Hohai University, Nanjing 210098, China*
[3]*College of Mechanics and Materials, Hohai University, Nanjing 210098, China*

Correspondence should be addressed to Di Feng; fengdi@hhu.edu.cn

Received 18 October 2021; Accepted 1 November 2021; Published 13 November 2021

Academic Editor: Gan Feng

There are numerous cracks on soil surface in nature. These cracks are mainly formed by the continuous water loss and shrinkage of soil under evaporation. Cracks have an important effect on the properties of soil. The analysis of soil moisture movement and cracking characteristics under evaporation is of great significance to the engineering construction in the cracked soil area. In this work, an experimental study was conducted to investigate the development of soil cracks. Crack geometrical parameters were acquired at various developmental stages. According to this, the crack evolution characteristic was described qualitatively. The law of soil water movement was analyzed through the numerical simulation of evaporation effect on cracked soil. The relationship between soil moisture content and crack width was revealed, and the dynamic prediction of crack development under evaporation was realized. The results show that the development and evaporation process of soil cracks can be divided into three distinct stages, and the longer the stable evaporation time, the greater the development of cracks.

1. Introduction

Cracks prevail in natural soil grounds in the background of global warming and frequent drought flood disaster. The cracks are mainly formed by the continuous water loss and shrinkage of soil under evaporation. The existence of cracks would cause important effect on soil properties. The cracks would not only reduce the soil strength [1], but also provide preferential pathways for fluid flow and increase water infiltration or contaminant solute transport into soils [2, 3]. Thus, the analysis of soil moisture movement and cracking characteristics under evaporation is of great significance to the engineering construction in the cracked soil area.

As the most important reason for the formation of soil cracks, the climate acts on soil as the engine, and the atmosphere provides state change of soil with solar radiation and rainfall infiltration ones. Evaporation links the soil and the atmosphere. Under the influence of climate, soil evaporates and shrinks continuously, which forms cracks. Many scholars studied the development rules of soil cracks in simulated climate through lab experiment. In order to investigate the desiccation cracks of clay liner in refuse landfill, Miller et al. [4] designed an experimental facility which can control climate factors such as temperature, rainfall, and wind speed and studied the development rules of cracks. Tang et al. [5–7] carried out a series of drying tests to study the dry shrinkage cracking property of swelled ground under different temperature. In the process of drying, the change of moisture content and the evolution of surface cracks were monitored in real time. The results showed that the critical moisture content during cracking was affected by temperature significantly. Liu et al. [8] adopted large-size compacted expansive soil samples to conduct crack development tests under various environmental humidity and temperature and discussed the influence of environmental humidity and temperature on the crack development law of expansive soil. The soil is prone to shrinkage and cracking under evaporation. Knowledge of the coupled behavior of cracking

and moisture-heat evolution is helpful for better understanding the mechanical performance of soil under evaporation. Wu et al. [9] conducted an evaporation experiment for clayey soil specimen. The fully coupled behavior of shrinkage, cracking, and moisture-heat evolution of the clay under evaporation was investigated.

In order to master the essence of development of crack, the mechanism of development of crack must be understood first. Many scholars carried out relevant research and reached some achievements. Lee et al. [10] proposed a finite element model of the crack development of brittle soil based on linear crack mechanics. The model calculated the stress under given tensile load at different dots around preexisting cracks, and the direction of the maximum stress was the one of crack development. For cohesive soil affected by drying and shrinkage function, Bronswijk [11] found the transformation relationship between the vertical settlement of soil and the width and 3D volume change of cracks. However, this model cannot be used to calculate crack spacing under given soil and boundary conditions. Morris et al. [12] analyzed the theoretical relationship between crack depth, soil properties, and given matrix suction distribution and proposed three methods for predicting soil crack depth. Konrad and Ayad [13, 14] developed a theoretical model of soil cracking based on the field tests, the principles of elasticity theory, and the crack mechanics and analyzed the relationship between the tensile strength, Poisson ratio, and other factors of soil and the development depth of cracks. Based on the theory of temperature stress and elasticity, Wu et al. [15] established a theoretical model for calculating the swelling and contraction deformation of soil by using moisture content changes. The mechanism of crack generation is revealed, and the critical wetting criterion for initial cracks of expansive soil is promoted.

At present, the research on the development process of soil cracks generally focuses on the description and influence of soil cracks at a certain moment, while the development process of cracks should be a dynamic process affected by climate conditions. The dynamic development law of soil cracks needs to be further investigated. It is necessary to establish a long-term dynamic prediction and tracking method for the development of soil cracks under evaporation. The objectives of this study are to (i) quantitatively describe the cracking characteristics of soil, (ii) analyze the soil water transport under evaporation, and (iii) establish a dynamic prediction method for crack development.

2. Experimental Study on the Development of Soil Surface Cracks

In this experiment, a soil sample was compounded under laboratory conditions, and cracks would be generated in this soil sample with suitable climate conditions. During the evaporation process, the development of cracks could be observed in the soil sample.

2.1. Materials. The soil sample taken from the Huangshan Slope was packed into a rectangular box and in an undersaturated state initially. Typical geotechnical properties of the soil, including dry unit weight, specific gravity, liquid limit, plastic limit, and expansive index [2], are given in Table 1. The soil is classified as silty clay with medium expansivity.

2.2. Experimental Setup. To study the development of soil crack under the effect of evaporation and the influence of climate on the development rule, an experimental apparatus was designed to observe the soil crack developing process. The experimental setup consists of a rectangular box with size of $1.0\,\mathrm{m} \times 1.0\,\mathrm{m} \times 0.5\,\mathrm{m}$ (as shown in Figure 1), which was made up of glass sheet. In order to reduce the boundary effect, the sides of the box were protected by plastic plate.

An open-area site without any obstructions was chosen as the test site to make soil sample completely exposed in natural conditions. In case of rain or inclement weather, the box was covered with a piece of glass sheet to prevent the increase of moisture. Once the cracks formed, the ruler was placed on the soil sample, and the breadth of the area in which the cracks were intensive was measured. The apparatus also includes an electronic balance, a digital camera, a ruler, a drying oven, and a temperature and humidity recorder.

2.3. Testing Procedures. The development of cracks in the soil sample during the evaporation process in nature condition was monitored. The entire experiment lasted about 20 days until the cracks that were observable with the naked eye became stable. In this process, the intermediate region in which the crack development was more obvious was selected to shoot. A ruler was placed aside as reference; meanwhile, the meteorological data such as temperature and humidity was recorded. The procedure is described as follows:

(1) Prepare test equipment and test material. Place soil sample in the glass box. Sign the region of $20\,\mathrm{cm} \times 20\,\mathrm{cm}$ with white line.

(2) Examine the cracks every 2 hours in the early developing period. Once the cracks appear, the sample is photographed from top at a fixed height. The meteorological data of the day is recorded by temperature and humidity measuring device and anemometer. The moisture content is measured through moisture content test with multiple soil samples that are taken from the site next to the observation area.

(3) The observation interval can be appropriately extended as the cracks become mature, which is indicated by the slow development of the width and length of cracks. In case of rain, the glass holder is covered with an organic glass plate. The experiment continues until the moisture content and the crack parameter change nonsignificantly. The development feature of cracks in vertical direction can be observed by disconnecting the plastic plate around the glass holder. The crack-surface morphology is observed by cutting the sample.

Table 1: Properties of the soil in the laboratory crack development test [2].

Soil property	Values
Dry unit weight of soil (kN/m^3)	16.9
Specific gravity of soil particles	2.71
Liquid limit (%)	49.3
Plastic limit (%)	26.8
Expansive index	53

Figure 1: Experimental setup.

(4) The geometrical parameters of cracks were obtained by image-processing techniques.

(5) Analyze the influence of climate conditions and moisture content on sample cracking at each stage.

2.4. Developing Process of Cracks in Natural Conditions. Representative pictures of cracks at different development stages are shown in Figure 2. Initially, the sample clung to the glass box wall, with no shrink. The sample began to shrink integrally and separate from the wall as the moisture content decreased, in which stage a significant shrinkage appeared at the beginning as the moisture content decreased while the shrinkage had no change in the later period. In this stage, in spite of significant decrease of moisture content, only global shrinkage existed in the sample without cracking. As the moisture evaporated further, a small crack appeared on the surface, which would extend along its direction until being obstructed by other cracks or the margin of the sample. Then, as the moisture content further decreased, the crack propagated longer and faster until several main cracks emerged steadily. The development of cracks ran through the whole sample surface, and a complex crack network formed eventually.

2.5. Analysis of the Geometric Parameters of the Cracks. In order to quantitatively study the development law of soil cracks, a digital imaging method [16] can be used to extract the crack parameters at various stages, including the number, length, width, and ratio of cracks. Crack ratio is defined as the ratio of the crack area to the total surface area of soil. A photograph of the cracks can be imported into the AutoCAD software and scaled to its full size based on the reference scales. The crack is treated as a straight line. AutoCAD then provides the information of the straight line. The geometric parameters of soil cracks are given in Table 2.

As shown in Figure 2 and Table 2, the initial formative period continued 2~3 days, in which the cracks decentralized and separated from each other; they were generated firstly in the form of a single crack, and then the quantity, length, and width of cracks increased slowly. Then, a primary crack across the observation area appeared, with a lot of secondary cracks derived and developed quickly. This period was named as the fast development period. The quantity of cracks reached 248 on the seventh day, which marked the formation of the shape of the crack network. The shrinkage of some microcracks due to the effect of the humidity outside led to the possible increase of the volume of the sample, which caused the fluctuation of the quantity of the cracks. The reflection of crack development was not only the increase in the quantity but also the increase in the length and the width. On the 12th day, the quantity decreased more significantly compared to the day before, which was mainly caused by the compression or closure of some secondary cracks due to the rapid growth of the primary crack. 18 days later, the quantity, length, and width of the cracks remained steady till the end of the development period, continuing 4~15 days. In the stable period, the total length of the cracks was about 1966 mm, and the width of the primary crack was about 22 mm, with average of 1.77 mm.

Figure 3 shows stages divided by the crack ratio in the whole development process of the cracks. Due to the inevitable operation error, some area might show lower moisture rate, where the critical moisture rate is reached first under the same evaporation conditions, leading to the early formation of cracks with low cracking rate. With the soil cracking, to further increase the boundary of evaporation, the crack width and length continued developing; in the meantime, the primary crack began to develop secondary cracks that were less than the primary crack in the width and length. From the energy perspective, the development of cracks released most of the energy. Moreover, the secondary cracks generally existed in the inside polygon, where the soil was cut into pieces by the primary crack and squeezed to some extent, resulting in the limitation of the lateral deformation. This stage was defined as the development period, in which the cracking rate increased quickly from 0.0049 to 0.1398. The last stage was the stable period of crack morphology, indicated by the crack network being basically stable. On the one hand, the length of primary and secondary cracks and the quantity of cracks did not increase anymore; on the other hand, the cracking rate had limited change as the crack width increased.

3. Numerical Simulation of Soil Moisture Movement under Evaporation

In order to study the soil moisture movement under evaporation, a coupling numerical model of soil fluid, air, and heat was established. Then, the variation rules of soil evaporation intensity and volumetric water content during fracture development test were analyzed.

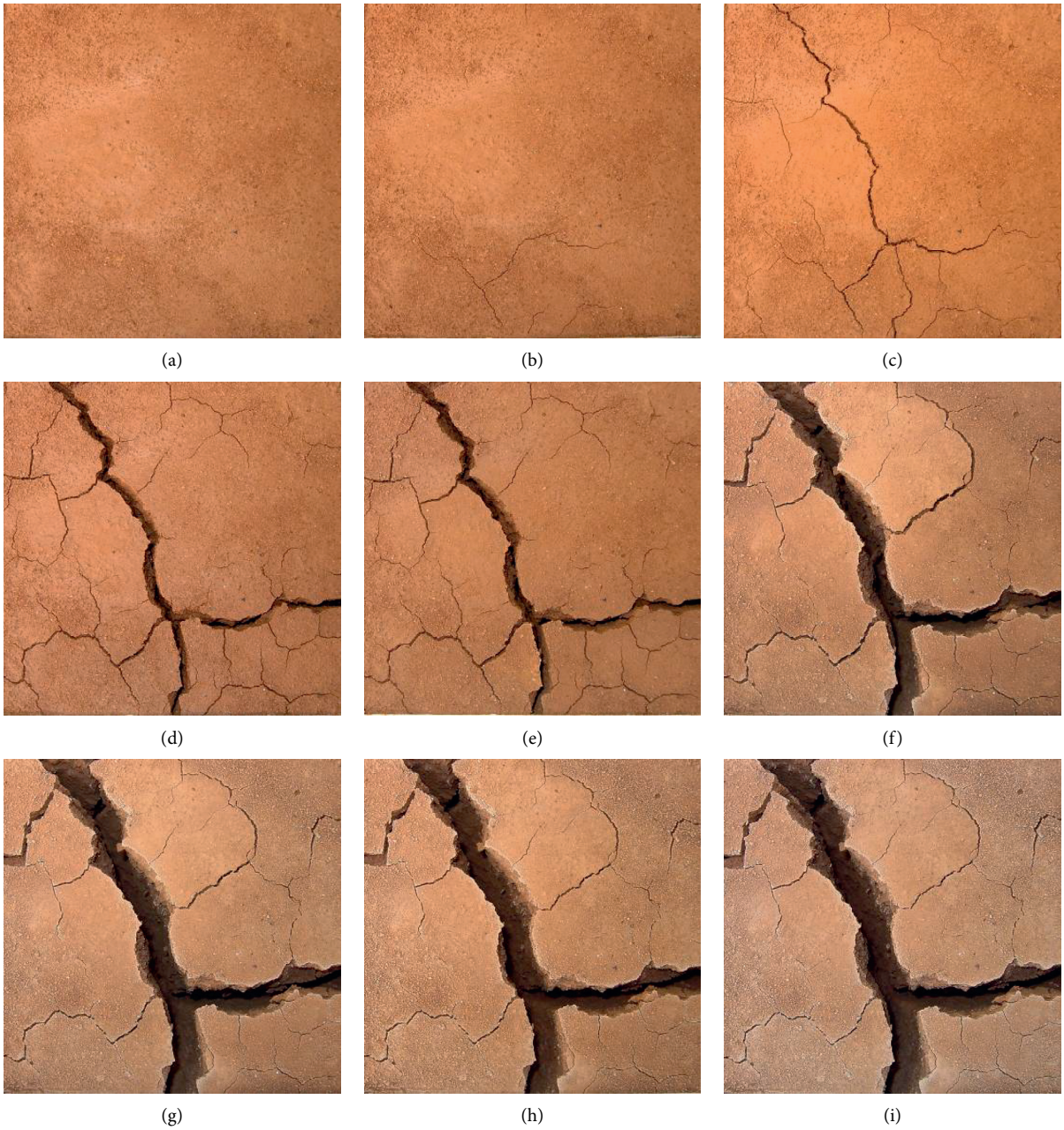

Figure 2: The process of crack development: (a) initial; (b) day 1; (c) day 4; (d) day 7; (e) day 10; (f) day 13; (g) day 16; (h) day 18; (i) final.

3.1. Coupling Numerical Model of Soil Fluid, Air, and Heat under Evaporation. Based on the water and vapor diffusion theory, Dalton [17] firstly proposed the functional relationship between the evaporation of evaporating surface, the water vapor pressure deficit, and the wind speed.

$$E_a = \frac{f(w)\Delta e}{P}, \tag{1}$$

where E_a is the evaporation of the free water surface; Δe is the vapor pressure deficit; P is the barometric pressure, ignoring its effect on the evaporation from water surface; and $f(w)$ is the wind speed function (a linear relationship).

Penman proposed a formula for calculating the water surface evaporation [18], based on the conservation of energy and the aerodynamic theory.

$$E_a = \frac{\Delta H + \gamma E_0}{\Delta + \gamma}, \tag{2}$$

where γ is the psychrometer constant, H is the surface net radiation, E_0 is the air dry rate, and Δ is the slope of the saturated vapor pressure curve in the current average temperature.

In addition to the influence of the buried depth and supply quantity of the underground water, the actual

Table 2: Soil crack geometric parameters.

Date (d)	Crack number	Length (mm)		Width (mm)		Crack ratio
		Total	Mean	Total	Mean	
1	78	332.071	4.257	29.707	0.381	0.004484
2	81	342.257	4.225	32.401	0.400	0.004988
3	94	392.258	4.172	42.245	0.449	0.008612
4	189	1166.746	6.173	118.011	0.624	0.018632
5	223	1723.469	7.728	201.063	0.901	0.04496
6	218	1744.748	8.003	206.823	0.948	0.056352
7	248	1883.845	7.915	229.436	0.925	0.058696
8	227	1880.641	8.212	209.641	0.923	0.068224
9	220	1898.565	8.475	205.261	0.933	0.07068
10	216	1887.872	8.699	219.594	1.016	0.071628
11	221	1937.768	8.728	251.492	1.137	0.083056
12	203	1928.239	9.498	271.748	1.338	0.104552
13	192	1983.805	10.332	264.378	1.376	0.108588
14	193	1914.034	9.917	282.093	1.461	0.11072
15	191	1914.888	10.025	298.899	1.564	0.121488
16	189	1951.585	10.325	307.211	1.625	0.136956
17	192	1948.225	10.147	313.315	1.631	0.13982
18	194	1967.865	10.143	342.946	1.767	0.151456
19	193	1969.143	10.202	343.812	1.781	0.152552
20	191	1966.256	10.294	338.937	1.774	0.152013

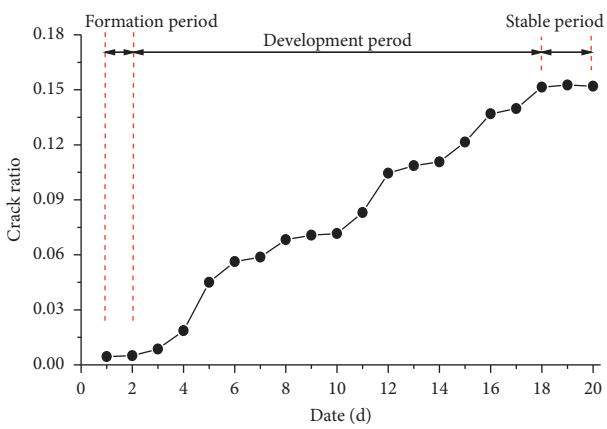

Figure 3: Crack development stages divided by crack ratio.

evaporation capacity of unsaturated soil would be primarily affected by climate factors, such as the net radiation of soil surface, humidity, temperature, and wind speed. Considering the climate factors mentioned above, Wilson [19] deduced the Penman–Wilson formula based on Penman evaporation formula to calculate the actual evaporation in the surface layer of unsaturated soil.

$$E = \frac{\Gamma R_n + \eta E_a}{\Gamma + \eta A}, \tag{3}$$

where E is the actual evaporation in the soil surface, Γ is the slope of the curve between the saturated evaporation and the temperature, R_n is net radiation of soil surface, η is humidity coefficient, and A is the reciprocal of the relative humidity of soil surface.

The osmosis of unsaturated soil reflects the non-isothermal process of the coupling between the temperature field and the humidity field. With sufficient sunshine and large temperature gradient, the movement of moisture is affected by temperature to some extent. Based on the water-gas-thermal coupling migration theory raised by Philip and De Vries [20, 21], Milly proposed the motion model of flow, representing the temperature difference between the liquid state and the gas state and the influence of gravity, capillary, and adsorption capacity [22, 23].

$$\frac{1}{\rho_w}\frac{\partial}{\partial x}\left(D_v\frac{\partial P_v}{\partial x}\right) + \frac{1}{\rho_w}\frac{\partial}{\partial y}\left(D_v\frac{\partial P_v}{\partial y}\right) + \frac{\partial}{\partial x}\left(k_x\frac{\partial(\psi + y)}{\partial x}\right) + \frac{\partial}{\partial y}\left(k_y\frac{\partial(\psi + y)}{\partial y}\right) + Q = \lambda\frac{\partial\psi}{\partial t}, \tag{4}$$

$$L_v\frac{\partial}{\partial x}\left(D_v\frac{\partial P_v}{\partial x}\right) + L_v\frac{\partial}{\partial y}\left(D_v\frac{\partial P_v}{\partial y}\right) + \frac{\partial}{\partial x}\left(\lambda_{tx}\frac{\partial T}{\partial x}\right) + \frac{\partial}{\partial y}\left(\lambda_{ty}\frac{\partial T}{\partial y}\right) + Q_t = \lambda_v\frac{\partial\psi}{\partial t}, \tag{5}$$

where D_v is the steam diffusion coefficient; ρ_w is the water density; P_v is the water vapor pressure in soil; ψ is the matric suction coefficient; k_x and k_y are the permeability coefficient of x and y direction, respectively; Q is the boundary flux; λ is the slope of indicatrix between soil and water; Q_t is boundary heat; L_v is latent heat of evaporation; λ_{tx} and λ_{ty} are the heat conductivity coefficient of soil of x and y direction, respectively; T is the absolute temperature; y is the level head; λ_v is the volumetric specific heat capacity; and t is the time.

The relationship between matric suction, temperature, and water vapor pressure in soil can be described by the formula below which is proposed by Edlefsen and Anderson [24].

$$P_v = P_{vs}\left(e^{(-\psi\cdot w)/(\rho\cdot R\cdot T)}\right) = P_{vs}h_{\text{air}}, \tag{6}$$

where w is the vapor molecular weight, h_{air} is the relative air humidity, R is the gas constant, and P_{vs} is the saturated vapor pressure.

Numerical model of coupling between liquid, gas, and heat in soil could be described by simultaneous equations of formulas (4)–(6). In addition, the rule of moisture migration could be solved by the finite element numerical method and realized through the program software of Vadose.

3.2. Numerical Analysis of Evaporation Effect. As shown in Figure 4, a two-dimensional finite homogeneous soil column with the size of 1.0 m × 0.5 m was established and divided into 50 units. Both sides of the model were defined as impervious boundaries, while the surface and the bottom were defined as free boundaries.

The initial state of soil was saturated state. The rainfall was set to be 0 mm/d. The meteorological data of 20 days was collected during the experiment, including the daily maximum and minimum temperature, the daily maximum and minimum humidity, and the mean value of wind speed, as shown in Figure 5.

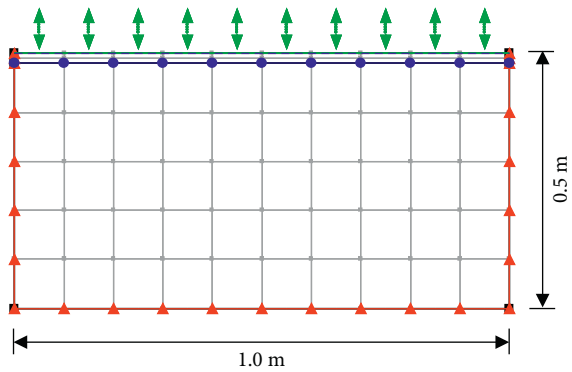

Figure 4: The numerical model of evaporation.

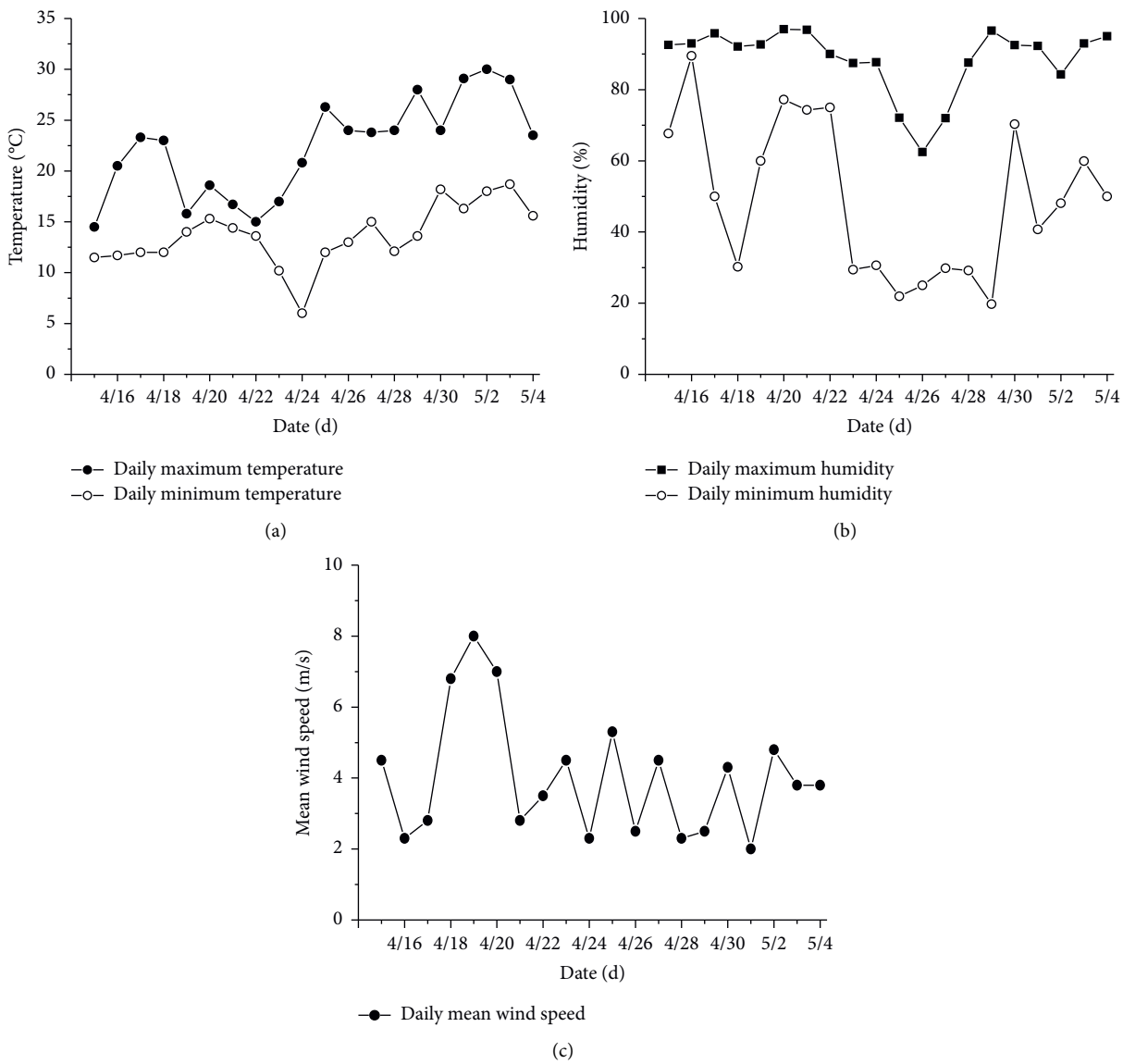

Figure 5: The curves of temperature, humidity, and wind speed with time: (a) temperature; (b) humidity; (c) wind speed.

As shown in Figure 6, the permeability coefficient was calculated using the formula of Van Genuchten selected according to the soil water characteristic curve that was estimated by improved model of Kovacs (shortened to MK model [25]) via the test of soil characteristics parameters and fitted by the model of Van Genuchten [26].

The coefficient of thermal conductivity function curve was calculated with Johansen method [27], while the coefficient of thermal conductivity of natural dry soil was calculated with dry density.

$$\lambda_{\text{dry}} = \frac{0.135r_d + 64.7}{2700 - 0.947r_d} \pm 20\%, \tag{7}$$

where r_d is dry density of soil and λ_{dry} is the coefficient of thermal conductivity of natural dry soil.

The coefficient of thermal conductivity of saturated soil was related to the composition of pore water and soil particles.

$$\lambda_{\text{sat}} = \lambda_s^{1-n}\lambda_w^n, \tag{8}$$

where λ_{sat} is the coefficient of thermal conductivity of saturated soil, λ_s is the coefficient of thermal conductivity of soil particles, λ_w is the coefficient of thermal conductivity of pore water, and n is the porosity.

The coefficient of thermal conductivity of unsaturated soil was connected with the saturated and dry coefficient of thermal conductivity and the degree of saturation.

$$\begin{aligned} \lambda_{u\text{sat}} &= \left(\lambda_{\text{sat}} - \lambda_{\text{dry}}\right)\lambda_e + \lambda_{\text{dry}}, \\ \lambda_e &= \log S_r + 1.0, \end{aligned} \tag{9}$$

where λ_{usat} is the coefficient of thermal conductivity of unsaturated soil, S_r is the degree of saturation, and λ_ε is the correction factor of S_r. Based on the formulas above, the relationship between the coefficient of thermal conductivity and volume moisture content was built as shown in Figure 7.

The volumetric heat capacity was defined as the absorption or release of energy per unit volume of soil as the temperature increased or decreased by 1°C, which was related to the composition of three phases in soil and their heat capacities. The effect of atmosphere can be ignored. For a unit volume of soil, the heat capacity can be described as follows:

$$\lambda_v = \lambda_{vs}\left(1 - V_w\right) + \lambda_{vw}V_w, \tag{10}$$

where λ_v is the volumetric heat capacity, λ_{vs} is the volumetric heat capacity of soil particles, λ_{vw} is the volumetric heat capacity of water, and V_w is the volume of liquid material per unit volume of soil. The relationship between the volumetric heat capacity of cracks and the volume moisture content can then be established according to the formula above, as shown in Figure 8.

3.3. Time Characteristics of Evaporation. The curve of volume moisture content on soil surface and soil evaporation intensity change over time is shown in Figures 9 and 10. The results implied that the soil surface evaporation process can be divided into three stages on the basis of the function of evaporation capacity and soil water supply capacity and the characteristics and rules of soil surface evaporation.

At the beginning of evaporation, the hydraulic conductivity decreased due to fast decline of the soil surface moisture content. However, due to the complement role of the increased suction gradient, the soil surface evaporation intensity was maintained at a stable level rather than declined with the drop of moisture content, roughly the same as free water surface evaporation intensity, which was the stable evaporation stage. In the early stage of the evaporation process, the migration of water caused by moisture movement and gaseous water movement was so weak that it could be ignored.

In the second stage of evaporation, the soil moisture content declined below the critical moisture content. When the soil moisture content was higher than the air-dried moisture content, the surface soil moisture stress decreased slowly approaching the saturated moisture stress. With the decline of water circulation, the gas flow increased gradually. The movement of water is carried out by the coexistence of liquid flow and gas flow. Therefore, the surface moisture flux was the important part of evaporation. Since the water carrying capacity of soil became weaker and weaker, the surface was unable to replenish evaporated water to decrease the surface moisture content. Then, the matrix suction entered into the phase of rapid growth, and the evaporation reduced consequently.

When the surface moisture content was below the air-dried moisture content, the water carrying capacity of soil became too weak to supply the evaporated water, which led to dry-soil formation on surface. The evaporation intensity changed slowly and steadily, depending on the control capacity of dry-soil moisture diffusion and dry-soil layer depth.

4. Discussion

The development process of cracks is a dynamic process affected by climate conditions. Under the effect of evaporation, the soil continuously lose water and shrinks, thus forming cracks. Crack width is an important parameter that characterizes cracking development. By establishing the relationship between the water content and the crack width, the dynamic prediction of crack development under soil evaporation can be realized.

As presented in Figure 11, the average crack width changed as the moisture content decreased in soil. It shows that after a sharp decline, the moisture content stayed steady at 6% eventually. After a short cracking process, the crack width increased quickly and gradually became stable in the end. The development of crack width consisted of 3 stages: slow development, fast development, and stable development. At the beginning, the desiccation crack was generated because of the existence of weakness somewhere on the surface as well as a larger shrinkage rate compared to the lower layer. The reason why the crack developed slowly at the start time was that the sample that stayed in a relatively high level of moisture content and contacted the external environment with only the surface underwent overall contraction. With the

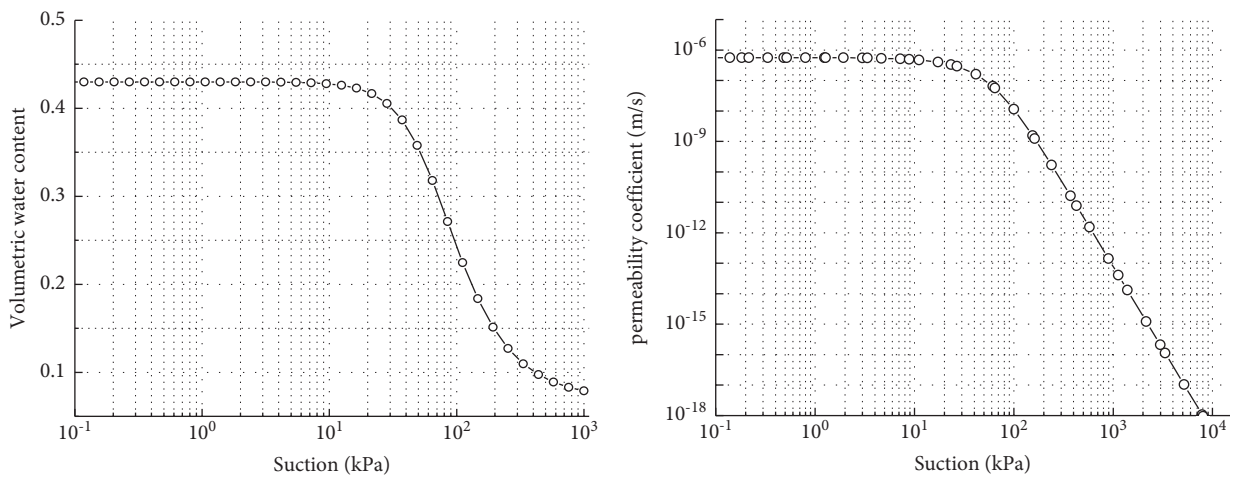

Figure 6: Hydraulic parameters of unsaturated soil: (a) soil water characteristic curve; (b) permeability function.

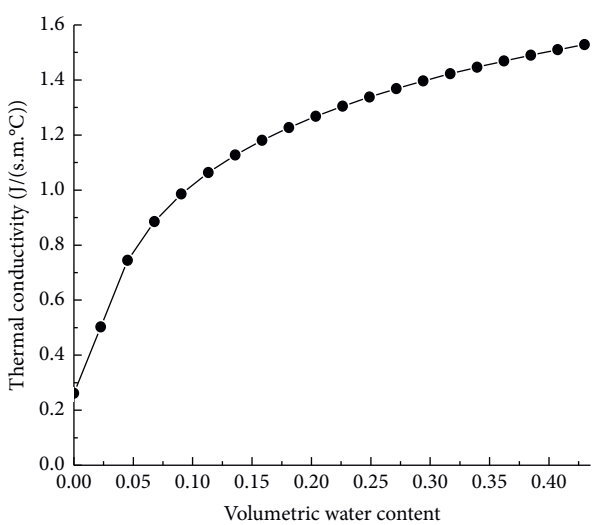

Figure 7: Thermal conductivity curve.

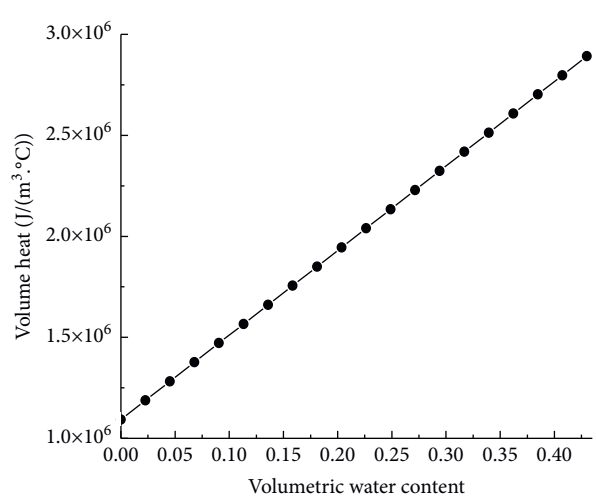

Figure 8: Volume heat curve.

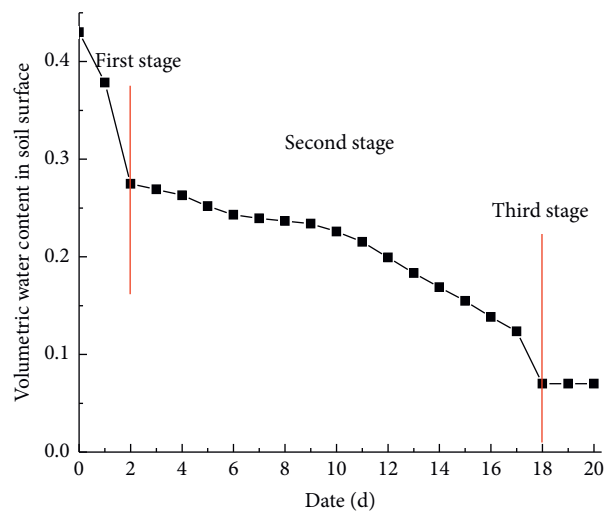

Figure 9: The change of volumetric water content on soil surface.

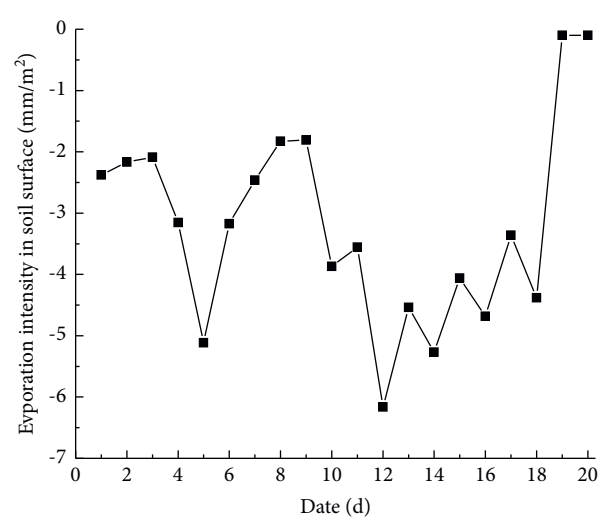

Figure 10: The change of evaporation intensity on soil surface.

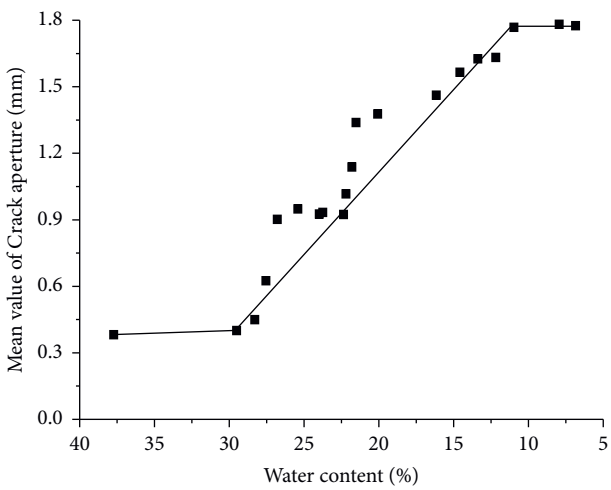

Figure 11: The relationship between mean value of crack aperture and water content.

generation of crack, the contact area between crack and external environment expanded quickly, leading to the increase of filtration rate and a sharp movement of crack. When the crack expanded to a certain degree, soil on both sides of the crack performed a stronger limitation with the increase of crack depth. Although the moisture content of soil declined, the matric suction was no longer the main factor controlling the soil properties. The slow development process indicated that the crack reached a stable stage.

For the crack in natural conditions, there was an obvious function relation between the moisture content and the crack width as described in Figure 10. Based on the time effect of soil evaporation, the crack width change with moisture content could be described quantitatively as follows:

$$\begin{cases} b = b_1, & \theta \le \theta_k, \\ b = m\theta_k + n, & \theta_c < \theta < \theta_k, \\ b = b_3, & \theta \le \theta_c, \end{cases} \tag{11}$$

where b_1 is the width of initial cracking soil, θ_k is the boundary of moisture content between the first and second stage of evaporation, θ_c is the air-dried moisture content, m and n are fitting parameters, and b_3 is the width of ultimate cracking soil. According to the calculation, the values of m and n are −0.077 mm and 2.617 mm, respectively. In the stable evaporation stage, the water content decreases from 29% to 11%, and the crack width increases from 0.39 mm to 1.77 mm.

5. Summary and Conclusions

In this paper, experimental and numerical analysis of soil cracking characteristics under evaporation are carried out. The following conclusions are drawn:

(1) Soil crack development test was carried out to observe the occurrence and development of cracks in soil samples during evaporation. By analyzing the geometric characteristic values of cracks in each stage, the development law of cracking is described quantitatively. The results show that the process of soil crack development under evaporation can be divided into three stages: crack formation stage, crack development stage, and crack stability stage.

(2) The law of soil water transport under evaporation was analyzed through numerical simulation of soil evaporation process in atmospheric environment. The evaporation process of soil surface can be divided into three stages. In the early evaporation stage which is called formation stage, the evaporation intensity of surface soil was maintained at a stable value instead of decreasing with the moisture content. In the second phase, the surface soil moisture decreased while evaporation was also reduced. In the third stage, evaporation of surface soil happened inside, and the changing rate of the evaporation intensity was generally very slow and steady.

(3) The functional relationship between the soil moisture content and the crack width under evaporation was established. The dynamic prediction of crack development was realized. The results showed that the water content decreased from 29% to 11%, while the crack width increased from 0.38 mm to 1.77 mm in the stable evaporation stage.

Data Availability

The data used to support the findings of this study are available from the corresponding author upon request.

Conflicts of Interest

The authors declare that they have no conflicts of interest.

Acknowledgments

This work was supported by the Fundamental Research Funds for the Central Universities (Grant no. 2018B04914), Central Public-Interest Scientific Institution Basal Research Fund grant funded by the Chinese government (Grant no. Y32003), and Transportation Science and Technology Project of Jiangsu Province, "Study on Key Technologies of Highway Protection by Slope Construction First Method."

References

[1] L. Yang and E. Liu, "Numerical analysis of the effects of crack characteristics on the stress and deformation of unsaturated soil slopes," *Water*, vol. 12, no. 1, p. 194, 2020.

[2] Y. Wang, D. Feng, and C. W. W. Ng, "Modeling the 3D crack network and anisotropic permeability of saturated cracked soil," *Computers and Geotechnics*, vol. 52, pp. 63–70, 2013.

[3] Q. Cheng, C. S. Tang, D. Xu, H. Zeng, and B. Shi, "Water infiltration in a cracked soil considering effect of drying-wetting cycles," *Journal of Hydrology*, vol. 593, no. 7566, 2020.

[4] C. J. Miller, J. Mi, and N. Yesilleer, "Experimental analysis of desiccation crack propagation in clay liners," *Journal of the American Water Resources Association*, vol. 34, no. 3, pp. 153–163, 1998.

[5] C. Tang, B. Shi, C. Liu, L. Zhao, and B. Wang, "Influencing factors of geometrical structure of surface shrinkage cracks in clayey soils," *Engineering Geology*, vol. 101, no. 3-4, pp. 204–217, 2008.

[6] C. Tang, Y. Cui, A. M. Tang, and B. Si, "Experiment evidence on the temperature dependence of desiccation cracking behavior of clayey soils," *Engineering Geology*, vol. 114, no. 3-4, pp. 261–266, 2010.

[7] C. Tang, Y. Cui, A. M. Tang, and B. Si, "Shrinkage and desiccation cracking process of expansive soil and its temperature-dependent behavior," *Chinese Journal of Geotechnical Engineering*, vol. 34, no. 12, pp. 2181–2187, 2012.

[8] G. Liu, Y. Chen, X. Zeng, and G. Zhang, "Effects of ambient air humidity and temperature on crack development of compacted expansive soils," *Chinese Journal of Geotechnical Engineering*, vol. 42, no. 2, pp. 259–268, 2020.

[9] C. Wu, Y. Wang, D. Feng, and Y. Zhou, "Experimental study on the coupled behavior of dynamic cracking and moisture-heat evolution of a clay under evaporation," *Bulletin of Engineering Geology and the Environment*, vol. 80, no. 6, pp. 4943–4955, 2021.

[10] F. H. Lee, K. W. Lo, and S. L. Lee, "Tension crack development in soils," *Journal of Geotechnical Engineering*, vol. 114, no. 8, pp. 915–929, 1988.

[11] J. Bronswijk, "Drying, cracking, and subsidence of a clay soil in a lysimeter," *Soil Science*, vol. 152, pp. 92–99, 1991.

[12] P. H. Morris, J. Graham, and D. J. Williams, "Cracking in drying soils," *Canadian Geotechnical Journal*, vol. 29, no. 2, pp. 263–277, 1992.

[13] J. M. Konrad and R. Ayad, "Desiccation of a sensitive clay: field experimental observations," *Canadian Geotechnical Journal*, vol. 34, pp. 850–858, 1997.

[14] J.-M. Konrad and R. Ayad, "A idealized framework for the analysis of cohesive soils undergoing desiccation," *Canadian Geotechnical Journal*, vol. 34, no. 4, pp. 477–488, 1997.

[15] J.-H. Wu, J.-P. Yuan, and C. W. W. Ng, "Theoretical and experimental study of initial cracking mechanism of an expansive soil due to moisture-change," *Journal of Central South University*, vol. 19, no. 5, pp. 1437–1446, 2012.

[16] J. H. Li and L. M. Zhang, "Geometric parameters and REV of a crack network in soil," *Computers and Geotechnics*, vol. 37, no. 4, pp. 466–475, 2010.

[17] J. Dalton, "Experimental essays on the constitution of mixed gases; on the force of steam or vapor from water and other liquids in different temperatures, both in a torricellian vacuum and in air; on evaporation and on the expansion of gases by heat," *Memoirs and Proceedings of the Manchester Literary and Philosophical Society*, vol. 5, pp. 535–602, 1802.

[18] H. L. Penman, "Natural evapotranspiration from open water, bare soil and grass," *Proceedings of the Royal Society of London*, vol. 193, pp. 120–146, 1948.

[19] G. W. Wilson, D. G. Fredlund, and S. L. Barbour, "Coupled soil-atmosphere modelling for soil evaporation," *Canadian Geotechnical Journal*, vol. 31, no. 2, pp. 151–161, 1994.

[20] J. R. Philip and D. A. De Vries, "Moisture movement in porous materials under temperature gradients," *Transactions—American Geophysical Union*, vol. 38, no. 2, pp. 222–232, 1957.

[21] D. A. De Vries, "Simultaneous transfer of heat and moisture in porous media," *Transactions—American Geophysical Union*, vol. 39, no. 5, p. 909, 1958.

[22] P. Milly, "Moisture and heat transport in hysteretic, inhomogeneous porous media a matric head-based formulation and a numerical model," *Water Resource Research*, vol. 18, pp. 489–498, 1982.

[23] P. C. D. Milly, "A linear analysis of thermal effects on evaporation from soil," *Water Resources Research*, vol. 20, no. 8, pp. 1075–1085, 1984.

[24] N. E. Edlefsen and A. B. C. Anderson, "Thermodynamics of soil moisture," *Hilgardia*, vol. 15, no. 2, pp. 31–298, 1943.

[25] P. J. Kamann, R. W. Ritzi, D. F. Dominic, and C. M. Conrad, "Porosity and permeability in sediment mixtures," *Ground Water*, vol. 45, no. 4, pp. 429–438, 2010.

[26] M. T. van Genuchten, "A closed-form equation for predicting the hydraulic conductivity of unsaturated soils," *Soil Science Society of America Journal*, vol. 44, no. 5, pp. 892–898, 1980.

[27] O. Johansen, *Thermal Conductivity of Soils*, University of Trondheim, Trondheim, Norway, 1975.

Hindawi
Mathematical Problems in Engineering
Volume 2021, Article ID 2060311, 12 pages
https://doi.org/10.1155/2021/2060311

Research Article

Application of Slope Radar (S-SAR) in Emergency Monitoring of the "11.03" Baige Landslide

Xu Wei [1,2] **and Feng Wenkai** [1]

[1] *Key Laboratory of Geohazard Prevention and Geoenvironment Protection, Chengdu University of Technology, Chengdu 610081, China*
[2] *China Geological Survey of Chengdu Center, Chengdu 610081, China*

Correspondence should be addressed to Feng Wenkai; fengwenkai@cdut.cn

Received 30 August 2021; Accepted 4 October 2021; Published 27 October 2021

Academic Editor: Gan Feng

On October 11 and November 3, 2018, the disaster chain of landslide-barrier lake occurred twice in Baige Village, Xizang Province. After the second sliding of the landslide, the danger of the landslide dam was eliminated by the manual excavation of the drain grooves. During this period, a ground-based interferometric synthetic aperture radar (GB-InSAR) called "S-SAR" was utilized for real-time monitoring and analyzing 48 selected target pixels on the residual deformation bodies of landslides (divided into K1, K2, and K3 deformation zones) for 8 days. Through the real-time deformation map of pixels in the monitoring area obtained by S-SAR, the ranges of five strong deformation regions were identified and delineated. Based on the apparent cumulative deformation-time curve of each target pixel, the overall deformation law of K1, K2, and K3 deformation zones could be monitored and analyzed in real time. Based on a curve graph of the deformation rate, acceleration, and time of each target pixel, the K1, K2, and K3 deformation zones were within a uniform deformation stage. Taking the target pixel point and the corresponding time in which the deformation rate and deformation acceleration had a large, abrupt jump at the same time as the position and time of the near-slip failure, the 11 positions and moments of the near-slip failure were counted. The results presented here may represent a workable reference for emergency monitoring and early warning of similar sudden geological disasters.

1. Introduction

In the early morning of October 11, 2018, a large-scale landslide occurred in Baige Village, Jiangda County of the Tibet Autonomous Region, referred to as the "10.11" landslide. The scope of the landslide is shown in Figure 1, the red dotted line. The 10.11 landslide blocked the Jinsha River and formed a barrier dam that was relieved after natural flood discharge. At GMT +8 17:40 on November 3, 2018, the back edge of the landslide area slid again. The scope of the landslide is shown in Figure 1, the yellow solid line; it blocked the river again and formed a larger lake. Excavation of the spillway was completed at GMT +8 16:00 on November 11. At GMT +8 8:00 on November 12, the water volume of the barrier lake reached $5.2 \times 10^8\ m^3$. The danger of flood discharge was successfully relieved at GMT +8 10:00 on November 12 as the barrier lake water storage capacity reached $5.2 \times 10^8\ m^3$. The dangers of flooding were successfully evaded, making this event an example of successful manual intervention in a major barrier lake. The landslide and subsequent flood affected approximately 102,000 citizens in Tibet, Sichuan, and Yunnan provinces. Approximately 86,000 people were relocated, and more than 3,400 homes were collapsed [1].

Failure prediction and early warning of landslides are a popular but challenging endeavour within the geological engineering field. Time-of-failure prediction methods that are based on kinematic parameters can be classified into two groups: empirical methods [2–9] and semiempirical methods [10–16], 2017). Other methods are often associated

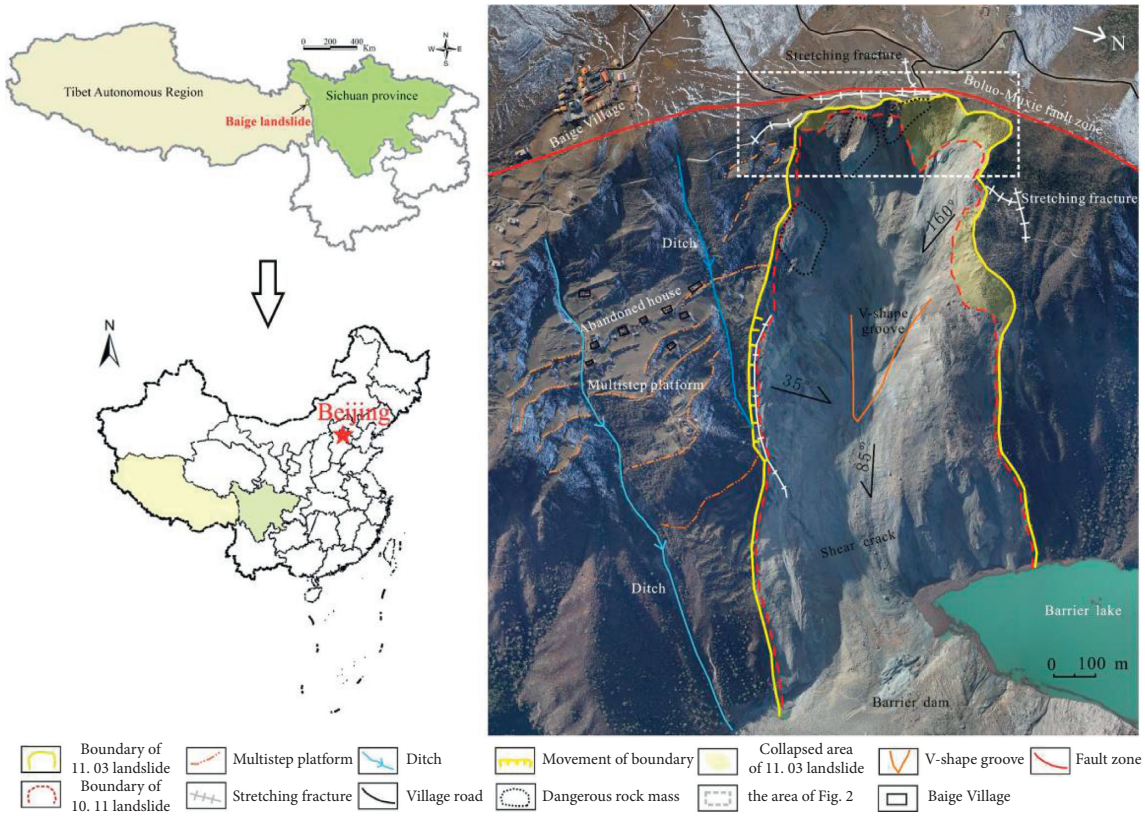

Figure 1: 11.03 Baige landslide plane.

with landslide prediction even though they do not actually provide an estimation of the time of failure: numerical methods [17–25] and methods for the definition of thresholds [26–32].

Future trends in landslide prediction will also be fostered by technological advancements in monitoring techniques. The most striking example is related to recent developments in interferometric satellites. A continuous check of satellite data would have permitted scientists to properly forecast deadly events such as the Xinmo landslide (Maoxian, China) in 2017 [33], which caused >100 casualties, and a landslide in an undisclosed copper open-pit mine that killed several workers [34]. Even terrestrial instruments are changing which were only recently considered as consolidated assumptions. For example, the capability of modern GB-InSAR apparatuses to monitor areas (not only single points) in a few tens of seconds enables us to further push the limits of what was considered (near) real-time monitoring [9, 35, 36]. GB-InSAR also has the advantage of performing measurements over a broad coverage area (instead of on single discrete points) [37].

Based on field investigation and the interpretation of UAV aerial images, the basic characteristics of the 11.03 landslide and the deformation pattern of the landslide mass were analyzed in this study. The Beidou displacement monitor and crack displacement metre data of the 11.03 landslide indicate that the main rock body experienced three separate accelerated stages before beginning to slide. During the excavation and construction of discharge grooves, we applied an S-SAR for deformation monitoring and early warning forecasting, delimited the K1, K2, and K3 areas, and identified 48 meaningful points on the cumulative deformation map. The revisiting time was 15 minutes with a total monitoring time of eight days. The strong deformation zone was identified accordingly. Near real-time monitoring of K1, K2, and K3 was performed, and the deformation evolution stages of the landslide were defined. We also conducted hazard area identification and judgement, sliding warning threshold value calculation, and slip damage identification and prediction before summarizing the radar monitoring results of the survey slope. The construction of a Weir Plug dam spillway and the removal of dangerous barrier lakes are recommended according to the results.

2. 11.03 Landslide Characteristics and Deformation Pattern

2.1. Basic Characteristics of Landslides. The 11.03 landslide was located in Jiangda Village, Tibet Autonomous Region. The geographical coordinates are longitude 98°41′52.15” and north latitude 31°4′54.91”. The landslide occurred at a linear distance of 144 km from the nearest major city, 65 km from Jiangda village and 17 km away from Baiyu town. The landslide is geographically characterized by the Hengduan Mountain Range and Jinsha River Valley of eastern Tibet, which is a typical tectonic erosion landform. The landslide area encompassed the Jinshajiang tectonic belt between Changdu-Simao and Dege-Zhongdian landmasses.

The peak acceleration of ground motion in the area where the landslide was located was 0.20 g. On August 12, 2013, the neighbouring Zuogong and Mangkang counties at the junction of the north latitude 30.0° and 98.0° east longitude experienced a 6.1 magnitude earthquake. There was no significant seismic activity in the area just prior to the landslide.

The elevation of the 11.03 landslide is 2880–3720 m. The height difference between the front and rear margin is approximately 840 m. The sliding direction of the main sliding body of the "10.11" landslide was 85°. The back edge and the left/right sides of the landslide are bounded by exposed fresh bedrock. The shear outlet is located at the foot of the slope approximately 70 m above the river surface. The slope profile of the landslide is in the form of a fold line with an average slope length of approximately 1420 m. Gullies developed on the right side of the landslide filled with seasonal running water. The plane shape is an irregular rectangle wider from the middle to the back and towards the front. The average slope width is approximately 570 m, and the landslide area is approximately 60×10^4 m^2. The lithology of the outcrop layer in the landslide area is the Proterozoic Xiongsong group ($P_t xn^a$). Gneiss assemblages lie in the west Wari ophitic belt (ψ_{w4}), as shown in Figure 1.

After the landslide occurred, there were several tensile fractures on the platform at the back edge, the longest of which was approximately 290 m, extending along the NNW direction, approximately parallel to the Borot-Muxie fault. The upper part of the left side boundary (the upstream side) of the landslide had a tensile crack, approximately 150 m in length, which was nearly parallel to the left side boundary. There was a tension crack in the middle and lower parts of the right side boundary (the downstream side) of the landslide, which was approximately 550 m in length and nearly parallel to the right side boundary. The downward fault of the crack was obvious. A bank slope landslide was on the right side of the south border, and there were seven displaced platforms from top to toe. The displacement direction was approximately 45°, roughly along with the airport for the Baige landslide slope foot. A total of 16 homes and 110 people were relocated in 2013.

2.2. Characteristics of Metamorphosis. Combined with topography and surface deformation signs, the slide body of the 11.03 landslide can be divided into the K1, K2, and K3 deformation zones.

The K1 deformation region was the posterior residual after two landslides. The main sliding body of the 11.03 landslide is shown in Figure 1 with a volume of approximately 356×10^4 m^3 [38]. The free face direction has a slope of 85°, a trailing surface with two landslides that further expanded the international airport. The free face was a nearly upright and inverted triangle, and there were still two pieces of dangerous rock in the middle. The opening condition was good, and there was a possibility of collapse. The volume was estimated to be approximately 55×10^4 m^3, and small stones often fell during monitoring, as shown in Figure 2.

The K2 deformation area was the slope body on the right side of the landslide. In the case of the 11.03 landslide, there was a small-scale collapse on the downstream side of the slope top, with a volume of approximately 12×10^4 m^3 [38]. The bounds of K2 were rectangular in shape, the surface direction was approximately 35°, with trailing edge boundaries visible through cracks from high to low, and the slope had the shape of a V groove under the direction of the fault. The back wall was staggered with an elevation difference of approximately 2-3 m. There was the possibility of collapse, and the falling direction was along the free surface, with a local estimated volume of approximately 240×10^4 m^3, often with surface soil collapse during monitoring, as shown in Figure 2.

The K3 deformation area was the left slope of the landslide, and the shallow surface rock and soil body also underwent small-scale collapse during the 11.03 landslide. The K3 area has a narrow width and can be divided into two parts. K3-1 is the upstream side of the upper slope, and the deformation body wall surface is smooth. The airport had a plane direction of approximately 160°, and the volume of the area was estimated to be approximately 120×10^4 m^3. During monitoring, topsoil and rock mass collapsing often occurred along the slide face, as shown in Figure 2. K3-2 was the lower part of the upstream side of the landslide, with an "inverted bell shape," and the overall stability was good. There was the possibility of shallow collapse, and an instability collapse causes a rise in the water level of barrier lake, and the estimated volume was approximately 62×10^4 m^3.

3. Principle of S-SAR Deformation Monitoring

The slope synthetic aperture radar (S-SAR) is a GB-InSAR monitoring and early warning system [39]. S-SAR allows for the long-range, continuous monitoring of fixed points. A preset slope deformation amount and deformation rate threshold can be optimized to facilitate early warning of disasters in regions where landslides are possible.

As shown in Figure 3(a), a high-precision linear rail in the S-SAR carries radar interferometer and transceiver bifurcations to continuously transmit high-frequency electromagnetic signals in a fixed-polarization manner; the signals are reflected by the slope target area so that echo signals are continuously received. SAR complex images of the monitoring area are obtained after pulse compression, beam sharpening, and imaging processing. At a fixed time interval (revisiting time) as the slope is monitored, two SAR complex images are created, as shown in Figure 3(b). If a target point on the slope or the target area is deformed slightly in the two image scans, the displacement of the space target moved from point A to point B, point A′ to point B′, which means when two radar images present interference, the corresponding pixel phase difference can be used to determine the displacement (deformation) of the two point targets. The interference unit within the corresponding phase values reflects the radar antenna and target as the slope of the line-of-sight (LOS) deformation. The deformation is the actual displacement component along the LOS direction, which is referred to here as the apparent deformation. The

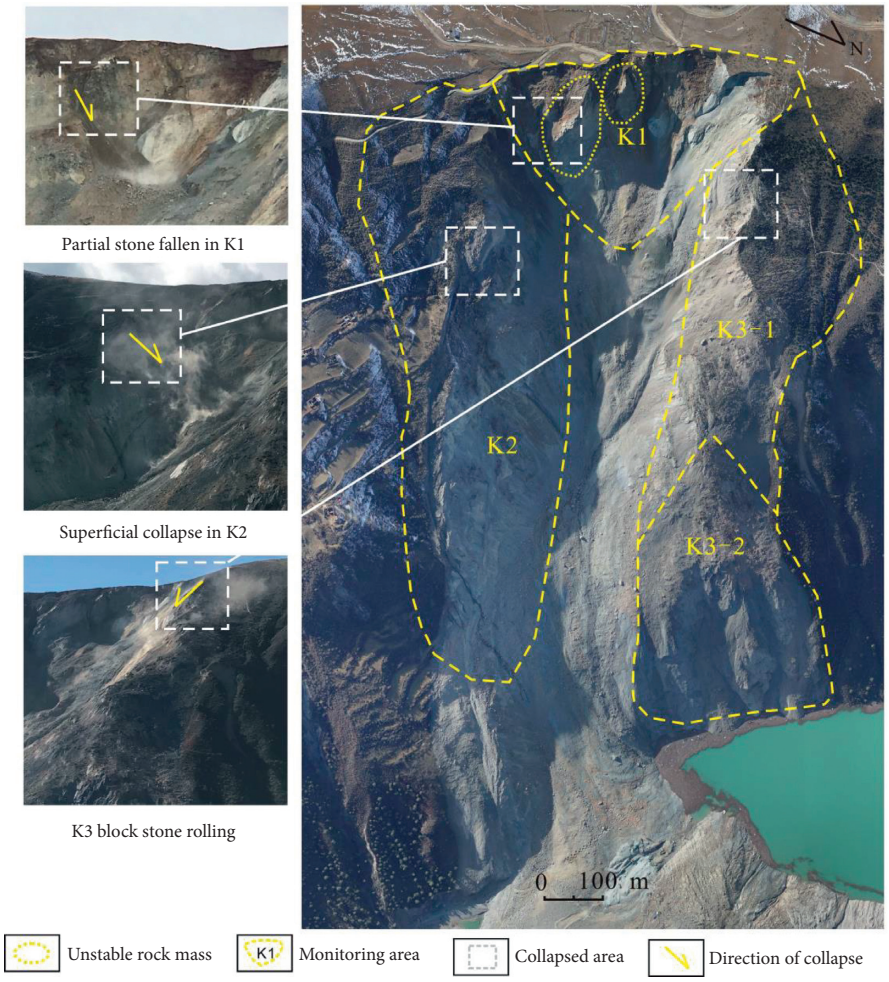

Figure 2: K1, K2, and K3 deformation zones.

symbol reflects that the deformation target moves relatively far from or near to the radar. Many researchers have verified the high accuracy of S-SAR [37].

4. Application of S-SAR in Emergency Management

4.1. Identification and Delineation of Strong Deformation Zones. The primary purpose of the S-SAR is to identify and determine the deformation conditions of a given slope surface. S-SAR results may divide the monitoring area into several continuously distributed pixels, where each pixel is the minimum unit of an S-SAR monitoring result. Different colors represent the variation of cumulative apparent deformation displacement of different pixels. The real-time deformation map of the monitoring area can be displayed on the computer of the slope radar, which can not only quickly identify the strong deformation area of the monitoring area but also click on any pixel to view the cumulative apparent deformation-time curve of the point. All the monitoring data of the point can be downloaded for later data analysis.

The monitoring period in this study was every 15 minutes beginning at GMT+8 14:20 on November 8, 2018, and ending at GMT+8 4:04 on November 16, 2018. The eight-day period was divided into two stages: the emergency construction stage (GMT+8 14:20 on November 8 to GMT+8 00:00 on December 12) and the postrelease stage (GMT+8 00:00 on December 12 to GMT+8 4:04 on November 16). To grasp the real-time deformation of K1, K2, and K3 areas, multiple target pixels were selected from several pixel points to monitor their deformation in real time. The principles of selection were as follows: (1) at the beginning of monitoring, because the distribution of the strong deformation zone in the monitoring area was not clear, the uniform selection method was adopted in K1, K2, and K3 deformation areas; (2) with the continuation of monitoring, the strong deformation area in the real-time deformation map of the monitoring was going to be gradually identified and updated, and the number of target pixels would be increased in the strong deformation area to strengthen the monitoring. By the end of the monitoring, a total of 48 target pixels were selected, including 11 target pixels (J1–J6, J39–J42, and J48) in the K1 deformation area, 8 target pixels (J7–J14) in the K2 deformation area, and 29 target pixels (J15–J38 and J43–J47) in the K3 deformation area, as shown in Figures 4 and 5.

The real-time pixel cloud deformation map shown in Figure 5(b) intuitively reflects the strength variations in the

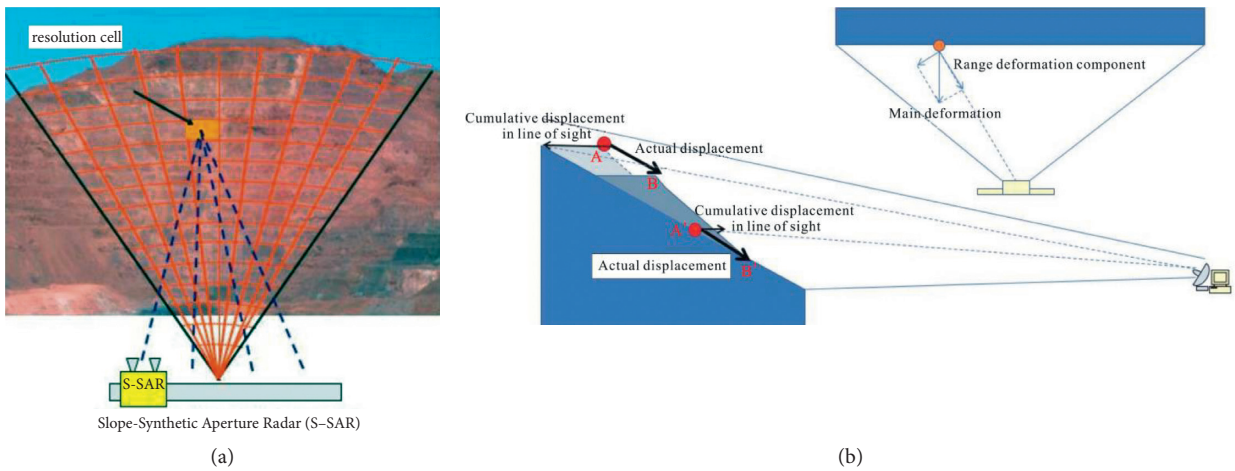

Figure 3: Schematic diagram of slope radar deformation monitoring. (a) The yellow highlighted area marks the S-SAR signal space in contrast to the real slope area; the resolution unit is a small fan-shaped surface element composed of a range-oriented resolution and spatial azimuth resolution. (b) Distance profile and azimuth diagram of actual target displacement on the monitored slope and shape variable monitored by S-SAR.

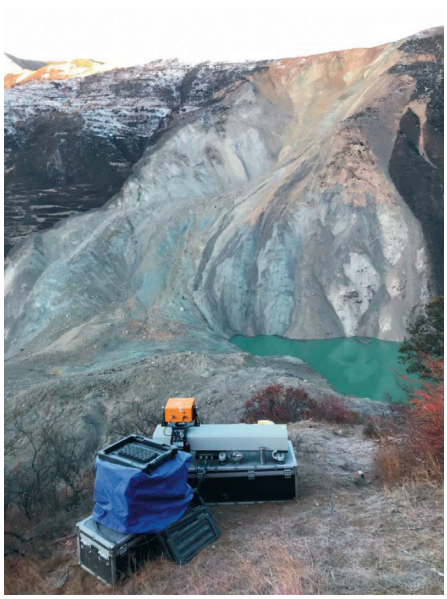

Figure 4: Field monitoring photos of the slope radar.

accumulated apparent deformation in the three deformation zones. Colors range from green, yellow, red, and light blue, corresponding to "weak" to "strong" deformation, respectively. The deployment map of the target pixels delimits the range of strong deformation zones, as shown in Figure 5(a). The deformation zones are mainly distributed in four distinct regions, and the characteristics of each deformation zone are shown in Table 1.

4.2. Near Real-Time Monitoring of Overall K1, K2, and K3 Area Deformation Rules. The S-SAR generates a cumulative apparent deformation-time curve of target pixels in near real time. In the emergency excavation stage, it is crucial that all relevant personnel fully understand the deformation pattern of the hazardous zone. Figures 6–8 show the cumulative apparent deformation-time curve of each target pixel (where slight cumulative deformation and no displacements occurred). As shown in Figure 6, in the emergency excavation stage, the accumulated apparent deformation at the lower part of the multiple free faces on the downstream side of the deformation body (J5) is the largest among the target pixels. The accumulated apparent deformation reached 49.7 mm at its peak. In the barrier lake release stage, the accumulated apparent deformation of the middle and upper parts of the free face on the downstream side of the deformation body (J39, J40, and J41) and the central part of the deformation body (J6) is the largest; the accumulated apparent deformation of J40 reached a maximum of 75.8 mm. The fitting formula of J40 and J5 is shown below. The fitting formula can provide a reference and basis for judging the deformation trend in the later stage.

$$\begin{aligned} J40&: \ y = -0.08t^5 + 1.835\times10^4 t^4 - 1.6\times10^9 t^3 + 6.9\times10^{13} t^2 - 1.5\times10^{18} t + 1.3\times10^{22}; \quad R^2 = 0.97, \\ J5&: \ y = -0.03t^5 + 7.03\times10^3 t^4 - 6.1\times10^8 t^3 + 2.65\times10^{13} t^2 - 5.75\times10^{17} t + 5\times10^{21}; \quad R^2 = 0.9799. \end{aligned} \tag{1}$$

The whole curve of the K1 deformation area presents undulating oscillation characteristics. In the two time periods from 19:10 on 13th to 3:27 on 14th and 19:03 on 14th to 2:05 on 15th, the cumulative apparent deformation-time curve steeply increases, and short-duration accelerated deformation appears to occur. The average deformation rate of

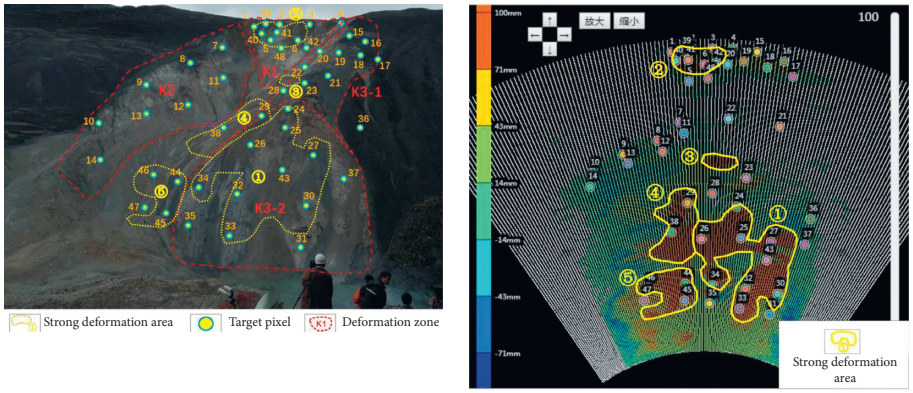

(a) (b)

Figure 5: (a) Deployment of S-SAR target pixels. (b) Real-time cumulative deformation map.

Table 1: Strong deformation area statistical characteristics.

No.	Location	Estimated area (m^2)	Cause of strong deformation
①	K3-2	61000	Shallow residual slope soil and cataclastic rock mass collapse
②	K1	14000	Slope face loose stone fall
③, ④	V-shaped groove area	13200	Top of V-shaped groove and falling blocks on both sides scrape the surface
⑤	Cut the exit	15400	Surface landslide deposits, shallow residual slope soil, and cataclastic rock mass collapse

each target pixel reached 1.88 mm/h and 1.39 mm/h, respectively.

As shown in Figure 7, deformation was largest in the central part of K2 (J13) at a maximum value of 39.8 mm at GMT+8 16:09 on November 12. The deformation characteristics of the K2 area were characterized by oscillation and time correlation. The oscillation is more obvious and occurs over a larger range in the K2 region than in the K1 region. The J13 and J10 curves are the most representative of these alternating peaks and troughs (with five of each in total). The appearance of wave peaks and troughs is consistent with thawing-freezing, day-to-night cycles. Peaks and troughs occur between 4 and 6p.m. and between 5 and 9a.m. The highest morning temperature in the landslide area was 7°C, and the low temperature was −10°C; the largest temperature difference was 17°C, occurring from 6p.m. to 5a.m. the following morning. As the temperature fell to below 0°C, water in the lower part of the slope surface soil and rock joints gradually froze and expanded. Between 9a.m. and 4p.m., the temperature gradually increased, and the resulting thawing increased the water content of the rock and soil mass, decreased the shear strength, and caused the collapse of the surface slope body at the target pixel.

As shown in Figure 8, in the middle part of the slope foot of the landslide where J44 is located, continuous collapse of the shallow surface rock and soil mass produced the maximum apparent deformation in the observation area. This target pixel also showed the largest accumulated apparent deformation among all target pixels. The curves of the K3 deformation zone continually increased over the observation period and fluctuated within a relatively small range. The fitting formula of J44 and J43 is shown below. The fitting formula can provide a reference and basis for judging the deformation trend in the later stage.

$$\begin{aligned} J44:\ & y = -0.58t^3 + 7.6\times 10^4 t^2 - 3.3\times 10^9 t + 4.783\times 10^{13}; \quad R^2 = 0.99, \\ J43:\ & y = 0.19t^3 - 2.52\times 10^4 t^2 + 1.1\times 10^9 t - 1.59\times 10^{13}; \quad R^2 = 0.99. \end{aligned} \tag{2}$$

4.3. Determining the Deformation Zone. The correct judgement of slope deformation evolution stages is the basis for accurate early landslide warning [40–42]. There are three basic deformation stages that occur as the landslide evolves: initial deformation, constant deformation, and accelerated deformation. The deformation rate and deformation acceleration of each target pixel can be calculated according to the accumulated apparent deformation data of each target pixel as obtained by the S-SAR. The stage that the deformation area has reached can then be determined by analyzing the deformation rate-time and deformation acceleration-time curve.

Take the J40 target pixel, which has the largest accumulated apparent deformation in the K1 area, as an example.

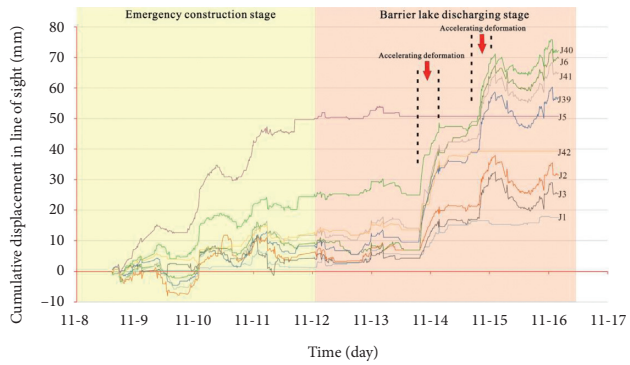

Figure 6: Cumulative apparent deformation-time curve of each target pixel in the K1 area. Note: a positive value represents the deformation target moving away from the radar, slipping or falling. A negative value represents the deformation target moving relatively close to the radar, i.e., being covered by rock-soil accumulation.

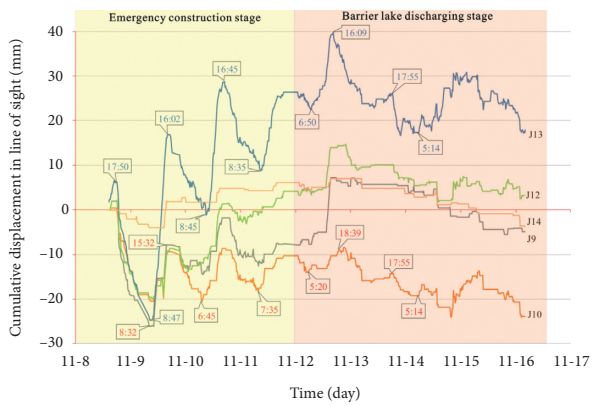

Figure 7: Cumulative apparent deformation-time history (day) curve of each target pixel in the K2 area.

Figures 9 and 10 show the relation curves of the J40 deformation rate and deformation acceleration/time, respectively. As shown in Figure 10, the deformation rate of the slope in the K1 deformation zone is basically 0 mm (15 min) across the whole monitoring period. Oscillations occur within 0.4 mm $(15\,\text{min})^{-1}$, representative of constant deformation characteristics. The curve shown in Figure 11 has a similar constant deformation rate-time curve with a deformation acceleration of approximately 0 mm $(15\,\text{min})^{-2}$. Oscillations have a mean value of approximately 0 at 0.03 mm $(15\,\text{min})^{-2}$. Within this range, again, constant deformation can be observed.

The J13 and J44 target pixels serve as additional examples as they have the largest cumulative deformation in the K2 and K3 areas. Their relation curves of deformation rate and deformation acceleration/time are shown in Figures 11–14. The four curves show similar characteristics to those in the K1 region. The deformation rate and deformation acceleration oscillate up at approximately 0; the amplitude of the deformation rate oscillations is 0.3 $(15\,\text{min})^{-1}$. Within the given range, the amplitude of oscillation of the deformation acceleration is 0.03 mm $(15\,\text{min})^{-2}$. Within this range, the K2 and K3 deformation zones are in a stage of constant deformation.

Before the landslide enters the critical slip stage, the acceleration shows a sharp oscillation. The amplitude of oscillation was limited to a certain range in the 11.03 Baige landslide. The S-SAR monitoring deformation acceleration critical slip warning value can be set according to 0.03 mm $(15\,\text{min})^{-2}$. This value is not fully accurate or unique but can be used to correctly identify any abnormal jumps in acceleration. The value can also be further adjusted as a warning indicator of an impending slide over a longer monitoring period.

4.4. Identification and Prediction of Local Slip Damage in the Deformation Zone. As shown in Figure 15, the velocity-time curve is based on the monitored deformation rate, deformation acceleration-time curve, and real-time dynamic deformation of the area. The acceleration deformation rate of each monitoring station may jump sharply at the same time corresponding to the moment and location of sliding damage; these data can be coupled with the visual surveillance and multiphase UAV aerial image contrast results. The location of target pixels under an impending slide must be reported immediately to headquarters to facilitate early warning. As shown in Figures 9–14, again with target pixels J40, J13, and J44 in the K1, K2, and K3 areas, respectively, as examples with the largest accumulated apparent deformation, 11 possible moments of imminent slip failure were identified (Table 2).

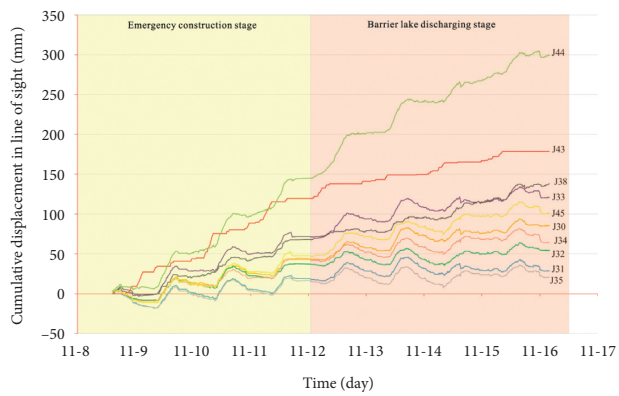

Figure 8: Cumulative apparent deformation-time history (day) curve of each target pixel in the K3 area.

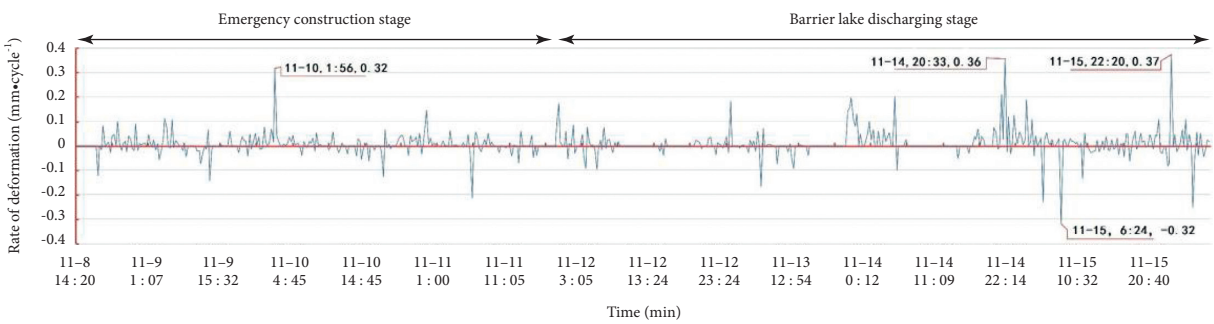

Figure 9: Deformation rate-time curve of K1 region J40. Note: as the above, the positive value indicates that the location of the pixel collapses or falls, and the apparent deformation increases; the negative value indicates that the location of the pixel is covered by the accumulation of rock and soil, and the apparent deformation decreases.

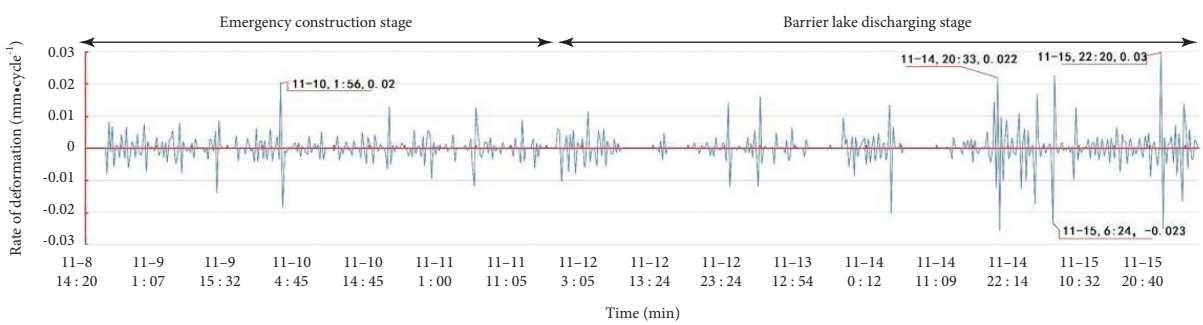

Figure 10: Deformation acceleration-time curve of K1 region J40. Note: a positive value represents an accelerated movement of the target. A negative value represents a decelerated movement of the target.

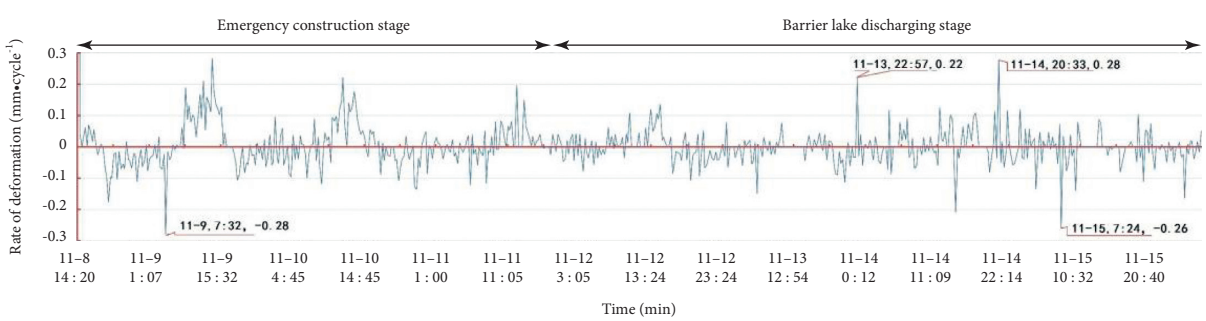

Figure 11: K2 J13 deformation rate-time curve. Rate of deformation: (mm•cycle^{-1}).

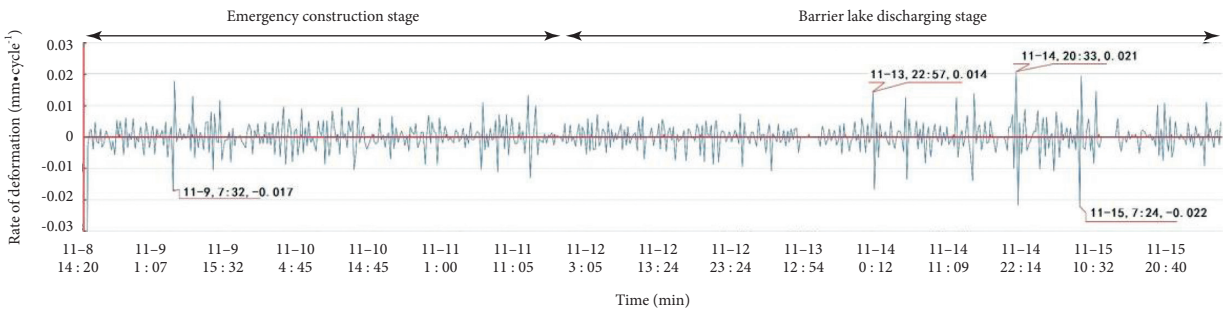

Figure 12: K2 J13 deformation acceleration-time curve.

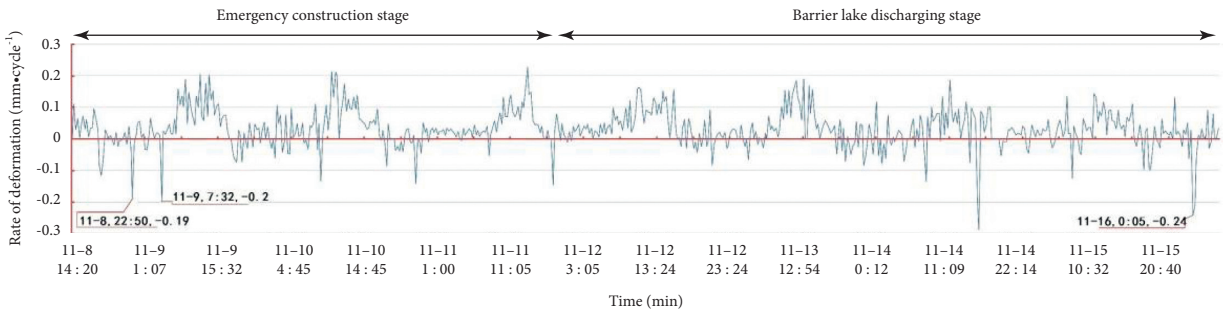

Figure 13: K3 J44 deformation rate-time curve.

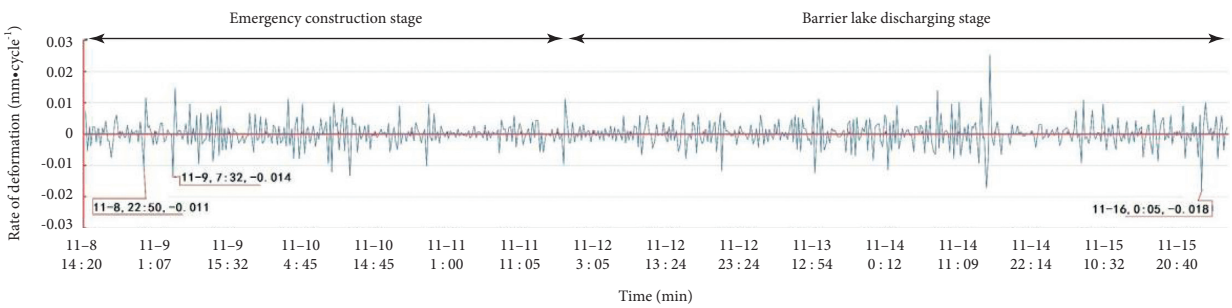

Figure 14: Deformation acceleration-time curve of J44 in the K3 region.

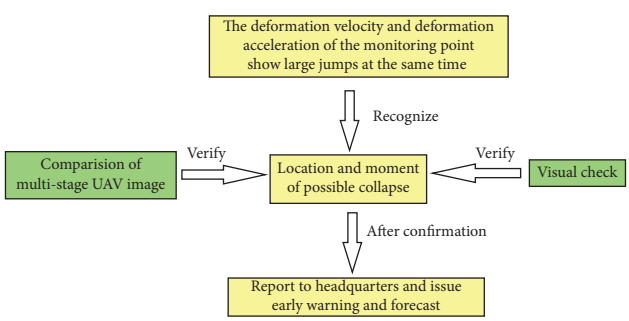

Figure 15: Flowchart of local critical slip failure identification and prediction.

Table 2: Possible locations and moments of imminent slip failure.

Position at which impending slip failure may occur	Moment of impending slip failure	Deformation rate (mm (15 min))	Deformation acceleration (mm (15 min))
J40	November 10, 01:56	0.32	0.02
J40	November 14, 20:33	0.36	0.022
J40	November 15, 06:24	0.32	0.023
J40	November 15, 22:20	0.37	0.03
J13	November 9, 07:32	0.28	0.017
J13	November 13, 22:57	0.22	0.014
J13	November 14, 20:33	0.28	0.021
J13	November 15, 07:24	0.26	0.022
J44	November 8, 22:50	0.19	0.011
J44	November 9, 07:32	0.2	0.014
J44	November 16, 00:05	0.24	0.018

5. Conclusion

On the basis of the field investigation and aerial photograph of the UAV, S-SAR was used in this study to carry out emergency landslide monitoring based on the 11.03 Baige landslide. The results can be summarized as follows:

1. After the 11.03 landslide, several tensile cracks emerged on the platform at the back edge and the left/right boundaries. The stability of the K1, K2, and K3 areas is relatively poor. Local rock falling and collapse of the shallow surface soil occurred during the monitoring period. Beidou displacement metre data indicate that the landslide mass experienced three separate iterations of accelerated deformation before the main sliding body began to slide.
(2) The S-SAR was applied to characterize the strong deformation area. The real-time pixel point cloud deformation map obtained via S-SAR was used to delimit four strong deformation areas in the deformed body. The overall deformation pattern of the K1, K2, and K3 areas was monitored in real time.
(3) Distinct deformation stages across the deformation zone were also effectively assessed in this study to identify an early warning imminent sliding value. The K1, K2, and K3 zones are all in constant deformation stages. The early warning value of acceleration corresponding to an impending landslide, according to the S-SAR data of the 11.03 Baige landslide, is 0.03 mm $(15\,\text{min})^{-2}$.
(4) Local near-slip failure in deformation areas was also predicted effectively in this study. The target pixels and the corresponding time at which the deformation velocity and acceleration sharply jumped were used to determine the points of failure—11 potentially problematic points were identified in total across the study area. Combined with visual monitoring and multiphase UAV aerial image comparison results, this study suggests there is a danger that should be immediately reported to headquarters for the purpose of early warning.

The general advantages, disadvantages, and raw monitoring data of S-SAR and GNSS displacement monitoring systems were comprehensively assessed to find that the S-SAR system provides reliable and suitable information for both emergency and long-term monitoring of geological disasters such as landslides. The S-SAR monitoring time was short, so the conclusions based on the monitoring data are limited. In the future, we will continue to carry out multimeans monitoring on the rock mass of the 11.03 landslide to better understand the deformation patterns and characteristics of the landslide. The deformation and failure mechanism of the Baige landslide also merit further research.

Data Availability

All data, models, and codes generated or used during the study appear in the submitted article.

Conflicts of Interest

The authors declare that they have no conflicts of interest.

Acknowledgments

This project was funded by the China Geological Survey (Grant nos. DD20190640 and 20190505), the Sichuan Provincial Youth Science and Technology Innovation Team Special Projects of China (Grant no. 2017TD0018), the Team Project of Independent Research of SKLGP (Grant no. SKLGP2016Z001), and the National Natural Science Foundation of China (Grant nos. 41702374 and 41772324).

References

[1] J. H. Deng, Y. J. Gao, Z. Q. Yu, and H. Xie, "Analysis on the formation mechanism and process of baige landslides damming the upper reach of Jinsha river, China," *Advanced Engineering Sciences*, vol. 51, no. 1, pp. 9–16, 2019.
[2] M. Saito and M. Uezawa, "Failure of soil due to creep," in *Proceedings of the 5th International Conference on Soil Mechanics and Foundation Engineering*, pp. 315–318, Mexico, North America, 1961.
[3] M. Saito, "Forecasting time of slope failure by tertiary creep," in *Proceedings of the 7th International Conference on Soil Mechanics and Foundation Engineering*, pp. 677–683, Mexico, North America, 1969.

[4] S. Hayashi, F. Komamura, and B.-W. Park, "On the forecast of time to failure of slope," *Landslides*, vol. 24, no. 4, pp. 11–18, 1988, https://doi.org/10.3313/jls1964.24.4_11.

[5] T Fukuzono, "A new method for predicting the failure time of a slope failure," in *Proceedings of the 4th International Conference and Field Workshop on Landslides*, pp. 145–150, 1985, https://doi.org/10.1016/0148-9062(87)91524-5.

[6] T. Fukuzono, "A method to predict the time of slope failure caused by rainfall using the inverse number of velocity of surface displacement," *Landslides*, vol. 22, no. 2, pp. 8–13, 1985, https://doi.org/10.3313/jls1964.22.2_8.

[7] T. Fukuzono, "Recent studies on time prediction of slope failure," *Landslide News*, vol. 4, pp. 9–12, 1990.

[8] T. Li, M. Chen, L. Wang, and Y. Zhou, "Time prediction of landslides using Verhulst inverse-function model," in *Proceedings of the 7th International Symposium on Landslides*, pp. 1289–1293, Trondheim, Norway, 1996.

[9] A. Mufundirwa, Y. Fujii, and J. Kodama, "A new practical method for prediction of geomechanical failure-time," *International Journal of Rock Mechanics and Mining Sciences*, vol. 47, no. 7, pp. 1079–1090, 2010, https://doi.org/10.1016/j.ijrmms.2010.07.001.

[10] B. Voight, "A method for prediction of volcanic eruptions," *Nature*, vol. 332, no. 6160, pp. 125–130, 1988, https://doi.org/10.1038/332125a0.

[11] B. Voight, "A relation to describe rate-dependent material failure," *Science*, vol. 243, no. 4888, pp. 200–203, 1989a, https://doi.org/10.1126/science.243.4888.200.

[12] B. Voight, "Materials science law applies to time forecasts of slope failure," *Landslide News*, vol. 3, pp. 8–11, 1989b.

[13] G. B. Crosta and F. Agliardi, "How to obtain alert velocity thresholds for large rockslides," *Physics and Chemistry of the Earth, Parts A/B/C*, vol. 27, no. 36, pp. 1557–1565, 2002, https://doi.org/10.1016/S1474-7065(02)00177-8.

[14] C. Kilburn, "Precursory deformation and fracture before brittle rock failure and potential application to volcanic unrest," *Journal of Geophysical Research*, vol. 117, no. B2, https://doi.org/10.1029/2011jb008703, Article ID B02211, 2012.

[15] Y. Lavallée, P. G. Meredith, D. B. Dingwell et al., "Seismogenic lavas and explosive eruption forecasting," *Nature*, vol. 453, no. 7194, pp. 507–510, 2008, https://doi.org/10.1038/nature06980.

[16] S. Hao, C. Liu, C. Lu, and D. Elsworth, "A relation to predict the failure of materials and potential application to volcanic eruptions and landslides," *Scientific Reports*, vol. 6, no. 1, Article ID 27877, 2016, https://doi.org/10.1038/srep27877.

[17] K. Chousianitis, V. Del Gaudio, I. Kalogeras, and A. Ganas, "Predictive model of Arias intensity and Newmark displacement for regional scale evaluation of earthquake-induced landslide hazard in Greece," *Soil Dynamics and Earthquake Engineering*, vol. 65, pp. 11–29, 2014, https://doi.org/10.1016/j.soildyn.2014.05.009.

[18] Z. Liu, J. Shao, W. Xu, H. Chen, and C. Shi, "Comparison on landslide nonlinear displacement analysis and prediction with computational intelligence approaches," *Landslides*, vol. 11, no. 5, pp. 889–896, 2014, https://doi.org/10.1007/s10346-013-0443-z.

[19] F. Miao, Y. Wu, Y. Xie, and Y. Li, "Prediction of landslide displacement with step-like behavior based on multialgorithm optimization and a support vector regression model," *Landslides*, vol. 15, no. 3, pp. 475–488, 2018, https://doi.org/10.1007/s10346-017-0883-y.

[20] J. Du, K. Yin, and S. Lacasse, "Displacement prediction in colluvial landslides, three gorges reservoir, China," *Landslides*, vol. 10, no. 2, pp. 203–218, 2013, https://doi.org/10.1007/s10346-012-0326-8.

[21] M. Krkač, D. Špoljarić, S. Bernat, and S. M. Arbanas, "Method for prediction of landslide movements based on random forests," *Landslides*, vol. 14, no. 3, pp. 947–960, 2017, https://doi.org/10.1007/s10346-016-0761-z.

[22] Z. Zou, J. Yan, H. Tang, S. Wang, C. Xiong, and X. Hu, "A shear constitutive model for describing the full process of the deformation and failure of slip zone soil," *Engineering Geology*, vol. 276, 2020 https://doi.org/10.1016/j.enggeo.2020.105766, Article ID 105766.

[23] Q. Wang, M. C. He, S. C. Li et al., "Comparative study of model tests on automatically formed roadway and gob-side entry driving in deep coal mines," *International Journal of Mining Science and Technology*, vol. 31, no. 04, pp. 591–601, 2021, https://doi.org/10.1016/j.ijmst.2021.04.004.

[24] Q. Yin, J. Wu, C. Zhu, M. He, Q. Meng, and H. Jing, "Shear mechanical responses of sandstone exposed to high temperature under constant normal stiffness boundary conditions," *Geomechanics and Geophysics for Geo-Energy and Geo-Resources*, vol. 7, no. 2, p. 35, 2021, https://doi.org/10.1007/s40948-021-00234-9.

[25] C. Zhu, M. C. He, X. H. Zhang, Z. G. Tao, Q. Yin, and L. F. Li, "Nonlinear mechanical model of constant resistance and large deformation bolt and influence parameters analysis of constant resistance behavior," *Rock and Soil Mechanics*, vol. 42, no. 7, pp. 1911–1924, 2021.

[26] L. Lombardi, M. Nocentini, W. Frodella et al., "The Calatabiano landslide (Southern Italy): preliminary GB-InSAR monitoring data and remote 3D mapping," *Landslides*, vol. 14, no. 2, pp. 685–696, 2017, https://doi.org/10.1007/s10346-016-0767-6.

[27] A. Segalini, A. Valletta, and A. Carri, "Landslide time-of-failure forecast and alert threshold assessment: a generalized criterion," *Engineering Geology*, vol. 245, pp. 72–80, 2018, https://doi.org/10.1016/j.enggeo.2018.08.003.

[28] D. Brox and W. Newcomen, "Utilizing strain criteria to predict highwall stability performance," in *Proceedings of the 10th ISRM Congress*, Sandton, South Africa, September 2003.

[29] Q. Xu, Y. Yuan, Y. P. Zeng, and R. Hack, "Some new prewarning criteria for creep slope failure," *Science China Technological Sciences*, vol. 54, no. 1, pp. 210–220, 2011.

[30] A. Cabrejo and N. Harries, "Effective slope monitoring for open cut coal mines," 2012, http://www.acarp.com.au/abstracts.aspx?RepId=C17023.

[31] X. Li, K. Peng, J. Peng, and D. Hou, "Experimental investigation of cyclic wetting-drying effect on mechanical behavior of a medium-grained sandstone," *Engineering Geology*, vol. 293, Article ID 106335, 2021.

[32] X. S. Li, K. Peng, J. Peng, and H. Xu, "Effect of cyclic wetting-drying treatment on strength and failure behavior of two quartz-rich sandstones under direct shear," *Rock Mechanics and Rock Engineering*, 2021, https://doi.org/10.1007/s00603-021-02583-z.

[33] E. Intrieri, F. Raspini, A. Fumagalli et al., "The Maoxian landslide as seen from space: detecting precursors of failure with Sentinel-1 data," *Landslides*, vol. 15, no. 1, pp. 123–133, 2018, https://doi.org/10.1007/s10346-017-0915-7.

[34] T. Carlà, P. Farina, E. Intrieri, H. Ketizmen, and N. Casagli, "Integration of ground-based radar and satellite InSAR data for the analysis of an unexpected slope failure in an open-pit mine," *Engineering Geology*, vol. 235, pp. 39–52, 2018, https://doi.org/10.1016/j.enggeo.2018.01.021.

[35] N. D. Rose and O. Hungr, "Forecasting potential rock slope failure in open pit mines using the inverse-velocity method," *International Journal of Rock Mechanics and Mining Sciences*, vol. 44, no. 2, pp. 308–320, 2007, https://doi.org/10.1016/j.ijrmms.2006.07.014.

[36] T. Carlà, P. Farina, E. Intrieri, K. Botsialas, and N. Casagli, "On the monitoring and early-warning of brittle slope failures in hard rock masses: examples from an open-pit mine," *Engineering Geology*, vol. 228, pp. 71–81, 2017, https://doi.org/10.1016/j.enggeo.2017.08.007.

[37] G. J. Dick, E. Eberhardt, A. G. Cabrejo-Liévano, D. Stead, and N. D. Rose, "Development of an early-warning time-of-failure analysis methodology for open-pit mine slopes utilizing ground-based slope stability radar monitoring data," *Canadian Geotechnical Journal*, vol. 52, no. 4, pp. 515–529, 2015, https://doi.org/10.1139/cgj-2014-0028.

[38] Q. Xu, G. Zheng, W. L. Li et al., "Study on successive landslide damming events of Jinsha River in Baige village on Octorber 11 and November 3,2018," *Journal of Engineering Geology*, pp. 1534–1551, 2018.

[39] X. Zheng, X. Yang, H. Ma et al., "Integrated ground-based SAR interferometry, terrestrial laser scanner, and corner reflector deformation experiments," *Sensors*, vol. 18, no. 12, Article ID 4401, 2018, https://doi.org/10.3390/s18124401.

[40] X. Li, Q. Xu, and R. Huang, "Research on prediction criterion for temporary prediction of landslide," *Chinese Journal of Geological Hazard and Control*, pp. 5–11, 2003.

[41] Q. Wang, Y. Wang, M. C. He et al., "Experimental research and application of automatically formed roadway without advance tunneling," *Tunnelling and Underground Space Technology*, vol. 114, Article ID 103999, 2021, https://doi.org/10.1016/j.tust.2021.103999.

[42] Q. Xu, Y. P. Zeng, J. P. Qian, and C.-J. Wang, "Study on a improved tangential angle and the corresponding landslide pre-warning criteria," *Geological Bulletin of China*, pp. 501–505, 2009.

Hindawi
Mathematical Problems in Engineering
Volume 2021, Article ID 8549094, 16 pages
https://doi.org/10.1155/2021/8549094

Research Article

Development and Application of the 3D Model Test System for Water and Mud Inrush of Water-Rich Fault Fracture Zone in Deep Tunnels

Yanhui Guo,[1] **Zhijun Kong**,[2] **Jin He**,[2] **and Ming Yan**[1]

[1]*Faculty of Public Safety and Emergency Management, Kunming University of Science and Technology, Kunming 650093, China*
[2]*College of Civil and Architectural Engineering, Yunnan Agricultural University, Kunming 650201, China*

Correspondence should be addressed to Yanhui Guo; guoyanhui0818@kust.edu.cn

Received 12 August 2021; Accepted 15 September 2021; Published 4 October 2021

Academic Editor: Gan Feng

In order to study the evolution process, damage characteristics, and occurrence mechanism of water and mud inrush disaster in deep tunnel fault zone with infiltration instability under complex conditions, a set of the three-dimensional physical model test systems of water and mud inrush flow-solid coupling in tunnel fault zones is developed. The system mainly comprises a rigid test frame, ground stress loading system, hydraulic loading system, multiple information monitoring and acquisition system, and mud and water protrusion recovery system. The system's main features are that it can meet the model's simulation of the ground stress field, water pressure, and other complex environments subjected to ground stress, and water pressure gradients can be controlled. The system is characterized by high rigidity, high-pressure strength, visualization, good sealing, and expandability. Taking the water fault zone of a well in the Dazhu Mountain Tunnel of the Darui Railway as the research object, the new fault zone and surrounding rock similar materials applicable to the flow-solid coupling model test are designed using the self-developed flow-solid coupling similar materials. The system is used for model tests to reveal the spatial and temporal changes of the surrounding rock stress field and seepage field during the tunnel excavation process. The test results show that the system is stable and reliable, and the research method and results are of guiding significance to the research of the same type of underground engineering.

1. Introduction

In recent years, China has developed into a country with the most significant number of tunnels and underground projects, the enormous scale, the most complex geological conditions, and the most diverse structural forms in the world [1–3]. More and more transportation infrastructure projects are shifting to the western mountainous and karst areas with a more complex topography and geological conditions. Tunnel construction faces new challenges, such as considerable buried depth, high ground stress, strong karst, high-water pressure, and complex structures [4–7], resulting in frequent disasters during the construction process. Statistics show that nearly 80% of traffic, water conservancy, and hydropower projects have experienced water and mud inrush disasters during the construction or operation. As a result, nearly 90% of the tunnels have been postponed or even forced to be suspended or rerouted, especially in areas with solid karst and high-water pressure; frequent geological disasters such as tunnel water bursting and mud bursting have brought great difficulties to construction, causing heavy casualties and economic losses [8–10].

Because of the main problems of high ground stress and high-water pressure in the construction of karst tunnels, it is essential to master the spatial and temporal changes of the surrounding rock stress field, displacement field, and seepage field during the tunnel excavation in such complex geological conditions to effectively prevent water and mud burst disasters and improve the stability of the tunnel surrounding rock. Due to the complexity of such tunnels' surrounding rock structure and environment, we should adopt various means to study them as far as possible, and the main research methods are theoretical analysis, numerical

calculation, and model test [11–17]. However, theoretical analysis has many limitations in dealing with nonlinear and discontinuous problems of complex rock masses. In contrast, numerical analysis methods cannot accurately portray the mechanical properties of the surrounding rock masses in terms of intrinsic model and calculation parameters selection and have inherent deficiencies in simulating the engineering response under complex conditions [18–20]. The geomechanical model test makes up for the shortage of theoretical analysis and numerical simulation. It can systematically and comprehensively reflect the characteristics of the surrounding rock and its spatial relationship with karst pipes and caves, more accurately simulate the tunnel excavation process, and visually reflect the physical and mechanical phenomena of the deep rock mass, which is a proven research tool [21, 22].

At present, the relevant research on geomechanical model test system device mainly includes the following: Zhu et al. [23] developed an extensive accurate triaxial loading geomechanical model test system, which can carry out horizontal lateral step load under entire triaxial stress state and successfully observe the fracture phenomenon and fracture process of surrounding rock of caverns with different large buried depths, which is helpful to the study of fracture mechanism; Zhang et al. [24] developed a model test system for water and mud inrush in fault fracture zone and studied the catastrophic evolution process and failure characteristics of water and mud inrush in tunnel during fault exposure; Li et al. [25–28] developed a new fluid-structure coupling model test system, which can be used for plane stress and plane strain model tests, and revealed the variation laws of surrounding rock displacement field, seepage field, and tunnel wall pressure during tunnel excavation; Li et al. [29, 30] developed a three-dimensional model test system for water inrush geological disasters in deep and long tunnels and obtained the minimum water separation safety thickness under different engineering conditions; Zhang [31] developed an ultrahigh-pressure 3D loading model test system with intelligent numerical control function, which revealed the collapse failure mode, nonlinear deformation characteristics, and stress change law of ancient karst cave formation. To sum up, there is a relative lack of geomechanical model tests related to water and mud inrush disasters in tunnels in fault fracture zones. There are mainly the following problems to be solved when using the above model test system to study water and mud inrush disasters in fault fracture zones: (1) The model size is small, it is impossible to carry out large-scale tests, and there is an apparent boundary effect. (2) Most of them focus on the stability of surrounding rock during tunnel excavation under the action of in situ stress, without considering the catastrophic evolution process of rock mass in fault fracture zone under the combined action of groundwater and excavation disturbance. (3) There are few studies on similar materials of filling medium in the fault fracture zone. At present, most of the fluid-solid coupling similar materials only consider physical indexes such as density and size, and few similar materials meet solid mechanical properties and permeability [32–35]. Less similar materials with different characteristics of surrounding rock and fault rock are applied to the same test simultaneously.

The test system of this study is mainly composed of a rigid test frame, in situ stress loading system, hydraulic loading system, multivariate information monitoring and acquisition system, and mud and water protrusions recovery system. The system's main feature is that it can meet the model's simulation of the complex environment such as in situ stress field and water pressure. The in situ stress and water pressure gradient are controllable. The system has significant stiffness, high bearing strength, visualization, good sealing, and strong expansibility. Taking the Yijingshui fracture zone of the Dazhu Mountain Tunnel of Darui railway as the research object, using the self-developed fluid-structure coupling similar material, a new fault fracture zone and surrounding rock that are suitable for fluid-structure coupling model test are designed in this paper. The system is used for model tests to reveal the surrounding rock stress field's temporal and spatial variation laws and seepage field during tunnel excavation.

2. Development of a 3D Model Test System for Water and Mud Inrush in Tunnel Fault Fracture Zones

The model test system is mainly composed of a rigid test frame, a ground stress loading system, a hydraulic loading system, a muddy water protrusion recovery system, and multiple information monitoring and acquisition systems. The test system has the advantages of significant stiffness, visualization, easy operation, and wide application. It can realize the study of the disaster mechanism of water inrush and mud inrush through tunnel monitoring data collection and multi-information analysis at each stage of the test process.

2.1. Model Rigid Test Stand. Figure 1 is the main body of the model rigid test frame. The test frame is seamlessly welded by a 1.2 cm thick steel plate, and the base is made of an I-beam of 0.5 cm thickness. Small holes are evenly opened on the brackets on both sides of the box to play a role in fixing and adjusting the height of the reaction frame. Other structures such as plexiglass and stiffened rib plates on the front and back sides of the box are connected by flanges, while waterproof treatment is done around.

In the experiment, the function of the pressure uniformly distributed plate is mainly to convert the concentrated force exerted by the jack on the plate into a uniformly distributed force and apply it to similar materials. The pressure uniform plate is designed with double handles, with a length of 98 cm and a width of 47 cm, which are slightly smaller than the internal dimensions of the test frame, which facilitates the lead-out of the sensor wires and water supply pipes. The design of the reaction force frame is 100 cm in length, 30 cm in width, and 15 cm in height. It is fixed on the test frame, and the position can be adjusted flexibly.

Figure 1: Main structure of the test frame.

2.2. Ground Stress Loading System. The ground stress loading system is composed of a separated hydraulic jack, hydraulic pump, pressure gauge, etc. Before system assembly, the in situ stress to be supplemented by the loading system shall be determined according to the geometric similarity ratio, stress similarity ratio, simulated surrounding rock bulk density, and actual buried depth of the test model. Combined with the area of the bearing area of the model, the real force to be applied can be calculated, and the measuring range of the jack top can be determined on this basis. Considering that the subsequent simulation test of water and mud inrush disaster, the movable position of reaction frame, and the filling height of materials during the test may be carried out for the deeper buried tunnel, the tonnage of separated hydraulic jack is 20 t, the stroke of piston rod is 10 cm, and the inner diameter of oil cylinder is 6.4 cm. The conversion relationship between supplementary in situ stress and pressure gauge reading is as follows [36, 37]:

$$\sigma_1 = \frac{\sigma_2 S}{10.24\pi}. \tag{1}$$

Among them, σ_1 is the pressure gauge reading; σ_2 is the ground stress to be added to the test; and S is the area of the model pressure zone.

2.3. Water Pressure Loading System. The hydraulic loading system is mainly composed of a gas-liquid composite constant pressure water tank, a high-pressure nitrogen cylinder, and auxiliary equipment, as shown in Figure 2. The constant pressure water tank is made of stainless steel and can withstand a pressure of 0.3 MPa. There are three holes on the top of the water tank: the water inlet, the air inlet, and the pressure gauge interface. The bottom of the water tank is the water outlet. The air inlet of the water tank is connected to a high-pressure nitrogen cylinder through a hose, and the water outlet is connected to a water outlet through a rubber tube with an inner diameter of 12 mm to provide water for the model. The volume of the high-pressure nitrogen cylinder is 40 L, and the gas pressure in the bottle is about 13 MPa. In order to meet the pressure required by the test, a pressure-reducing valve is arranged at the gas outlet to reduce the output pressure in the bottle, thereby providing a stable air pressure source.

2.4. Multivariate Information Monitoring and Acquisition System. The multi-information monitoring and acquisition system includes monitoring components and data acquisition systems. The monitoring components used in the test mainly include micro earth pressure box, pore water pressure sensor, displacement meter, high-definition filming instruments, and others, which monitor the signals of surrounding rock stress, pore water pressure, displacement, and macro process of surrounding rock from fracture generation to water and mud emergence through the tunnel excavation process and hydraulic loading process, respectively. The earth pressure cell used for monitoring is a DMTY earth pressure cell, with a measuring range of 500 kPa, a specification of 28×10 mm, a sensitivity coefficient of 0.256~0.270 kPa/$\mu\varepsilon$, a full bridge connection, and a bridge resistance of 350 Ω. The self-contained line includes two power lines. Moreover, two signal lines can work in the water-saturated medium. The element for monitoring pore water pressure is the DMKY pore water pressure sensor produced by the same company, with a range of 200 kPa, a specification of 32×15 mm, and a sensitivity coefficient of 0.100~0.106 kPa/$\mu\varepsilon$. Working at 120% of the rated range, the miniature sensor used in the test is shown in Figure 3.

The data acquisition system includes strain gauges and data acquisition software, as shown in Figure 4. According to the number of embedded sensors, select the XL2118A24 static resistance strain gauge. This model has 24 data acquisition channels, measuring stress, strain, force, and other physical quantities. The operating mode of the instrument has two kinds of automatic control of the machine and external control of the computer. When using external computer control, as long as the USB connection line equipped with the instrument is used to connect the strain gauge with the computer equipped with this type of data acquisition software and set the sensor's parameters, the real-time data acquisition can be realized.

2.5. Muddy Water Protrusion Material Recovery System. The mud and water protrusion recovery system includes a 0.2 mm diameter cylindrical filter sieve, a water sealing ring, a 0.03 mm diameter cylindrical filter sieve, a transparent plastic panel, a water storage container, a capacity scale plate, a wheel bracket, a positioning scale, and a water outlet. The water seal ring is set at the connection of each layer of filter sieve, the transparent plastic panel is installed on the sidewall of the cylindrical filter sieve with 0.03 mm particle size, and the bottom of the water storage container is rounded. The

(a) (b)

Figure 2: Gas-liquid composite constant pressure water tank and high-pressure nitrogen cylinder. (a) Constant pressure water tank. (b) High-pressure nitrogen cylinder.

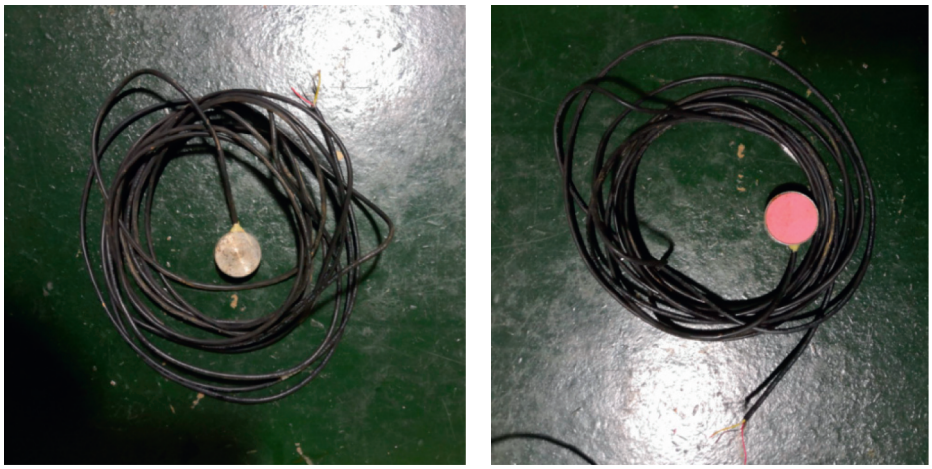

(a) (b)

Figure 3: Microsensor. (a) Earth pressure box. (b) Pore water pressure sensor.

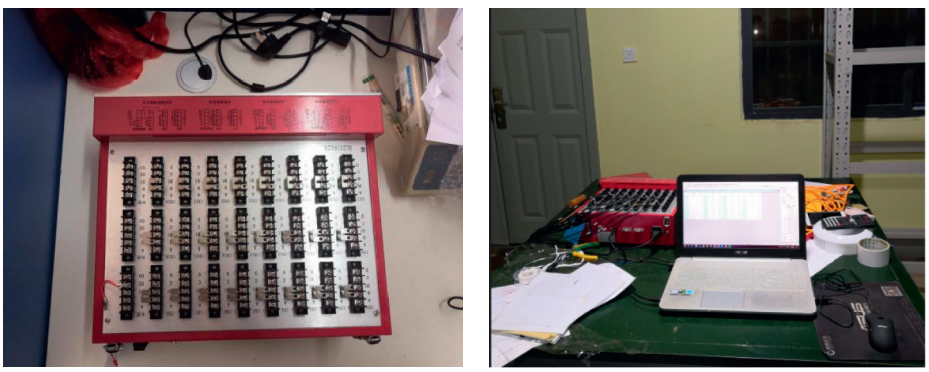

(a) (b)

Figure 4: Data acquisition system. (a) Static resistance strain gauge. (b) Data acquisition instrument.

capacity scale plate is located on the sidewall of the water storage container, and the water outlet is installed at the lowest point of the water storage container. The retractable wheel bracket is located at the bottom of the water storage container, and the positioning scale can adjust the level and height of the mud and water protrusion recovery system.

The tunnel water and mud inrush fluid-solid coupling 3D visualization physical model test system is shown in Figure 5.

Figure 5: Tunnel water and mud inrush fluid-solid coupling 3D visualization physical model test system.

3. Model Test of Water and Mud Inrush in the Tunnel Fault Fracture Zone

3.1. Project Overview. The Dazhu Mountain Tunnel of the Darui Railway is located in Baoshan City, Yunnan Province, crossing the southern section of the famous Hengduan Mountains in western Yunnan Province, starting and ending at mileage D2K110 + 524~ D2K125 + 008, with a total length of 14484 m, of which 13803 m is the length of the single tunnel line main cavern; 680 m is the large span section area; and the maximum depth of the tunnel is 995 m. The longitudinal slope of the tunnel is designed as a small "man" character slope, except for the exit section 2750 m for 3% uphill, other sections of the maximum longitudinal slope of 23.5%, and the overall terrain north high south low.

As shown in Figure 6, the tunnel's area has a complex geological environment and well-developed fault structures. It has traversed six faults, including Wulishao, Yanzi's Nest, Shuizhai, Yijingshui Fault, Shiguandi Fault, and Banjiazhai as well as the Jinjiashan syncline, and there are threefold structures including Yangjiashan inverted anticline and five karst areas. The Dazhu Mountain Tunnel is rich in groundwater. According to the relationship between the excavated water volume and the designed water volume of the revealed section, it is estimated that the maximum water inflow of the tunnel can reach three times the original design, that is, 360000 m^3/d. Since the start of the Dazhu Mountain Tunnel, the tunnel has suffered deep water and mud inrush disasters, with about 200 million m^3 of water gushing, which is equivalent to 15 West Lakes. This paper chooses the IV grade weak surrounding rock, which accounts for about 30% of the main tunnel of the Dazhu Mountain Tunnel, as the prototype of the similar model test surrounding rock, and the geometric dimensions of the excavation section (width 6.16 and height 9.41 m) of the surrounding rock of the tunnel are used as the model, a prototype of excavation section size.

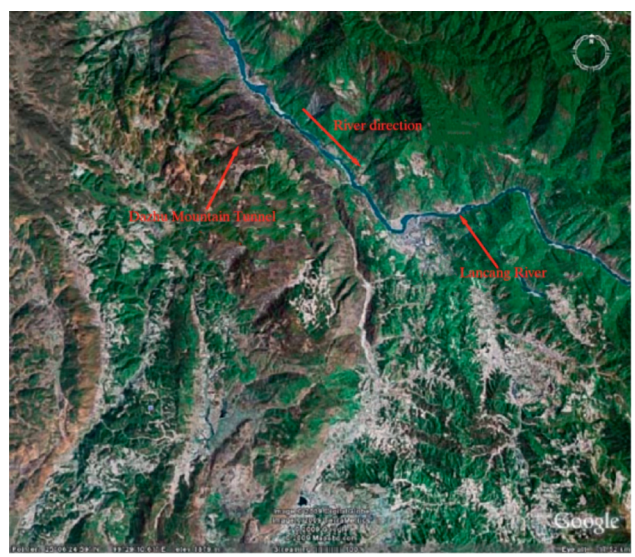

Figure 6: Topographic map of the Dazhu Mountain Tunnel.

3.2. Fluid-Structure Coupling Similarity Theory. When conducting similar model tests, the model and prototype should be made to satisfy similar geometry, dynamics, and physics relationships between materials or media [38]. However, due to the objective conditions, it is impossible to achieve complete similarity between the model and the prototype, and it is often necessary to perform a similar transformation of the model.

The ratio of the same physical quantity between the prototype (P) and the model (M) in the similar model test is called the similarity ratio (C), and the mathematical expression between the three is [39]

$$C_x = \frac{X_P}{X_M}. \tag{2}$$

X is the similar physical quantities, including geometry l, capacitance γ, stress σ, compressive strength σ_c, tensile strength σ_t, strain ε, cohesion c, internal friction angle ψ, Poisson's ratio μ, and permeability coefficient k.

According to the similarity theory of fluid-solid coupling, the mathematical model of fluid-solid coupling in continuous media is used, and the seepage equation, equilibrium equation, and effective stress equation can be expressed as follows [40–42].

Seepage equation is

$$K_x\frac{\partial^2 p}{\partial^2 x}+K_y\frac{\partial^2 p}{\partial^2 y}+K_z\frac{\partial^2 p}{\partial^2 z}=S\frac{\partial p}{\partial t}+\frac{\partial e}{\partial t}+W. \quad (3)$$

Equilibrium equation is

$$\sigma_{ij,i}+X_j=\rho\frac{\partial^2 u_i}{\partial t^2}. \quad (4)$$

Effective stress equation is

$$\sigma_{ij}=\overline{\sigma_{ij}}+\alpha\delta p, \quad (5)$$

where K_x, K_y, and K_z are the permeability coefficients in the x, y, and z directions, respectively; P is the water pressure; S is the water storage coefficient; e is the volume strain; W is the source-sink term; σ_{ij} is the total stress tensor; $\overline{\sigma_{ij}}$ is the effective stress tensor; X_j is the volume force; ρ is the density; α is the bolt effective stress coefficient; and δ is the Kronecker notation.

Assume that the similarity ratio of each parameter of the prototype (P) and the model (M) is

$$\begin{cases} G_P=C_G G_M;\ E_P=C_E E_M;\ x_P=C_x x_M, \\ \lambda_P=C_\lambda\lambda_M;\ e_P=C_e e_M;\ U_P=C_U U_M, \\ X_P=C_X X_M;\ \rho_P=C_\rho\rho_M;\ t_P=C_t t_M. \end{cases} \quad (6)$$

From equation (6),

$$\begin{cases} \dfrac{\partial e_P}{\partial x_P}=\dfrac{C_e}{C_x}\dfrac{\partial e_M}{\partial x_M}, \\ \nabla^2 u_P=\dfrac{C_u\nabla^2 u_M}{C_x^2}, \\ \dfrac{\partial^2 u_P}{\partial t_P^2}=\dfrac{C_u}{C_t^2}\dfrac{\partial u_P}{\partial t_M^2}. \end{cases} \quad (7)$$

Combining equation (3) with its geometric equation and physical equation, the equation containing only the displacement component is obtained as

$$\begin{cases} G\nabla^2 u+(\lambda+G)\dfrac{\partial e}{\partial x}+X=\rho\dfrac{\partial^2 u}{\partial t^2}, \\ G\nabla^2 v+(\lambda+G)\dfrac{\partial e}{\partial y}+Y=\rho\dfrac{\partial^2 v}{\partial t^2}, \\ G\nabla^2 w+(\lambda+G)\dfrac{\partial e}{\partial z}+Z=\rho\dfrac{\partial^2 w}{\partial t^2}, \end{cases} \quad (8)$$

where $\nabla^2=\partial^2/\partial x^2+\partial^2/\partial y^2+\partial^2/\partial z^2$ is the Laplace operator symbol; $\lambda=\mu E/[(1+\mu)(1-2\mu)]$ is the Lamé constant; E is the modulus of elasticity; μ is the Poisson ratio; $G=E/(2(1+\mu))$ is the shear modulus of elasticity; $e=\partial/\partial x^2+\partial/\partial y^2+\partial/\partial z^2$ is the volume strain; and X, Y, and Z are the volume forces in the x, y and z directions, respectively.

It can be obtained by formulas (6)–(8):

$$C_G\frac{C_u}{C_x^2}=C_\lambda\frac{C_e}{C_x}=C_G\frac{C_e}{C_x}=C_X=C_\rho\frac{C_u}{C_t^2}, \quad (9)$$

where C_G is the shear elastic modulus similar ratio, C_u is the displacement similar ratio, C_x is the geometric similar ratio, C_λ is the Lamé constant similar ratio, C_e is the volume strain similar ratio, C_X is the volume weight similar ratio, C_ρ is the density similar ratio, and C_t is the time similar ratio.

According to seepage equation (3), considering that the similar test material is a uniform continuous medium, let $K_x=K_y=K_z=K$ and introduce the function

$$\begin{cases} K_P=C_K K_M, \\ K_S=C_S S_M;\ Q_P=C_Q Q_M, \\ y_P=C_y y_M;\ z_P=C_z z_M. \end{cases} \quad (10)$$

Here, $C_x=C_y=C_z=C$; substituting formula (10), then

$$\frac{C_K C_P}{C_x^2}=\frac{C_K C_P}{C_y^2}=\frac{C_K C_P}{C_z^2}=\frac{C_S C_P}{C_t}=\frac{C_e}{C_t}=C_w. \quad (11)$$

Here, C_P is the water pressure similarity ratio, C_t is the time similarity ratio, and C_w is the source-sink term similarity ratio.

Because $C_e=1$, $C_P=C_\gamma C_l$, $C_t=\sqrt{C_l}$, and $C_l=C_x=C_y=C_z$, it can be deduced that the source and sink terms are similar $C_w=1/\sqrt{C_l}$, the water storage coefficient is similar $C_S=1/(C_\gamma\sqrt{C_l})$, and the permeability coefficient is similar $C_K=\sqrt{C_l}/C_\gamma$.

3.3. Model Test Similarity Ratio. The geometric similarity ratio is $C_l=80$ selected according to the size of the test frame of the tunnel water and mud inrush model test system, the peak pressure provided by the loading system, and the actual situation of the model test object. The bulk density similarity ratio is $C_\gamma=1.2$ as the primary similarity ratio, and the prototype and model can be derived from the similarity theory. The other physical and mechanical parameters and hydraulic property parameters are similar to the following examples:

Dimensionless similarity (Poisson's ratio, strain, and internal friction angle): $C_\mu=C_\varepsilon=C=1$.

Similarity ratio of elastic modulus, stress, strength, and cohesion: $C_E=C_\sigma=C_R=C_c=C_\gamma C_l=96$.

Permeability coefficient similarity ratio: $C_K=\sqrt{C_l}/C_\gamma=7.45$.

3.4. Proportioning Selection of Similar Materials for Fluid-Solid Coupling in the Model Test. Taking the Dazhu Mountain Tunnel Engineering of the Darui Railway as the research background, a large amount of grade IV weak surrounding rock and the corresponding excavation section size existing in the tunnel construction are used as the basis of the model test. According to the physical and mechanical parameters of the grade IV surrounding rock in the study area, combining fluid-solid coupling similarity theory and

model test research, the similarity ratios of physical and mechanical parameters and hydraulic properties of similar materials are obtained, and the parameters of surrounding rock under ideal conditions are obtained, as shown in Table 1.

According to the test results of similar material parameters of each ratio and the ideal material, comparison can be obtained from the best ratio of similar materials for the surrounding rock of the tunnel water and mud inrush model test. The finalized similar material ratio is shown in Table 2. When the content of red clay is 6.35%, that is, the ratio of mountain sand : red clay : cement : water is equal to 12 : 0.95 : 0.7 : 1.3, the physical and mechanical parameters and hydraulic properties of similar materials in the surrounding rock are close to those of the similar ideal materials; specifically, the material capacity is between the ideal material capacity, while the material compressive strength and permeability coefficient differ from the similar ideal materials in the range of 1.01%~2.46%. The difference between the compressive strength and permeability coefficient of the material and the similar ideal material ranges from 1.01% to 2.46%, indicating that the ratio of similar material can better meet the requirements of the surrounding rock material in the model test. A similar material of fault zone was selected as the solution with the lowest permeability coefficient among the ratios, that is, 1 : 1 : 0.4 for red clay : sand : gravel, and the material permeability coefficient was 5.39×10^{-4} cm/s.

3.5. The Overall Plan Design of the Experiment. According to the geometric similarity ratio of the model test and the size of the excavation section of the prototype, the model test tunnel has a section width of 7.7 cm and a height of 11.76 cm. The interlaced distance between the filling fault and the tunnel designed by the experiment is twice the hole diameter, the interlacing angle is 60°, the fault thickness is 12.5 cm, and the inclined extension length is 18.75 cm. The corresponding actual thickness and length are 10 m and 15 m, respectively, buried in the upper part of the fault. The water outlet device provides stable water pressure for the fault and is used to simulate the high-pressure and water-rich faults encountered in tunnel construction. The test simulates the buried depth of the tunnel 500 m, and the filling height of similar materials in the rigid test box is about 92 cm, which is 40 cm higher than the tunnel vault. Since the ground stress provided by the filling material does not meet the requirements of the model test, additional supplements must be made through the ground stress loading system. The vertical stress is about 106 kPa, and the stress reaches a predetermined value through stepwise loading.

After the in situ stress loading is completed and the material deformation is stable, draw the tunnel excavation contour line at the reserved excavation position using the wooden tunnel section made with a ratio of 1 : 1 and carry out the tunnel excavation. The test adopts the full-section excavation method. Data collection is performed simultaneously as the excavation, and the excavation is stopped after the excavation length reaches 42 cm. Then turn on the water pressure loading system to supply water to the fault. The water pressure loading adopts a step-by-step pressurization method. The initial water pressure is 10 kPa, and the subsequent increase is 5 kPa (when the software monitoring data is stable, it can continue to be loaded to the lower water pressure); until the water and mud inrush occurs in the tunnel, the test is deemed to be over.

3.6. Monitoring Arrangement. Using model tests to study the disaster mechanism of tunnel filling-type fault water and mud inrush is mainly realized by analyzing the monitoring data obtained during the test. Before the test, the monitoring section, monitoring points, and corresponding monitoring elements should be selected scientifically and reasonably according to the test purpose and test requirements so that the data collected by the test can accurately and comprehensively reflect the surrounding rock and fault filling during the evolution of the tunnel water and mud inrush. The dynamic change characteristics of objects can also achieve the purpose of reducing monitoring costs.

In order to study the change law of multiple information such as surrounding rock and fault stress and seepage pressure during the model test, the central monitoring components of the test include earth pressure box and pore water pressure sensor. Along the tunnel excavation direction, the test designed a total of 2 monitoring sections, which were set at 1/2 position ($Y = 25$ cm) and 3/4 position ($Y = 29.69$ cm) in the direction of fault tendency. Monitoring section 1 has earth pressure boxes and pore water pressure sensors arranged around the tunnel, one time the diameter and two times the tunnel's diameter. The primary function of the earth pressure boxes is to monitor the changes in the surrounding rock stress during tunnel excavation and water pressure loading. The pore water pressure gauge is used to monitor the seepage pressure information of the antioutburst rock mass between the tunnel and the fault. Three earth pressure boxes are arranged on the monitoring section 2, which correspond to the placement of the pore water pressure gauges on the monitoring section 1, which are used to monitor the stress changes of the antioutburst rock mass between the tunnel and the fault. The overall monitoring plan is shown in Figure 7.

3.7. Model Filling. In order to meet the requirements of compactness and uniformity of the model body, this test uses layered filling and layer-by-layer compaction. The model filling process is shown in Figure 8. The specific steps are as follows:

(1) Before filling the materials, embed five prefabricated glass plates into the high-strength plexiglass opening positions at the front and rear of the rigid test frame (excluding the holes at the reserved tunnel excavation positions), and contact the plates with the glass. Apply glass glue to seal the part, then wrap the edge of the prefabricated wooden board with double-sided tape, and embed it in the hole at the tunnel excavation position on the plexiglass (for easy removal of the wooden board during excavation). After

Table 1: Surrounding rock prototype and ideal similar material parameters.

Material type	Bulk density, γ/kN/m^3	Compressive strength, σ/MPa	Permeability coefficient, k/cm/s
Raw rock	20~23	38	4.23×10^{-4}
Ideal similar material	16.67~19.17	0.396	5.68×10^{-5}

Table 2: Ratio and performance parameters of similar materials for surrounding rock.

Similar material ratio	Bulk density, γ/kN/m^3	Compressive strength, σ/MPa	Permeability coefficient, k/cm/s
12 : 0.95 : 0.7 : 1.3	18.16	0.40	5.54×10^{-5}

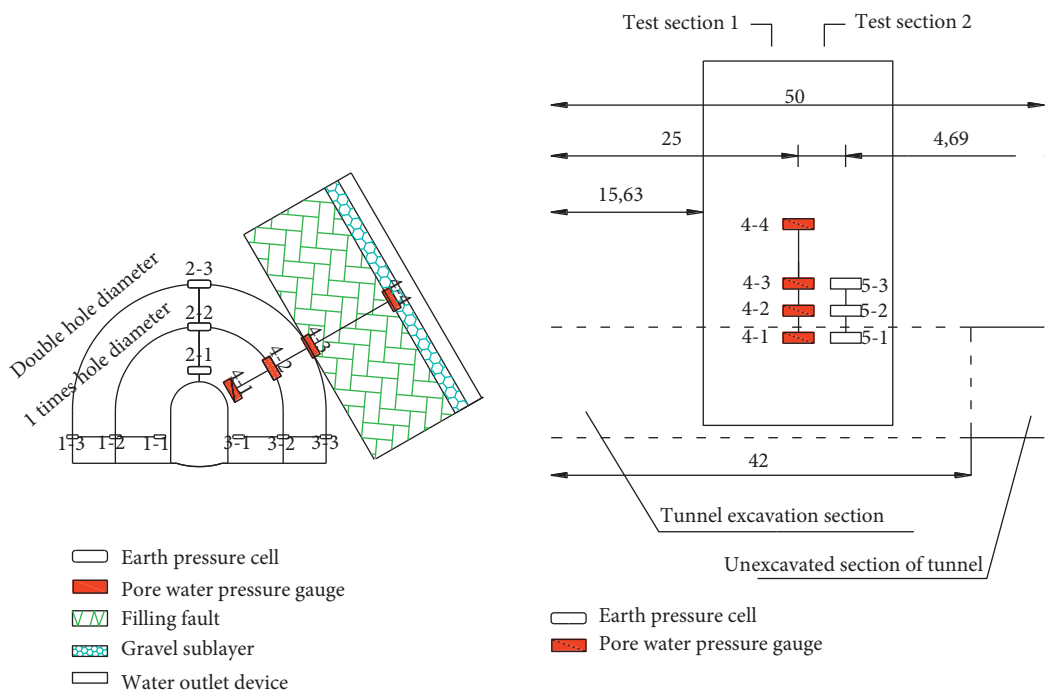

Figure 7: Design of the monitoring scheme.

(a) (b) (c)

Figure 8: Continued.

Figure 8: Model body production process. (a) Embedded glass panel. (b) Filling materials. (c) Layer compaction. (d) Mold positioning. (e) Embedded monitoring elements. (f) Molding. (g) Filling fault buried water pipe. (h) Install reaction frame and jack. (i) Hydraulic loading.

completion, put six pieces in front and back. The stiffening ribs are connected to the test frame by bolts.

(2) Screen the raw materials required for the test, weigh the screened materials according to the selected similar material ratio, and weigh 120.4 kg of mountain sand, 9.5 kg of red clay, and 7.02 kg of cement each time and pour them into the mixer for mixing. After stirring evenly, pour in weighed 13.1 kg of water and stir for about 20 minutes.

(3) Spread the mixed similar material in layers from bottom to top in the rigid test box, and then pound it manually. When the filling reaches the designed fault position, the prefabricated fault mold is positioned by tape measure, protractor, and other instruments and then continue to fill the similar material and compact the fixed mold.

(4) When the height of material filling exceeds the height of the buried monitoring element, the monitoring element is buried at the designated position, and then the similar material is backfilled into the recess and compacted. All data lines are finally led uniformly from the gap position between the pressure equalization plate and the box.

(5) When the material filling height reaches the design height of the fault, take out the mold and fill it with similar materials and gravel layers in sequence, bury the water outlet device, then continue to fill similar materials to the total design height, and scrape the top surface of the model body. After leveling, press the reaction frame and jack, place the pressure uniform plate on the top surface of the compacted and flattened model body, and finally load it to the initial ground stress step by step using a stepwise loading method.

3.8. Model Excavation and Testing. After the model was deformed and stabilized, start to excavate the tunnel. Debug the test system before excavation, remove the stiffening ribs and planks at the tunnel excavation position, use the prepared tunnel excavation control mold to draw the tunnel excavation contour line at the excavation site, and carry out the tunnel excavation (as shown in Figure 9). Excavation simultaneously collects surrounding rock stress change data.

After the tunnel excavation is completed, use the hydraulic loading system to load the water pressure. During the loading

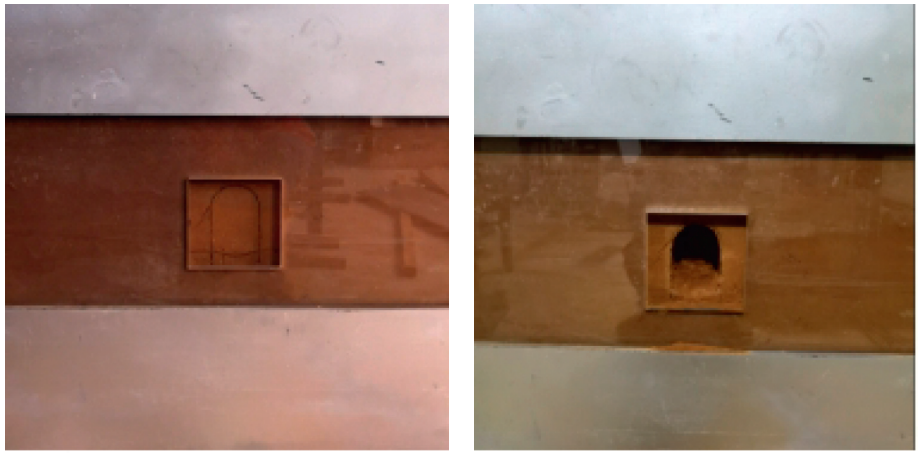

(a) (b)

Figure 9: Basic process of model excavation. (a) Excavation contour line. (b) Tunnel excavation.

process, the changes of surrounding rock stress, seepage pressure, and other data shall be paid attention to, but the water inrush position in the tunnel and the formation process of the inrush channel shall be paid the HD shooting system record attention. A particular person shall be specially assigned for data acquisition, photography, and recording until the physical model test of water and mud inrush in the tunnel is completed.

4. Analysis of Model Test Results

4.1. Stress Change Law of Surrounding Rock during Excavation. Tunnel excavation will destroy the original stress balance state in the surrounding rock and cause the redistribution of the surrounding rock stress field within a specific range. As shown in Figure 10, the vertical stress of the monitoring points on the left side wall and the right-side wall of the tunnel generally showed a slight change in the initial stage of tunnel excavation, and then the stress value of each monitoring point increased significantly in the middle of the excavation and finally tended to be stable. Among them, the vertical stress values of the left- and right-side walls (1-1 monitoring points and 3-1 monitoring points) around the tunnel of the No. 1 monitoring section increased by about 42.68 kPa and 41.25 kPa, respectively, and the arch ring around the tunnel of No. 2 monitoring section (monitoring point 5-1). The vertical stress increases by approximately 21.27 kPa; the vertical stress on the right wall (monitoring point 3-2) at one time the hole diameter of the No. 1 monitoring section increases by approximately 9.49 kPa. The vertical stress on the right wall (3-3 monitoring point) increased by about 1.93 kPa, and the difference between the two was 7.56 kPa. From the above analysis, it can be seen that the tunnel excavation will cause the vertical stress of the surrounding rock at the sidewall and the arch ring to increase, and the increase is affected by the distance from the excavation contour.

4.2. Influence of Test Loading Water Pressure on the Catastrophic Evolution Characteristics of Water and Mud Inrush in Tunnels. Figure 11 shows the variation of pore water

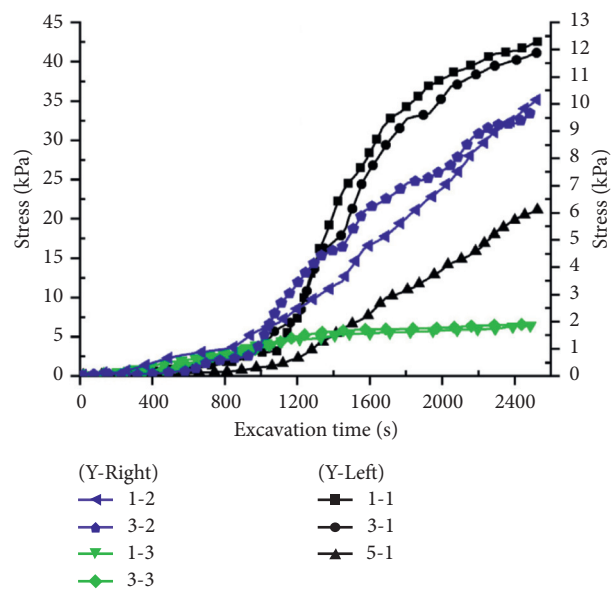

Figure 10: Stress change law of the measuring point during the excavation stage.

pressure at the measurement points inside the antiburst rock and fault at different hydraulic loading stages. Among them, the range of loading water pressure is 10~45 kPa. Under the same loading water pressure condition, the pore water pressure of each measuring point decreases with the vertical distance between the measuring point and the upper boundary of the fault. Taking the water pressure loading to 20 kPa and 40 kPa as an example, when the loading water pressure is at 20 kPa, the pore water pressure values at measuring points 4-1, 4-2, 4-3, and 4-4 are, respectively, 1.78 kPa, 3.65 kPa, and 14.51 kPa. And when the loading water pressure rises to 40 kPa, each pore water pressure of the measuring points changed to 5.34 kPa, 8.55 kPa, 35.31 kPa, and 39.78 kPa, compared with the 20 kPa loading water pressure, an increase of 200.00%, 134.24%, 143.35%, and 102.75% year-on-year. In addition, Figure 11(d) shows

that the pore water pressure at measurement point 4-1 was always close to the water pressure loading value at that stage at different water pressure loading stages, indicating that laying a gravel sublayer between the outlet device and the fault can effectively reduce the attenuation of the water pressure through the gravel sublayer and achieve the effect of evenly distributing the water pressure.

In different hydraulic loading stages, the pore water pressure at the same measurement point increases with the increase of loading water pressure, and when the water pressure is loaded step by step, the pore water pressure at measurement points 4-1 and 4-2 far from the gravel sublayer is nonlinear, while the measurement points 4-3 and 4-4 near the gravel sublayer are linear. When the loading water pressure increased from 10 kPa to 45 kPa, the pore water pressure values of measurement point 4-1 and measurement point 4-2 increased from 0.59 kPa to 5.93 kPa and 1.52 kPa to 9.78 kPa, respectively, with an increase of 905.08% and 543.42%, which can be seen from Figures 11(a) and 11(b) under the condition of adjacent loading water pressure; the increased value of pore water pressure at these two measuring points has noticeable difference and shows nonlinear growth. When the loading water pressure increases from 10 kPa to 45 kPa, the pore water pressure of measurement points 4-3 and measurement point 4-4 increases from 4.37 kPa to 40.83 kPa and 9.76 kPa to 44.83 kPa, respectively, with the growth rate of 834.32% and 359.32%, respectively. The slope of the curves in Figures 11(c) and 11(d) shows that the pore water pressure at these two measurement points increases with the loading water pressure and shows a linear increase.

In order to study the characteristics of the hydraulic gradient changes inside the antiburst rock and fault, the local hydraulic gradient of two adjacent points can be calculated based on the pore water pressure values of two adjacent measurement points and the distance between measurement points, that is, the adjacent hydraulic gradient. The hydraulic gradient variation law inside the model body is obtained according to the pore water pressure value and the adjacent distance of each measurement point, as shown in Figure 12.

Figure 12 shows that as the vertical distance from the upper boundary of the fault increases, the hydraulic gradient inside the model body first increases and then decreases. Taking the hydraulic gradient change when the loading water pressure is 20 kPa as an example, the vertical distance from the upper boundary of the fault is within the range of 0~12.5 cm, and the hydraulic gradient inside the model body is 0.409. When the distance increases to 12.5~18.38 cm, the hydraulic gradient is 1.847, which is a 351.59% increase compared with the hydraulic gradient in the previous range, and within the range 18.38~24.26 cm, the hydraulic gradient becomes 0.318, a decrease of 82.78% year-on-year. Since the hydraulic gradient inside the fault is smaller than the hydraulic gradient in the part of the rock body close to the fault, the head loss per unit length of the permeation path when the water flows through the fault is smaller than the head loss through this part of the rock body.

From the comparison of hydraulic gradients in different hydraulic loading stages, it can be seen that the vertical distance from the upper boundary of the fault is within the range of 0~12.5 cm. With the increase of loading water pressure, the hydraulic gradient gradually decreases, at 12.5~18.38 cm and 18.38 cm. In the range of 24.26 cm, the hydraulic gradient increases with the increase of the loading water pressure. Taking the change of hydraulic gradient within the range of 0~12.5 cm as an example, when the loading water pressure is 10 kPa, 20 kPa, 30 kPa, and 40 kPa, the corresponding hydraulic gradients are 0.431, 0.409, 0.375, and 0.358, which are lower than the previous stage. The ranges were 5.10%, 8.31%, and 4.53%, respectively.

4.3. Evolution Process of Water Inrush and Mud Outburst in the Fault Fracture Zone. After the completion of tunnel excavation, the hydraulic loading stage shall be carried out. The test adopts the step-by-step pressurization method to load the water pressure, the initial water pressure is 10 kPa, and the loading water pressure of each stage is 5 kPa. In order to make the pressure water have full seepage coupling with surrounding rock materials and fault filling materials, it can be loaded to the lower water pressure only after the software monitoring data is stable. During the test, make records of seepage or water and mud inrush under different loading water pressures, and the records are shown in Table 3.

At the beginning of the hydraulic loading stage, the tunnel seepage area gradually expanded from the right arch wall to the excavated palm face, the top of the arch, the left arch wall, and other locations. When the loading water pressure was 15 kPa, water seepage occurred in the right arch wall, and as the water pressure increased during the test, the seepage area gradually expanded to the left arch wall away from the water-filled fault, and the seepage volume of the tunnel as a whole continued to increase.

When the loading water pressure rises to 40kPa, there is a small stream of water flowing out of the arch wall on the right side of the monitoring section; when the water pressure is loaded to 45kPa, the surrounding rock of the right arch wall falls off partially, and cracks are produced, and streams of water flow out; when the water pressure continues to increase to 50kPa, the water gushing out from the tunnel keeps increasing, and the gushing out is a mixture of mud and sand, indicating that the surge channel gradually connected, and there are apparent precursors of water and mud inrush; when the water pressure after loading to 55kPa, seepage instability of right arch wall occurs, the mud water mixture in the fault erupted suddenly, the water and mud inrush forms, and subsequently, the fault in the gravel was washed out by the flow of water. After a while, the water and mud inrush was stable, and the water stored in the surrounding rock began to dissipate. After the test, part of the fault filling was deposited at the bottom of the tunnel. The specific process of tunnel water and mud inrush is shown in Figure 13.

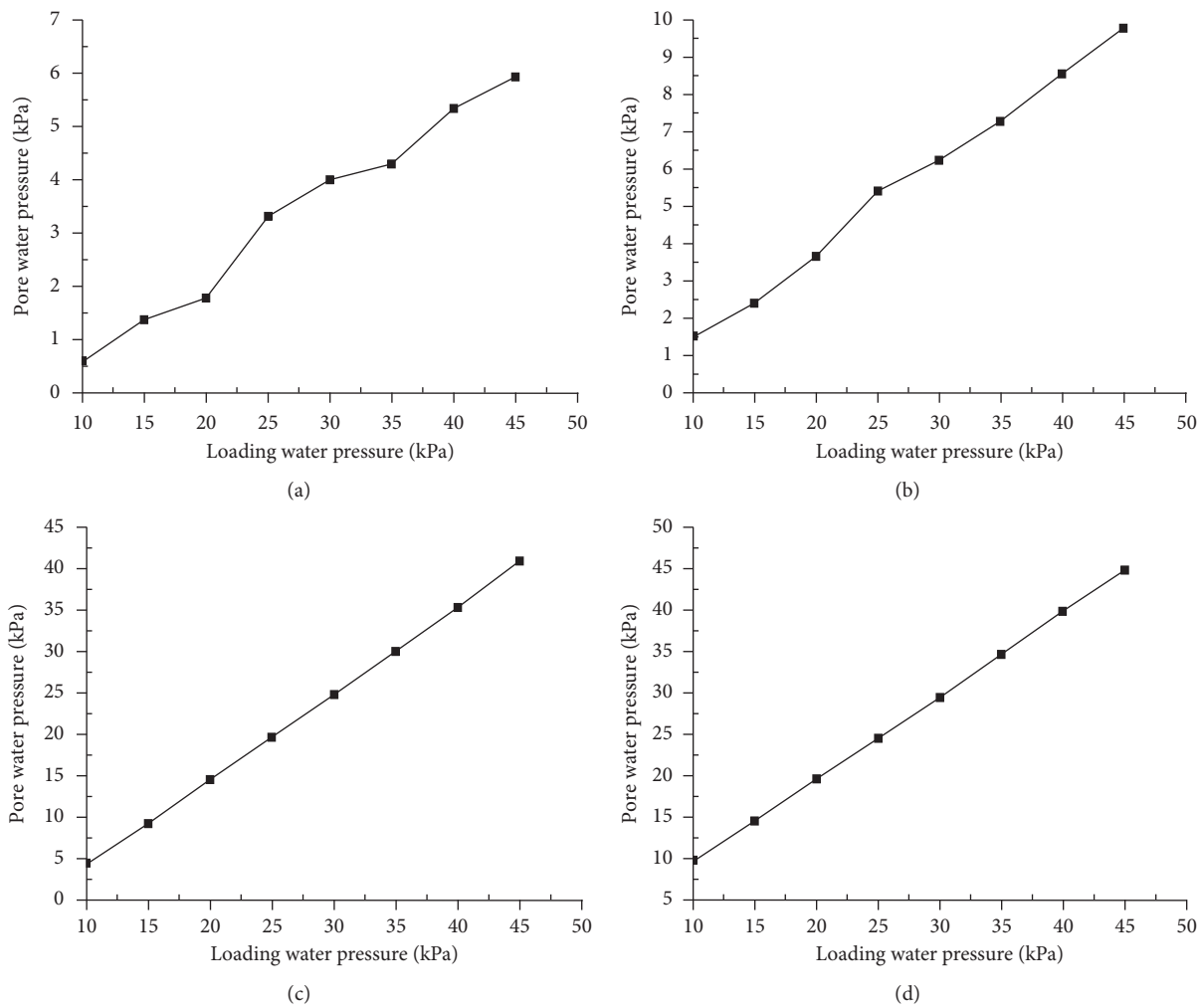

Figure 11: Pore water pressure variation rules at different monitoring points under different loading water pressures. (a) Monitoring point 4-1. (b) Monitoring point 4-2. (c) Monitoring point 4-3. (d) Monitoring point 4-4.

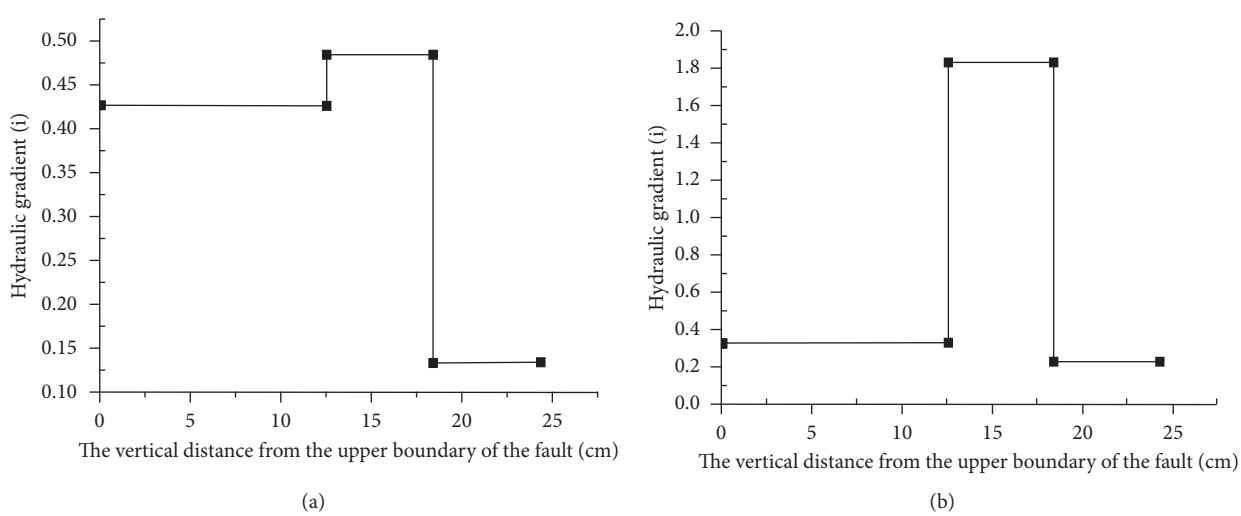

Figure 12: Continued.

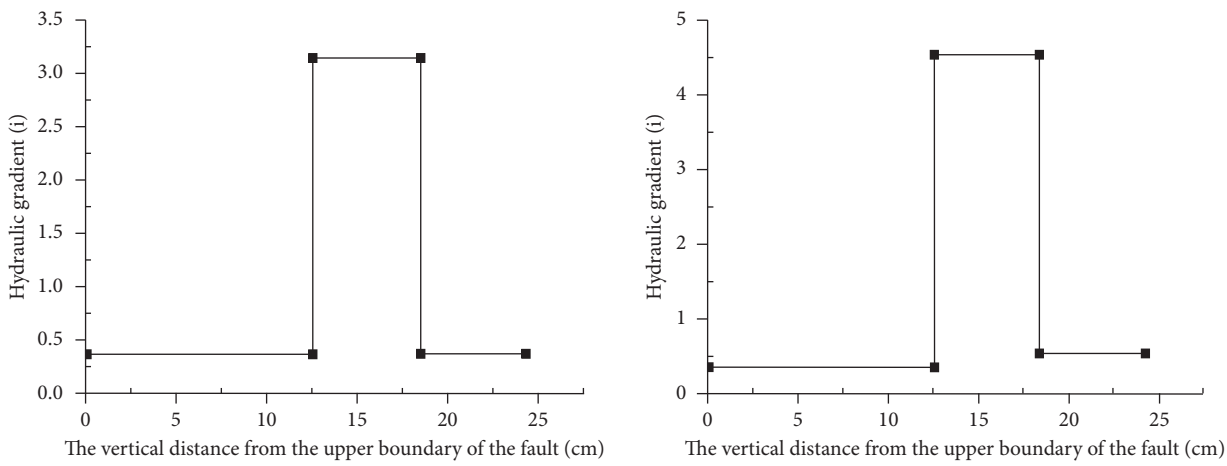

Figure 12: Hydraulic gradient under different loading water pressures. (a) Loading water pressure 10 kPa. (b) Loading water pressure 20 kPa. (c) Loading water pressure 30 kPa. (d) Loading water pressure 40 kPa.

Table 3: Seepage state of the tunnel under different loading water pressures.

Loading steps	Loading water pressure/kPa	Test phenomenon record
0	10	No obvious phenomenon
1	15	There is a small amount of water seepage on the right arch wall
2	20	A small amount of water flows out of the hole
3	25	Water seepage on the vault and tunnel surface
4	30	Water seepage in the left arch wall
5	35	The change is not obvious, it is still water seepage from the excavation surface
6	40	There is a small puddle of water flowing out of part of the right wall
7	45	Cracks occurred in the arch wall on the right, and water flowed out
8	50	Mud-water mixture flowing out
9	55	Large amounts of water and mud

(a) (b) (c)

Figure 13: Continued.

(d) (e) (f)

Figure 13: Catastrophic evolution process of water inrush and mud inrush in tunnel. (a) Water seepage of right arch wall. (b) The cracks produce mud-water mixture outflow. (c) Water inrush formation. (d) Mud and gravel gush out. (e) Water inrush stability. (f) End of test.

5. Conclusions

(1) Aiming at the significant problem of water and mud inrush in fault fracture zone during tunnel construction in mountainous plateau area, a three-dimensional visual, physical model test system suitable for fluid-solid coupling under high ground stress and high-water pressure is developed, which is composed of rigid test frame, in situ stress loading system, water pressure loading system, mud and water outburst recovery system, and multivariate information monitoring and acquisition system. It has the advantages of diversified monitoring information, good sealing, visualization, easy operation, and strong expansibility.

(2) Using the model test system, using the self-developed fluid-solid coupling similar material, a model test of water and mud inrush in the tunnel fault fracture zone is designed according to the engineering example. The data of surrounding rock stress and pore water pressure during tunnel excavation are monitored, and the essential characteristics of surrounding rock stress and deformation are mastered; the catastrophic evolution process of water and mud inrush in tunnel fault fracture zone is reproduced.

(3) In the tunnel excavation stage, the radial stress of the surrounding rock at the vault decreases due to the stress release, while the vertical stress of the surrounding rock at the sidewall increases. With the advance of the excavation face, the change of surrounding rock stress at each measuring point in the monitoring section is to maintain a stable change at first, then change sharply, and finally gradually tend to be stable. In the tunnel excavation process, the closer to the excavation contour, the more pronounced the change of surrounding rock stress is affected by excavation. In the stage of water pressure loading, the surrounding rock stress and pore water pressure at each measuring point increase first and then decrease with the increase of loading water pressure.

Data Availability

The data used to support the findings of this study are included within the article.

Conflicts of Interest

The authors declare that they have no conflicts of interest.

Acknowledgments

This study was supported and funded by the China Chile International (Regional) Cooperation and Exchange Key Projects of the National Natural Science Foundation of China (no. 41861134008), the General Projects of Yunnan Basic Research Program (no. 2018FB075), and the Key R&D Projects in Yunnan Province (no. 202003AC100002).

References

[1] Y. Zhou, S. C. Li, L. P. Li, Q. Q. Zhang, and S. S. Shi, "New technology for fluid-solid coupling tests of underground engineering and its application in experimental simulation of water inrush in filled-type karst conduit," *Chinese Journal of Geotechnical Engineering*, vol. 37, no. 7, pp. 1232–1240, 2015.

[2] K. Wang, S. C. Li, Q. S. Zhang et al., "Development and application of new similar materials of surrounding rock for a solid-liquid coupling model test," *Rock and Soil Mechanics*, vol. 37, no. 9, pp. 2521–2533, 2016.

[3] S. C. Li, X. D. Feng, S. C. Li, L. P. Li, and G. Y. Li, "Research and development of a new similar material for solid-fluid

coupling and its application," *Chinese Journal of Rock Mechanics and Engineering*, vol. 29, no. 2, pp. 281–288, 2010.

[4] A. H. Liu, S. Q. Peng, X. B. Li, and H. J. Chen, "Development and application of similar physical model experiment system for water inrush mechanism in deep mining," *Chinese Journal of Rock Mechanics and Engineering*, vol. 28, no. 7, pp. 1335–1341, 2009.

[5] J. Zhang and Z. J. Hou, "Experimental study on simulation materials for solid-liquid coupling," *Chinese Journal of Rock Mechanics and Engineering*, vol. 23, no. 18, pp. 3157–3161, 2004.

[6] Q. X. Huang, W. Z. Zhang, and Z. C. Hou, "Study of simulation materials of aquifuge for solid-liquid coupling," *Chinese Journal of Rock Mechanics and Engineering*, vol. 29, no. Supp.1, pp. 2813–2818, 2010.

[7] W. X. Li, G. Wang, W. Z. Du, P. F. Wang, J. H. Chen, and W. B. Sun, "Development and application of a true triaxial gas–solid coupling testing system for coal seepage," *Rock and Soil Mechanics*, vol. 37, no. 7, pp. 2109–2l18, 2016.

[8] J. Xu, S. J. Peng, G. Z. Yin, Y. Q. Tao, H. W. Yang, and W. Z. Wang, "Development and application of three–axial servo–controlled seepage equipment for hot–fluid–solid coupling of coal containing methane," *Chinese Journal of Rock Mechanics and Engineering*, vol. 29, no. 5, pp. 907–914, 2010.

[9] J. P. Yang, W. Z. Chen, H. M. Tian, and G. J. Wu, "Development of thermo-gaseous-mechanical coupling triaxial testing system of low permeability medium and its application," *Journal of rock mechanics and engineering*, vol. 28, no. 12, pp. 2377–2382, 2009.

[10] G. Z. Yin, W. P. Li, J. Xu et al., "Development and application of fracturing and seepage experimental system for multi-physical field and multiphase coupling of porous media," *Journal of rock mechanics and engineering*, vol. 35, no. S1, pp. 2853–2861, 2016.

[11] W. M. Yang, H. Wang, X. Yang et al., "Development and application of model test system for water inrush in high—geostress and high hydraulic pressure tunnels," *Journal of rock mechanics and engineering*, vol. 36, no. S2, pp. 3992–4001, 2017.

[12] Q. Wang, M. He, S. Li et al., "Comparative study of model tests on automatically formed roadway and gob-side entry driving in deep coal mines," *International Journal of Mining Science and Technology*, vol. 31, no. 4, pp. 591–601, 2021.

[13] W. B. Sun and S. C. Zhang, "Development of floor water invasion of mining influence simulation testing system and its application," *Journal of rock mechanics and engineering*, vol. 34, no. S1, pp. 3274–3280, 2015.

[14] Y. L. Luo, Q. Wu, M. L. Zhan, and J. C. Sheng, "Development of seepage-erosion-stress coupling piping test apparatus and its primary application," *Journal of rock mechanics and engineering*, vol. 32, no. 10, pp. 2108–2114, 2013.

[15] C. He, Z. Li, S. Z. Yang, Y. W. Luo, and W. B. Yang, "Development and application on mined tunnel seepage model test system for construction and operation period," *Chinese Journal of highway*, vol. 30, no. 5, pp. 114–121 + 131, 2017.

[16] Q. Wang, Y. Wang, M. C. He et al., "Experimental research and application of automatically formed roadway without advance tunneling," *Tunnelling and Underground Space Technology*, vol. 114, p. 2021.

[17] W. Z. Zhang, "Development and application of 3D large—scale simulation experiment system of water inrush caused by collapse column," *Journal of China University of mining and technology*, vol. 45, no. 1, pp. 56–61, 2016.

[18] L. M. Yin, W. J. Guo, and J. T. Chen, "Development of true triaxial rock test system of coupled stress-seepage and its application," *Journal of rock mechanics and engineering*, vol. 33, no. S1, pp. 2820–2826, 2014.

[19] L. P. Li, S. Liu, S. C. Li et al., "Development of testing system for coupled seepage and triaxial stress measurements and its application to permeability characteristic test on filling medium," *Geotechnical mechanics*, vol. 38, no. 10, pp. 3053–3061, 2017.

[20] L. P. Li, *Study on Catastrophe Evolution Mechanism of Karst Water Inrush and its Engineering Application of High-Risk Karst Tunnel*, Shandong University, Jinan, China, 2009.

[21] C. Zhu, M. C. He, X. H. Zhang, Z. G. Tao, Q. Yin, and L. F. Li, "Nonlinear mechanical model of constant resistance and large deformation bolt and influence parameters analysis of constant resistance behavior," *Rock and Soil Mechanics*, vol. 42, no. 7, pp. 1911–1924, 2021.

[22] Z. Tao, Y. Shu, X. Yang, Y. Peng, Q. Chen, and H. Zhang, "Physical model test study on shear strength characteristics of slope sliding surface in Nanfen open-pit mine," *International Journal of Mining Science and Technology*, vol. 30, no. 3, pp. 421–429, 2020.

[23] W. S. Zhu, Q. B. Zhang, Y. Li, L. F. Sun, L. Zhang, and W. H. Zheng, "Development and application of large geomechanical model test system under true triaxial load," *Journal of rock mechanics and engineering*, vol. 29, no. 1, pp. 1–7, 2010.

[24] Q. S. Zhang, D. M. Wang, S. C. Li, X. Zhang, Y. H. Tan, and K. Wang, "Development and application of model test system for inrush of water and mud of tunnel in fault rupture zone," *Chinese Journal of Geotechnical Engineering*, vol. 39, no. 3, pp. 417–426, 2017.

[25] S. C. Li, K. Wang, L. P. Li et al., "Development and application of an extendable model test system for water inrush simulation in subsea tunnel," *Chinese Journal of Rock Mechanics and Engineering*, vol. 33, no. 12, pp. 2409–2418, 2014.

[26] S. C. Li, S. G. Song, L. P. Li et al., "Development on subsea tunnel model test system for solid_fluid coupling and its application," *Chinese Journal of Rock Mechanics and Engineering*, vol. 32, no. 5, pp. 883–890, 2013.

[27] S. C. Li, L. P. Li, S. C. Li et al., "Development and application of similar physical model test system for waler inrush of underground engineering," *Journal of Mining and Safety Engineering*, vol. 27, no. 3, pp. 299–304, 2010.

[28] S. C. Li, Y. Zhou, L. P. Li et al., "Development and application of a new similar material for underground engineering fluid-solid coupling model test," *Chinese Journal of Rock Mechanics and Engineering*, vol. 31, no. 6, pp. 1128–1137, 2012.

[29] L. Li, X. L. Rong, M. Y. Wang, H. Lu, Y. P. Xia, and Z. C. Zhang, "Development and application of 3D model test system for water inrush geohazards in long and deep tunnels," *Chinese Journal of Rock Mechanics and Engineering*, vol. 35, no. 3, pp. 491–497, 2016.

[30] L. Li, M. Y. Wang, P. X. Fan, Y. H. Cheng, Z. Z. Li, and H. M. Jiang, "Development of loading and unloading apparatus for model test in deep underground engineering," *Geotechnical mechanics*, vol. 37, no. 01, pp. 297–304, 2016.

[31] Q. Y. Zhang, W. Xiang, Y. Zhang, C. Wang, and C. C. Liu, "Development and application of ultra high pressure3D loading model test system with intelligent numerical control function," *Chinese Journal of Rock Mechanics and Engineering*, vol. 35, no. 8, pp. 1628–1637, 2016.

[32] X. S. Li, K. Peng, J. Peng, and D. Hou, "Experimental investigation of cyclic wetting-drying effect on mechanical

behavior of a medium-grained sandstone," *Engineering Geology*, vol. 293, p. 2021.

[33] J. W. Bai, *Study on Delayed Water Inrush Mechanism of Fault and Prevention and Control Key Technology in Deep Rock Mass*, Shandong University, Jinan, China, 2018.

[34] Q. Yin, J. Y. Wu, C. Zhu, M. C. HE, and Q. X. Meng, "Shear mechanical responses of sandstone exposed to high temperature under constant normal stiffness boundary conditions," *Geomechanics and Geophysics for Geo-Energy and Geo-Resources*, vol. 7, no. 2, 2021.

[35] X. S. Li, K. Peng, J. Peng, and H. Xu, "Effect of cyclic wetting-drying treatment on strength and failure behavior of two quartz-rich sandstones under direct shear," *Rock Mechanics and Rock Engineering*, vol. 6, 2021.

[36] Y. C. Mo, *Stability Research on High Water Pressure Filled Karst Caves Tunnel*, Southwest Jiaotong Universit, Chengdu, China, 2009.

[37] R. Zhang, Z. Jiang, H. Zhou, C. Yang, and S. Xiao, "Groundwater outbursts from faults above a confined aquifer in the coal mining," *Natural Hazards*, vol. 71, no. 3, pp. 1861–1872, 2014.

[38] W. P. Li, Q. M. Liu, and R. H. Sun, "Theoretical and experimental study on vadose conversion of water inrush later occurred from structure broken zone," *Coal Science and Technology*, vol. 39, no. 11, pp. 10–13, 2011.

[39] W. H. Sui and Q. H. Dong, "Variation of pore water pressure and its precursor significance for quicksand disasters due to mining near unconsolidated formations," *Chinese Journal of Rock Mechanics and Engineering*, vol. 27, no. 9, pp. 1908–1916, 2008.

[40] X. Wang, z. Tan, M. Wang, M. Zhang, and H. Ming, "Theoretical and experimental study of external water pressure on tunnel lining in controlled drainage under high water level," *Tunnelling and Underground Space Technology*, vol. 23, no. 5, pp. 552–560, 2008.

[41] Y. Q. Hu, Y. S. Zhao, and D. Yang, "3D solid-liquid coupling experiment study into deformation destruction of coal stope," *Journal of Liaoning Technical University*, vol. 26, no. 4, pp. 520–523, 2007.

[42] L. Y. Yu, H. W. Jing, B. S. Xu, and Y. C. Wang, "Solid-fluid coupling analogous material test for subsea tunnel," *Journal of Central South University*, vol. 46, no. 3, pp. 983–990, 2015.

Hindawi
Mathematical Problems in Engineering
Volume 2021, Article ID 2583707, 11 pages
https://doi.org/10.1155/2021/2583707

Research Article

Investigation on Rock Strata Fracture Regulation and Rock Burst Prevention in Junde Coal Mine

Fengnian Wang,[1,2] **Gan Li**,[2,3] **and Chi Liu**[4]

[1]*State Key Laboratory for Geomechanics and Deep Underground Engineering, China University of Mining and Technology (Beijing), Beijing 100083, China*
[2]*School of Mechanics and Civil Engineering, China University of Mining and Technology (Beijing), Beijing 100083, China*
[3]*Ningbo University, Ningbo 315000, China*
[4]*State Key Laboratory of Hydroscience and Engineering, Tsinghua University, Beijing 100084, China*

Correspondence should be addressed to Gan Li; ligan303@126.com

Received 28 August 2021; Accepted 12 September 2021; Published 26 September 2021

Academic Editor: Feng Xiong

Through the establishment of structural mechanics model, this paper analyzes the fracture of super thick rock stratum. Through the model, it can be seen that the fracture of low-level super thick rock stratum produces large elastic energy release and dynamic load, which is easy to produce disasters such as rock burst. The numerical calculation shows that under the influence of low hard and thick rock stratum, the leading area of coal mine roadway will produce energy concentration, and the coal pillar will also produce energy accumulation. Thick rock stratum is in bending state and has large bending elasticity. Coal pillar has large compression elasticity, which is the main reason for rock burst. The accumulation of elastic properties of overburden and rock burst caused by coal pillar energy storage can be effectively controlled by using advanced presplitting blasting, coal seam drilling pressure relief, and strengthening support.

1. Introduction

In China, the geological conditions of coal mine are complex, and the underground mining is gradually developed from shallow to deep. In recent years, in the process of coal mining, rock burst caused by many factors, such as improper mining design, coal pillar setting, unknown geological conditions, and high in situ stress, has caused huge casualties and property losses. The rock burst disaster in engineering practice has challenged the existing accident mechanism research, treatment scheme, and prediction theory. Many experts have done a lot of research, e.g., Guo et al. [1] studied the mechanical properties and fracture process characteristics of deep buried granite specimens under different initial confining pressure and unloading rate combinations. Based on the analysis of the causes of dynamic disasters, Liang et al. [2] proposed a reasonable filling height of goaf under special geological conditions in order to fully eliminate mine disasters. Jiao et al. [3] analyzed the correlation between fault structure and temporal and spatial characteristics of rock burst by collecting rock burst events occurred near fault in the process of deep mining. He et al. [4, 5] developed the key technologies such as roof directional presplitting technology, negative Poisson's ratio high prestressed constant resistance support technology, and coal gangue plugging support technology, which are conducive to reducing the stress concentration of coal pillar and rock burst accidents. Ning et al. [6] put forward and applied the soft and strong support body as the support form of gob side entry retaining. In the early stage of roof movement, the soft strong support has good compressibility, which can not only relieve the roof pressure and strong impact load but also reduce the support resistance and prevent the support from being crushed. Zhu et al. [7] analyzed and evaluated the risk of rock burst, considering the coupling behavior of stress distribution and overlying strata movement. Based on the principle of strain

energy balance, the height of pressure relief zone above the goaf of an underground mining area is determined for the first time. Kong et al. [8] studied the deformation and rock burst risk of roadway under different dynamic and static loads. Dou et al. [9] systematically studied the relationship between elastic wave velocity and coal sample stress and put forward the positive correlation between elastic wave velocity and stress under uniaxial compression. Wang et al. [10, 11] analyzed the distribution characteristics of stress field under gob side entry retaining with roof cutting. Wang et al. [12] studied the failure mechanism of marble under cyclic loading and unloading conditions and provided theoretical basis for rock dynamic disaster prediction. With the development of mining activities, the self-stable state of high stress balance of coal pillar is easily broken by the impact energy formed by the sudden collapse of key strata [13, 14]. Therefore, the rock burst of coal pillar in overlying coal area is the result of static load and dynamic load [15, 16]. At present, the more effective control methods of rock burst mainly include pressure relief, support reinforcement, presplitting roof, and eliminating coal pillar [17, 18].

Through theoretical analysis, numerical calculation, and field engineering practice, this paper analyzes the occurrence mechanism and control measures of rock burst from the perspective of energy distribution. The characteristics of advance and lateral energy distribution of roadway under low-level and thick rock stratum are put forward. The strategy of controlling rock burst by means of advanced presplitting is put forward.

2. Engineering Geological Conditions

Junde minefield is located in the southern end of Hegang coalfield. The fold of the minefield is simple. The coal measure strata is a NNE trending, east dipping monoclinic structure, with local undulate. There are 128 faults in the minefield. Most of them are tension and torsion normal faults. Among them, 62 faults have a drop of more than 30 m, 27 faults have a drop of 15–30 m, and the rest of the faults have a drop of less than 15 m. Most of them are in direct contact with the quaternary system.

9103 working face adopts strike longwall comprehensive mechanized mining method. The strike of the working face is 1637 m, the average length of the working face is 168 m, and the mining height is 3.6 m. The occurrence of coal seam in the working face is stable, mainly massive and small bright coal, a small amount of dark coal, and the coal quality is good. The thickness of the coal seam is 8.21–14.15 m, with an average thickness of 11.18 m. The coal seam is mined in layers, and the recoverable reserves are 4.304 million tons. According to the drilling data and roadway observation, the pseudoroof of the coal seam is 0.2–3.33 m carbon shale, the direct roof of the coal seam is 5.2–14.9 m gray siltstone, and the main roof is coarse sandstone, and there is conglomerate locally. The roof condition is shown in Figure 1.

The results of in situ stress measurement show that the maximum principal stress is approximately in horizontal direction, near east-west direction, which is unfavorable to the north-south direction of roadway support. In this area, the maximum principal stress ranges from 22.8 MPa to 27.3 MPa, near east-west direction; minimum principal stress range is 10.1–12.8 MPa, near vertical direction. At present, the conveyor roadway and return air roadway are arranged in the north-south direction, which is approximately vertical to the maximum principal stress, and the roadway is prone to large deformation, which is not conducive to the maintenance of the roadway.

After mining, the original stress field will redistribute, and the coal and rock will have different degrees of damage and movement. The overlying strata affected by mining include the strata that participate in the movement along the advancing direction and the strata that participate in the movement along the working face direction. The stress field is divided into abutment pressure distribution in front of working face and lateral stress field. When the support pressure is too large, the accumulated elastic energy of coal is greater than its bearing capacity, which will lead to failure and even rock burst. At the same time, because of the high strength and thickness of the roof, the release of elastic energy during breaking is easy to produce rock burst [19, 20].

As shown in Figure 2, it shows the movement diagram of overlying strata in the direction of coal seam advancement. When the strata fall behind and the weight of the overlying strata is transferred to the front of the working face, the peak of support pressure will eventually appear, which is easy to lead to rock burst. At the same time, the overlying strata fracture will release the accumulated bending elastic energy of the rock beam, resulting in energy transfer and rock burst.

The calculation of the first fracture weighting step of the thick rock beam is shown in formula (1), and the periodic weighting step is shown in the following formula:

$$v_\varepsilon = \int_{t_0}^{t_1} \sigma\colon \delta\varepsilon = \int_0^1 t\sigma\colon (t\delta\varepsilon) = \sigma\colon \varepsilon \int_0^1 t\delta t = \frac{1}{2}\sigma\colon \varepsilon = \frac{1}{2}\sigma_{ij}\varepsilon_{ij}, \tag{1}$$

$$C_i = -\frac{1}{2}C_{i-1} + \frac{1}{2}\sqrt{C_{i-1}^2 + \frac{4M_s^2[\sigma_s]}{3\gamma(M_s + M_c)}}, \tag{2}$$

where M_S, M_C are the thickness of the lower (supporting) strata and the upper (following) strata of the rock beam, m; σ_S is the allowable tensile stress of lower (supporting) rock stratum, MPa; r is the average unit weight of rock mass, kg/$m3 \times 103$; C_i, $C_{i\text{-}1}$ are the weighting step of the same period and the weighting step of the last period, m.

There is a strong correlation between the overlying strata movement along the working face direction and the working face length. The longer the working face length is [21, 22], the higher the development height of the fracture arch is. The shorter the length of working face is, the smaller the development height of fracture arch is. However, under the influence of low-level thick rock, the development of fracture arch height has a strong correlation with the position of thick rock, and its development process is different from that of common fracture arch.

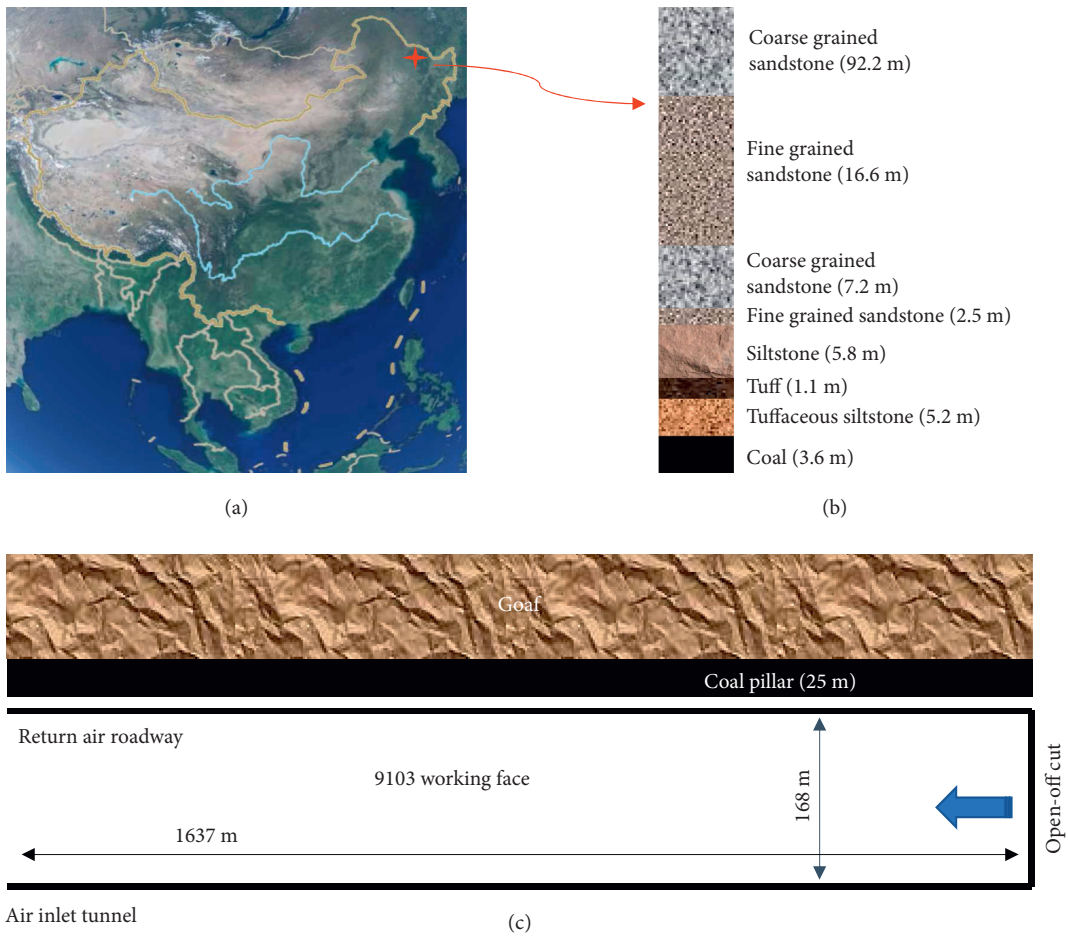

Figure 1: Location and overview of the study target structural mechanics model and disaster mechanism of coal seam mining under low position and extremely thick strata (map source: official website of the Ministry of Natural Resources of China).

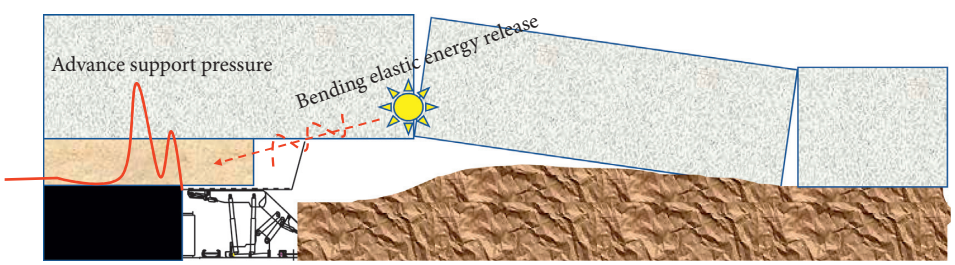

Figure 2: Fracture model of overlying strata.

According to the analysis in Figure 3, the height of the fracture arch is always below the low position thick rock beam before the low position thick rock beam is broken. In the strike long arm mining method, with coal pillar roadway protection, the weight of low position thick rock beam is shared by the embedded end of rock beam and coal pillar. When the embedded part of the thick rock beam cracked, the weight of the low thick rock beam was transferred from the fracture line of the rock beam to the coal pillar. Before the fracture, the overhanging roof of the low position thick rock beam is large, and it has high-strength bending elastic energy and gravitational potential energy.

3. Numerical Calculation Model and Results

3.1. Numerical Calculation Model and Its Parameters. According to the comprehensive histogram of 9103 working face in Junde Coal Mine, the initial three-dimensional numerical model is established with the help of 3DEC numerical simulation analysis software, as shown in Figure 4. The model is 2000 m long, 500 m wide, and 450 m high. Mohr–Coulomb model is adopted as the constitutive model of the numerical model. The selection of rock mechanics parameters in the model is determined based on the rock mechanical parameters obtained in the

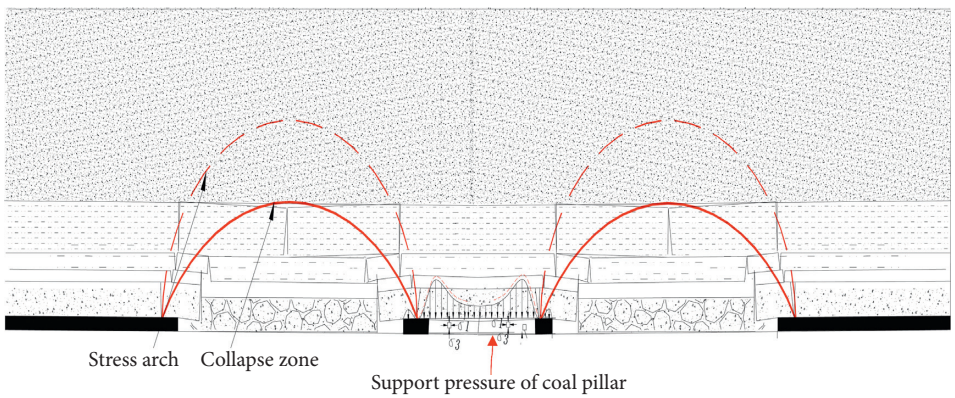

Figure 3: Lateral support pressure of stope.

laboratory and the inversion based on the field measured data, as shown in Table 1. The bottom boundary of the model is fully constrained in X, Y, and Z directions, and the top is free.

According to the identification of the impact tendency of 17 layers in Junde Coal Mine, the following conclusions can be drawn: the average failure time of coal sample is 485.2 ms, the average impact energy index is 4.108, the average elastic energy index is 2.531, and the uniaxial compressive strength is 15.176 MPa, which belongs to weak impact tendency; the tensile strength of the rock sample is 1.8 MPa, the thickness of the roof is 14.4 m, the elastic modulus is 95.5 GPa, the load per unit width of the overlying strata is 0.0378 MPa, and the bending energy index is 821.928, which is strongly impact-prone.

3.2. Strata Movement Law and Energy Response in Strike Mining Direction. According to the strength theory, if the local stress of coal and rock mass is too large and exceeds its own strength, rock burst will be induced. According to energy theory, rock burst will be induced when the energy of mechanical system of stope surrounding rock exceeds the energy needed to maintain the equilibrium state [23, 24].

For linearly elastic materials, the strain energy density is shown in the following equation:

For an isotropic linear elastic material, the strain energy density is

$$v_\varepsilon(\varepsilon) = \frac{1}{2}\sigma : \varepsilon = \mu\varepsilon : \varepsilon + \frac{1}{2}\lambda tr^2(\varepsilon) = \mu tr(\varepsilon : \varepsilon) + \frac{1}{2}\lambda tr^2(\varepsilon). \tag{3}$$

The strain energy density can also be given by the three principal strains (eigenvalues) of the strain tensor.

$$v_\varepsilon(\varepsilon_1, \varepsilon_2, \varepsilon_3) = \mu\left(\varepsilon_1^2 + \varepsilon_2^2 + \varepsilon_3^2\right) + \frac{1}{2}\lambda(\varepsilon_1 + \varepsilon_2 + \varepsilon_3)^2. \tag{4}$$

Using the principal stress expression form,

$$v_\varepsilon(\sigma_1, \sigma_2, \sigma_3) = \frac{1+\nu}{2E}\left(\sigma_1^2 + \sigma_2^2 + \sigma_3^2\right) - \frac{\nu}{2E}(\sigma_1 + \sigma_2 + \sigma_3)^2. \tag{5}$$

When the model excavation is 75 m, the peak area of abutment pressure is about 2 m in front of the working face, the highest value is about 43 MPa, and the influence range of advance abutment pressure is about 50 m. The upper thick rock is not fractured, and the change of elastic energy caused by mining is about 50 m in front of the working face. The maximum energy accumulation is 4e10 J, as shown in Figure 5.

When the model is excavated for 175 m, the huge thick rock is fractured, the peak area of abutment pressure is about 5 m in front of the working face, the highest value is about 36.7 MPa, and the influence range of advance abutment pressure is about 125 m. The change of elastic energy caused by mining is in the range of about 125 m in front of the working face, as shown in Figure 6.

3.3. Distribution Characteristics of Lateral Stress. Different mining parameters (mainly referring to the length of working face) lead to different overlying strata movement and lateral stress distribution. According to the theoretical analysis and field observation, we know that the influence range of lateral abutment pressure caused by overlying huge thick strata is large, and the stress concentration factor is high, especially when the coal pillar is reserved, the elastic energy accumulated on the coal pillar is very dangerous.

As shown in Figure 7, according to the simulation, when the working face length is 145 m, the fracture arch stops when it develops to the bottom of the thick rock, but the thick rock has slight bending deformation. The influence range of front abutment pressure is 0–180 m, and the peak area of abutment stress is about 25 m. When the length of the second working face is 150 m, 25 m coal pillar is reserved, and the fracture arch stops when it develops to the bottom of the thick rock, but cracks appear in the thick rock, and there is a large bending deformation. The deformation of coal pillar is large, and the gathering elastic energy is large, so it is easy to produce rock burst.

When the length of the working face is 298 m, the huge thick strata fracture, the influence range of lateral support is 0–190 m, the peak area of support pressure is about 18 m, and the range of internal stress field is about 0–5 m.

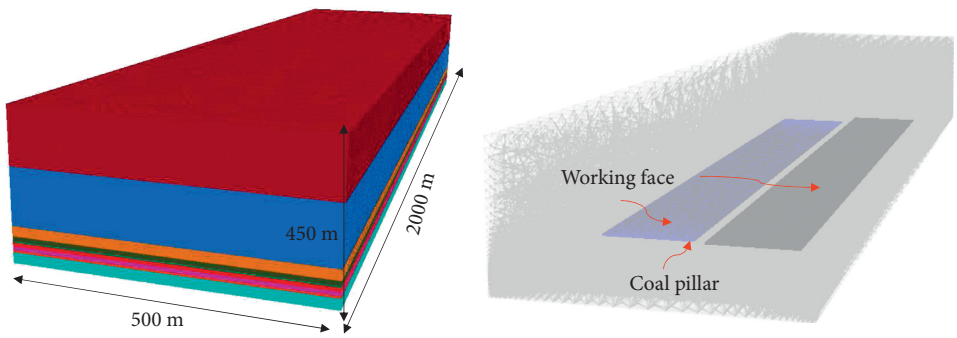

Figure 4: Numerical calculation model.

Table 1: Rock mechanics parameters.

Lithology	Compressive strength (R/MPa)	Elastic modulus (E/MPa)	Poisson's ratio	Cohesion (C/MPa)	Internal friction angle	Density
Coarse sandstone	10.934	1413.5275	0.2618	1.6863	20.02	1.8172
Medium sandstone	7.777	1030.5988	0.231	1.5554	20.02	1.7171
Fine sandstone	9.471	1346.3219	0.2156	1.8711	20.79	1.7402
Siltstone	9.394	1211.5411	0.231	1.9789	20.79	1.7094
Tuff	8.296	1069.9324	0.204	1.7476	18.36	1.5096

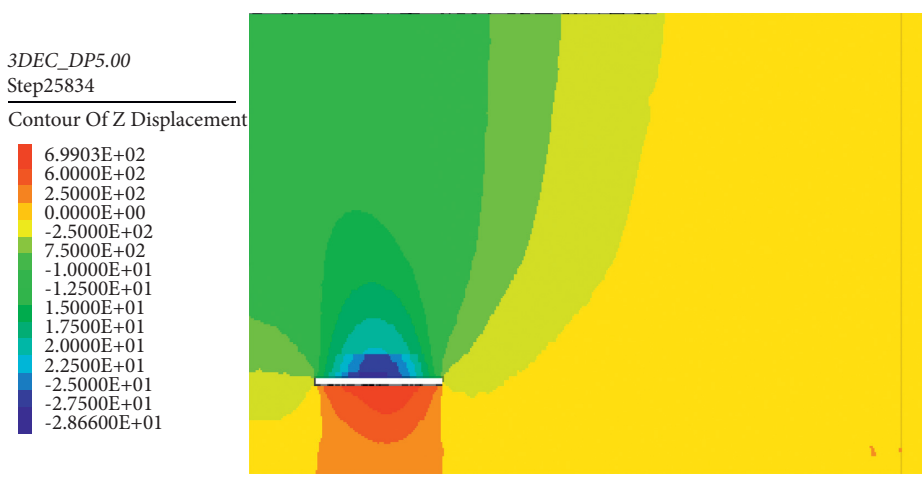

(a)

Figure 5: Continued.

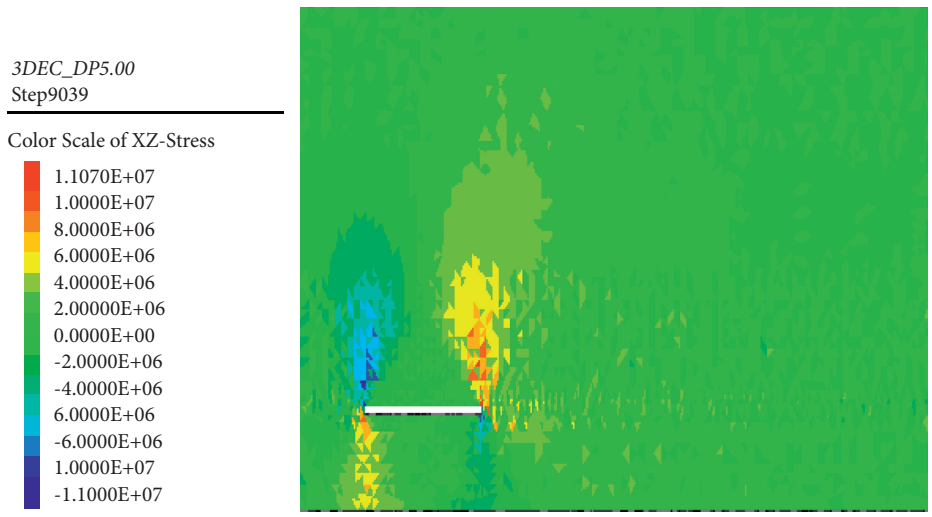

(b)

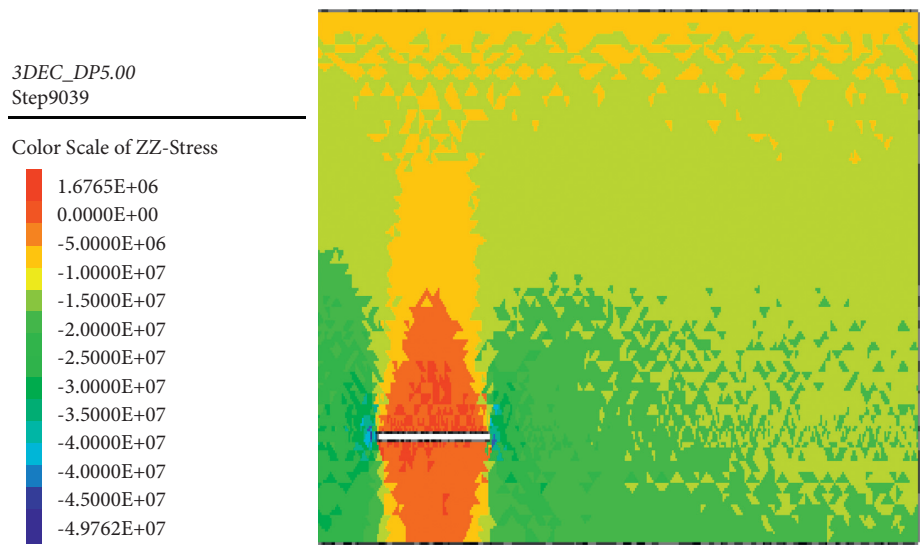

(c)

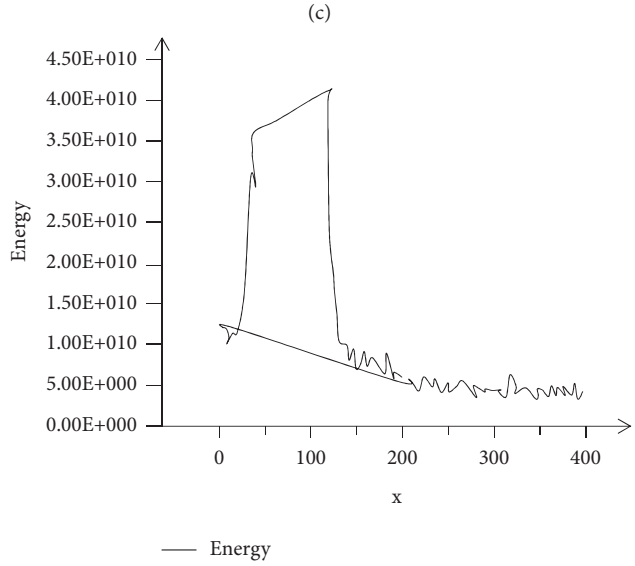

(d)

Figure 5: Distribution of displacement, stress, and energy under the condition of 75 m strike advance. (a) Displacement characteristics, (b) shear stress, (c) vertical stress, and (d) energy distribution characteristics.

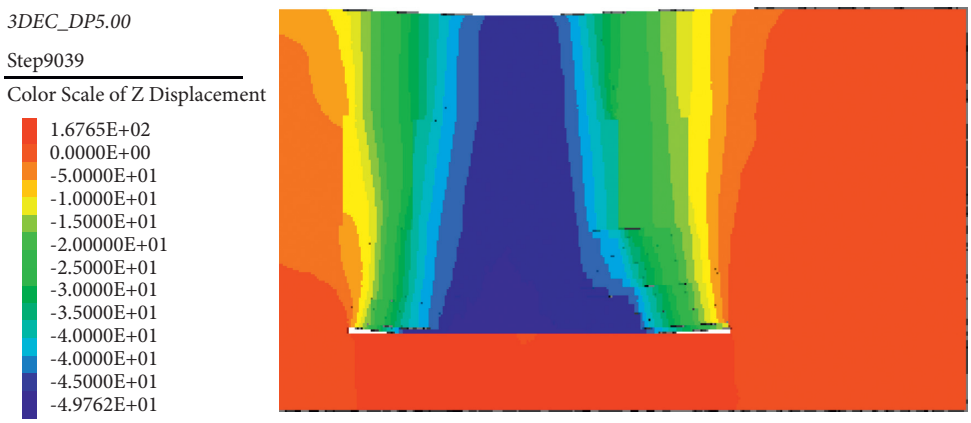

(a)

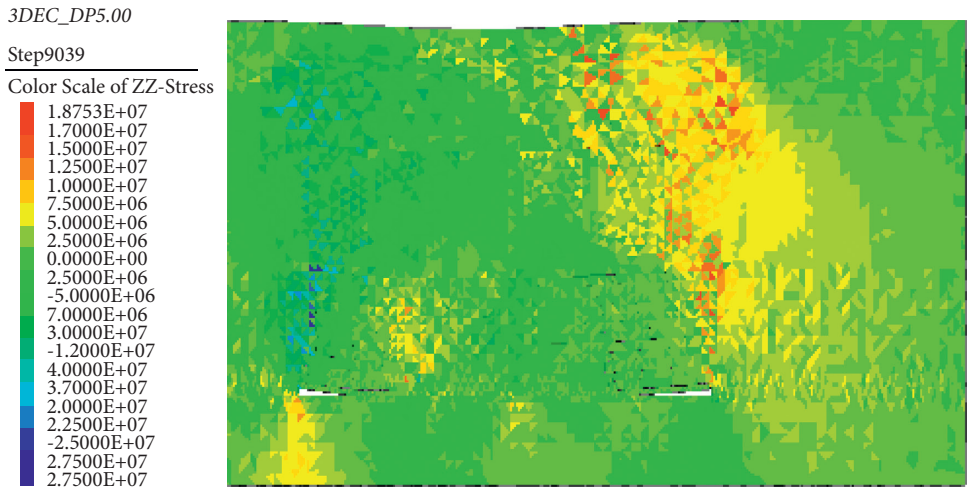

(b)

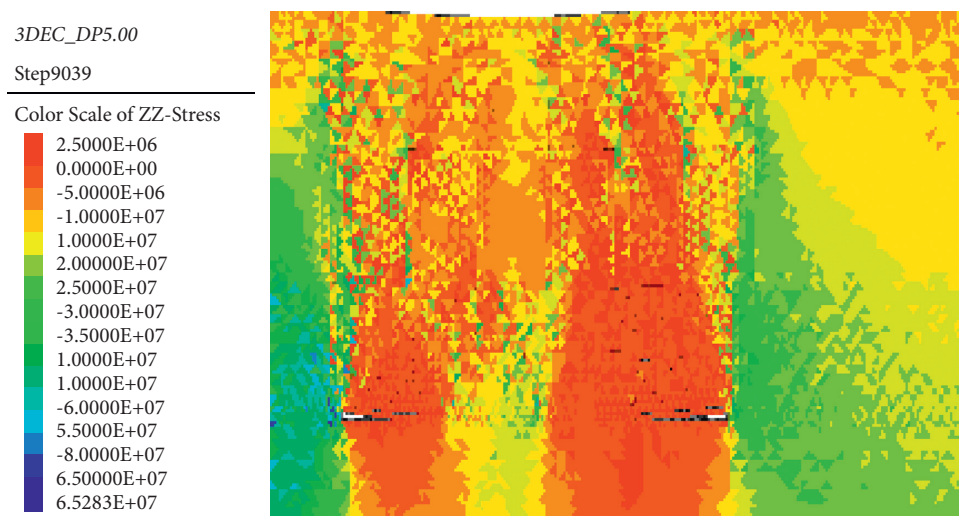

(c)

Figure 6: Continued.

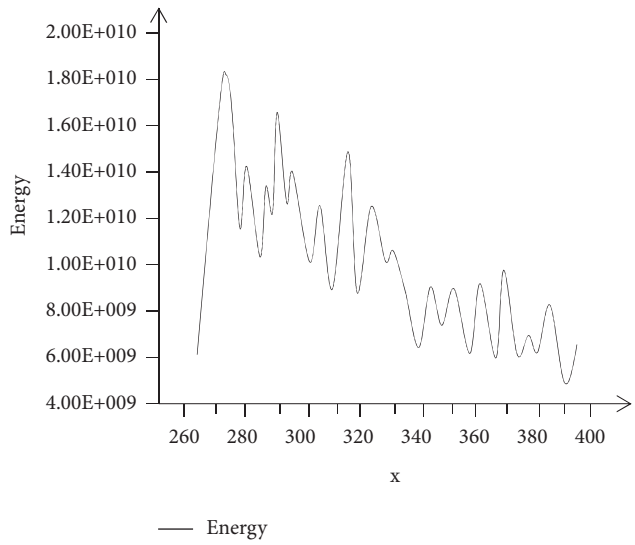

(d)

Figure 6: Distribution of displacement, stress and energy under 175 m strike advance. (a) Displacement characteristics, (b) stress, (c) vertical stress, and (d) energy distribution characteristics.

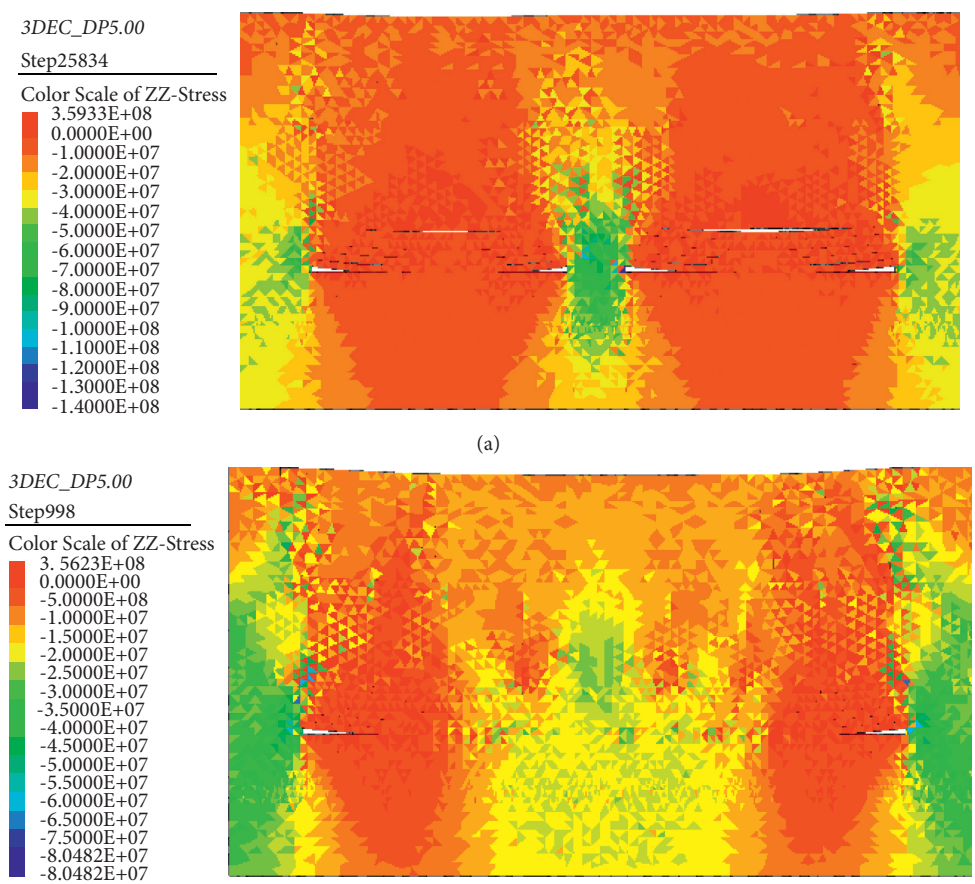

Figure 7: Stope stress characteristics under different working face lengths. (a) Cloud chart of lateral stress when working face length is 150 m. (b) Cloud chart of lateral stress when working face length is 298 m.

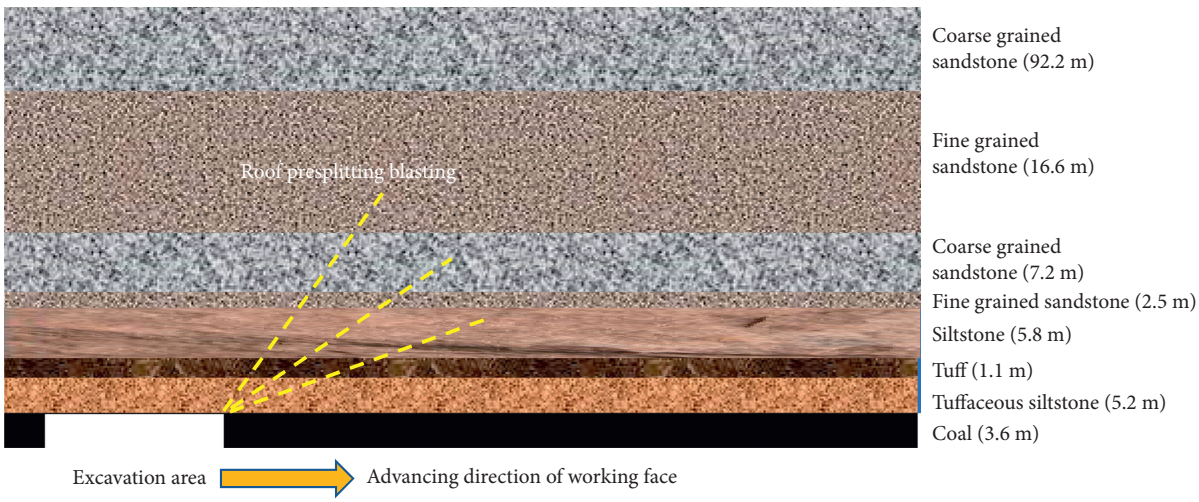

Figure 8: Advance presplitting blasting.

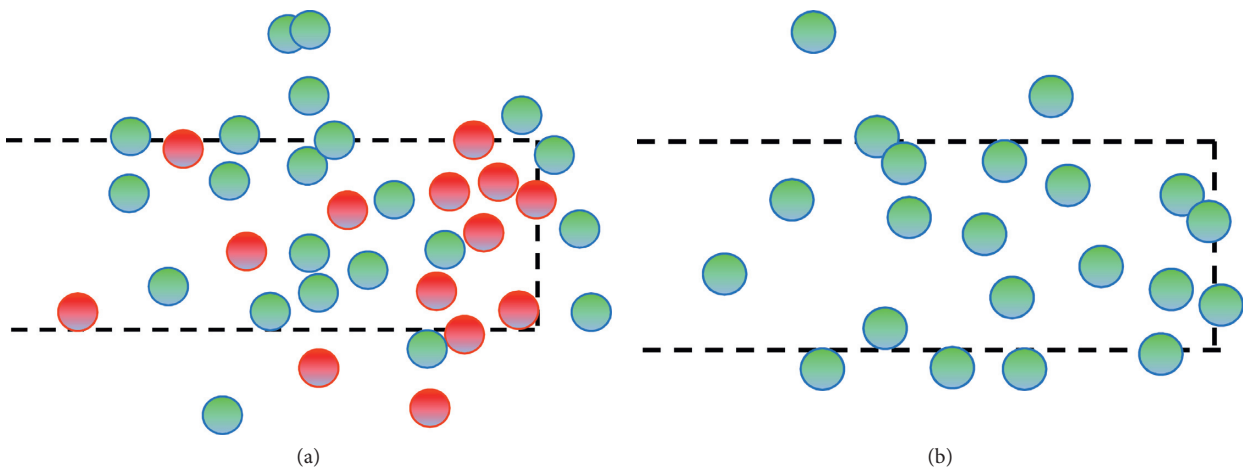

Figure 9: Influence of comprehensive treatment measures on microseism of working face, (a) in working face without comprehensive treatment, and (b) microseism of working face after comprehensive treatment.

According to theoretical analysis, field measurement, and numerical simulation, it should be determined that the length of working face is greater than 298 m, and after the rock strata collapse and stress redistribution of the previous working face is stable, gob side entry retaining or gob side entry driving should be carried out in the internal stress field, so as to avoid rock burst caused by elastic energy accumulation of overlying strata and energy stored in coal pillar of the previous working face.

4. Control Measures

In order to reduce the accumulation of elastic properties, three methods are mainly used: advance presplitting blasting, coal seam drilling pressure relief, and strengthening support. As shown in Figure 8, three boreholes are constructed in each group for roof presplitting blasting, with elevation angles of 6°, 23°, and 40° and hole length of 80 m and hole spacing of 20 m. By strengthening the support, the excessive expansion of the loose zone is limited to reduce the convergence deformation of the surrounding rock of the roadway and enhance the antiexpansion and anti-impact ability of the surrounding rock. The support section is supported by 4 anchor cables, 3 anchor bolts, and combined W-type steel belt.

Figure 9 shows the difference of microseismic distribution between two adjacent working faces before and after adopting control measures. The red sphere indicates that the microseismic energy is greater than 10e6 J, and the green sphere indicates that the energy is between 10e5 J and 10e6 J. After adopting comprehensive measures, the phenomenon of microseismic energy greater than 10e6 J disappears in the mining process. The overall number of microseisms also decreased. After the treatment, there is no big rock burst phenomenon in the mining face.

5. Conclusion

This paper expounds the dynamic basis of rock burst, analyzes the influence of overburden movement on rock burst,

and verifies it by theoretical calculation and numerical simulation.

(1) The causes of rock burst accidents in the process of excavation are as follows: the upper working face is short, the thick rock stratum is in bending state, the greater bending elastic property is accumulated, the greater compression elastic property is accumulated in the coal pillar, the width of the reserved coal pillar exceeds the "range of internal stress field", and the roadway is located in the peak area of abutment pressure. There are many risks of rock burst in the roadway maintained in the peak area of abutment pressure.

(2) The causes of rock burst accidents in the process of mining are as follows: the length of the working face in the upper section is short, the movement of the main roof (especially the extremely thick rock) is not sufficient, resulting in the storage of high-strength bending elastic energy, the wide isolation coal pillar, resulting in a large area of suspended roof, the accumulation of high-strength compression elastic energy and bending elastic performance of the roof, the fracture of the extremely thick rock in the roof, and the compression of the coal wall. It results in the release of large area roof bending elastic energy and coal wall compression elastic property.

(3) According to the experiment, it is known that when the working face is advanced to 235 m or so, the huge thick strata fracture occurs. With the advance of the working face, the abutment pressure transfers to the front of the coal wall, and its influence range gradually increases with the advance of the working face, and the leading influence distance is about 50 m. When the length of the working face is 298 m, the huge thick strata fracture occurs, the influence range of lateral support is 0–190 m, the peak area of support pressure is about 18 m, and the range of internal stress field is about 0–5 m.

(4) Advance presplitting blasting, coal seam drilling pressure relief, and strengthening support can effectively control the overburden aggregation performance and rock burst caused by coal pillar energy storage.

Data Availability

The data are available and explained in this article; readers can access the data supporting the conclusions of this study.

Conflicts of Interest

The authors declare no conflicts of interest.

Acknowledgments

This work was supported by the National Key Research and Development Plan (No. 2018YFC1504902) and the National Natural Science Foundation of China (41941018).

References

[1] J. Guo, P. Liu, J. Fan, X. Shi, and X. Huang, "Influence of confining pressure unloading rate on the strength characteristics and fracture process of granite using lab tests," *Advances in Materials Science and Engineering*, vol. 2021, no. 10, 16 pages, Article ID 7925608, 2021.

[2] W. Liang, Y. P. Cheng, and C. Xu, "The controlling effect of thick-hard igneous rock on pressure relief gas drainage and dynamic disasters in outburst coal seams," *Natural Hazards*, vol. 66, no. 2, pp. 1221–1241, 2013.

[3] Z. Jiao, Q. Yuan, P. Zou, and B. Shi, "Case study of the characteristics and mechanism of rock burst near fault in yima coalfield, China," *Shock and Vibration*, vol. 2021, no. 11, 12 pages, Article ID 9950273, 2021.

[4] M. He, Q. Wang, and Q. Wu, "Innovation and future of mining rock mechanics," *Journal of Rock Mechanics and Geotechnical Engineering*, vol. 13, no. 1, 21 pages, 2021.

[5] C. Zhu, M. C. He, M. Karakus, X. H. Zhang, and Z. Guo, "The collision experiment between rolling stones of different shapes and protective cushion in open-pit mines," *Journal of Mountain Science*, vol. 18, no. 5, pp. 1391–1403, 2021.

[6] J. Ning, J. Wang, X. Liu, K. Qian, and B. Sun, "Soft-strong supporting mechanism of gob-side entry retaining in deep coal seams threatened by rockburst," *International Journal of Mining Science and Technology*, vol. 24, no. 6, pp. 805–810, 2014.

[7] G. A. Zhu, L. M. Dou, and A. Y. Cao, "Assessment and analysis of strata movement with special reference to rock burst mechanism in island longwall panel," *Journal of Central South University*, vol. 24, no. 012, pp. 2951–2960, 2017.

[8] P. Kong, L. Jiang, and J. Jiang, "Numerical analysis of roadway rock-burst hazard under superposed dynamic and static loads," *Energies*, vol. 12, 2019.

[9] L. Dou, T. Chen, S. Gong, H. He, and S. Zhang, "Rockburst hazard determination by using computed tomography technology in deep workface," *Safety Science*, vol. 50, no. 4, pp. 736–740, 2012.

[10] Q. Wang, Z. Jiang, B. Jiang, H. Gao, Y. Huang, and P. Zhang, "Research on an automatic roadway formation method in deep mining areas by roof cutting with high-strength bolt-grouting," *International Journal of Rock Mechanics and Mining Sciences*, vol. 128, Article ID 104264, 2020.

[11] Q. Wang, Y. Wang, M. He et al., "Experimental research and application of automatically formed roadway without advance tunneling," *Tunnelling and Underground Space Technology*, vol. 114, no. 3, Article ID 103999, 2021.

[12] Y. Wang, W. K. Feng, R. L. Hu, and C. H. Li, "Fracture evolution and energy characteristics during marble failure under triaxial fatigue cyclic and confining pressure unloading (FC-CPU) conditions," *Rock Mechanics and Rock Engineering*, vol. 54, no. 2, pp. 799–818, 2021.

[13] X. Lai, H. Xu, J. Fan et al., "Study on the mechanism and control of rock burst of coal pillar under complex conditions," *Geofluids*, vol. 2020, no. 2, 19 pages, Article ID 8847003, 2020.

[14] S. He, D. Song, and Z. Li, "Mechanism and prevention of rockburst in steeply inclined and extremely thick coal seams for fully mechanized top-coal caving mining and under gob filling conditions," *Energies*, vol. 13, 2020.

[15] W. Guo, Y. Li, D. Yin, S. Zhang, and X. Sun, "Mechanisms of rock burst in hard and thick upper strata and rock-burst controlling technology," *Arabian Journal of Geosciences*, vol. 9, no. 10, p. 561, 2016.

[16] G. Li, Y. Hu, and Q. B. Li, "Inversion method of in-situ stress and rock damage characteristics in dam site using neural network and numerical simulation—a case study," *IEEE Access*, vol. 99, p. 1, 2020.

[17] D. Guo, X. Kang, Z. Lu, and Q. Chen, "Mechanism and control of roadway floor rock burst induced by high horizontal stress," *Shock and Vibration*, vol. 2021, no. 4, 13 pages, Article ID 6745930, 2021.

[18] J. Cao, L. Dou, G. Zhu, J. He, S. Wang, and K. Zhou, "Mechanisms of rock burst in horizontal section mining of a steeply inclined extra-thick coal seam and prevention technology," *Energies*, vol. 13, no. 22, p. 6043, 2020.

[19] Z. Liu, W. Ma, and S. Tian, "Study on the mechanical behavior of double primary support of soft rock tunnel under high ground stresses and large deformation," *Advances in Civil Engineering*, vol. 2020, no. 8, 9 pages, Article ID 8832797, 2020.

[20] X. Li, S. Chen, E. Wang, and Z. Li, "Rockburst mechanism in coal rock with structural surface and the microseismic (MS) and electromagnetic radiation (EMR) response," *Engineering Failure Analysis*, vol. 124, no. 3, Article ID 105396, 2021.

[21] F. L. He, L. Xu, and H. K. Wu, "Deviatoric stress transfer and stability of surrounding rock in large-section open-off cut roof," *Yantu Gongcheng Xuebao/Chinese Journal of Geotechnical Engineering*, vol. 36, no. 6, pp. 1122–1128, 2014.

[22] H. Kang, Y. Wu, F. Gao, J. Lin, and P. Jiang, "Fracture characteristics in rock bolts in underground coal mine roadways," *International Journal of Rock Mechanics and Mining Sciences*, vol. 62, pp. 105–112, 2013.

[23] G. Li, W. Ma, S. Tian, Z. Hongbo, F. Huabin, and W. Zou, "Groundwater inrush control and parameters optimization of curtain grouting reinforcement for the jingzhai tunnel," *Geofluids*, vol. 2021, no. 7, 10 pages, Article ID 6634513, 2021.

[24] J. Tang, S. Li, G. Qin et al., "Experiments on mechanical response and energy dissipation behavior of rockburst-prone coal samples under impact loading," *Shock and Vibration*, vol. 2021, no. 2, 10 pages, Article ID 9924456, 2021.

Hindawi
Mathematical Problems in Engineering
Volume 2021, Article ID 5611786, 11 pages
https://doi.org/10.1155/2021/5611786

Research Article

Difference of Microfeatures among Diagenetic Facies in Tight Sandstone Reservoirs of the Triassic Yanchang Formation in the Midwestern Region, Ordos Basin

Jian Shi,[1,2] **Xiaolong Wan**,[1,2] **Qichao Xie**,[1,2] **Shuxun Zhou**,[1,2] **Yan Zhou**,[3] **Dazhong Ren**,[4] **and Rongjun Zhang**[4]

[1]*Exploration and Development Research Institute of PetroChina Changqing Oilfield Company, Xi'an, Shaanxi 710018, China*
[2]*National Engineering Laboratory for Exploration and Development of Low-Permeability Oil & Gas Fields, Xi'an, Shaanxi 710018, China*
[3]*CNPC Logging Applied Research Institute, Xi'an 710077, China*
[4]*Xi'an Key Laboratory of Tight Oil (Shale Oil) Development, Xi'an Shiyou University, Xi'an, Shaanxi 710065, China*

Correspondence should be addressed to Jian Shi; shijian2371@163.com

Received 28 June 2021; Accepted 14 August 2021; Published 2 September 2021

Academic Editor: Feng Xiong

Based on the background of sedimentary characteristics, a large amount of core and thin section analysis, taking Chang 6 reservoir of Yanchang Formation in the central and western Ordos Basin as an example, through the application of scanning electron microscopy, high-pressure mercury injection, nuclear magnetic resonance and microscopic water drive oil model, and other experimental test methods, the diagenetic facies types and microscopic pore structure characteristics of tight sandstone reservoirs are discussed and analyzed in depth. The results show that the average porosity loss rate caused by early diagenesis compaction in the study area is 50.62%, which is the main reason for reservoir compactness. The cementation further causes porosity loss, and the later dissolution increases the reservoir space in the study area to a certain extent. Different diagenetic facies reservoirs not only have obvious differences in porosity evolution characteristics but also have significant differences in pore throat radius distribution characteristics, movable fluid occurrence characteristics, and water drive oil characteristics. The pore throat distribution with radius greater than R_{50}~R_{60} determines the permeability. The difference in movable fluid saturation mainly depends on the connectivity of the relative large pore space corresponding to the relaxation time greater than the cut-off value of T_2. The size of pore throat radius has a good control effect on water flooding efficiency.

1. Introduction

In recent years, with the decreasing of conventional oil and gas resources, the world has increased the exploration and development of unconventional energy, especially tight oil and gas [1–9]. Compared with conventional sandstone reservoirs, tight sandstone reservoirs are characterized by small pore throats (micro- and nanoscale), complex pore structure, and strong micro- and macroheterogeneity [10]. Among them, the pore microstructure, pore type, pore evolution and control factors, and reservoir performance parameters have become the focus of tight oil reservoir research [11, 12]. The Ordos Basin is an early area of tight oil and gas exploration and development in China. The tight oil and gas resources are very rich and have broad prospects for exploration and development [13–15]. The Ordos Basin is the second largest sedimentary basin in my country. It is structurally located on the western edge of the North China Craton [16, 17]. The internal structure of the basin is relatively simple and the stratum is relatively gentle. The overall appearance is large monoclinic with wide and gentle on the east flank and steep and narrow on the west flank (Figure 1).

During the deposition process of Yanchang Formation in the Ordos Basin, the target reservoir rocks were

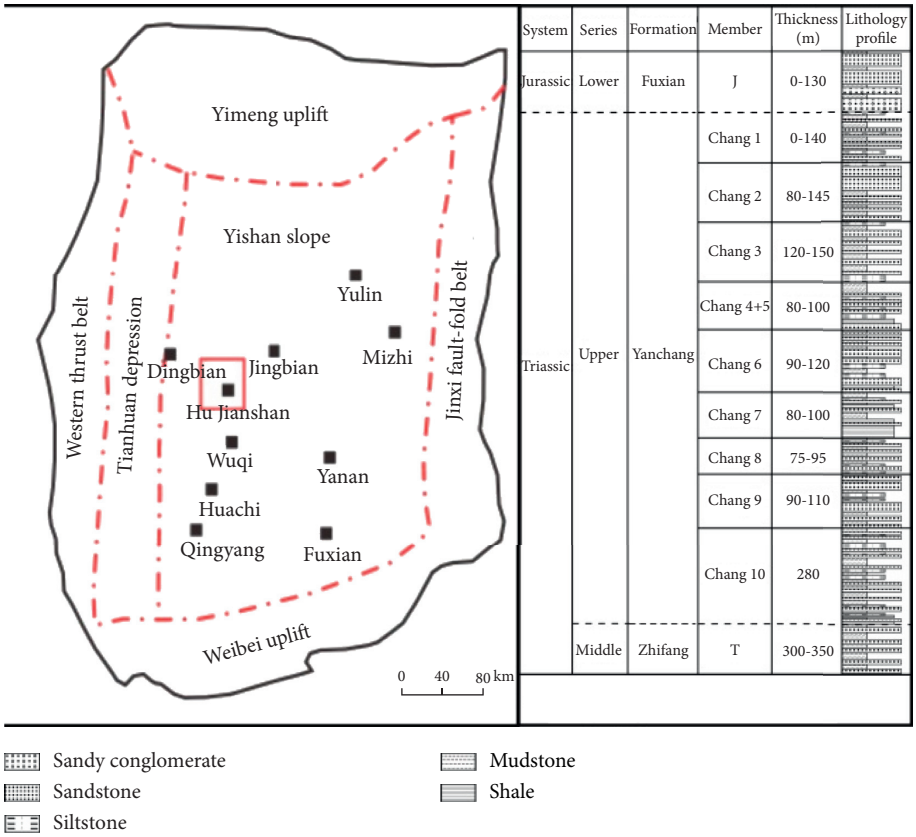

Figure 1: Geographical location of the midwestern regions, Ordos Basin.

compacted due to compaction and cementation, and a large number of micro- and nanoscale pore throats developed [18–20]. The types and distribution characteristics of micropore throats restrict the quality and development effect of tight sandstone reservoirs. Due to the different degree of diagenesis, the micropore throat parameters of tight sandstone reservoirs are significantly different. Even if the permeability level is the same, the pore throat parameters and distribution law may also show different characteristics. The complex pore throat structure characteristics lead to the changeable occurrence state and distribution characteristics of fluid in the pore throat, which directly restricts the next exploration and development. Therefore, it is necessary to analyze the microscopic pore structure characteristics under different diagenesis, hoping to provide reference for the optimization of high quality target areas of tight sandstone reservoirs. Based on the auxiliary experimental results of casting thin section, scanning electron microscope, X-ray diffraction, and cathodoluminescence, the microscopic pore structure and seepage characteristics of the study area were studied by high-pressure mercury injection, nuclear magnetic resonance, and microscopic water flooding experiments. The differences of microscopic characteristics of different diagenetic phases were analyzed, and the main influencing factors of microscopic characteristics were clarified, so as to provide guidance for further understanding the heterogeneity of tight sandstone reservoirs and evaluating the effective reservoir distribution.

2. Experimental Principle and Sample Information

2.1. Pore Throat Structure Test. The mercury injection experiment is one of the important methods to analyze the microscopic pore throat structure of the reservoir. The high-pressure mercury intrusion experiment is based on the Washburn equation by converting the mercury entry or exit pressure and the pore diameter to achieve different pore diameters and mercury entry saturations. The corresponding relationship between the pore size distribution characteristics is further obtained. It is widely used to obtain reservoir microscopic pore structure parameters based on high-pressure mercury intrusion experiments to characterize reservoir quality [21, 22]. The high-pressure mercury intrusion experiment adopts AutoPore IV9510 automatic mercury intrusion instrument from Mike Company, the maximum working pressure of the instrument is 414 MPa, and the measuring range of pore throat radius is 0.003~1000 μm.

2.2. Movable Fluid Occurrence Test. Place the fluid-containing sample in a static magnetic field, and start to make the hydrogen nuclei contained in the fluid in the rock sample show nuclear magnetic resonance with a suitable radio frequency pulse. Remove the effect of the radio frequency pulse on the rock sample, and the hydrogen nuclei will immediately

release energy and appear. For nuclear magnetic resonance signals with a gradual decrease in energy, the time corresponding to this process is the relaxation time [23, 24], and the T_2 spectrum curve characteristics of the transverse T_2 relaxation time and T_2 attenuation are usually used for movable fluid occurrence and pore throat analysis of distribution. Different pore sizes have different corresponding relaxation times. The larger the T_2 relaxation time, the larger the pore size, and on the contrary, the smaller the pore. Therefore, the T_2 spectrum can be used to reflect the development of the pore radius. Since the pore radius is too small, a large capillary force will obstruct the fluid flow and be constrained. At this time, the corresponding T_2 relaxation time is the T_2 cut-off value ($T_{2\text{cutcff}}$). The fluid that is less than the cut-off value of T_2 is called immovable fluid, and when it is more, it is called movable fluid. Nuclear magnetic resonance T_2 spectrum measurement uses RecCore-3000 nuclear magnetic resonance core analyzer, the system frequency is 2~5 MHz continuously adjustable, the magnetic induction intensity is 0.0940~0.1175 T, and the frequency accuracy is 0.01 Hz.

2.3. Microscopic Water Driving Oil Test. First, the core sample is made into a thin slice model of approximately 2.5cm × 2.5cm × 0.05 cm, and fluids that simulate crude oil and formation water are prepared according to the viscosity of the crude oil and the salinity of formation water in the study area, and dyes are added to dye red and blue, respectively. It is convenient to distinguish under the electron microscope. Make the simulated oil and simulated water flow into the sample model under a certain pressure. Through the use of electron microscope and microscopic image acquisition technology to observe the seepage mode and displacement effect of oil and water in the microscopic pore structure of the sample, it can intuitively reflect the characteristics of oil and water in the microscopic pore structure [25]. This microwater drive oil experiment was mainly implemented at the State Key Laboratory of Continental Dynamics of Northwest University through real sandstone microwater drive experiment equipment.

2.4. Sample Information. The tight sandstone reservoirs of the Yanchang Formation in the central and western regions of the Ordos Basin developed delta front subfacies deposits. From the experimental analysis of core physical properties, casting thin sections, scanning electron microscope, and cathodoluminescence of 180 core samples, it is known that the rock types are mainly feldspar sandstone, lithic feldspar sandstone, and feldspar lithic sandstone. Select 10 representative samples from them to further carry out the experimental analysis of high-pressure mercury intrusion, nuclear magnetic resonance, and microscopic water flooding models (Table 1).

3. Diagenesis Characteristics

3.1. Diagenesis Types

3.1.1. Compaction. In the early stage of diagenesis, the loose clastic minerals of the sediments due to the overlying pressure were gradually compacted to close contact. During the process, the pore water was discharged one after another and slowly consolidated into rock. Compaction played an important role after the sand body was deposited. With the deepening of burial, detrital particles often exhibit directional arrangement, close contact relationship, multiple rigid fractures, multiple plastic deformations, etc., and at the same time, a large number of pores are reduced. It will cause great damage to the storage space and seepage capacity of the reservoir, which is an important reason for the deterioration of the reservoir quality. The controlling factors are mainly the pressure of the overlying formation, the ratio of impurity bases, and the compressive resistance of particles [26–28]. Through the observation of thin slices under the microscope, it can be found that the rigid quartz particles exhibit directional arrangement, and the particles are mostly point-line and line contact relationships. In some samples, it can be found that the particles are in concave-convex contact relationship and the phenomenon of particle fracture (Figure 2(a)). Plastic minerals such as plastic cuttings and mica have relatively soft characteristics and are prone to deforming during the compaction process and fill in the particle space, thereby affecting the porosity (Figure 2(b)).

3.1.2. Cementation. Cementation is the effect of the fluid in the rock consolidating the clastic minerals, causing pore blockage in the process, which is the main reason for the further destruction of the physical properties of the reservoir. The cementation in the study area is more obvious, mainly including authigenic clay minerals, carbonates, and siliceous cements.

(1) Clay Mineral Cementation. The formation of clay minerals is mainly determined by the mineral composition, fluid characteristics, and temperature conditions. There are various types of clay minerals in the study area, with high content of chlorite, illite, and kaolinite.

Through the microscopic identification, the chlorite in the study area is mainly attached to the surface of the particles in the shape of a crust, which develops in the shape of small sharp flakes or scales (Figure 2(c)), and the chlorite is continuously distributed in a film shape (Figure 2(d)). It can not only consolidate the particles, but also have a certain protective effect on the particles and pores. However, a large number of developed chlorites are often easy to fill small pores and even throats, causing physical damage.

The illite cementation in the study area is generally developed, mainly in the form of thin film filaments and bridges, which occur in the intergranular pores, often divided into pores and roars, and the overall continuity is poor (Figures 2(e) and 2(f)). Illite easily cuts the pore space, thereby reducing the connectivity between each other, causing the pores to become micropores, and the throats are mostly blocked, which reduces the storage performance and seepage capacity of the reservoir to a certain extent.

The study area is dominated by authigenic kaolinite, with good crystal shape, mostly in the form of hexagonal plate and vermicular aggregates filled in the pore space

Table 1: Sample information table.

Well number	Depth, m	Porosity, %	Gas permeability, $\times 10^{-3}\ \mu m^2$	Experimental test	Rock type	Sedimentary facies	Horizon
A144	2193.9	9.39	0.098	Microscopic water driving oil, NMR	Feldspar sandstone	Deltaic front subfacies	Chang 6
H393	2247.3	10.80	0.253				
A36	1945.2	10.8	0.137				
Y182	2101.2	12.3	0.083	HPMI	Lithic feldspar sandstone		
A211	1922.6	8.9	0.058				
Y144	2178.4	8.4	0.027				
H185	2226.5	11.75	0.085				
H248	2037.1	10.08	0.023	Microscopic water driving oil, NMR	Feldspar lithic sandstone		Chang 8
A296	2197.6	10.6	0.126				
H26	2199.9	6.4	0.016				

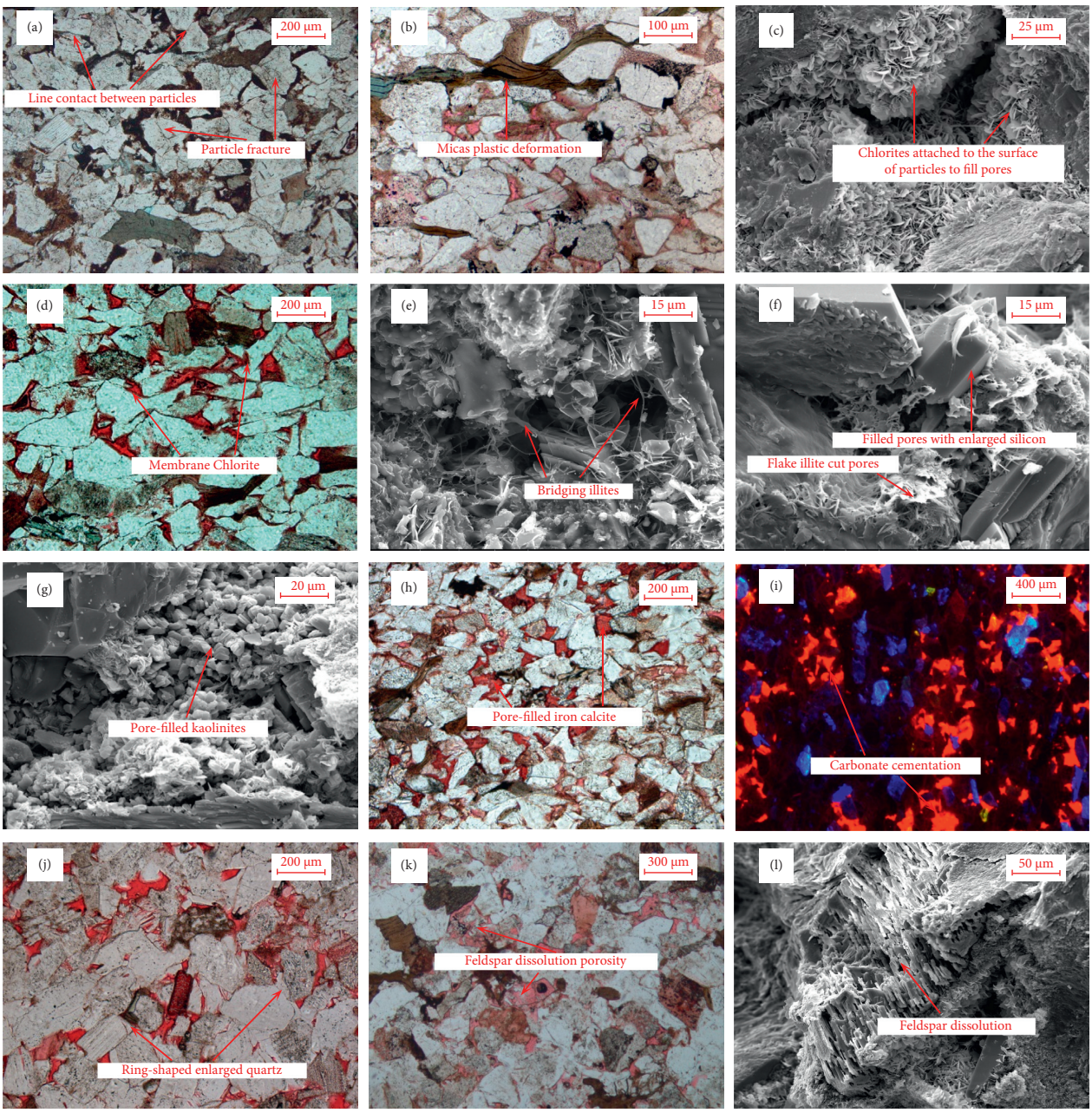

Figure 2: Microscope figures of typical diagenetic phenomena of samples.

(Figure 2(g)), which is mostly found in primary intergranular pores and intergranular dissolved pores. Kaolinite cement blocks the pores, resulting in a reduction in pore space and a more complex pore structure. At the same time, the porosity and seepage rate of the reservoir are reduced and the heterogeneity of the reservoir is enhanced. However, kaolinite has more developed intercrystalline pores, which can increase the micropores in the pore space, and it often appears dark brown under thin-film microscope.

(2) Carbonate Cementation. Using the statistics of the thin slice experiment data of the sample and the observation under the microscope, it is found that different degrees of carbonate cementation and filling of pores have occurred in the study area. The cementation is dominated by iron calcite (Figure 2(h)). The pores are filled by carbonate, which leads to the loss of a large amount of pore space, and the structure between particles is more complex and diverse.

The carbonate in the early diagenesis is mainly calcite in the form of micrite and microcrystalline. When the carbonate ions in the early pore medium reach the saturated state, the early carbonate cement will be precipitated, resulting in a large amount of filling of the pore space. However, calcite filling also improves the ability of sandstone to resist compaction to a certain extent and plays a certain role in the formation of secondary pores for subsequent dissolution. In the middle and late stages, iron ions are often precipitated due to the mutual transformation between rock cuttings and other dark minerals and clay minerals, which are easy to form with the calcite formed in the early stage. The iron calcite is distributed in intergranular pores and dissolved pores (Figure 2(i)), making the reservoir rock dense.

(3) Silicone Cementation. The siliceous cementation in the study area is mainly manifested by the development of secondary quartz enlargement and authigenic quartz. The secondary enlargement of grade II and III quartz is more common under the microscope, and the edge of the quartz grain is locally developed (Figure 2(j)), and the ring edge is rare. Its formation is mainly related to the mutual transformation of clay minerals and the dissolution of silicate minerals and is controlled by the size of the growth space. It is more common in sandstone reservoirs with small interstitial content. The development of secondary enlarged edges occupies part of the intergranular pore space, which is not conducive to the preservation of intergranular pores. In addition, under the scanning electron microscope, it can be seen that the quartz particles surrounded by the chlorite film have enlarged quartz edges where the local chlorite film is not developed. The authigenic quartz crystals are often filled in the residual intergranular pores.

3.1.3. Corrosion. According to the casting thin section of the sample and the statistics of the experimental data of the scanning electron microscope and the observation under the microscope, the dissolution in the study area is mainly the dissolution of feldspar (0.78%), followed by the dissolution of cuttings (0.13%). The total content of dissolved pores accounts for 28.6% of the total porosity, which improves the reservoir performance and pore-throat connectivity to a certain extent. Feldspar is dissolved to produce secondary dissolution pores (Figure 2(k)), which often dissolve along the joint surface (Figure 2(l)). Some feldspars may disappear due to the excessively strong dissolution degree, and the dissolution of lithic debris can be seen locally.

3.2. Evolution Characteristics of Porosity

3.2.1. The Influence of Diagenesis on Porosity. Quantitative analysis of compaction is carried out by calculation of porosity after porosity. After compaction, the remaining porosity can be used for the current cement content, intergranular pore content, micropore content, measured porosity, and the total displayed under the thin-film microscope. The correlation between the porosity contents is brought into formulas (i)–(iii) in Table 2, and the porosity after compaction can be calculated. According to the contact relationship between particles and cement observed under the microscope, it can help to divide the sequence of the development of different cements, and start to develop with strong dissolution as the boundary, and divide the cement into early and midlate. In the early stage, it was mainly thin-film chlorite, grade I quartz secondary enlargement, calcite, and other cements. In the middle and late stages, it was mainly grade II~III quartz ring enlargement edge, pom-shaped chlorite, kaolinite, iron calcite, illite, etc. Putting the relevant volume fraction into formulas (iv) and (v) in Table 2, the lost porosity and porosity of the early cementation and the middle and late cementation can be obtained, respectively. The increase in porosity and porosity increase rate due to dissolution are given in formulas (vi) and (vii) in Table 2.

The calculation results show (Table 3) that the sorting coefficient is mainly distributed between 1.11 and 1.73, with an average of 1.43, which is biased towards fineness. The main distribution range of the initial porosity is 32.96%~39.68%, with an average of 36.92%, showing a nearly normal distribution, slightly biased towards the roughness. The remaining porosity after compaction in the early diagenesis is mainly distributed between 10.23% and 30.14%, with an average of 18.51%, and the porosity loss rate is between 30.22% and 73.83%, with an average of 50.62%. The remaining porosity distribution ranges from 3.39% to 10.52% after cementation, with an average of 8.13%. The porosity loss caused by early cementation and metasomatism ranges from 1.13% to 14.72%, with an average of 3.96%. The porosity distribution of the middle and late cementation loss ranges from 2.25% to 13.1%, with an average of 6.42%. The secondary dissolution porosity produced by dissolution is 0.34~7.47%, with an average of 2.26%. It shows that when the pore volume of the reservoir is greatly reduced, the dissolved pores increase the storage space of the reservoir in the study area to a certain extent. However, the wider distribution range has strong uneven characteristics.

Table 2: Quantitative calculation method of sandstone porosity evolution.

Porosity evolution parameter	Formula	Remarks
Initial porosity	$\Phi_1 = 20.91 + 22.9/S_d$ (i)	Φ_1 represents the original porosity of the unconsolidated sandstone, %; S_d represents the Trask sorting coefficient, $S_d = (P_{25}/P_{75})^{1/2}$ (in which P_{25} and P_{75} represent the corresponding granular diameter of 25%-in-content particles and 75%-in-content particles in the accumulative granularity curve, respectively, mm)
Porosity after compaction	$\Phi_2 = C + (P_1 + P_2) \times P_3/P_4$ (ii) $F_a = (\Phi_1 - \Phi_2)/\Phi_1$ (iii)	Φ_2 represents the porosity after compaction, %; C represents the cement content, %; P_1 represents the surface porosity of intergranular pores, %; P_2 represents the surface porosity of original micropores, %; P_3 represents the measured porosity of the sample, %; P_4 represents the total surface porosity, %; P_a represents the porosity loss due to compaction, %; F_a represents the ratio of porosity loss due to compaction, %
Porosity after cementation	$\Phi_3 = \Phi_2 - C$ (iv) $F_b = (\Phi_2 - \Phi_3) \times 100\%/\Phi_1$ (v)	Φ_3 represents the porosity after compaction and cementation, %; F_b represents the ratio of porosity loss due to cementation, %
Dissolution increases porosity	$\Phi_4 = P_5 \times P_3/P_4$ (vi) $F_c = \Phi_4 \times 100\%/\Phi_1$ (vii)	Φ_4 represents the increased porosity due to dissolution, %; P_5 represents the total dissolution pore surface area, %; F_c represents the ratio of porosity loss due to dissolution, %

Table 3: Statistics of porosity evolution in diagenesis.

Compaction	Initial porosity, %		Porosity after compaction, %		The ratio of porosity loss due to compaction, %			
	Range	Average	Range	Average	Range	Average		
	32.96~39.68	36.87	10.23~30.14	18.43	30.22~73.83	50.54		
Cementation	Porosity loss due to early cementation, %		Porosity loss due to the midlate cementation, %		Porosity after compaction and cementation, %			
	Range	Average	Range	Average	Range	Average		
	1.13~14.72	3.96	2.25~13.1	6.42	3.39~10.52	8.19		
Corrosion	Increased porosity due to dissolution, %		Final calculation of porosity, %		Porosity measured by gas, %		Error, %	
	Range	Average	Range	Average	Range	Average	Range	Average
	0.34~7.47	2.21	4.82~13.87	10.33	4.35~16.77	10.75	0.79~20.3	6.89

3.2.2. Porosity Evolution Differences of Different Types of Diagenetic Facies. On the basis of thin section observation and identification data analysis and statistics, by analyzing the response correlation between different mineral characteristics, pore types and distribution characteristics, and macro- and microcharacteristics, the main control minerals, pore types, and other characteristics are shown. Four types of diagenetic facies are divided: the residual chlorite-membrane intergranular-pore diagenetic facies, the feldspar dissolution diagenetic facies, the clay mineral cemented microporous diagenetic facies, and the carbonate cemented tight diagenetic facies (Figure 3).

Formulas (i)~(vii) in Table 2 are used to establish the porosity evolution simulation equations of four different diagenetic facies in the study area. Through the above studies, it is found that, according to the diagenetic evolution process, a large number of minerals and fluids continue to resist compaction, fill pores, and dissolve particles in the pore space of sediments. However, the effects of different diagenesis in different regions and environments are also different, which can be proved by the porosity evolution characteristics of diagenetic facies. The final calculated porosity of residual chlorite-membrane intergranular-pore diagenetic facies is 12.28%. The dissolution porosity of feldspar dissolution diagenetic facies increased the most, with an average of 3.95%. Clay mineral cemented microporous diagenetic facies lost the most porosity due to the middle and late cementation, with an average of 8.11%. The compaction of carbonate cemented tight diagenetic facies leads to the smallest loss of porosity, while the early cementation leads to the largest loss of porosity, which is 17.12%.

4. Differences in Microscopic Characteristics of Different Diagenetic Facies

4.1. Differences in Pore Throat Structure. Through the analysis of the size distribution of different types of pore throats and the control of physical properties in Figure 4, it is found that the main peak value of mercury inflow and permeability contribution value of the residual chlorite-membrane intergranular-pore diagenetic facies are both at >1 μm. The main peak values of mercury inflow and permeability contribution from pore throats of the feldspar dissolution diagenetic facies are both between 0.5 μm and 1 μm. Due to the later cementation, the pore throat of the clay mineral cemented microporous diagenetic facies is seriously damaged, the pore throat configuration is poor, the number of mesopore throats is reduced, the pore throat mercury intake decreases, the cumulative mercury intake

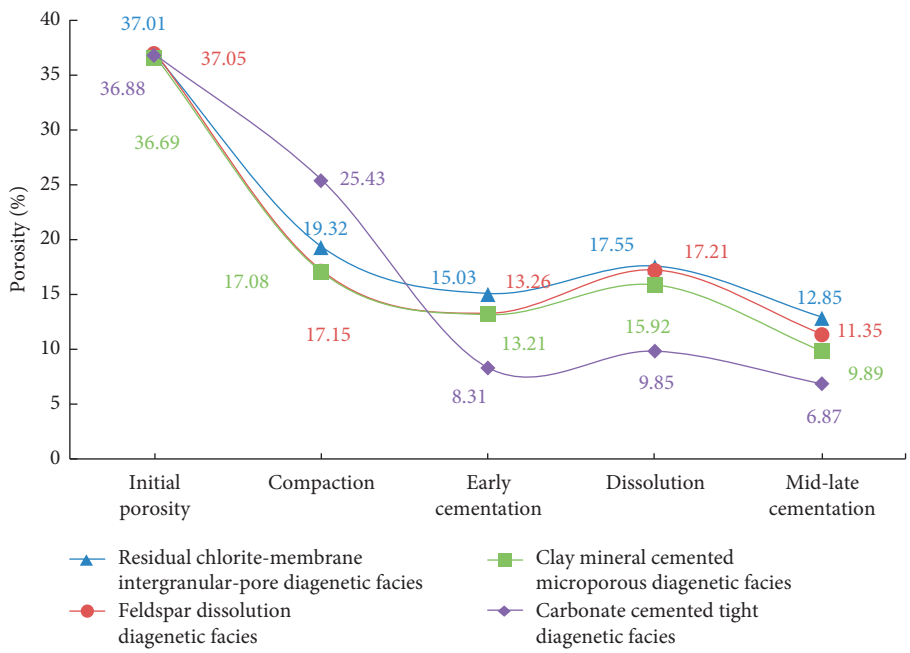

Figure 3: Pore evolution process of different diagenetic facies.

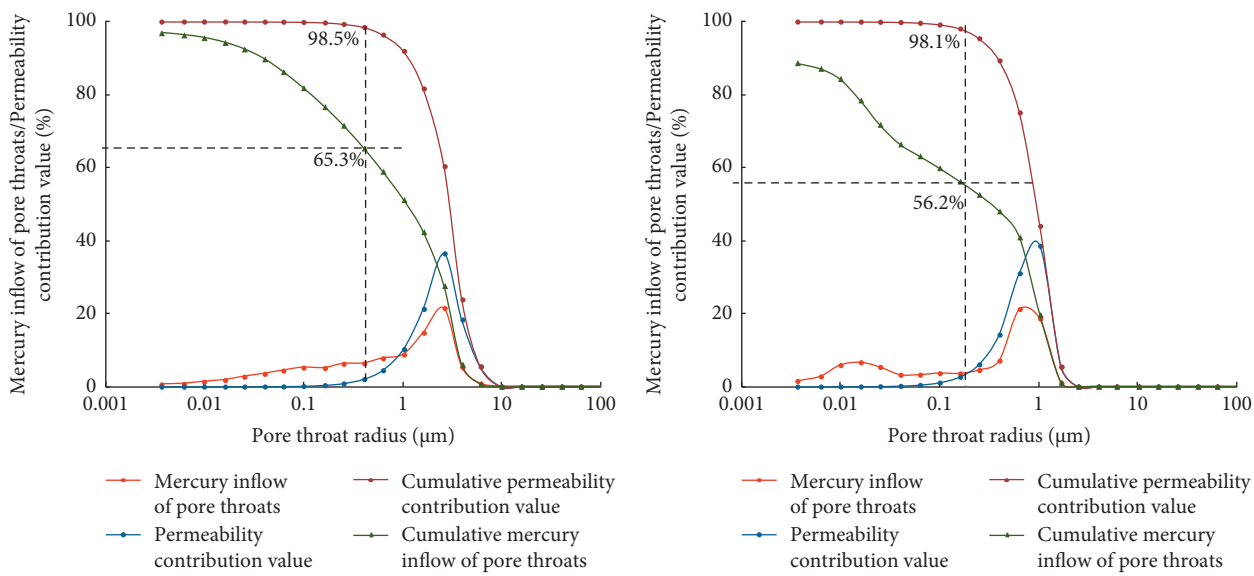

(a) (b)

Figure 4: Continued.

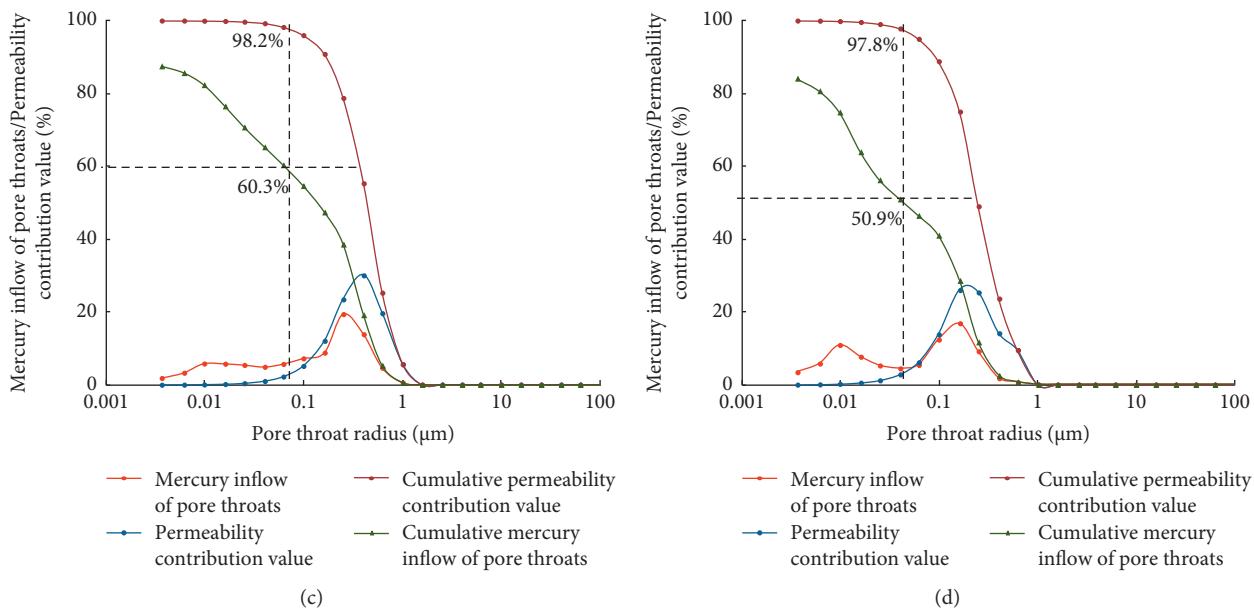

Figure 4: Different types of pressure curves and pore throat distribution characteristics. (a) Residual chlorite-membrane intergranular-pore diagenetic facies, A3, 1945.2 m. (b) Feldspar dissolution diagenetic facies, Y182, 2101.2 m. (c) Clay mineral cemented microporous diagenetic facies, A211, 1922.6 m. (d) Carbonate cemented tight diagenetic facies, Y144, 2178.4 m.

decreases, and the main peak of the pore throat radius of the contribution value of permeability and permeability is between 0.1 μm~0.5 μm. The pore throats of the carbonate cemented tight diagenetic facies have almost disappeared. Unimodal is the main morphology that contributes to the pore throat radius interval and permeability. Permeability contribution rate and pore throat mercury ingress are the least. The main peak value of pore throat mercury ingress and permeability contribution value of pore throat radius are both at <0.1 μm.

In the initial stage of mercury intrusion experiment, for samples with different permeability, the relatively large pore throat occupies a small proportion. However, the cumulative permeability contribution value rose rapidly to about 98% within the radius of the large pore throat. The cumulative mercury saturation in this interval is also increasing rapidly, and the curve is relatively steep, but the steepness is not as steep as the cumulative permeability contribution rate. The cumulative mercury saturation achieved in this interval is mainly distributed between 49% and 66%. Subsequently, mercury continued to enter the sample, and the cumulative permeability contribution curve showed a flat trend with a slow increase rate. However, the increase rate of accumulated mercury saturation did not decrease significantly. It shows that the relatively large pore throat mainly controls the permeability, and the relatively small pore throat has little effect on the permeability, but has a certain storage capacity. Through analysis of mercury intrusion samples in the study area, it was found that the average mercury saturation of about 29.5% was controlled by relatively small pore throats. The permeability of the study area is mostly controlled by pore throats with a radius larger than R_{50}~R_{60}.

When the characteristics of mercury injection curves of different diagenetic facies are compared, it is found that the permeability contribution curve shifts to the left as the sample permeability decreases, indicating that the greater the permeability, the larger the proportion of relatively large pore throats, and vice versa. The diagenetic facies pore throat radius distribution is obviously different, which determines the permeability difference.

4.2. Differences in the Occurrence Characteristics of Movable Fluids. The movable fluid saturation of the residual chlorite-membrane intergranular-pore diagenetic facies samples of the chlorite membrane is the highest, which is 58.5%, of which the movable pore space corresponding to the relaxation time greater than the T_2 cut-off value is 44.8%, and the movable pore space corresponding to the T_2 cut-off value is less than 13.7%. The morphological characteristics of the T_2 spectrum curve before centrifugation showed a double-peak shape with high left and low right, and the T_2 cut-off value was 4.97 ms. After centrifugation, the morphological characteristics of the T_2 spectrum curve changed to a near-single peak shape (Figure 5(a)).

The movable fluid saturation of the feldspar dissolution diagenetic facies samples is medium, 35.66%, in which the movable pore space corresponding to the relaxation time greater than the T_2 cut-off value is 23.6%, and the movable pore space corresponding to the T_2 cut-off value is 12%. The morphological characteristics of the T_2 spectrum curve before centrifugation showed a double-peak shape of left high and right low type. After centrifugation, the right peak of the T_2 spectrum curve decreased to a greater extent (Figure 5(b)).

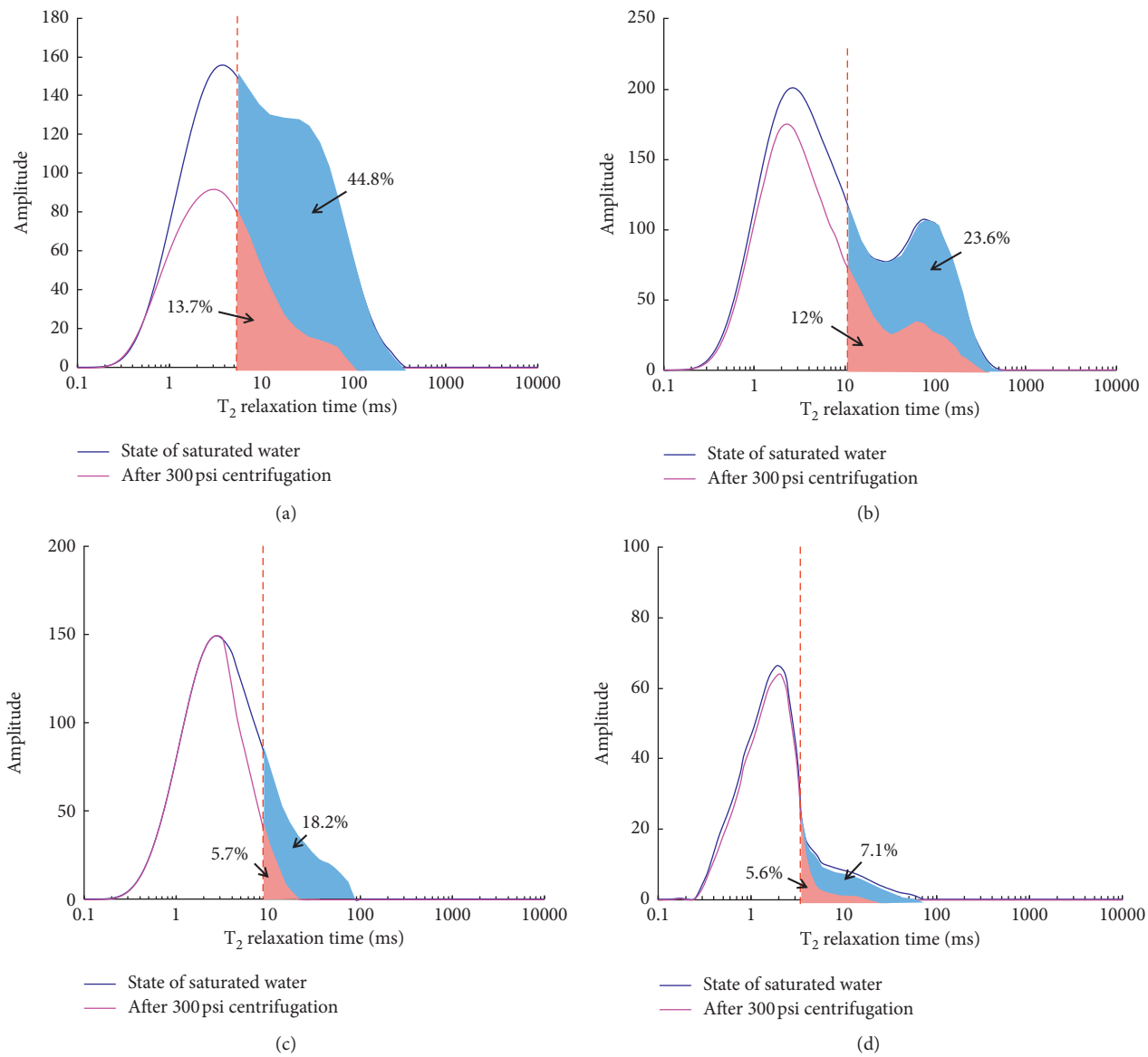

Figure 5: NMR T_2 spectrum distribution of different diagenetic facies. Note: the blue area is the movable pore space corresponding to the relaxation time greater than the T_2 cut-off value, the pink area is the movable pore space corresponding to the relaxation time less than the T_2 cut-off value, and the dashed line is the T_2 cut-off value. (a) Residual chlorite-membrane intergranular-pore diagenetic facies, H393, 2247.3 m. (b) Feldspar dissolution diagenetic facies, H185, 226.5 m. (c) Clay mineral cemented microporous diagenetic facies, A296, 2197.6 m. (d) Carbonate cemented tight diagenetic facies, H26, 2199.9 m.

The movable fluid saturation of the clay mineral cemented microporous diagenetic facies sample is relatively small, 23.9%, of which the movable pore space corresponding to the relaxation time greater than the T_2 cut-off value is 18.2%, and the movable pore space corresponding to the T_2 cut-off value is 5.7%. The T_2 spectrum curve before centrifugation is characterized by a single peak shape, and the T_2 spectrum curve shape after centrifugation mainly changes in the region greater than the T_2 cut-off value (Figure 5(c)).

The movable fluid saturation of the carbonate cemented tight diagenetic facies sample is the lowest at 12.69%, of which the movable pore space corresponding to the relaxation time greater than the T_2 cut-off value is 7.1%, and the movable pore space corresponding to the T_2 cut-off value is 5.6%. The morphological characteristics of the T_2 spectrum curve before centrifugation showed a single peak shape, and the shape of the T_2 spectrum curve after centrifugation hardly changed significantly (Figure 5(d)).

According to the above research and analysis, it is found that the movable fluid saturation and movable fluid porosity of the sandstone core samples of the low permeability reservoirs in the study area are generally low and have a large distribution range, and the microscopic pore structure heterogeneity is strong and the difference is large. The T_2 cut-off value is generally low. Most of the samples before and after centrifugation are smaller than the T_2 cut-off value. The curve shape changes little. The area where the movable fluid

saturation changes greatly is mainly the blue area, indicating the difference in the movable fluid saturation in the study area. It mainly depends on the degree of connectivity of the relatively large pore space corresponding to the relaxation time greater than the T_2 cut-off value, and the movable fluid saturation varies significantly between different diagenetic facies.

5. Conclusions

(1) The early compaction of diagenesis in the study area resulted in an average porosity loss rate of 50.62%, the overall cementation caused a porosity loss rate of about 27.8%, and the dissolution increased the secondary porosity to an average of 2.26%. The porosity evolution characteristics of different diagenetic facies are obviously different, and the final calculated porosity of the residual chlorite-membrane intergranular-pore diagenetic facies is the largest, with an average of 12.28%. The dissolution porosity of the feldspar dissolution diagenetic facies increases the most, with an average of 3.95%. The clay mineral cemented microporous diagenetic facies lose the most porosity due to the middle-late cementation, with an average of 8.11%. The carbonate cemented tight diagenetic facies lead to the smallest loss of porosity, while the early cementation leads to the largest loss of porosity, with an average of 17.12%.

(2) There are obvious differences in pore throat radius distribution characteristics, movable fluid occurrence characteristics, and water drive characteristics of different diagenetic facies. The size distribution of the pore throat radius controls the seepage capacity. The larger the proportion of relatively large pore throats, the greater the permeability and the stronger the seepage capacity. The pore throat distribution with a radius greater than R_{50}~R_{60} determines the permeability. The difference of movable fluid saturation mainly depends on the degree of connectivity of the relatively large pore space corresponding to the relaxation time greater than the T_2 cut-off value.

Data Availability

The underlying data supporting the results are from Changqing Oilfield Database.

Conflicts of Interest

The authors declare that they have no conflicts of interest.

Acknowledgments

This work was funded by National Science and Technology Major Project of the Ministry of Science and Technology of China (2017ZX05013-004 and 2017ZX05069-003), Open Foundation of Key Laboratory of Coal Resources Exploration and Comprehensive Utilization, Ministry of Natural Resources (KF2021-3), Shaanxi Provincial Key Research and Development Program (2021GY-140), Opening Foundation of Shaanxi Key Laboratory of Advanced Stimulation Technology for Oil & Gas Reservoirs (20JS120), National Natural Science Foundation of China (51934005 and 52074226), and Young Science and Technology Talents Foundation of Shaanxi Province (2019KJXX-054).

References

[1] M. He, Q. Wang, and Q. Wu, "Innovation and future of mining rock mechanics," *Journal of Rock Mechanics and Geotechnical Engineering*, vol. 13, no. 1, pp. 1–21, 2021.

[2] C. Zhu, M.-C. He, M. Karakus, X.-H. Zhang, and Z. Guo, "The collision experiment between rolling stones of different shapes and protective cushion in open-pit mines," *Journal of Mountain Science*, vol. 18, no. 5, pp. 1391–1403, 2021.

[3] C. Zhu, M. He, M. Karakus, X. Zhang, and Z. Tao, "Numerical simulations of the failure process of anaclinal slope physical model and control mechanism of negative Poisson's ratio cable," *Bulletin of Engineering Geology and the Environment*, vol. 80, no. 4, pp. 3365–3380, 2021.

[4] F. Wu, R. Gao, J. Liu, and C. Li, "New fractional variable-order creep model with short memory," *Applied Mathematics and Computation*, vol. 380, Article ID 125278, 2020.

[5] F. Wu, H. Zhang, Q. Zou, C. Li, J. Chen, and R. Gao, "Viscoelastic-plastic damage creep model for salt rock based on fractional derivative theory," *Mechanics of Materials*, vol. 150, Article ID 103600, 2020.

[6] Q. Wang, Y. Wang, M. C. He et al., "Experimental research and application of automatically formed roadway without advance tunneling," *Tunnelling and Underground Space Technology*, vol. 114, no. 3, 2021.

[7] B. Li, R. Bao, Y. Wang, R. Liu, and C. Zhao, "Permeability evolution of two-dimensional fracture networks during shear under constant normal stiffness boundary conditions," *Rock Mechanics and Rock Engineering*, vol. 54, no. 3, pp. 1–20, 2021.

[8] C. N. Zou, R. K. Zhu, S. T. Wu et al., "Types, characteristics, genesis and prospects of conventional and unconventional hydrocarbon accumulations: taking tight oil and tight gas in China as an instance," *Acta Petrolei Sinica*, vol. 33, no. 2, pp. 173–187, 2012.

[9] H. Gao, M. Q. He, P. Y. Zhao, L. B. Dou, and C. Wang, "Comparison of geological characteristics of Chang 7 shale oil in Ordos basin and typical shale oil in north America," *Petroleum Geology and Experiment*, vol. 40, no. 2, pp. 133–140, 2018.

[10] X. P. Yang, W. Z. Zhao, C. N. Zou, and M. J. Chen, "Origin of low-permeability reservoir and distribution of favorable reservoir," *Acta Petrol Sinica*, vol. 28, no. 4, pp. 57–61, 2007.

[11] P. H. Nelson, "Pore-throat sizes in sandstones, tight sandstones, and shales," *AAPG Bulletin*, vol. 93, no. 3, pp. 329–340, 2009.

[12] R. G. Loucks, R. M. Reed, S. C. Ruppel, and D. M. Jarvie, "Morphology, genesis, and distribution of nanometer-scale pores in siliceous mudstones of the mississippian barnett shale," *Journal of Sedimentary Research*, vol. 79, no. 12, pp. 848–861, 2009.

[13] H. Yang, S. X. Li, and X. Y. Liu, "Characteristics and resource prospects of tight oil and shale oil in Ordos basin," *Acta Petrolei Sinica*, vol. 34, no. 1, pp. 1–11, 2013.

[14] Q. L. Guo, N. Wu, N. S. Chen, H. J. Ren, Z. Yang, and H. B. Xie, "An assessment of tight oil resource in 7th oil reservoirs of Yanchang formation Ordos basin," *Acta Petrolei Sinica*, vol. 38, no. 6, pp. 658–665, 2017.

[15] H. Wu, C. L. Zhang, Y. L. Ji et al., "Pore throat size characterization of tigh sandstone and its control on reservoir physicalp roperties: a case study of Yanchang formation,

eastern Gansu, Ordos basin," *Acta Petrolei Sinica*, vol. 38, no. 8, pp. 876–887, 2017.

[16] Y. Yang, W. Li, and L. Ma, "Tectonic and stratigraphic controls of hydrocarbon systems in the Ordos basin: a multicycle cratonic basin in central China," *AAPG Bulletin*, vol. 89, no. 2, pp. 255–269, 2005.

[17] S. X. Li, X. Q. Deng, J. L. Pang, J. W. Lv, and X. Liu, "Relationship between petroleum accumulation of mesozoic and tectonic movement in Ordos basin," *Acta Petrolei Sinica*, vol. 28, no. 4, pp. 798–807, 2010.

[18] B. Bai, R. K. Zhu, S. T. Wu, J. W. Cui, T. Su, and T. T. Li, "New microthroat structural characterization techniques for unconventional tight hydrocarbon reservoir," *China Petroleum Exploration*, vol. 19, no. 3, pp. 78–86, 2015.

[19] Q. Wang, P. A. Peng, W. Z. Zhang, J. Z. Liu, and C. L. Yu, "Quantitative full-component hydrocarbon-generating simulation and crude oil mobility evaluation of shale in 7th member of Yanchang formation, Ordos basin," *Acta Petrolei Sinica*, vol. 3, no. 5, pp. 541–553, 2018.

[20] J. Yu, X. Yang, B. Li, X. J. Liu, and J. F. Tian, "A method of determining movable fluid saturation of tight oil reservoirs: a case study of tight oil reservoirs in seventh member of Yanchang formation in Heshui area," *Petroleum Geology and Experiment*, vol. 36, no. 6, pp. 767–772, 2014.

[21] R. E. Liu, F. J. Sun, X. F. Wei, X. Q. Shan, H. Zhao, and J. Lin, "Difference of reservoir microscopic features of the quartz sandstone and litharenite of the 2nd member of Shanxi formation,upper paleozoic in middle east Ordos basin," *Petroleum Exploration and Development*, vol. 32, no. 5, pp. 56–58, 2005.

[22] B. S. Nabawy, Y. Géraud, P. Rochette, and N. Bur, "Pore-throat characterization in highly porous and permeable sandstones," *AAPG Bulletin*, vol. 93, no. 6, pp. 719–739, 2009.

[23] W. M. Wang, H. K. Guo, and Z. H. Ye, "The evaluation of development potential in low permeability oilfield by the aid of NMR movable fluid detecting technology," *Acta Petrolei Sinica*, vol. 22, no. 6, pp. 40–44, 2001.

[24] K. Zheng, H. M. Xu, J. W. Chen, and Y. H. Wang, "Movable fluid study of low permeability reservoir with nuclear magnetic resonance technology," *Geoence*, vol. 27, no. 3, pp. 710–718, 2013.

[25] P. Li, W. Sun, B. Wu, Y. Gao, and K. Du, "Occurrence characteristics and influential factors of movable fluids in pores with different structures of Chang 63 reservoir, Huaqing oilfield, Ordos basin, China," *Marine and Petroleum Geology*, vol. 97, pp. 480–492, 2018.

[26] K. Al-Ramadan, S. Morad, J. N. Proust, and I. Al-Aasm, "Distribution of diagenetic alterations in siliciclastic shoreface deposits within a sequence stratigraphic framework: evidence from the upper jurassic, boulonnais, NW France," *Journal of Sedimentary Research*, vol. 75, no. 5, pp. 943–959, 2005.

[27] S. A. Stonecipher, "Applied sandstone diagenesis practical petrographic solutions for a variety of common exploration, development, and production problems," *SEPM Short Course*, vol. 50, p. 143, 2000.

[28] A. M. Wolela and E. H. Gierlowski-Kordesch, "Diagenetic history of fluvial and lacustrine sandstones of the hartford basin (triassic-jurassic), newark supergroup, USA," *Sedimentary Geology*, vol. 197, no. 1-2, pp. 99–126, 2007.

Hindawi
Mathematical Problems in Engineering
Volume 2021, Article ID 3158504, 8 pages
https://doi.org/10.1155/2021/3158504

Research Article

Analysis of Microscopic Main Controlling Factors for Occurrence of Movable Fluid in Tight Sandstone Gas Reservoirs Based on Improved Grey Correlation Theory

Xuefei Lu,[1] Fengjuan Dong,[2,3] Xiaolong Wei,[4] PengTao Wang,[5] Na Liu,[6,7] and Dazhong Ren[2,3]

[1]*College of Sciences, Xi'an Shiyou University, Xi'an 710065, Shaanxi, China*
[2]*College of Petroleum Engineering, Xi'an Shiyou University, Xi'an 710065, Shaanxi, China*
[3]*Shaanxi Key Laboratory of Advanced Stimulation Technology for Oil & Gas Reservoirs, Xi'an Shiyou University, Xi'an 710065, Shaanxi, China*
[4]*Changqing Downhole Technology Company, Petro China Chuanqing Drilling Engineering Company Limited, Xi'an 710065, Shaanxi, China*
[5]*Sinopec Green Source Thermal Energy Development Co., Ltd, Xianyang 712000, Shaanxi, China*
[6]*Research Institute of Exploration and Development, Petro China Changqing Oilfield Company, Xi'an 710018, Shaanxi, China*
[7]*National Engineering Laboratory for Exploration and Development of Low Permeability Oil and Gas Fields, Xi'an 710018, Shaanxi, China*

Correspondence should be addressed to Xuefei Lu; luxuefei80@126.com

Received 8 July 2021; Accepted 16 August 2021; Published 21 August 2021

Academic Editor: Feng Xiong

Tight sandstone reservoirs have the characteristics of poor physical properties, fine pore throats, and strong microheterogeneity compared with conventional reservoirs, which results in complicated movable fluid occurrence laws and difficult mining. Taking the tight sandstone gas reservoir of He 8 formation in Sulige gas field as an example, based on physical property test analysis, constant velocity mercury injection, and nuclear magnetic resonance experiments, an optimized gray correlation calculation model is established by improved gray correlation theory, which quantitatively characterizes the influence of microscopic pore structure parameters of different types of tight sandstone gas reservoirs on the occurrence of movable fluids, and the main controlling microgeological factors for the occurrence of movable fluid in tight sandstone gas reservoirs with close/similar physical properties are selected. The results show that the occurrence of movable fluid in Type I reservoirs is mainly affected by the effective pore-throat radius ratio, the saturation of mercury in the total throat, and the effective pore radius, and the occurrence of movable fluid in Type II reservoirs is mainly affected by the effective throat radius per unit volume and total throat mercury saturation and mainstream throat radius. Moreover, the occurrence state of movable fluids in Type II reservoirs is controlled by the throat radius stronger than that of Type I reservoirs. It has important guiding significance for the efficient development of tight sandstone gas reservoirs.

1. Introduction

The exploration and development of tight sandstone oil and gas in unconventional oil and gas occupy an increasingly important position in the field of oil and gas exploration in China [1–3]. Under the coupling action of time, temperature, pressure, and other factors, the creep characteristics of rock particles at different buried depths are different, resulting in different types of reservoirs with different pore structure characteristics, storage and seepage capabilities [4–7]. Pores and throats are the main channels for controlling fluid seepage [8, 9]. The size and distribution of pores and throats affect the connectivity and seepage capacity of pores and throats [10, 11]. A large number of

studies have shown that the proportion set of movable fluids includes reservoir, storage capacity, and fluid storage characteristics, and it is more ideal to characterize the physical properties of ultra-low permeability reservoirs. However, the tight sandstone reservoirs have the characteristics of poor physical properties, small pore throats, and strong microheterogeneity [12–15] compared with conventional reservoirs, which leads to complex reservoirs of movable fluids and difficult mining. At present, new technologies and methodologies are introduced by many scholars to discuss the occurrence of movable fluids in tight reservoirs and their main controlling factors and have achieved certain results. For example, some scholars combine high-pressure mercury intrusion, nitrogen adsorption, image analysis, and other technical methods with nuclear magnetic resonance experiments to reveal the influence of microgeological factors on the occurrence of movable fluids in the reservoir. Studies have shown that the recoverability of oil and gas reservoirs is mainly affected by the pore structure and the occurrence characteristics of movable fluids; the microscopic pore structure characteristics have a significant impact on movable fluids [16–19].

However, their research mainly uses qualitative analysis methods to describe the impact of reservoir microgeological factors on the occurrence of movable fluids. The interaction between various factors has not been considered, and it is difficult to accurately quantify the impact of microgeological factors on the reservoir movable fluids, which has become one of the technical bottlenecks restricting the development of tight oil and gas reservoirs. Therefore, taking the tight sandstone reservoir of He8 formation in Sulige gas field as an example, based on the physical properties of the reservoir, constant velocity mercury intrusion, and nuclear magnetic resonance experiments, the scientific determination resolution coefficient is introduced, and the improved gray correlation analysis model is established to determine the main controlling factors affecting the occurrence of movable fluids in tight sandstone gas reservoirs with near/similar physical properties. It provides reliable microscopic geological basis for finding the "sweet spot" of tight sandstone reservoir and its further efficient development.

2. Experiments and Methods

2.1. Experiments

2.1.1. Experimental Samples and Test Methods

(1) Before Testing, Wash the Sample With Oil. The sample was washed with methanol and dichloromethane mixture in the Soxhlet extracter. When the fluorescence of the washing fluid was very low and unchanged, the washing oil was considered to be finished, and the sample was dried continuously by microwave at 100°C for 24 h.

(2) Porosity-Permeability Test. The experimental methods were strictly carried out in accordance with SY/T6385-1999 "Test method for porosity and permeability of overburden rocks" [20]. FYKS-1 porosity-permeability tester with high temperature and overburden pressure has tested the porosity and permeability. The main technical parameters are as follow: The effective pressure of simulated formation is less than 70 MPa; the effective temperature of simulated formation is less than 150°C; applicable core is $\Phi 25 \times 25 \sim 80$ mm or $\Phi 38 \times 40 \sim 80$ mm; measuring range of permeability is $(0.01 \sim 8000) \times 10^{-3}\ \mu m^2$, measuring range of porosity is less than 50%; measurement precision of permeability is less than 10% for low permeability reservoir and 5% for medium and high permeability reservoir; measurement precision of porosity is 0.5%.

(3) NMR Experiment. The nuclear magnetic resonance T_2 spectrum was measured by MicroMR20-025 from Newmai Company. The main frequency intensity was 23 MHz, the core diameter was 25 mm, the length was 2–4 cm, the echo interval was 0.2 ms, the waiting time was 6 s, and the echo number was 8000. The experimental method is strictly in accordance with SY/T6490-2014 "Laboratory measurement specification for nuclear magnetic resonance parameters of rock samples" [21]. The experiment was carried out at 22°C.

(4) CVMI Experiment. The experimental method was strictly carried out in accordance with GB/T29171-2012 "Rock capillary pressure measurement" [22]. The maximum mercury injection pressure in the constant rate mercury injection test was 0.006895 MPa.

(5) Scanning Electron Microscope. The experimental method was strictly carried out in accordance with SY/T 5162-2014 "Analytical method of rock sample by scanning electron microscope" [23].

(6) Casting Sheet Observation. The experimental methods were strictly carried out in accordance with SY/T 5913-2004 "Rock thin section preparation" [24].

2.2. Dimensionless Method. It is necessary to standardize each parameter [25] for making the parameters comparable, due to the different dimensions of different parameters and the large difference in value. The method is as follows:

(1) For the parameters (excluding parameters other than the effective pore-throat radius ratio) which are positively correlated with reservoir microscopic pore-throat structure characteristics and movable fluid saturation, divide directly by their maximum value.

(2) For parameters that are negatively related to characteristic parameters of reservoir microscopic pore throat structure and saturation of movable fluid (effective pore-throat radius ratio), the maximum value is used to subtract the difference of the parameters and then divided by the maximum value.

2.3. Improved Grey Relevance Theory. The concept of relevance analysis is proposed by Grey system theory, which can provide mathematical analysis methods to clarify the relationship between various factors in the system and find the

most influential factors [26–28]. In the traditional gray correlation analysis method, the resolution coefficient is not quantified but a fixed value 0.5, without considering the distortion of the correlation degree measurement caused by the abnormal value in the data. The improved gray correlation analysis method introduces the quantization process of the resolution coefficient, which makes the calculation process more reasonable [29–31]. The steps are as follows:

The absolute value of reference sequence and the reference sequence subtraction at each point is

$$\Delta_{0i}(k) = \left|X_0(k) - X_i(1)\right|. \tag{1}$$

Maximum range is

$$\Delta_{\max} = \max_i \max_k = \left|X_0(k) - X_i(k)\right|. \tag{2}$$

Minimum range is

$$\Delta_{\min} = \max_i \max_k = \left|X_0(k) - X_i(k)\right|. \tag{3}$$

Correlation coefficient is

$$\varepsilon_{0i}(k) = \frac{\Delta_{\min} + \rho\Delta_{\max}}{\left|\mathbf{X}_0(\mathbf{k}) - \mathbf{X}_i(\mathbf{k})\right| + \rho\Delta_{\max}}, \tag{4}$$

where $\varepsilon_{0i}(k)$ is the relative difference between the comparison curve $X_i(k)$ and the reference curve $X_0(k)$ at time i, which is called the correlation coefficient of $X_i(k)$ to $X_0(k)$ at time i. In order to weaken the influence of the correlation coefficient distortion caused by too large size and enhance the significant difference between correlation coefficients, a coefficient or resolution is artificially introduced, and its value is between 0~1. The quantization method is as follows:

$$\nabla_{ij} = \left|X_0(j) - X_i(j)\right|, \quad (i = 1, 2, \ldots, m;\ j = 1, 2, \ldots, n). \tag{5}$$

Assuming that ∇_θ is the average value of the absolute difference of indicators, then

$$\nabla_\theta = \left(\frac{1}{m}\right)\sum \nabla_{ij}, \quad (i = 1, 2, \ldots, m;\ j = 1, 2, \ldots, n). \tag{6}$$

Let $\varepsilon = \nabla_\theta/\nabla_{\max}$, where $\nabla_{\max} = (\max \nabla_{ij})$.

The value of ρ follows the following principles:

If $1/\varepsilon > 3$, that is, abnormal value, $\varepsilon \le \rho \le 1.5\varepsilon$, let $\rho = 1.5\varepsilon$.

If $2 \le 1/\varepsilon \le 3$ that is, the normal value, $1.5\varepsilon \le \rho \le 2\varepsilon$, let $\rho = 2\varepsilon$.

If $0 < 1/\varepsilon < 2$ that is, the normal value, $2\rho > 1$, let $\rho \in (0.8, 1)$, and 1 is used in this paper.

3. Analysis of Microcontrolling Geological Factors of Movable Fluid Occurrence

3.1. Reservoir Physical Properties and Movable Fluid. Porosity and permeability are not only indicators to characterize reservoir quality, but also closely related to the difficulty and effectiveness of oil and gas field exploitation [19]. It is show that, porosity is distributed in the range of 6.9%~18.3%, with an average of 11.735%; permeability is distributed in the range of $0.065 \times 10^{-3}\,\mu\text{m}^2$ ~$0.747 \times 10^{-3}\,\mu\text{m}^2$, with an average value of $0.291 \times 10^{-3}\,\mu\text{m}^2$, by physical testing and analysis of 10 representative cores in the reservoir of the He 8th member of the study area, and it belongs to a typical tight sandstone gas reservoir. Reservoir porosity has a positive linear correlation with permeability (Figure 1), but the correlation is not strong ($R^2 = 0.488$), which shows that the pore structure of the reservoir is complex, and the physical properties of the reservoir and the fluid flow capacity are controlled by a variety of microgeological factors.

It is found that the movable fluid saturation of the He 8th member in the study area is between 5.38%~32.67%, with an average of 17.56% (Table 1), which based on some scholars' research on the movable fluid of He 8 formation in the east of Sulige gas field.

We have the conclusion that there is a different degree of overlap in information for a single characteristic parameter, by in-depth analysis of the constant velocity mercury intrusion and physical property analysis results of 10 core samples from He 8 reservoir. Therefore, the reservoir quality factor is introduced, denoted by RQI = $\sqrt{K/\phi}$ [19], and it divides the reservoir into two types: I (RQI ≥ 0.15) and II (RQI < 0.15) (Table 1).

3.2. Microscopic Pore Structure Characteristics of Reservoir. According to the analysis of casting thin sections and scanning electron microscope data (Figure 2), it can be seen that the reservoir space types of tight sandstone reservoir in He 8 in the study area only include residual intergranular pores, dissolution pores, and intercrystalline pores. It is shown that the pores of the tight sandstone reservoirs in He 8 formation of the study area are macropores, and the pore size and distribution interval are similar, the main pore radius distribution interval is between 120 μm~150 μm and most of the throats belong to the fine throat-thin throat, and the pore throat radius is relatively large (Table 2), based on previous research and analysis of Wang Daofu's pore classification standard and Li Daopin's throat classification standard. The pore-throat configuration relationship of different types of reservoirs is analyzed by mercury margin, which can be denoted by β, and the calculation formula of mercury ingress margin is

$$\beta = \frac{S_t - S_p}{0.01S^2}, \tag{7}$$

where S_t (%) is throat Saturation of Mercury, S_p (%) is pore mercury saturation, and S (%) is total mercury saturation.

It is found that the mercury ingress margin for type I reservoirs is 0.24~1.47, the average value is 0.837; the mercury ingress margin of type II reservoirs is 2.09~3.7, and the average value is 2.958; the percentage of mercury ingress in the throat of type I and II reservoirs is gradually increasing, and the reservoir is gradually controlled by the throat, based on the constant velocity mercury intrusion experiment results of 10 rock samples from the He 8th reservoir in the study area and using formula (1) to calculate the mercury ingress margin of each sample. At the same

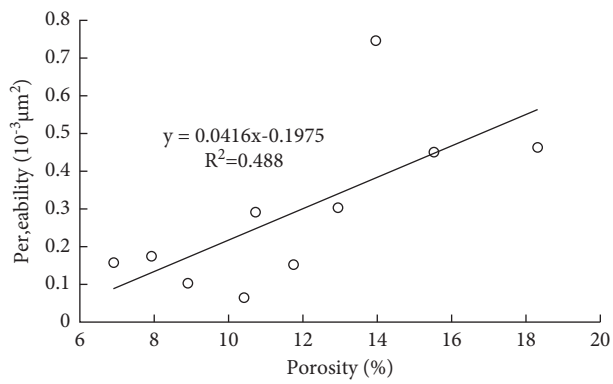

Figure 1: Relationship between porosity and permeability of He 8 tight sandstone reservoir.

Table 1: Laboratory results of samples in the east of Sulige gas field with nuclear magnetic resonance technique [16].

Sample no	$\Phi/(\%)$	$K/(10^{-3}\ \mu m^2)$	RQI	$S_m/(\%)$	Type
1#	13.96	0.747	0.23	26.35	I
2#	18.30	0.463	0.16	13.78	I
3#	10.41	0.065	0.08	5.38	II
4#	15.52	0.45	0.17	32.67	I
5#	8.89	0.104	0.11	8.48	II
6#	12.95	0.304	0.15	21.88	I
7#	10.74	0.291	0.16	26.05	I
8#	6.90	0.157	0.15	17.39	I
9#	7.93	0.174	0.14	15.62	II
10#	11.75	0.154	0.11	8.02	II

time, the analysis of the relationship between each microscopic pore structure characteristic parameter and movable fluid saturation found (Figure 3) showed that only mercury intake margin and effective pore throat radius ratio were negatively correlated with movable fluid saturation, while other parameters were positively correlated with movable fluid saturation, and the correlation was significantly different.

3.3. Grey Correlation Degree between Micropore Structure Characteristic Parameters and Movable Fluid Saturation. The movable fluid and micropore characteristic parameters of 10 samples from the He 8 tight sandstone reservoir in Sulige Gas Field were selected as the research object (Tables 1 and 2), Based on the results of reservoir classification, the same type of reservoir is used and the improved grey correlation theory is selected to quantitatively characterize the influence of the microscopic pore structure characteristic parameters of near/similar reservoirs on the occurrence of movable fluids.

According to the relevant data of each parameter in Tables 1 and 2, the movable fluid saturation and the characteristic parameters of the micropore are regarded as the parent sequence and the subsequence, respectively Taking the improved gray correlation theory, determine the gray correlation degree ranking between the microscopic pore structure characteristic parameters of the near/similar reservoirs and the movable fluid saturation, as shown in Table 3.

It can be seen from Table 3 that the relationship between the characteristic parameters of microscopic pore throats and the movable fluid saturation and their rankings show that the movable fluid saturation of Type I reservoirs is mainly affected by the effective pore-throat radius ratio, the total throat mercury saturation, and the effective pores radius. These three characteristic parameters reflect the pores, throat size, and pore-throat configuration relationship and determine the effective way of fluid passage and the degree of restraint in the pores, indicating that the existence law of movable fluid in this type of reservoir is restricted by the connection of effective pore throats. Movable fluid saturation in Type II reservoirs is mainly affected by three factors:

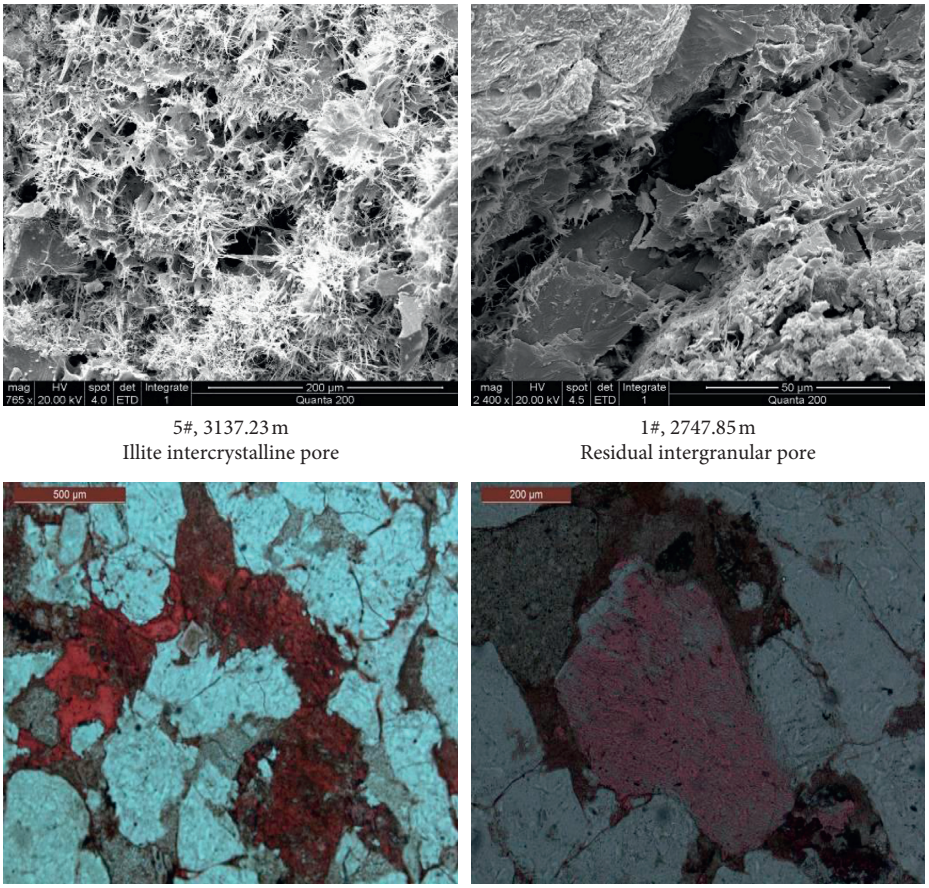

5#, 3137.23 m
Illite intercrystalline pore

1#, 2747.85 m
Residual intergranular pore

4#, 3137.23 m, 12/5000
Dissolved pores and residual filamentous clay minerals

7#, 2627.66 m
Feldspar dissolved pore

Figure 2: The reservoir space types of tight sandstone reservoir in He 8 in the study area.

Table 2: Pore structure parameters of the He 8 reservoir in the east of Sulige gas field [16].

Sample no	Total pore mercury saturation (%)	Mercury saturation total throat	Effective pore radius (μm)	Effective throat radius (μm)	Main flow throat radius (μm)	Effective throat volume (puv) ml/cm^3	Effective pore volume (puv) m^3	Effective pore throat radius ratio	Sorting coefficient	Mercury margin	Type
1#	15.48	35.36	153.31	0.910	0.881	0.017	0.037	227.5	0.26	0.77	I
2#	12.46	23.80	152.57	0.689	0.636	0.043	0.027	235.5	0.21	0.86	I
3#	2.44	18.17	118.04	0.544	0.665	0.019	0.002	563.2	0.10	3.70	II
4#	24.88	32.99	149.23	0.982	1.126	0.051	0.031	214.6	0.36	0.24	I
5#	5.76	13.50	143.99	0.656	0.487	0.012	0.013	432.5	0.20	2.09	II
6#	19.31	32.86	144.28	0.645	0.733	0.043	0.025	227.5	0.24	0.50	I
7#	10.57	33.69	143.99	0.704	0.815	0.017	0.036	263.5	0.19	1.18	I
8#	8.48	24.82	136.40	0.743	0.613	0.019	0.014	194.6	0.16	1.47	I
9#	2.88	25.48	116.73	0.620	0.632	0.009	0.021	241.7	0.21	2.81	II
10#	0.79	28.48	129.15	0.643	0.314	0.031	0.016	352.8	0.07	3.23	II

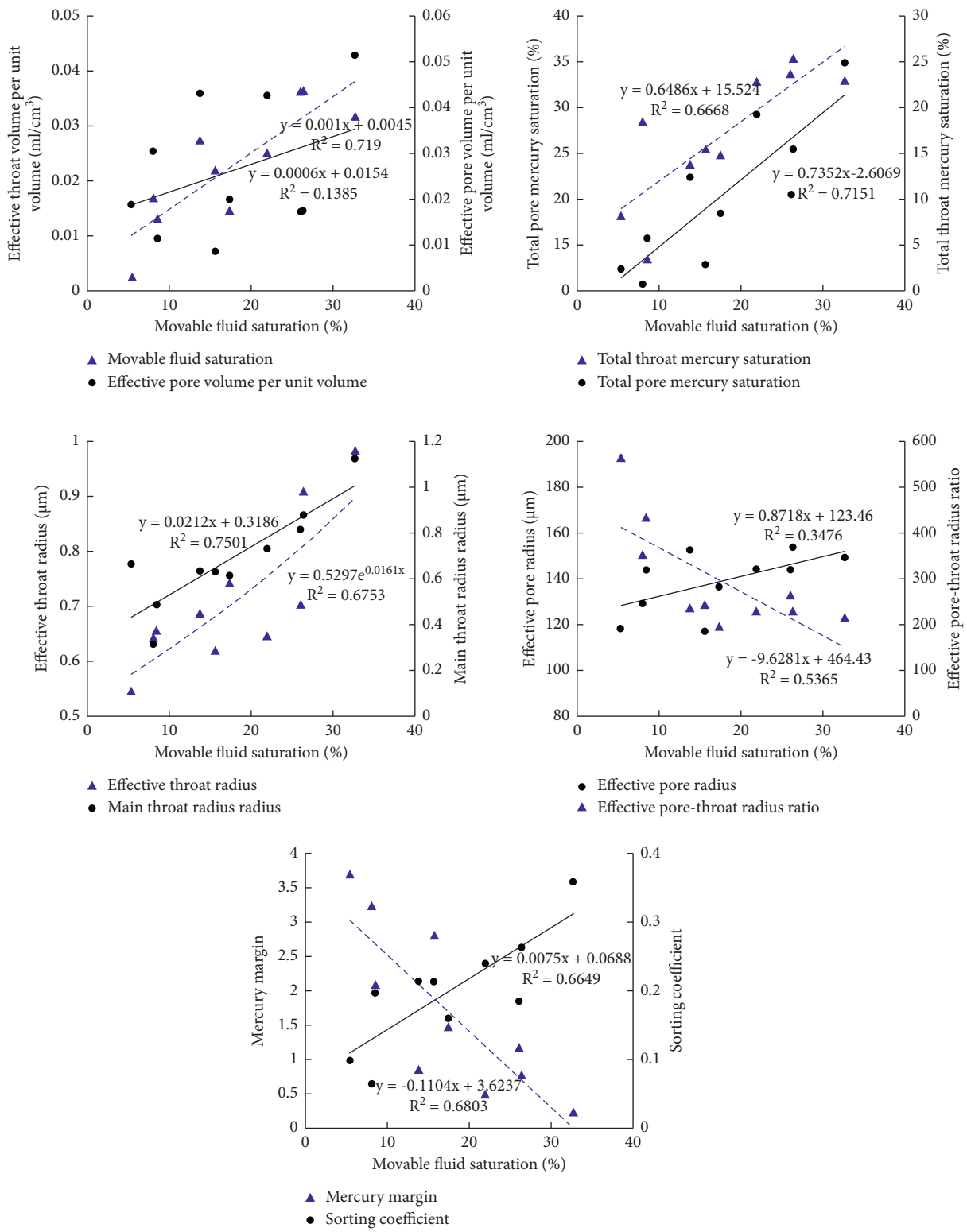

Figure 3: Relationship between micro pore structure characteristic parameters and movable fluid saturation.

Table 3: Correlation degree and ranking of microscopic pore-throat characteristic parameters and movable fluid saturation.

	Effective pore throat radius ratio weighted average	Mercury saturation of total throat	Weighted average of effective pore radius	Effective pore volume per unit volume	Effective throat radius weighted average	Total pore mercury saturation	Main flow throat radius	Effective throat volume per unit volume	Sorting coefficient	Reservoir types of
Correlation	0.806	0.756	0.735	0.731	0.723	0.708	0.695	0.673	0.455	I reservoir
Ranking	1	2	3	4	5	6	7	8	9	
Correlation	0.792	0.803	0.796	0.711	0.674	0.712	0.802	0.810	0.715	II reservoir
Ranking	5	2	4	8	9	7	3	1	6	

effective throat volume per unit volume, total throat mercury saturation, and mainstream throat radius. We can get the conclusion that the presence of fluid in the effective throat of this type of reservoir has absolute control over the distribution of movable fluid.

4. Results and Conclusions

(1) The average value of pores in He 8 tight sandstone reservoir of the study area is 11.735%, and the average of permeability is $0.291\times10^{-3}\,\mu m^2$, which is a typical tight sandstone reservoir. Taking the size of the reservoir quality factor as the evaluation criterion, the reservoir is divided into two types, I and II, and the quality of the reservoir gradually deteriorates, and the physical properties of similar reservoirs are similar.

(2) Using different types of reservoirs as data sets, the improved grey correlation theory was used to quantitatively characterize the influence of the microscopic pore structure of reservoirs with near/similar physical properties on the occurrence of movable fluids. Among them, the movable fluid saturation of Type I reservoirs is mainly affected by the effective pore-throat radius ratio, the total throat saturation of mercury, and the effective pore radius. The movable fluid saturation of Type II reservoirs is mainly affected by the effective throat volume per unit volume, the influence of the mercury saturation of the total throat and the radius of the mainstream throat. Therefore, the occurrence state of movable fluids in Type II reservoirs is controlled by the throat radius stronger than in Type I reservoirs.

(3) It is shown that the reservoirs in He 8 tight sandstone reservoir of the study area are mainly of throat type, and the mercury ingress margin of type I reservoirs is significantly less than that of type II reservoirs; the proportion of mercury in the throats of type I and II reservoirs is gradually increasing, and the reservoirs are affected by throats. The control effect is gradually increasing. Based on the constant velocity mercury injection experiment, the "mercury ingress margin" was introduced to analyze the pore-throat configuration relationship of different types of reservoirs in He 8 tight sandstone reservoir of the study area.

Data Availability

The data used to support the results of this study are included within the manuscript.

Conflicts of Interest

The authors declare that there are no conflicts of interest.

Acknowledgments

This work was financially supported by the National Natural Science Foundation of China (41802166 and 51934005), Shaanxi Provincial Key Research and Development Program (2021GY-140), Opening Foundation of Shaanxi Key Laboratory of Advanced Stimulation Technology for Oil & Gas Reservoirs (20JS120), Open Foundation of Key Laboratory of Coal Resources Exploration and Comprehensive Utilization, Ministry of Natural Resources (KF2021-3), and Shaanxi Provincial Key Research and Development Program (2021GY-140).

References

[1] J. H. Fu, J. Yu, and L. M. Xu, "New progress in exploration and development of tight oil in ordos basin and main controlling factors of large-scale enrichment and exploitable capacity," *China Petroleum Exploration*, vol. 20, no. 5, pp. 9–19, 2015.

[2] H. Yang, S. X. Li, and X. Y. Liu, "Characteristics and resource prospects of tight oil and shale oil in ordos basin," *Acta Petrolei Sinica*, vol. 34, no. 1, pp. 1–11, 2013.

[3] C. N. Zou, *Unconventional Petroleum Geology*, Geological Publishing House, Beijing, China, 2011.

[4] C. Zhu, M. He, M. Karakus, X. Zhang, and Z. Tao, "Numerical simulations of the failure process of anaclinal slope physical model and control mechanism of negative poisson's ratio cable," *Bulletin of Engineering Geology and the Environment*, vol. 80, no. 4, pp. 3365–3380, 2021.

[5] Y. Wang, W. K. Feng, R. L. Hu, and C. H. Li, "Fracture evolution and energy characteristics during marble failure under triaxial fatigue cyclic and confining pressure unloading (FC-CPU) conditions," *Rock Mechanics and Rock Engineering*, vol. 54, no. 2, pp. 799–818, 2021.

[6] F. Wu, H. Zhang, Q. L. Zou et al., "Viscoelastic-plastic damage creep model for salt rock based on fractional derivative theory," *Mechanics of Materials*, vol. 150, Article ID 103600, 2020.

[7] Q. Yin, J. Wu, C. Zhu et al., "Shear mechanical responses of sandstone exposed to high temperature under constant normal stiffness boundary conditions," *Geomechanics and Geophysics for Geo-Energy and Geo-Resources*, vol. 7, no. 2, p. 35, 2021.

[8] E. Aliakbardoust and H. Rahimpour-Bonab, "Effects of pore geometry and rock properties on water saturation of a carbonate reservoir," *Journal of Petroleum Science and Engineering*, vol. 112, pp. 296–309, 2013.

[9] Y. J. Gong, S. B. Liu, M. J. Zhao, H. B. Xie, and K. Y. Liu, "Characterization of micro pore throat radius distribution in tight oil reservoirs by NMR and high pressure mercury injection," *Petroleum Geology & Experiment*, vol. 38, no. 3, pp. 389–394, 2016.

[10] G. Desbois, J. L. Urai, P. A. Kukla, J. Konstanty, and C. Baerle, "High-resolution 3D fabric and porosity model in a tight gas sandstone reservoir: a new approach to investigate microstructures from mm to nm-scale combining argon beam cross-sectioning and SEM imaging," *Journal of Petroleum Science and Engineering*, vol. 78, no. 2, pp. 243–257, 2011.

[11] N. Liu, Z. H. Zhou, D. Z. Ren et al., "Distribution characteristics and controlling factors of movable fluid in tight sandstone gas reservoir: a case study of the eighth member of xiashihezi formation and the first member of Shanxi formation in western sulige gas field," *Lithologic Reservoirs*, vol. 31, no. 6, pp. 14–25, 2019.

[12] G. Wang, X. Chang, W. Yin, Y. Li, and T. Song, "Impact of diagenesis on reservoir quality and heterogeneity of the upper triassic chang 8 tight oil sandstones in the Zhenjing area, ordos basin, China," *Marine and Petroleum Geology*, vol. 83, pp. 84–96, 2017.

[13] A. Sakhaee-Pour, "Decomposing J-function to account for the pore structure effect in tight gas sandstones," *Transport in Porous Media*, vol. 116, no. 2, pp. 453–471, 2017.

[14] B. Bai, R. K. Zhu, S. T. Wu et al., "Multi-scale method of nano (micro)-CT study on microscopic pore structure of tight sandstone of Yanchang formation, ordos basin," *Petroleum Exploration and Development*, vol. 40, no. 3, pp. 329–333, 2013.

[15] D. K. Liu, W. Sun, D. Z. Ren et al., "Feature of pore-throat structures and movable fluid in tight gas reservoir: a case from He 8 formation of permian xiashihezi Formation and the 1st member of permian Shanxi formation in the western area of sulige gas field, ordos basin," *Natural Gas Geoscience*, vol. 27, no. 12, pp. 2136–2145, 2016.

[16] D. Z. Ren, W. Sun, T. Lu et al., "Microscopic geological factors of movable fluid distribution in the tight sandstone gas reservoir: taking the He 8 reservoir in the east of sulige gas field as an example," *Geoscience*, vol. 6, no. 29, pp. 1409–1417, 2015.

[17] Y. Ren, W. Sun, X. Zhang et al., "Characteristics of movable fluids and study of production performance in different flow units of low-permeability reservoir: an example from the chang 6 block of the jiyuan oilfield in ordos basin," *Geology and Exploration*, vol. 52, no. 5, pp. 974–984, 2016.

[18] H. X. Ming, W. Sun, L. L. Zhang, and Q. Wang, "Impact of pore structure on physical property and occurrence characteristics of moving fluid of tight sandstone reservoir: taking He 8 reservoir in the east and southeast of sulige gas field as an example," *Journal of Central South University (Science and Technology)*, vol. 46, no. 12, pp. 4556–4567, 2015.

[19] D. Z. Ren, W. Sun, F. J. Dong, H. Hang, and X. F. Qu, "Characteristics of movable fluids in the chang 81 reservoir, yanchang formation in huaqing oilfield, ordos basin and the influencing factors," *Geology and Exploration*, vol. 51, no. 4, pp. 797–804, 2015.

[20] State Bureau of Petroleum and Chemical Industry, *The Porosity and Permeability Measurement of Core in Net Confining Stress: SY/T6385-1999*, Petroleum Industry Press, Beijing, China, 1999.

[21] National energy administration, *Standard for Laboratory Measurement of NMR Parameters of Rock Samples: SY/T6490-2014*, Petroleum Industry Press, Beijing, China, 2015.

[22] Standardization Administration of China, *Rock Capillary Pressure Measurement: GB/T29171-2012*, Petroleum Industry Press, Beijing, China, 2012.

[23] National Energy Administration, *Analytical Method of Rock Sample by Scanning Electron Microscope: SY/T 5162-2014*, Petroleum Industry Press, Beijing, China, 2014.

[24] National development and reform commission, *Rock Thin Section Preparation: SY/T 5913-2004"*, Petroleum Industry Press, Beijing, China, 2004.

[25] F. J. Dong, X. F. Lu, and Y. P. Ma, "Comprehensive evaluation of methane reservoirs based on TOPSIS," *Geology and Exploration*, vol. 51, no. 3, pp. 587–591, 2015.

[26] X. F. Lu, F. J. Dong, X. S. Bo, Y. Cao, and H. Huang, "Quantitative characterization of the effect of micro pore structure on reservoir quality of tight sandstone reservoirs based on improved grey correlation theory," *Mathematics in Practice and Theory*, vol. 51, no. 4, pp. 99–108, 2021.

[27] F. J. Dong, X. F. Lu, M. Y. Liu, and X. J. Rao, "Correlation analysis of microscopic geological factors and micro cracks based on the grey association," *Geology and Exploration*, vol. 52, no. 5, pp. 950–955, 2016.

[28] S. Y. Xie, Y. Wang, Y. B. Xie, and H. B. Li, "Application of grey system theory to determining order of ICA decrypted images," *Journal of Northwestern Polytechnical University*, vol. 33, no. 1, pp. 153–158, 2015.

[29] Z. Q. Zhang, B. Q. Hu, Y. Li, and J. H. Wei, "Study of growth poles and factors driving land consolidation in guangxi based on improved grey relational analysis method," *Journal of Agricultural Resources and Environment*, vol. 36, no. 4, pp. 431–440, 2019.

[30] Y. B. Dong and Z. S. Duan, "New determination method for identification coefficient of grey relational grade," *Journal of Xi'an University of Architecture & Technology*, vol. 40, pp. 589–592, 2008.

[31] X. F. Lu, X. Y. Wang, Y. F. Yang, and J. N. Xue, "The optimization model for reducing RON loss in gasoline refining process," *Geofluids*, vol. 2021, Article ID 5520942, 10 pages, 2021.

Hindawi
Mathematical Problems in Engineering
Volume 2021, Article ID 7163598, 17 pages
https://doi.org/10.1155/2021/7163598

Research Article

Innovative Control Technique for the Floor Heave in Goaf-Side Entry Retaining Based on Pressure Relief by Roof Cutting

Guangyuan Yu,[1,2] **Jiong Wang**,[1,2] **Jinzhu Hu**,[1,2] **Daoyong Zhu**,[1,2] **Han Sun**,[1,2] **Xingen Ma**,[1,3] **Wei Ming**,[1,2] **and Wenfei Li**[1,2]

[1]*State Key Laboratory of Geomechanics & Deep Underground Engineering, China University of Mining & Technology, Beijing 100083, China*
[2]*School of Mechanics and Civil Engineering, China University of Mining & Technology, Beijing 100083, China*
[3]*Huaneng Coal Technology Research Co., Ltd, Beijing 100070, China*

Correspondence should be addressed to Jiong Wang; wangjiong0216@163.com

Received 8 July 2021; Accepted 9 August 2021; Published 19 August 2021

Academic Editor: Feng Xiong

To solve the difficulty in controlling floor heave of a retained goaf-side roadway, a new control technique was investigated from the perspective of the pressure relief by roof cutting by combining mechanical analysis, numerical simulation, and engineering tests. The mechanical principle of controlling the floor heave based on pressure relief by roof cutting was attained by analyzing the movement of overlying strata and mechanical characteristics of key blocks before and after the roof cutting. A new technique for controlling the floor heave based on pressure relief by roof cutting was proposed. Research results have shown that after performing pressure relief by roof cutting, the caved gangues in the goaf can support the overlying strata and, thereby, change the movement law thereof and weaken the abutment pressure on the coal wall. Furthermore, the pressure exerted on the roadway floor by the coal wall is lowered to prevent plastic deformation of the floor, thus controlling floor heave in the roadway; a new integrated technique for controlling the floor heave based on pressure relief by roof cutting, flexible yielding, controlling with double-direction-control anchor bolts, and controlling with reinforcing anchor cables is developed, and the technological processes of support, cutting, and protection are summarised. The results of field testing showed that, after applying the new technique, the average floor heave amount of the roadway declines by 64% and the average speed of the floor heave up to 231 m behind the working face decreases by 61%.

1. Introduction

Gob-side entry retention (GER), as an important technique in coal mining system without pillars [1–4], can improve the recovery rate of coal resources, reduce the rate of tunnelling of roadways, and avoid the waste of resources [5], owing to which it has been widely used in various coal mines in countries such as China, Germany, Poland, and the United Kingdom and has achieved remarkable economic and social benefits [6]. As a conventional material for roadway sidewall supporting, concrete blocks are characterised by large support resistance in the early stage, large rate of increase in resistance, favorable roof-cutting effect, and favorable sealing effect of the goaf. They are widely used in goaf-side entry retaining [7]. However, different degrees of floor heaves occur in nearly all retained goaf-side roadways including those by building concrete blocks alongside. With the increase in mining depths and roadway cross-section, the floor heave increases [8]. Especially for soft rock roadway, not only does it have a low strength but it also exhibits extremely strong rheology and undergoes large creep deformation, including that of severe extrusion [9]. As a result, the roadway floor cannot be reused as often. A small portion of roadway floors is hard to repair, or are beyond repair, thus causing the failure of gob-side entry retaining. This greatly affects the safe and efficient mining of the coal face [10].

The most commonly used techniques to control floor heave of roadways are reinforcement and pressure-relief

methods. In terms of the former, the following studies have been conducted: Bai et al. [11] proposed to control floor heave by reinforcing the floor using hydraulic expansion bolts anchored through their length. He et al. [12] proposed a floor heave control technique focusing on controlling the roof, two sidewalls, and base angle. Liu et al. [13] came up with a comprehensive method, involving the use of a reverse-arch concrete floor, grouting in deep and shallow holes, and highly prestressed, combined cables, aiming to control floor heave of roadways in fractured soft rock mass found in deep mines. By analyzing the effects of multiple means of controlling floor heave in deep roadways, Xie and Chang [14] proposed the use of overexcavation and grouting-backfilling to control floor heave and deformation. As for pressure-relief methods, Gao et al. [15] controlled floor heave of roadways through blasting pressure relief in deep boreholes drilled from the floor. Sun [16] proposed to control floor heave of roadways by pressure relief via cutting grooves at base angles of roadways. Zhao et al. [17] studied floor heave in a mining roadway beneath a goaf-surrounded coal pillar and proposed the control of the floor heave in the roadway by pressure relief through drilling boreholes from the floor beside the coal pillar, while grouting reinforcement was used in the floor near the goaf. Based on theoretical analysis and numerical simulation, Gong et al. [18] derived a method to control floor heave of a roadway through pressure relief by drilling boreholes from the sidewalls of the roadway. Han et al. [19] proposed to control floor heave in mining roadways by excavating a pressure-relief groove on the floor. Wang et al. [20] used hydraulic fracturing to cut the roadway roof, thus reducing the floor heave. Although numerous studies have been undertaken on the techniques available to control floor heave in roadways, the proposals focus on two aspects: reinforcement and pressure relief. Despite certain inhibitory effects on the floor heave, the reinforcement methods fail to weaken the driving force of the floor heave. Although the pressure-relief methods allow floor strata to be located in a stress-reduction zone by loosening blasting, groove cutting, and borehole drilling, they are also likely to enlarge the plastic zone in surrounding rocks of roadways, which is unbeneficial to the maintenance of the roof and sidewalls [21]. Meanwhile, the hydraulic fracturing can make the rock strata to undergo shear or tensile failure along the primary fracture [22], but it also has drawbacks such as huge construction volumes, slow speed, and low efficiency [23]. In comparison, the bidirectional cumulative tensile blasting method, as a type of the cumulative blasting technique, is characterized by advantages including small construction volumes, favorable shaping effect, little damage to surrounding rocks, and use of a low specific charge [24]. Many researches indicate that roof cutting through bidirectional cumulative tensile blasting can optimize the stress state in the rock surrounding a roadway [25, 26], so it is expected to become a new technique for controlling floor heave in gob-side entries.

On this basis, against the background of a conveyor gateway in the working face of a retained goaf-side roadway by building concrete blocks beside in Faer Coal Mine, the aim of this study were threefold: (1) the movement of overlying strata and mechanical characteristics of the floor of the retained goaf-side roadway before and after pressure relief by roof cutting were explored through theoretical analysis and numerical simulation. Furthermore, the mechanical principle of controlling floor heave by the virtue of pressure relief by roof cutting was obtained; (2) a new integrated technique for controlling floor heave combining pressure relief by roof cutting, flexible yielding, controlling with double-direction-control anchor bolts, and controlling with reinforcing anchor cables, based on pressure relief by roof cutting, was proposed; moreover, the technological processes of support, cutting, and protection were determined, and the field test was conducted; (3) the field monitoring revealed that the average floor heave amount of the retained goaf-side roadway with the new technique dropped by 64%, and the roadway can satisfy the requirement for reuse without undercutting, delivering a favorable control effect on the floor heave.

2. Control Principle of Pressure Relief by Roof Cutting over Floor Heave

2.1. Theoretical Analysis. The pressure relief by roof cutting can reduce the length of the lateral cantilever beam, and combining with the breaking and swelling characteristics of gangue, the surrounding rock stress environment of the gob-side entry can be effectively alleviated [27]. In addition, as a protective cushion, the gangue dump can effectively absorb the kinetic energy of the roof caving process [28] so as to reduce the impact of roof collapse on the floor.

Without roof cutting, the immediate roof in the goaf is caved over a low height, and caved gangues cannot then fill the goaf after being bulked. This leaves a large unfilled space between the suspended main roof and gangue piles in the goaf, as shown in Figure 1(a); after roof cutting, the presence of the cut in the roof leads to an increase in the caving height of the immediate roof of the goaf, and thereby an increase in the volume of the caved gangues. In this way, the goaf can be filled with bulked gangues, thus shrinking the unfilled space between the suspended main roof and gangue piles, as shown in Figure 1(b). According to the bulking characteristics of the caved gangues, the distance u between gangue piles and the suspended main roof can be calculated according to the following equation:

$$u = H_G - H_{c1}(k-1) - \Delta H, \tag{1}$$

where u, H_G, H_{c1}, k, and ΔH denote the distance between gangue piles and the suspended main roof, mining height, caving height of the immediate roof, bulking factor of rock in the immediate roof, and amount of floor heave in the goaf, respectively.

After the immediate roof is caved, the mass of the rock suspended in the goaf is transferred to coal sides through the rock beam of the main roof, thus increasing the pressure on the coal sides. In this case, the coal sides are still elastically compressed due to failing to reach their ultimate strength and, therefore, the abutment pressure decreases monotonically, with the peak at the coal walls [29], as shown in Figure 1.

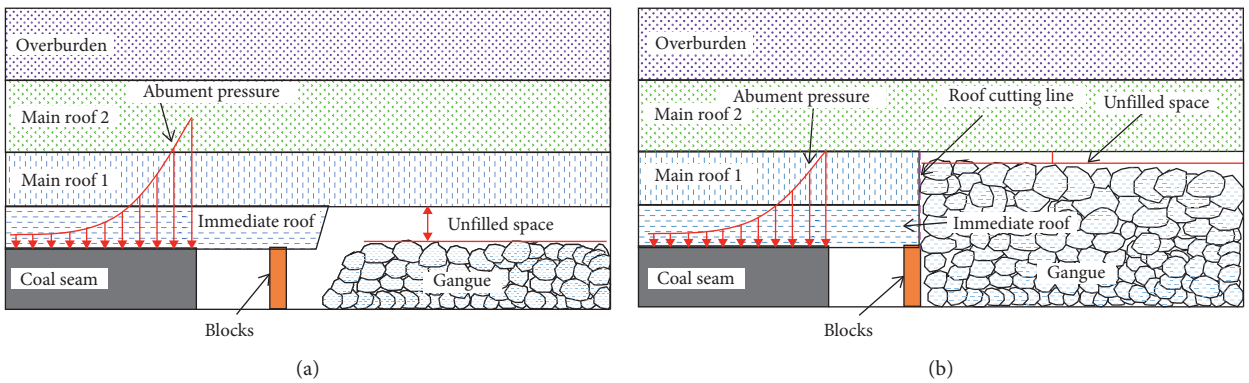

Figure 1: Filling conditions of the goaf after the immediate roof is caved. (a) Conventional mining. (b) Pressure relief by roof cutting.

The rock beam begins to be supported by gangues after it subsides over a certain height, thus making contact with the gangues. The bearing load increases with the increase in the compression of the gangues. Under this condition, as the coal is under elastic compression, the immediate roof below the main roof, coal, and gangues can be considered as elastic media. As a result, the stress prevailing during that subsidence and deformation before fracture of the main roof satisfies the Winkler assumption for an elastic foundation. It is feasible to establish a mechanical model before the fracture of the main roof, as shown in Figure 2.

According to the Winkler assumption for elastic foundation, the deflection of the rock beams of the main roofs above the goaf and coal seams is separately established in the coordinate system, as shown in the following equations:

$$EI\frac{d^4 w_1(x)}{dx^4} + k_1[w_1(x) - u] = q_0, \tag{2}$$

$$EI\frac{d^4 w_2(x)}{dx^4} + k_1 w_2(x) = q_0, \tag{3}$$

where E, I, and $\omega(x)$ refer to the elastic modulus, moment of inertia, and the deflection of the subsidence zone of the rock beam of the main roof, respectively; k_1 and k_2 separately denote the elastic foundation coefficients of gangue piles and coal seams; u and q_0 represent the distance between the gangue piles and the main roof and the load of the overlying strata on the rock beam of the main roof, respectively.

Assuming $\beta_1 = \sqrt[4]{(k_1/4EI)}$ and $\beta_2 = \sqrt[4]{(k_2/4EI)}$, equations (2) and (3) are solved to reveal the deflections of the main roof above the goaf and coal, as shown in the following equations:

$$\omega_1 = e^{-\beta_1 x}\left(\frac{\beta_1 - \beta_2}{\beta_1 + \beta_2}\sin\beta_1 x - \cos\beta_1 x\right)\bullet\left(\frac{q_0}{k_1} + u\right) + \frac{q_0}{k_1} + u, \tag{4}$$

$$\omega_2 = e^{\beta_2 x}\left(\frac{\beta_2 - \beta_1}{\beta_1 + \beta_2}\sin\beta_2 x + \cos\beta_2 x\right)\bullet\left(\frac{q_0}{k_1} + u\right)\bullet\frac{\beta_1^2}{\beta_2^2} + \frac{q_0}{k_2}. \tag{5}$$

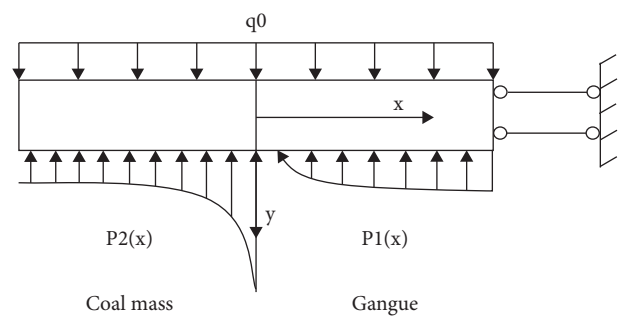

Figure 2: Sketch of the stress before the fracture of the main roof.

Therefore, the pressure p_1 on gangues in the goaf and pressure p_2 on coal are separately calculated according to the following equations:

$$p_1(x) = k_1 e^{-\beta_1 x}\left(\frac{\beta_1 - \beta_2}{\beta_1 + \beta_2}\sin\beta_1 x - \cos\beta_1 x\right)\bullet\left(\frac{q_0}{k_1} + u\right) + q_0, \tag{6}$$

$$p_2(x) = k_2 e^{\beta_2 x}\left(\frac{\beta_2 - \beta_1}{\beta_1 + \beta_2}\sin\beta_2 x + \cos\beta_2 x\right)\bullet\left(\frac{q_0}{k_1} + u\right)\bullet\frac{\beta_1^2}{\beta_2^2} + q_0. \tag{7}$$

As shown in equation (7), the pressure p_2 applied to the coal sides is mainly related to the distance u between the main roof and gangue piles under the same burial depth and geological conditions. Moreover, pressure p_2 increases with u. By substituting equation (2) into equation (7), the relationship between the pressure p_2 on the coal sides and the caving height of the immediate roof can be attained as follows:

$$p_2(x) = k_2 e^{\beta_2 x}\left(\frac{\beta_2 - \beta_1}{\beta_1 + \beta_2}\sin\beta_2 x + \cos\beta_2 x\right) \bullet\left(\frac{q_0}{k_1} + H_G - H_{c1}(k-1) - \Delta H\right)\bullet\frac{\beta_1^2}{\beta_2^2} + q_0. \quad (8)$$

It can be seen from equation (8) that the pressure p_2 on the coal sides decreases with the growth of the caving height H_{c1} of the immediate roof on the premise of ignoring the influence of floor heave in the goaf and keeping the mining height of the working face the same. In addition, roof cutting by blasting artificially increases the caving height H_{c1} of the immediate roof, thus decreasing the abutment pressure p_2 on the coal sides.

The rock beam of the main roof may be fractured at the end after it subsides by a certain amount and an external stress field dependent on the mass of overlying strata is formed outside the fracture line. In this case, the supporting capacity of coal within a certain range away from the roadway side reduces, and coal seams are divided into elastic and plastic zones according to the abutment pressure, as shown in Figure 3.

The pressure in the plastic zone in the external stress field can be calculated according to the following equation [30]:

$$\sigma_y = \left(\sigma_c + \frac{C}{f}\right)\left(1 + \frac{\alpha x}{h - \alpha x_0}\right)^{2f/\alpha}, \quad (9)$$

$$\alpha = \arctan\frac{y_0}{x_0}, \quad (10)$$

where σ_y, σ_c, and C refer to the pressure applied on coal seams, the compressive strength of the plastic zone in coal seams, and the cohesion of the interfaces between the coal seam with the roof and floor, respectively; f, α, h, and y_0 represent the coefficient of internal friction of coal seams, compression angle of coal seams, the mining height of the coal, and compression of the coal seams, respectively.

Previous research [29] pointed out that the abutment pressure in the plastic zone increases with the increasing compression angle of coal mass when x_0 is kept unchanged. In equation (10), the compression angle is shown to be positively correlated with the amount of compression of the coal, and the compression of coal is mainly induced by rotation and subsidence of the overlying rock beams. According to equations (1) and (5), the rotation and subsidence of the main roof decreases after pressure relief by roof cutting. Thus, the compression angle of the coal reduces, and the pressure in the plastic zone in the external stress field decreases.

The pressure in the elastic zone in the external stress field is mainly composed of two parts: the deadweight of the rock beam outside the fracture line and the mass of the suspended rock transferred from the overlying nonfractured strata. Coal is mainly subjected to elastic deformation; thus, it can be supposed that the abutment pressure in the elastic zone is still related to the subsidence of the overlying nonfractured rock beam and increases therewith. After pressure relief by roof cutting, the filling effect of gangues weakens the subsidence of the overlying strata, as shown in Figure 3, thus reducing the abutment pressure of the elastic zone in the external stress field.

Above all, pressure relief by roof cutting can decrease the final subsidence of the main roof and its overlying strata by increasing the total thickness of the caved strata. Therefore, it decreases the abutment pressure applied to the coal sides before the fracture of the rock beam of the main roof and after the stabilization of the surrounding strata.

2.2. Numerical Simulation

2.2.1. Engineering Situation. In Faer coal mine located in Liupanshui City, Guizhou Province, China, working face 31004 with a strike length of 983.9 m and a dip length of 105.8–217.8 m in the central part of No. 3 mining area was tested. The coal seams with a thickness of 0.59–2.2 m (an average of 1.8 m) showed an average dip angle of 14° along the strike and were mined by longwall retreat mining along the strike. The roof was controlled by the fully caving method, and the overall height of the coal seam was mined in one operation (Figure 4(a)). The immediate roof and the main roof were composed of silty mudstone with a thickness of 3.1 m and fine sandstone with a thickness of 6.98 m, respectively, while the immediate floor and the main floor were composed of mudstone with a thickness of 2.6 m and fine sandstone with a thickness of 8.42 m, respectively (Figure 4(b)).

The cross-section of the retained roadway was a rectangle measuring 4.7 m × 2.6 m (width × height). The roadway roof was supported by anchor bolts, anchor cables, ladder beams, and metal mesh. Anchor bolts with a diameter of 20 mm and a length of 2000 mm were arranged at spacings of 750 mm × 800 mm. Anchor cables with diameters of 15.24 mm and lengths of 5000 mm were arranged at spacings of 1800 mm × 1600 mm. Anchor bolts, ladder beams, and metal mesh were used for supporting the coal wall. The anchor bolts were arranged at spacings of 1000 mm × 800 mm and had a diameter of 18 mm and a length of 1800 mm. C30 steel concrete with a density of about 2450 kg/m^3 was used to cast blocks with a mass of about 45 kg, each measuring 650 mm × 190 mm × 190 mm (length × width × thickness). The composition of concrete blocks is water (9.8%), C30 cement (17.6%), fly ash (1.8%), sand (24.5%), and gravel (46.3%). The support system is shown in Figure 5.

2.2.2. Establishment of a Numerical Calculation Model. Numerical simulation is a popular method used to study rock mechanics and engineering and mining problems [31]. Continuum modeling approaches are appropriate with regard to large-scale engineering problems; therefore, the continuous-medium software Flac3D was selected to simulate the deformation characteristics of a roadway roof in the process of roadway retention.

To reveal changes in the stress distribution in the roadway floor before and after roof cutting, a numerical

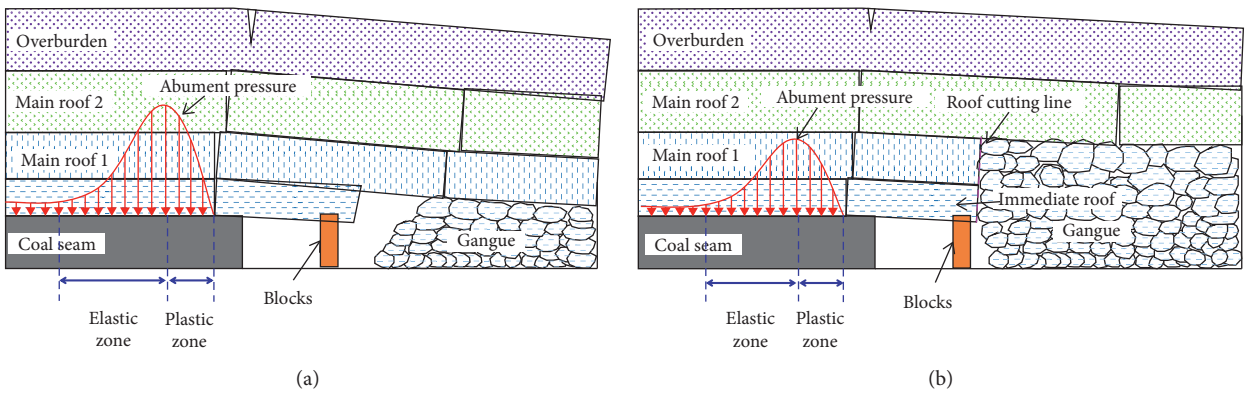

Figure 3: Distribution of the external stress field. (a) Conventional mining condition. (b) Pressure relief by roof cutting.

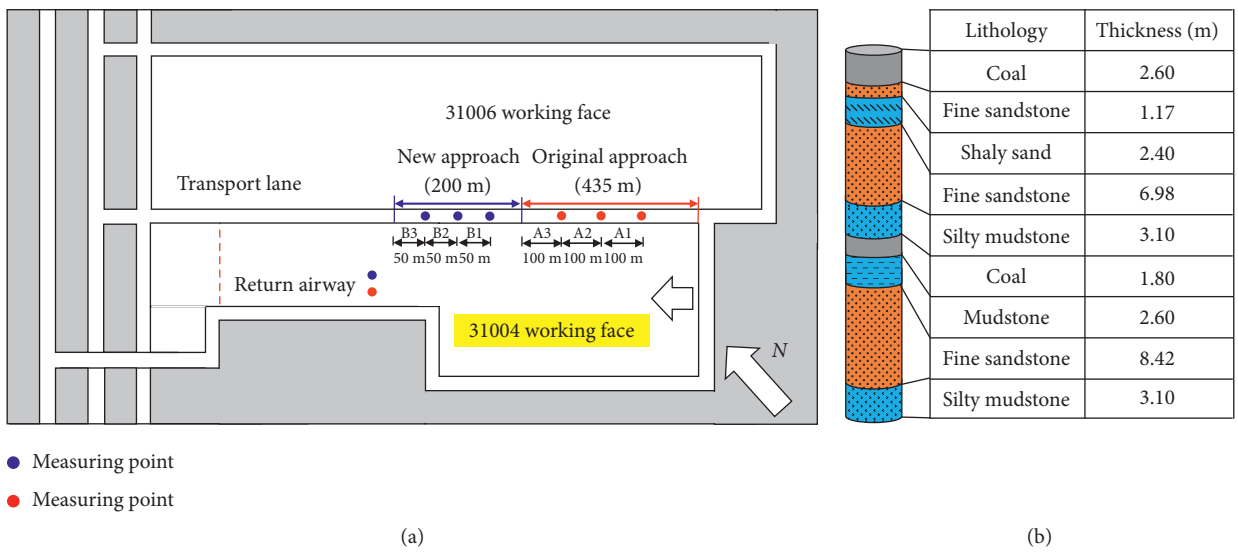

Figure 4: Plan layout and lithologic histogram of the working face in the test. (a) Plan layout. (b) Lithologic histogram of the working face.

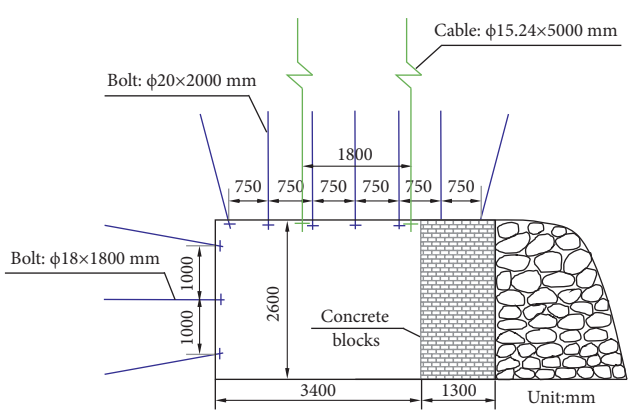

Figure 5: Support parameters for the block wall and GER.

calculation model was built by using the three-dimensional finite difference software (Flac3D) based on geological conditions around the 31004 working face in Faer coal mine (Figure 6). The model measured 300 m × 100 m × 85 m (length × width × height) and the working face with the length of 200 m were simulated. The thickness of coal seams was 2.2 m, and the roadway section measured 3.4 m × 2.6 m. The width of the concrete blocks was 1.3 m. The constitutive model used was the Mohr–Coulomb model, and null elements were used to simulate the working face, roadway excavation, and slitting of the roof. The slotting height in the simulation was 5 m. The stoping face was excavated step-by-step in 5 m increments. After excavation over 60 m, the final results were calculated. The lithology distribution and physicomechanical parameters of the model are summarised in Table 1.

2.2.3. Analysis of Simulated Results. The data pertaining to the vertical stress on the floor of the retained haulageway were extracted to draw a nephogram with the range of data extraction in Figure 7.

Figure 8 shows the nephogram for the vertical stress in floor. It can be seen from the figure that before pressure relief by roof cutting (Figure 8(a)), the stress concentration in the floor mainly occurs at the coal wall around the roadway during gob-side entry retention. Although a low stress

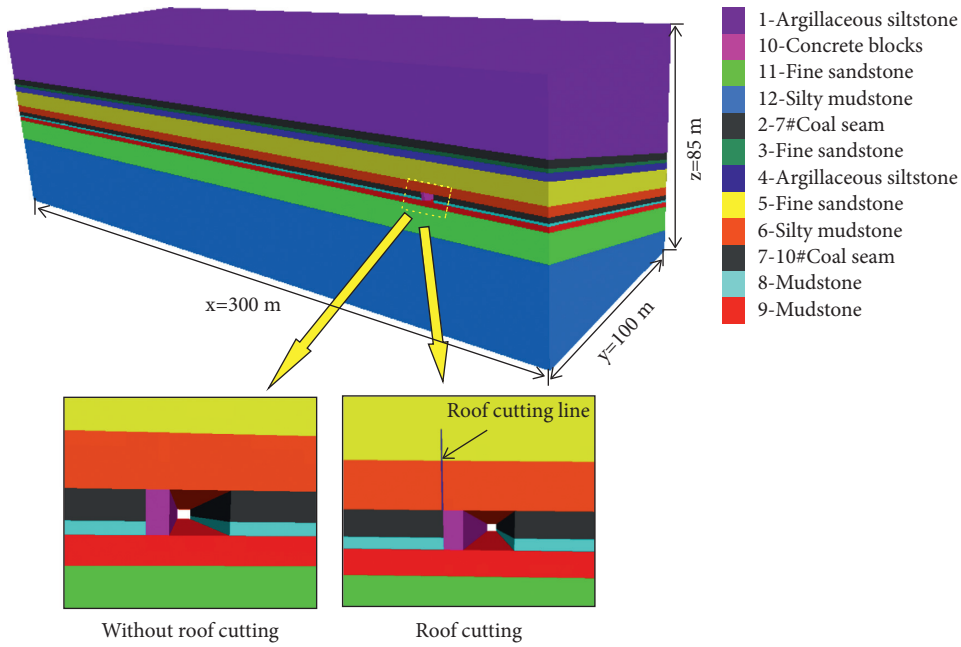

Figure 6: Numerical calculation model.

Table 1: Physicomechanical parameters of strata.

Lithology	Density/(kg/m^3)	Bulk modulus/(GPa)	Tensile strength/(MPa)	Shear modulus/(GPa)	Angle of internal friction/(°)	Cohesion/(MPa)
Argillaceous siltstone	2,350	3.36	4.21	2.3	35	1.8
Fine sandstone	2,570	6.25	9.5	3.57	31	2.4
Silty mudstone	2,400	10.76	1.64	3.2	30	1.4
Coal seam	1,370	2.8	0.4	1.2	27	0.6
Mudstone	2,463	3.94	1.68	2.6	30	1.2
C30 concrete block	2,350	7.6	2.5	11.2	32	2.1

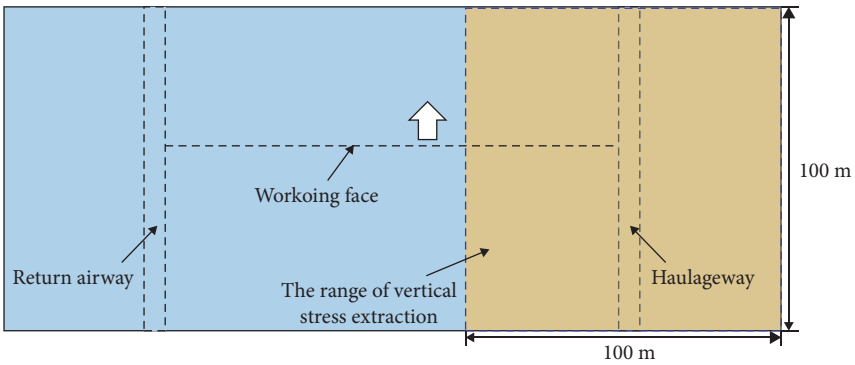

Figure 7: Extraction position of vertical stress.

concentration also appears in the floor below the concrete blocks, its average stress is much lower than that of the coal wall, implying that the coal wall acts as the main bearing body of the overburden pressure during gob-side entry retention and the overburden pressure can be transferred to the floor strata below the coal wall through the coal wall. After pressure relief by roof cutting (Figure 8(b)), the stress concentration is still found in the coal wall, while the stress is significantly lower than that beforehand. This shows that pressure relief by roof cutting cannot significantly change the spatial distribution characteristics of the stress on the floor but can reduce the abutment pressure on the coal wall.

To show the spatial distribution of the positions with lowering vertical stress on the floor under the effect of pressure relief by roof cutting, the stress difference is calculated based on Figures 8(a) and 8(b) to draw the

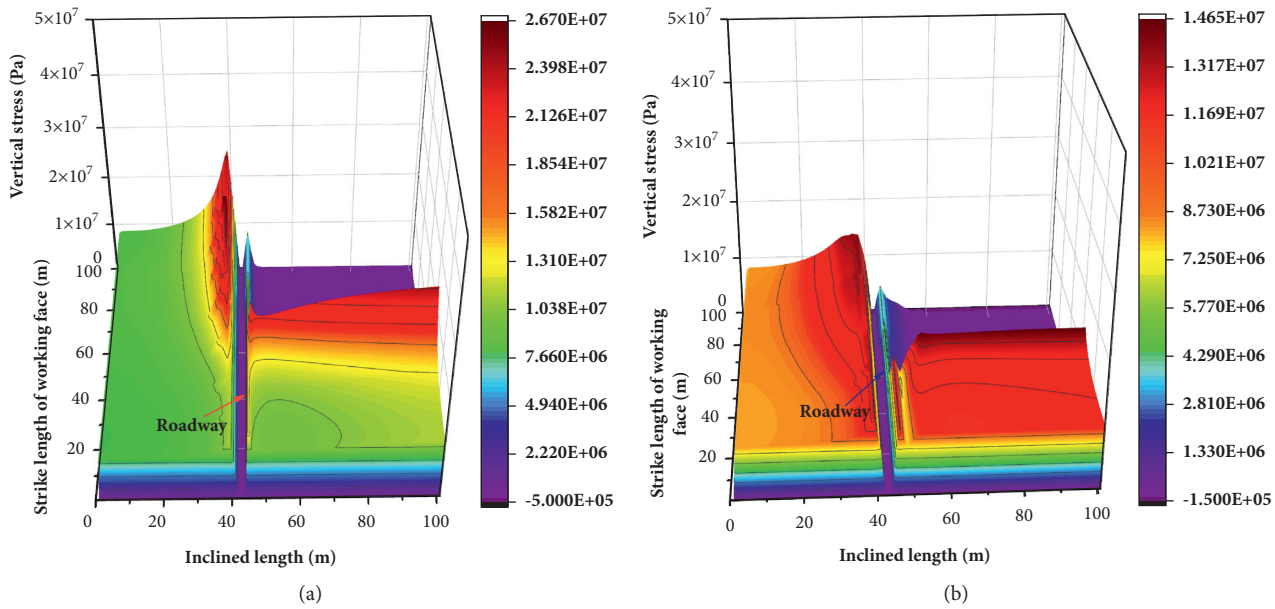

Figure 8: Nephograms of the vertical stress distribution on the floor. (a) Before pressure relief by roof cutting. (b) After pressure relief by roof cutting.

nephogram of the stress difference. In the nephogram, a positive value represents the reduction in the vertical pressure on the floor after roof cutting. A larger value corresponds to a larger reduction in the pressure (Figure 9). The figure shows that pressure relief by roof cutting can decrease the pressure on the floor at three positions (i.e., the coal wall to the rear of the working face, the concrete blocks, and the working face), in which the pressure on the coal wall is the most significantly lowered.

To quantify the changes in vertical stress on the floor of the coal wall during gob-side entry retention before and after pressure relief by roof cutting, survey lines for the pressure were established at 5-m intervals on the floor in the rear of the working face. The survey lines extended from the coal wall along the dip direction of the working face to the boundary of the model. The vertical stresses measured by the survey lines were extracted, and the distribution of the survey lines is shown in Figure 10.

Figure 11 shows the distribution of the vertical stresses taken from different survey lines. As shown in the figure, in terms of the area affected by pressure relief by roof cutting, pressure relief by roof cutting causes significant reduction in the vertical pressure within 15 m from the coal wall; as for the reduction in peak vertical pressure, within 60 m to the rear of the working face, the means of the peak vertical stress before and after roof cutting are 2.3×10^7 and 1.3×10^7 Pa, respectively: the latter declines by 43.5% relative to the former.

Above all, due to the movement of the overlying strata in the goaf during gob-side entry retention, the vertical stress concentration is generated on the floor in the side of the coal wall and below the block wall in the section of the retained roadway. Pressure relief by roof cutting fails to change the spatial distribution characteristics of the vertical stress on the floor during gob-side entry retention but can reduce the vertical stress. According to the results obtained by numerical simulation, pressure relief by roof cutting can weaken the vertical stress on the floor at up to 15 m from the coal wall; after pressure relief, the peak vertical stress on the floor in the side of the coal wall within 60 m of the rear of the working face decreases (on average) by 43.5%, showing a significant pressure-relief effect.

2.3. Comprehensive Analysis. After mining the working face, the abutment pressure P_a higher than the in-situ stress P_0 will be generated in the coal wall of the retained goaf-side roadway and applied to the roadway floor. Furthermore, the floor strata are subjected to lateral stress-relief after being compressed, leading to the increase in the horizontal stress; in comparison, the pressure P_a' lower than the in-situ stress is formed on the building blocks shielded by overlying strata. The peak abutment pressure P_a on the coal wall is calculated according to the following equation [32]:

$$P_a = nP_0, \tag{11}$$

where P_a, n, and P_0 denote the peak abutment pressure, the stress concentration factor (generally, 1.5 to 4.0), and the in-situ stress, respectively.

According to the above analysis, a mechanical model of the rib and floor can be established (Figure 12). With the advance of the working face, P_a' and P_a both gradually increase. As a result, floors are subjected to plastic failure, and continuous shear-sliding planes are generated. Under the effects of the abutment pressure and the horizontal stress N on the floors, the active state zone AOC will laterally shift to the passive state zone ADE, causing the rock mass to bulge upwards, thus triggering the floor heave (Figure 12(a)).

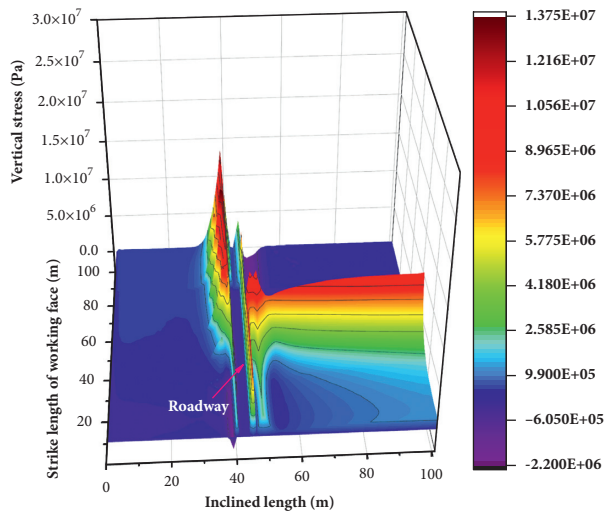

Figure 9: Nephograms of the difference of the vertical stress distribution at the floor before and after the roof cutting.

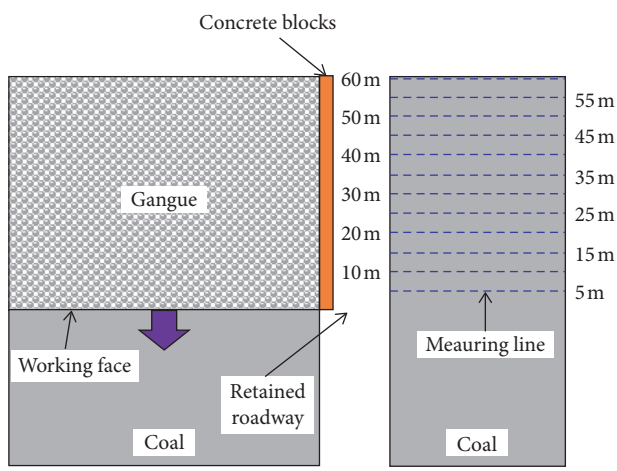

Figure 10: Distribution of survey lines for the vertical stress analysis.

B, P_u, q, and P'_u represent the width of the abutment pressure zone, the ultimate bearing capacity of the floor, the pressure of backfill layer or track bed or reaction force of the floor support, and the pressure of concrete blocks on the floor, respectively; $\alpha = 45^\circ - (\varphi/2)$.

Based on Terzaghi's theory, when floor strata in the range of OCDE are in the plastic state in terms of the limit equilibrium, the ultimate average concentrated stress (or ultimate bearing capacity of the floor) of the sidewall corresponding to width B is expressed as [33]

$$P_u = \frac{1}{2}\gamma B N_r + q N_q + C N_c, \tag{12}$$

where N_r, N_q, and N_c indicate the coefficients of bearing capacity and are functions of the angle of internal friction in floor strata. $N_r \approx 2(N_q + 1)\tan\varphi$, $N_q = e^{\pi \tan\varphi}\tan^2(45^\circ + (\varphi/2))$, and $N_c = (N_q - 1) \times \cot\varphi$. C, φ, and γ denote the average bonding force, angle of internal friction, and unit weight of rock mass of the floor, respectively.

In the range of width B, the average concentrated stress on sidewalls is approximated as follows [32]:

$$P_n = \frac{1}{2} n P_0 + \frac{L}{2B} P_0, \tag{13}$$

where L, P_0, and n indicate the width of the elastic pressure zone in the pressure zone, in-situ stress, and stress concentration coefficient, respectively.

It can be seen from Section 2.1 that pressure relief by roof cutting can reduce the abutment pressure applied to the coal wall. As shown in equation (11), under the condition that the in-situ stress P_0 remains the same, the peak abutment pressure P_a is lowered, and, therefore, the stress concentration factor n decreases. It can be seen from equation (13) that the mean concentrated stress P_n applied on floors within width B linearly monotonically increases with the stress concentration factor n. Thus, P_n reduces with decreasing n. At $P_n < P_u$, the floor strata are stable and are not subjected to floor heave (Figure 12(b)).

Therefore, the mechanical principle of pressure relief by roof cutting in controlling the floor heave entails weakening the abutment pressure applied to the coal wall by changing the movement characteristics of overlying strata; this further

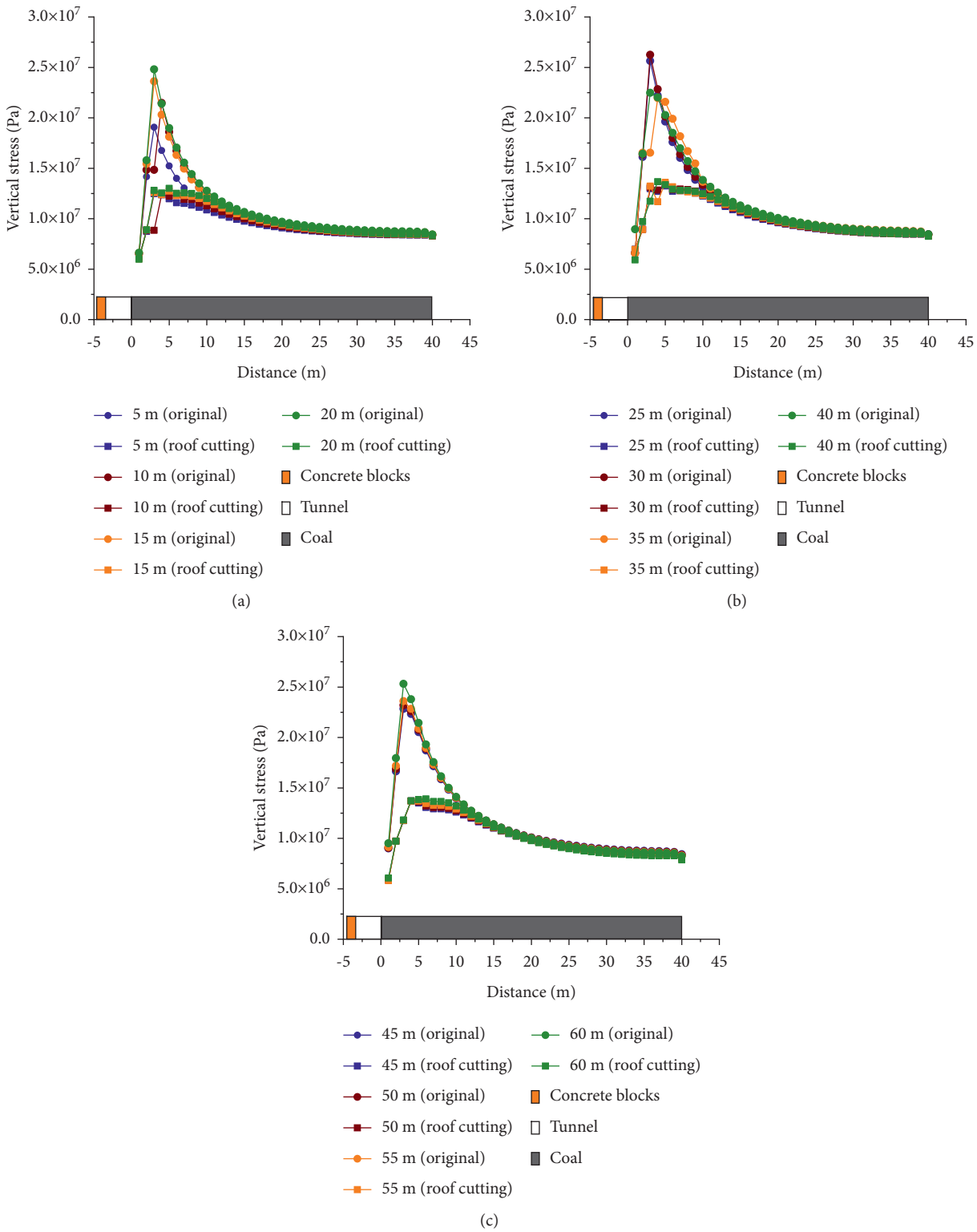

Figure 11: Distribution of vertical stresses in different parts before and after roof cutting. (a) 5 to 20 m behind the working face, (b) 25 to 40 m behind the working face, and (c) 45 to 60 m behind the working face.

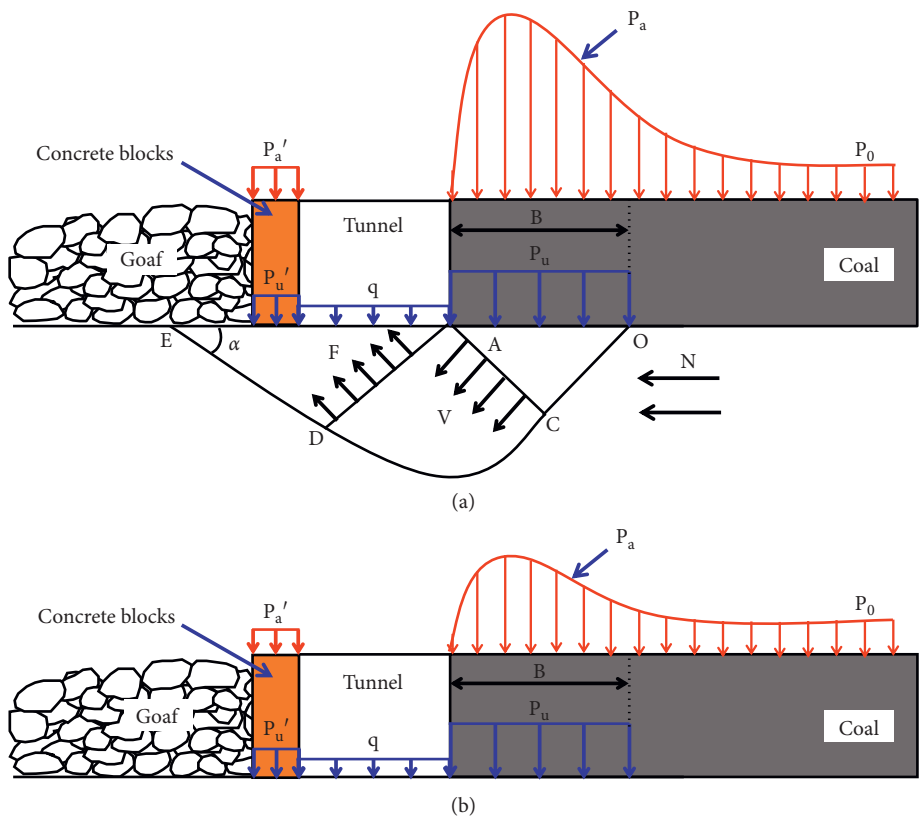

Figure 12: Stress of tunnel rib and floor. (a) Conventional mining condition. (b) Pressure relief by roof cutting.

lowers the pressure exerted by the coal wall on the roadway floor so that the floor strata are not subject to significant plastic and shear failure, thus controlling the floor heave in such roadways.

3. Key Technique and Technological Processes of Pressure Relief by Roof Cutting in Controlling Floor Heave

3.1. Key Technique

3.1.1. Directional Presplitting Blasting. As one of presplitting blasting, directional presplitting blasting differs from traditional presplitting blasting. It changes the dynamic process of the interaction between detonation waves and surrounding rocks through effective combination of binding energy tubes and ordinary mining explosives. That is, the tangent tensile stress is formed along the direction of the cumulative explosion after ignition. The detonation pressure is transformed into the tensile effect on surrounding rocks to the maximum extent, thus forming an effective fracture surface along the axial direction of roadways [34].

The model for a binding energy tube is shown in Figure 13: holes and slots for cumulative explosion are linearly distributed on the left and right-hand sides of the binding energy tube. After explosives in the binding energy tube are ignited, the tube will curb the propagation of the detonation products. The holes for cumulative explosion linearly distributed in the two sides of the binding energy tube offer the space for pressure relief of the detonation products. As a result, high-energy flows are formed at the holes and impact the hole wall, thus causing the generation of initial cracks in the rock mass.

Thereafter, the high-temperature, high-pressure, and high-speed gases generated due to detonation are still preferentially released from the holes for cumulative explosion following the detonation products in the early period. Moreover, they rapidly propagate along the extension direction of the binding energy tube under the guidance of the slots for cumulative explosion to form air wedges, driving the extension and coalescence of radial initial cracks (Figure 14). Additionally, the detonation products impact the blast hole walls to generate explosion-induced stress waves. Furthermore, compressive stress is generated in the rocks in the radial direction of the blast holes, while a concomitant tensile stress is formed in the circumferential direction. Owing to the tensile strength of rocks being much less than the compressive strength, rocks are fractured under the effect of circumferential tensile stress to form the radial fractures, thus forming an effective fracture surface along such roadways [35].

3.1.2. Coalescence Conditions of Cracks. After cumulative explosions in a single hole, a damaged fracture zone is formed around the hole. To form an effective crack surface along the strike of the roadway roof, it is necessary to perform cumulative explosions with interconnected holes

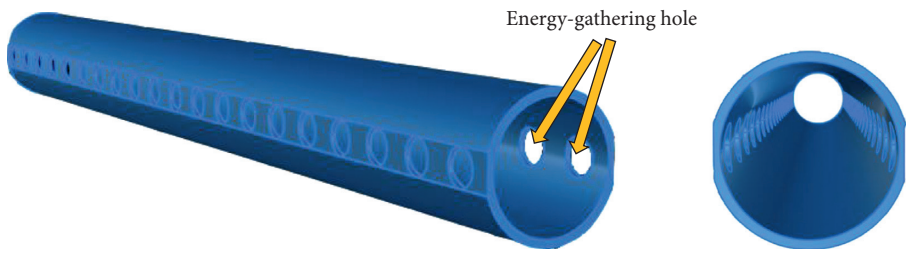

Figure 13: The model for a binding energy tube.

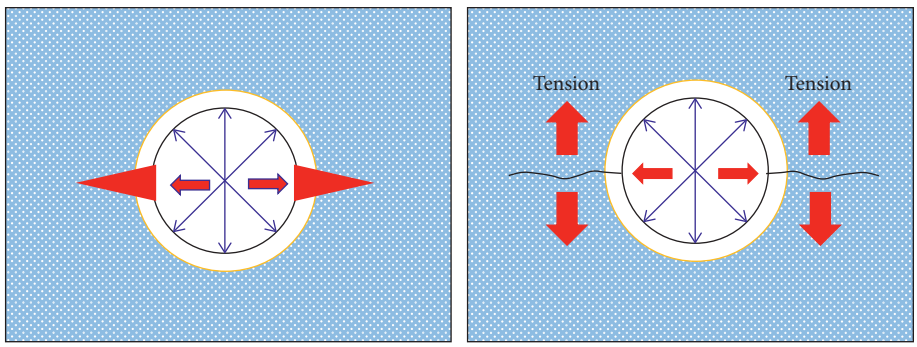

Figure 14: The working principle of a directional presplitting blasting.

and make the damaged fracture zones around adjacent blast holes superimposed. Based on the working principle of directional presplitting blasting, it is feasible to establish a mechanical model for the dynamic rock fracture during cumulative explosion with interconnected holes (Figure 15).

According to the attenuation of the explosion-induced stress waves after explosives are ignited, the damage range R_s of the explosion-induced stress can be calculated as shown in the following equation [36]:

$$R_s = r_b\left[\frac{\lambda p_r}{(1 - D_0)\sigma_t + p}\right]^{1/\alpha}, \tag{14}$$

where λ, D_0, σ_t, p, α, p_r, and r_b refer to the lateral pressure coefficient, the initial damage in rocks, the tensile strength of rock mass, the in-situ stress, the attenuation index of the explosion-induced stress waves in rock mass, the peak pressure of the detonation products, and the radius of the blast holes, respectively.

To guarantee the coalescence of fractures in adjacent blast holes, the spacing d between blast holes should satisfy the following equation [37]:

$$d \le 2r_b\left[\frac{\lambda p_r}{(1 - D_0)\sigma_t + p}\right]^{1/\alpha}. \tag{15}$$

As shown in equation (15), during directional presplitting blasting with interconnected holes, a continuous crack surface should be formed along a specific direction if a reasonable spacing between blast holes is designed, thus effectively cutting the roof strata. The field test (Figure 16) showed that effective cracks are formed between blast holes during directional presplitting blasting with interconnected holes, and the surrounding rocks in other directions remain undamaged.

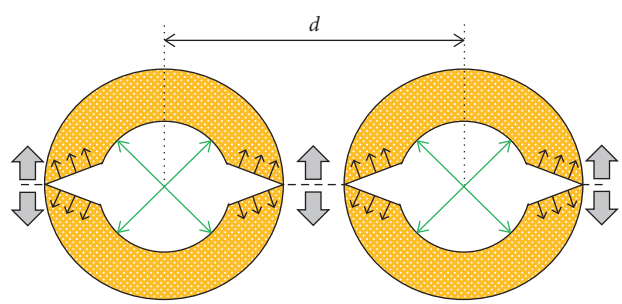

Figure 15: The mechanical model for a directional presplitting blasting with interconnected holes.

3.2. Technological Processes. According to the above analysis, the abutment pressure applied on the coal wall leads to floor heave in roadways, while the vertical pressure of the block wall on the floor can inhibit the floor heave to some extent. In addition, rocks are complex geological bodies containing natural microcracks. Cracked rocks are prone to form macrocracks under external conditions, such as engineering disturbances and multifield coupling stress, and results in rock failure [38]. Due to the complexity of rock mass, it is difficult to change its nonlinear characteristics by manual interference, therefore effective reinforcement is necessary [39]. Therefore, while controlling the floor heave, it is essential to reinforce the roof and block wall to prevent plastic failure.

The stress environment of the coal beside the roadway is improved through pressure relief and support to reduce the damage to the floor and enhance the stability of the block walls, thus achieving the goal of controlling the floor heave. Based on this idea, the comprehensive control technique of

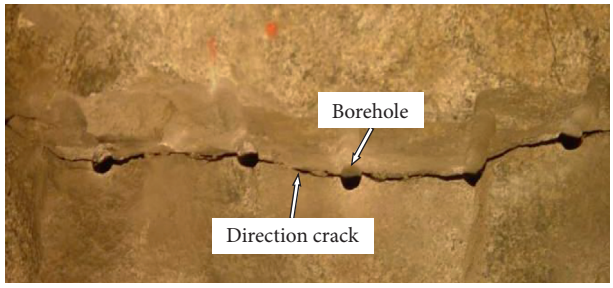

Figure 16: The effect of the directional presplitting blasting with interconnected holes [35].

integrating pressure relief by roof cutting, flexible yielding, roadway wall control with double-direction-control bolts, and roof control with reinforcing anchor cables was proposed to solve the difficulties in controlling the floor heave during GER with building blocks. The technological processes of comprehensive control technique for the floor heave are divided into three steps (Figure 17).

Step 1. Support: Advanced reinforcement of roofs; to prevent the immediate roof from showing quite a large settlement after roof cutting through blasting and thereby influencing the global stability of roadways, it is necessary to reinforce the roadway roof with anchor cables before roof cutting. Moreover, the length of the anchor cables should exceed the cutting depth of the roof not be less than 1.5 m to ensure that the anchored end of the anchor cables lies within the stable roof strata.

Step 2. Cutting: Pressure relief by roof cutting; first, the blast holes are drilled along the designed positions at which it is required that the drilling depth and angle are the same and the blast holes are linearly distributed. The holes are then charged for blasting. The orientation of holes in the binding energy tube should be consistent with the desired direction of extension of cracking. The charge weight in holes, sealing length, and the number of blast holes during each detonation should conform to the design scheme.

Step 3. Protection: Reinforcement of block walls; after pressure relief by roof cutting, the block walls are set with the advance of the working face. While constructing the block walls, the walls are reinforced with double-direction-control anchor bolts combined with ladder-type steel bars; in addition, a certain space for yielding is preserved between walls and the roadway roof, which is filled with flexible materials.

After completing these steps, the overlying strata in the goaf are automatically caved as the working face advances to form a roadway. Under the effect of pressure relief by roof cutting, the gangues in the goaf can support the overlying strata and reduce the rotational subsidence. Furthermore, it can reduce the abutment pressure on the coal wall, thus limiting floor heave in the roadway.

4. Field Test

4.1. Parameter Design. By combining the design with the lithology of the roof and mining mode of the working face, the following design parameters are finally determined:

(1) The roof is reinforced by using two rows of ordinary anchor cables with a length of 7 m made of steel strands with a diameter of 21.6 mm. The first and second rows of anchor cables are, respectively, 600 and 1800 mm from the roof cutting line. The spacing and row spacing of anchor cables are set as 1200×1600 mm (Figure 18(a)).

(2) According to the theory of bulking of a rock mass, the cutting depth of the roof during presplitting is designed as follows [31]:

$$H_F = \frac{M - \Delta H_1 - \Delta H_2}{K - 1}. \tag{16}$$

(i) H_F, M, ΔH_1, ΔH_2, and K denote the cutting height (m) of the roof, the mining height (m), the roof subsidence (m), the floor heave (m), and the bulking factor (1.45) of the roof strata.

(ii) According to the prevailing conditions in Faer Coal Mine, the maximum mining height is determined to be 2.2 m. Ignoring the roof subsidence and floor heave in the goaf, the cutting depth of the roof is calculated to be 4.9 m after substituting the mining height into the equation. Eventually, the depth of the roof cut vertically upward is determined to be 5 m.

(iii) The class-3 emulsion explosives (measuring φ 32×300 mm) are applied during downhole blasting and three rolls of explosives are distributed in each hole (Figure 18(b)). The energy is accumulated along the strike of the roadway with the sealing length of 2 m and the spacing between blast holes of 500 mm.

(3) The block wall is reinforced with double-direction-control anchor bolts. The anchor rod is right-handed full thread steels with φ of 18 mm and a length of 1600 mm. Three rows of anchors are installed: the anchors arranged in the top and bottom of the wall

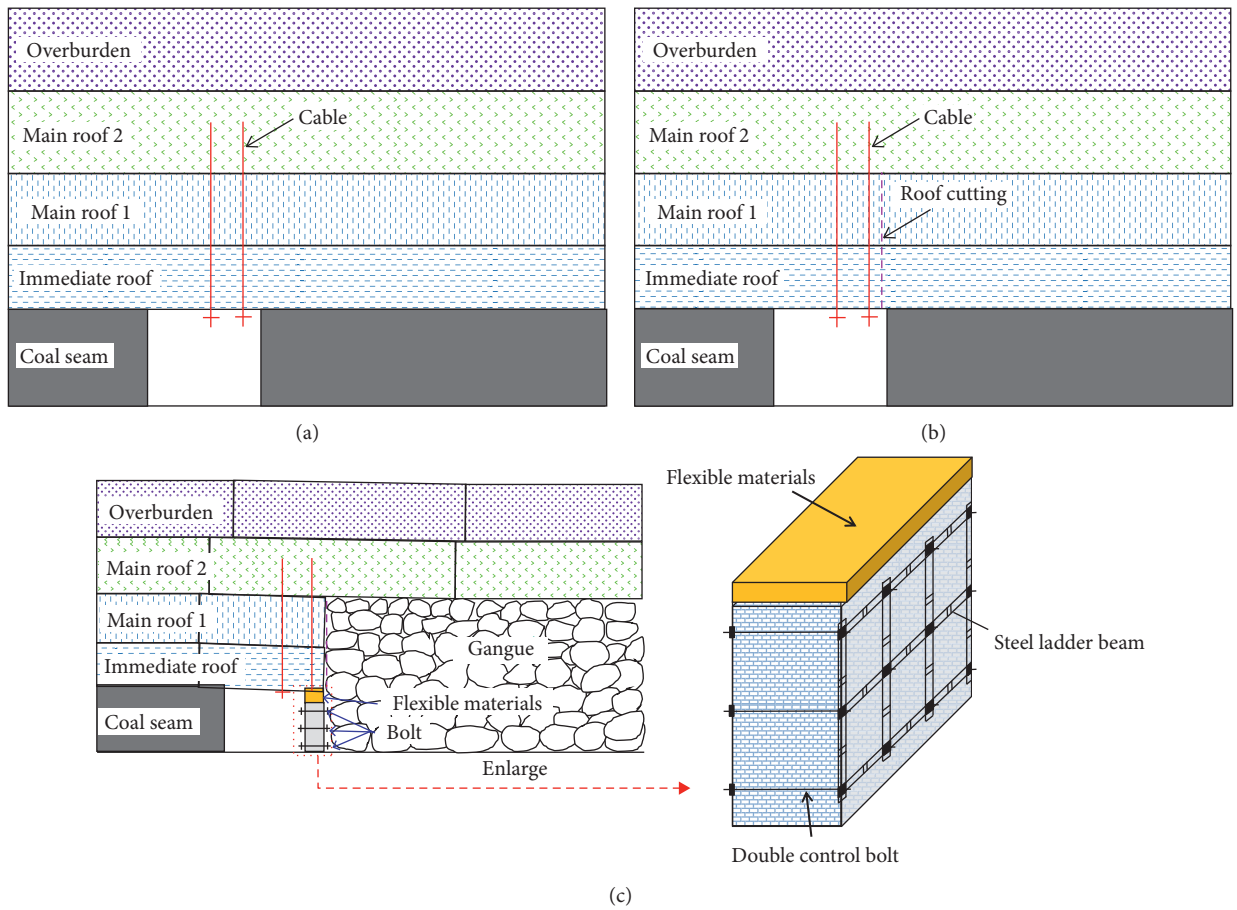

Figure 17: Technological processes. (a) Support: advanced reinforcement of roofs. (b) Cutting: pressure relief by roof cutting. (c) Protection: reinforcement of block walls.

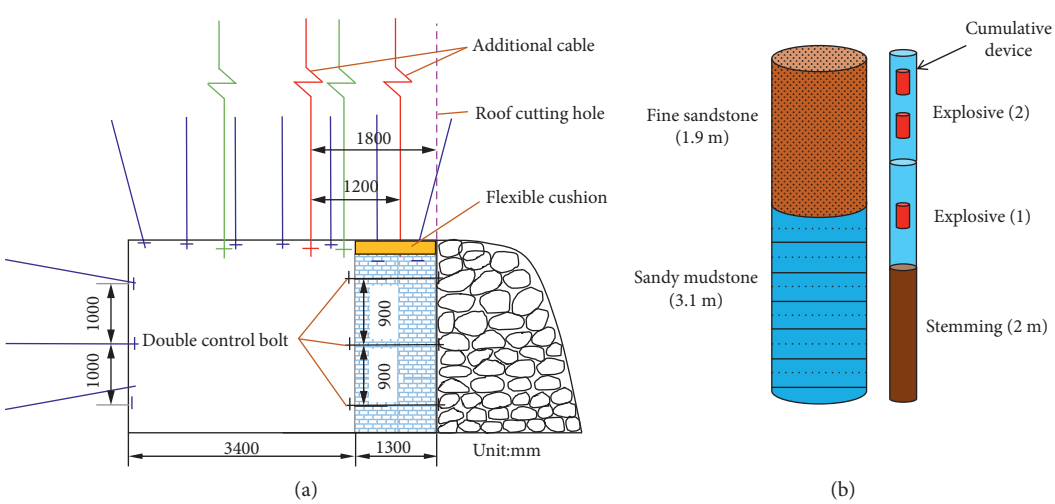

Figure 18: The new control scheme for floor heave and charge structure. (a) The control scheme for floor heave; (b) charge structure.

are both 300 mm from the top of the wall and the floor, with the spacing and row spacing of anchors set to 900 × 1000 mm. The lateral and longitudinal ladder-type steel bars are distributed on the anchors on the outer side of the wall (roadway side) and lapped end-to-end. The lap joint is fixed with the supporting pallet and nuts. The space for the yield of 200 mm is retained between the wall top and the

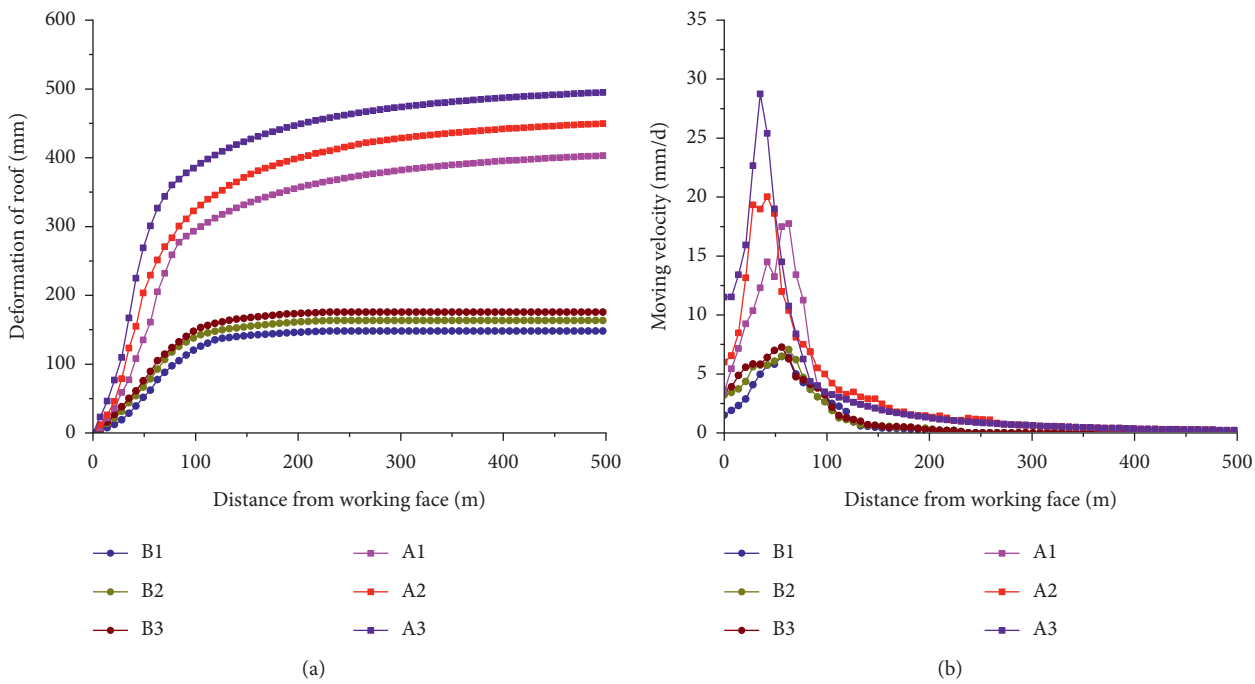

Figure 19: Comparison of the floor deformation before and after the controlling floor heave. (a) Comparison of the amount of deformation. (b) Comparison of the rate of deformation.

Figure 20: The control effect on floor heave. (a) Before control. (b) After control.

roadway roof and filled with high-water-content materials injected by using flexible bags (Figure 18(a)).

4.2. Effect Analysis. The aforementioned technical scheme is applied to the conveyor gateway of No. 31004 working face. After completion, the convergence of the roadway floor during gob-side entry retention is monitored. The distribution of the monitoring points is shown in Figure 4(a). Points A1 to A3 represent the measuring points for the floor heave of the roadway before control scheme, with a spacing of 100 m; points B1 to B3 are monitoring points for the floor heave of the roadway after control scheme, and are at a spacing of 50 m. The rate of convergence of the floor during gob-side entry retention calculated according to the convergence of the floor and a comparison is made with the deformation characteristics of the floor before controlling the floor heave (Figure 19).

Figure 19 shows the comparison of the deformation of the floor before and after controlling the floor heave: the roadway is persistently subjected to the floor heave during gob-side entry retaining under the original technical scheme. It can be seen from research [40] that the floor heave process of roadway has obvious creep characteristics. Until reaching the position 500 m to the rear of the working face, the average floor heave amount at three monitoring points is 450 mm; after applying the new technique for controlling the

floor heave, the floor heave does not occur any longer around a position some 231 m to the rear of the working face. The average floor heave in the roadway is 162.3 mm after controlling the floor heave, and the total floor heave decreases by 64% compared with that before; the average rate of floor heave is 6.4 mm/d within the first 231 m to the rear of the working face under the original technical scheme; after applying the comprehensive control technique for floor heave, the average rate of floor heave is 2.5 mm/d within the first 200 m to the rear of the working face (a reduction of 61%). The roadway floor shows favorable evenness after controlling the floor heave and multiple undercutting operations before roadway retention and reuse are avoided, which can satisfy the requirement on the reuse of the roadway (Figure 20).

5. Conclusions

The mechanical principle of controlling the floor heave based on pressure relief by roof cutting was explored by using theoretical analysis and numerical simulation; furthermore, a novel control technique for floor heave with pressure relief by roof cutting as the core and its technological processes were determined. Moreover, according to the engineering example, the application effect of the technique in engineering practice was discussed. The following conclusions are drawn:

(1) Based on the theory of beam on elastic foundation, a mechanical model for the main roof was established, and the mathematical relationship between the abutment pressure on the coal sides and the caving height of the immediate roof in the goaf was derived. On this basis, the mechanical principle for controlling the floor heave based on pressure relief by roof cutting was attained. To be specific,

(i) Pressure relief by roof cutting increases the caving height of the immediate roof in the goaf. In this case, after being bulked, the caved gangues can be filled into the goaf and support the suspended main roof, which reduces the subsidence amount of the main roof and thus decreases the abutment pressure on the coal sides.

(ii) After the pressure applied to the coal sides drops, the pressure transferred to the roadway floor through the coal sides also decreases. Thus, the floor is not subjected to significant plastic failure, thus controlling floor heave in the roadway.

(2) Through numerical simulation, the pressure-relief effect of the roof cutting through blasting was verified. Under the effect of pressure relief by roof cutting, the abutment pressure within the first 15 m from the roadway sidewall is reduced; after pressure relief by roof cutting, the average peak vertical stress on the floor in the side of the coal wall within the gob-side entry retention range of 0 to 40 m to the rear of the working face decreases by 43.5%, showing a remarkable pressure-relief effect.

(3) A new integrated technique for controlling the floor heave based on pressure relief by roof cutting, flexible yielding, controlling with double-direction-control anchor bolts, and controlling with reinforcing anchor cables centred on pressure relief by roof cutting was proposed. The technological processes involving three steps, *i.e.*, support, cutting, and protection, were summarised.

(4) The field test result shows that the roadway floor becomes stable at a position some 231 m to the rear of the working face after employing the new technique. Compared with the original technique, the average floor heave amount during gob-side entry retention decreases by 64%; the average rate of floor heave within the first 231 m to the rear of the working face drops by 61%, delivering a favorable control effect on the floor heave.

Data Availability

The data used to support the findings of this study are available from the corresponding author upon request.

Conflicts of Interest

The authors declare that there are no conflicts of interest regarding the publication of this paper.

Acknowledgments

This research was funded by the National Natural Science Foundation of China (No. 52074300) and the State Key Laboratory for GeoMechanics and Deep Underground Engineering, China University of Mining & Technology, Beijing (No. SKLGDUEK2020).

References

[1] M. C. He, H. P. Xie, S. P. Peng, and Y. D. Jiang, "Study on rock mass mechanics in deep mining," *Chinese Journal of Rock Mechanics and Engineering*, vol. 24, no. 16, pp. 2803–2813, 2005.

[2] X. Z. Hua, "Study on gob-side entry retaining technique with roadside packing in longwall top-coal caving technology," *Journal of Coal Science and Engineering*, vol. 10, no. 1, pp. 9–12, 2004.

[3] A. Azadeh, M. Osanloo, and M. Ataei, "A new approach to mining method selection based on modifying the Nicholas technique," *Applied Soft Computing*, vol. 10, no. 4, pp. 1040–1061, 2010.

[4] H. Basarir, Y. Sun, and G. Li, "Gateway stability analysis by global-local modeling approach," *International Journal of Rock Mechanics and Mining Sciences*, vol. 113, pp. 31–40, 2019.

[5] D. Y. Zhu, W. L. Gong, Y. Su, and A. Guo, "Application of high-strength lightweight concrete in gob-side entry retaining in inclined coal seam," *Advances in Materials Science and Engineering*, vol. 2020, Article ID 8167038, 20 pages, 2020.

[6] S. R. Xie, E. Wang, D. D. Chen et al., "Failure analysis and control mechanism of gob-side entry retention with a 1.7-m

flexible-formwork concrete wall: a case study," *Engineering Failure Analysis*, vol. 117, 2020.

[7] J. B. Bai, H. Q. Zhou, and C. J. Hou, "Development of support technology beside roadway in goaf-side entry retaining for next sublevel," *Journal of China University of Mining & Technology*, vol. 33, no. 2, pp. 183–186, 2004.

[8] X. Z. Hua, X. Y. Lu, and Y. F. Li, "Prevention and control technology of floor heave in gob-side entry retaining with large section of deep mine," *Coal Science and Technology*, vol. 41, no. 3, pp. 100–104, 2013.

[9] F. Wu, H. Zhang, Q. L. Zou, C. B. Li, J. Chen, and R. Gao, "Viscoelastic-plastic damage creep model for salt rock based on fractional derivative theory," *Mechanics of Materials*, vol. 150, 2020.

[10] M. Yang and X. Z. Hua, "Development orientation and status of floor heave for gob-side entry retaining in China," *Safety in Coal Mines*, vol. 46, no. 12, pp. 213–217, 2015.

[11] J. B. Bai, W. F. Li, X. Y. Wang et al., "Mechanism of floor heave and control technology of roadway induced by mining," *Journal of Mining & Safety Engineering*, vol. 28, no. 1, pp. 1–5, 2011.

[12] M. C. He, G. F. Zhang, G. L. Wang, Y. L. Xu, C. Z. Wu, and Q. D. Tang, "Research on mechanism and application to floor heave control of deep gateway," *Chinese Journal of Rock Mechanics and Engineering*, vol. 28, pp. 2593–2598, 2009.

[13] Q. S. Liu, X. W. Lie, X. Huang, and B. Liu, "Research on the floor heave reasons and supporting measures of deep soft-fractured rock roadway," *Journal of China Coal Society*, vol. 38, no. 4, pp. 566–571, 2013.

[14] G. X. Xie and J. C. Chang, "Study on overcutting-bolting & grouting-backfilling concrete to control the floor heave of deep mine," *Journal of China Coal Society*, vol. 35, no. 8, pp. 1242–1246, 2010.

[15] L. S. Gao, X. J. Zheng, Y. C. Wang et al., "Study on mechanism of pressure relief by deep hole blasing and technique system to control floor heave on the road way floor," *China Mining Magazine*, vol. 29, no. 8, pp. 104–110, 2020.

[16] J. Sun, "Numerical simulation of grooving method for floor heave control in soft rock roadway," *International Journal of Mining Science and Technology*, vol. 21, no. 1, pp. 49–56, 2011.

[17] H. B. Zhao, Y. H. Liu, H. Cheng et al., "Mechanism and prevention measures of asymmetric floor heave in mining roadway of Huipodi coal mine," *Journal of Mining Science and Technology*, vol. 5, no. 6, pp. 638–647, 2020.

[18] J. Lu, P. L. Gong, and P. Li, "Research on the mechanism of floor heave and borehole pressure relief technology in deep soft rock roadway," *Journal of Mining Science ang Technology*, vol. 46, no. 6, pp. 35–41, 2019.

[19] L. Han, S. Y. Hou, and X. K. Zhang, "Mechanism and control technology of floor heave in mining roadway of large dip coal seam," *Safety in Coal Mines*, vol. 49, no. 3, pp. 209–212, 2018.

[20] J. J. Wang, J. H. Wang, X. G. Ma et al., "Research on pressure relief by hydraulic fracturing technology of 68310 ventilation roadway in Duerping coal mine," *Modern Mining*, vol. 36, no. 11, pp. 72–75, 2020.

[21] Z. A. Cao, Y. M. Liu, M. S. Gao et al., "Study on down-ward borehole bolt and grouting reinforcement technology of mine soft and weak mudstone roadway floor," *Coal Science and Technology*, vol. 44, no. 3, pp. 12–17, 2016.

[22] G. Feng, Y. Kang, X. Wang, Y. Hu, and X. Li, "Investigation on the failure characteristics and fracture classification of shale under brazilian test conditions," *Rock Mechanics and Rock Engineering*, vol. 53, no. 7, pp. 3325–3340, 2020.

[23] B. Su, B. Ma, Y. J. Feng et al., "Development of new-style multi-function drilling machine platform and its application in hydro-fracture," *Coal Mining Technology*, vol. 20, no. 4, pp. 140–142, 2015.

[24] M. C. He, W. F. Cao, and R. L. Shan, "New blasting technology-bilateral cumulative tensile explosion," *Chinese Journal of Rock Mechanics and Engineering*, vol. 12, pp. 2407–2051, 2003.

[25] Q. Wang, M. C. He, S. C. Li et al., "Comparative study of model tests on automatically formed roadway and gob-side entry driving in deep coal mines," *International Journal of Mining Science and Technology*, vol. 31, no. 4, pp. 591–601, 2021.

[26] Q. Wang, Y. Wang, M. C. He et al., "Experimental research and application of automatically formed roadway without advance tunneling," *Tunnelling and Underground Space Technology*, vol. 114, no. 3, 2021.

[27] Y. Zhang, H. C. Xu, P. Song, X. M. Sun, M. C. He, and Z. B. Guo, "Stress evolution law of surrounding rock with gob-side entry retaining by roof cutting and pressure release in composite roof," *Advances in Materials Science and Engineering*, vol. 2020, Article ID 1961680, 15 pages, 2020.

[28] C. Zhu, M.-C. He, M. Karakus, X.-H. Zhang, and Z. Guo, "The collision experiment between rolling stones of different shapes and protective cushion in open-pit mines," *Journal of Mountain Science*, vol. 18, no. 5, pp. 1391–1403, 2021.

[29] Z. Q. Song, *Practical Method of Mine Pressure Control*, China University of Mining and Technology Press, Xuzhou, China, 1988.

[30] Y. L. Tan, *Ground Pressure and Strata Control*, China Coal Industry Publishing House, Beijing, China, 2008.

[31] B. Li, R. Bao, Y. Wang, R. Liu, and C. Zhao, "Permeability evolution of two-dimensional fracture networks during shear under constant normal stiffness boundary conditions," *Rock Mechanics and Rock Engineering*, vol. 54, no. 3, pp. 1–20, 2021.

[32] J. Z. Yang, "A study on mechanism of tunnel floor-heave," *Yunnan Metallurgy*, vol. 27, no. 4, pp. 12–15, 1998.

[33] J. F. Pan, "Start-up principium of rock burst in whole coal roadway floor in half-island face," *Journal of China Coal Society*, vol. 36, no. S2, pp. 332–338, 2011.

[34] M. C. He, P. F. Guo, X. H. Zhang, and J. Wang, "Directional presplitting of roadway roof based on bidirectional shaped sharge tension blasting theory," *Explosion and Shock Waves*, vol. 38, no. 4, pp. 795–803, 2018.

[35] X. Y. Zhang, J. Z. Hu, H. J. Xue et al., "Innovative approach based on roof cutting by energy-gathering blasting for protecting roadways in coal mines," *Tunnelling and Underground Space Technology*, vol. 99, pp. 1–12, 2020.

[36] H. Jia and Y. Xu, "Study on stress damage zone in excavation of rock mass," *Chinese Journal of Rock Mechanics and Engineering*, vol. 26, pp. 3489–3942, 2007.

[37] M. C. He, Y. B. Gao, J. Yang et al., "An energy-gathered roof cutting technique in no-pillar mining and its impact on stress variation in surrounding rocks," *Chinese Journal of Rock Mechanics and Engineering*, vol. 36, no. 6, pp. 1314–1325, 2017.

[38] G. Feng, X. C. Wang, M. Wang, and Y. Kang, "Experimental investigation of thermal cycling on fracture characteristics of

granite in a geothermal-energy reservoir," *Engineering Fracture Mechanics*, vol. 235, 2020.

[39] C. Zhu, M. C. He, X. H. Zhang, Z. G. Tao, Q. Yin, and L. F. Li, "Nonlinear mechanical model of constant resistance and large deformation bolt and influence parameters analysis of constant resistance behavior," *Rock and Soil Mechanics*, vol. 42, no. 7, pp. 1911–1924, 2021.

[40] F. Wu, R. B. Gao, J. Li, and C. B. Li, "New fractional variable-order creep model with short memory," *Applied Mathematics and Computation*, vol. 380, 2021.